Analysis of Stellar Activity and Orbital Dynamics in Extrasolar Planetary Systems

Dissertation
zur Erlangung des Doktorgrades
des Department Physik
der Universität Hamburg

vorgelegt von
Sebastian Schröter
aus Lübeck, Schleswig-Holstein

Hamburg
2012

Gutachter der Dissertation:	Prof. Dr. J. H. M. M. Schmitt Prof. Dr. A. Reiners
Gutachter der Disputation:	Prof. Dr. P. H. Hauschildt Prof. Dr. R. Banerjee
Datum der Disputation:	04.05.2012
Vorsitzender des Prüfungsausschusses:	Dr. R. Baade
Vorsitzender des Promotionsausschusses:	Prof. Dr. P. H. Hauschildt
Dekan der MIN Fakultät:	Prof. Dr. H. Graener

Zusammenfassung

Das Forschungsgebiet der extrasolaren Planeten, dessen Anfänge weniger als zwei Jahrzehnte zurückliegen, erlebt zur Zeit eine rasante Entwicklung ausgelöst durch Weltraumteleskope wie CoRoT und Kepler. Diese Observatorien überwachen Tausende von Sternen über lange Zeiträume mit bisher unerreichbarer Genauigkeit und Zeitauflösung, um Sternbedeckungen durch Planeten zu beobachten.

Magnetische Aktivität des Sterns kann einen bedeutenden Einfluss auf die Entwicklung eines Sternsystems mit eng umlaufenden Planeten haben. Die hochenergetische Strahlung führt zu Evaporationsprozessen und Massenverlust in der Atmosphäre des Planeten. Extrasolare Planetensysteme mit einem aktiven Stern sind dann besonders interessant, wenn der Planet die Sternscheibe bei einem Transit bedeckt. In diesem Fall ermöglicht der Planet, die räumliche Auflösung von durch Aktivität bedingten Strukturen in photosphärischen, chromosphärischen und koronalen Schichten der Sternatmosphäre.

Diese Arbeit ist der Untersuchung von Orbitdynamik und stellarer Aktivität in drei außergewöhnlichen Exoplanetensystemen vermöge boden- und weltraumgestützter Photometrie, sowie optischer und Röntgenspektroskopie gewidmet.

Der erste Teil dieser Arbeit handelt von photometrischen Untersuchungen des Exoplanetensystems TrES-2. Aufgrund der fast streifenden Bedeckung durch seinen heißen Jupiter und der geringen Aktivität des Sterns ist dieses System besonderes geeignet, um Veränderungen der Orbitgeometrie über größere Zeiträume zu verfolgen. Unsere Analyse von Vielfarben-Photometrie weist auf eine Inklinationsänderung des Planeten hin, die sich auf den Einfluss eines äußeren Störkörpers von Jupitermasse zurückführen lässt. Nachuntersuchungen anderer Autoren konnten unsere Ergebnisse jedoch nicht bestätigen. Wir klären den Sachverhalt durch eine Analyse der ersten vier Quartale von Kepler-Daten von TrES-2, die keine Hinweise auf eine Inklinationsänderung entsprechender Größe zeigen.

Im nächsten Teil wird der außergewöhnlich aktive Zentralstern im Planetensystem CoRoT-2 betrachtet. Wir charakterisieren die Eigenschaften des Sterns im optischen und Röntgenbereich mittels einer Zeitserie von VLT/UVES-Spektren und einer 15 ks Aufnahme des Chandra-Teleskops, die beide während eines Transits gewonnen wurden. Die optischen Daten werden durch verschiedene Verfahren hochauflösender Spektralanalyse untersucht und erlauben Rückschlüsse auf die stellaren Parameter, Entfernung und Alter des Systems. Die Daten bestätigen, dass CoRoT-2A einen Begleitstern späten Spektraltyps hat, der gravitativ an das System gebunden ist. Die Röntgendaten zeigen koronale Emission von CoRoT-2A, der vermutlich gleichaltrige Begleitstern bleibt jedoch undetektiert. Der heiße Jupiter ist dem intensiven hochenergetischen Strahlungsfeld des Sterns ausgesetzt. Dies führt zu einer langsamen Evaporation der planetaren Atmosphäre.

Bei der Untersuchung der zeitaufgelösten Spektren ist es erstmals gelungen, zeitabhängige Deformationen der chromosphärischen Emissionskerne der Ca II H- und K-Linien während des Transits nachzuweisen. Wir benutzen diesen Effekt, um die räumliche Struktur und Ausdehnung der Chromosphäre von CoRoT-2A zu bestimmen.

Die vorliegende Arbeit schließt mit einer Untersuchung des Planetensystems CoRoT-7, in dem der erste Transit einer Supererde beobachtet worden ist. Wir kombinieren Röntgenbeobachtungen von XMM-Newton und Archivdaten von optischer VLT/UVES-Spektroskopie des Systems, um nachzuweisen, dass die beiden Gesteinsplaneten CoRoT-7b und CoRoT-7c starker UV- und Röntgenstrahlung des Sterns ausgesetzt sind. Wir schätzen den Einfluss der hochenergetischen Strahlung ab, den diese über den Massenverlust des Planeten auf die Entwicklung des Systems gehabt haben kann.

Abstract

The area of exoplanet research, which emerged less than two decades ago, was revolutionized with the advent of space-based photometers like CoRoT and Kepler. These observatories provide long-term monitoring of thousands of stars with unprecendented accuracy and high time resolution to detect transiting planets.

Magnetic activity of the host star can have a substantial influence on the evolution of a planetary system with close-in planets. The high-energy radiation strongly heats the planetary atmosphere leading to evaporation and mass loss. Exoplanetary systems hosting an active star are particularly interesting if the planet transits the stellar disk, because in this case the planet allows to spatially resolve activity-related photospheric, chromospheric and coronal features in the host star's atmosphere.

This work is dedicated to the study of orbital dynamics and stellar activity in three landmark exoplanetary systems using ground- and space-based photometry as well as optical and X-ray spectroscopy.

The first part of this work presents photometric studies of the TrES-2 exoplanetary system. The nearly grazing transit of its hot Jupiter and the low level of variability of the host star make this system particularly suited to study long-term changes in the orbital geometry of the planet. Our analysis of multi-color ground-based photometry indicates a secular change in the inclination of the planetary orbit, which we interpret as the result of an external Jovian mass perturber in the system. Follow-up studies by other authors were, however, unable to confirm our results. We resolve the issue with an analysis of the first four quarters of Kepler data of TrES-2, which clearly rule out an inclination change of the expected size.

The following part focuses on the exceptionally active planet-hosting star CoRoT-2A. We provide a characterization of the star in the optical and X-ray regime using a series of high-quality VLT/UVES spectra and a 15 ks Chandra exposure, both obtained during planetary transits. The optical data are analyzed to derive the fundamental stellar parameters, distance, and age of the system using complementary methods of high-resolution stellar spectroscopy. They confirm the presence of a late-type stellar companion that is gravitationally bound to the system. The X-ray data provide a clear detection of coronal X-ray emission from CoRoT-2A, however, unexpectedly, its likely coeval stellar companion remains undetected. The close-in hot Jupiter is found to be immersed in an intense field of high-energy radiation from its host star, which leads to a gradual evaporation of the planetary atmosphere.

We further provide an analysis of our time-resolved spectroscopic data and report the first detection of a planet-induced deformation of the Ca II H and K emission-line cores during the transit. We use this effect to resolve the spatial structure and extent of the chromosphere of CoRoT-2A.

The work at hand closes with a study of the CoRoT-7 system, known for hosting the first transiting super-earth. X-ray observations obtained with XMM-Newton are combined with archival optical VLT/UVES spectra to show that the rocky planets CoRoT-7b and CoRoT-7c are prone to ultraviolet and X-ray emission from their host star. We estimate the effect that planetary mass loss due to high-energy irradiation could have had on the evolution of the system.

Contents

Part I.

Introduction

1. Preface

"Le silence éternel de ces espaces infinis m'effraie."

– B. Pascal, Pensées

Nature is both staggering and fascinating in its callousness towards the fate of humankind. The 17th century mathematician and physicist Blaise Pascal was perhaps the first philosopher of modern times, who forsaw that sciences would ask too much of us: What is the role of human beings in these silent and infinite spaces we call Universe?

Nearly four centuries later, astronomers are much closer to finding an answer to closely related questions: What makes the Solar System a special place? Are there other worlds like our own? Today, a large number of extra-solar planetary systems is known, some similar to ours, others completely different. The study of these planetary systems is the key to understand our own cosmic history. However, before we take a look at more distant worlds to study their dynamics under the influence of stellar activity and perturbing objects, which is the main focus of this work, let us shortly review the present knowledge about the origin of our own Solar System.

1.1. The formation of the Solar System

The Solar System formed from the gravitational collapse of a giant molecular cloud. One slowly rotating and contracting fragment, the pre-solar nebula, flattened to form a protoplanetary disk, about 100 AU in radius, with a hot and dense accreting protosun at its center (e.g., Williams, 2010).

The disk contains dust grains, which grow through coagulation. The first step is the formation of calcium-aluminium rich inclusions in the protoplanetary disk some 4.569 billion years ago. These inclusions glue together with chrondrules to form the first chondrites. Their age can be estimated based on short-lived, extinct radionuclides like ^{26}Al and ^{60}Fe, which could have been injected into the Solar nebula by a nearby supernova (Gounelle & Meibom, 2007) or locally created due to high-energy irradiation from the active protosun (Williams, 2010). The standard scenario is that the chondrules gather together to form grains and asteroids and finally planetary embryos within several million years. However, recent results indicate that some iron meteorites and achondrites, which are assumed to be pieces of a differentiated body, are in fact as old as the chondrites (Kleine et al., 2005). Thus, it seems likely that planetesimals formed shortly after the formation of the first chondrites and suffered destructive collisions afterwards. These collision products are the seeds for the formation of the planets.

As soon as planets have formed in a protoplanetary disk, they start to migrate towards the host star. While

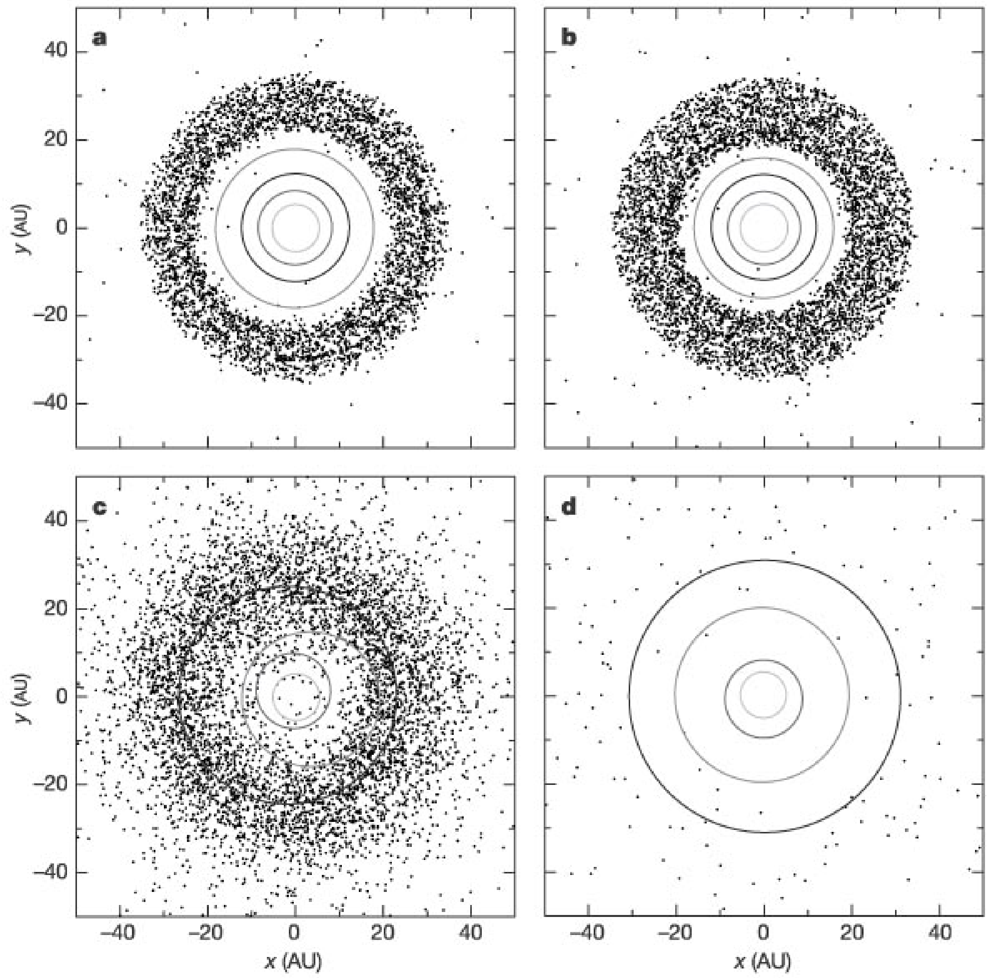

Figure 1.1.: The four panels correspond to snapshots taken from the Nice simulation showing the four giant planets and the planetesimal disk (a) at the beginning of planetary migration, (b) just before and (c) after the beginning of Late Heavy Bombardement, and (d) 200 Myr later. Figure taken from Gomes et al. (2005).

this migration naturally emerges from numerical simulations and is also underlined by the large number of exoplanetary systems with close-in giant planets, this result seems to be in conflict with the present configuration of our Solar System. However, recent numerical models (the *Nice model*; Gomes et al., 2005; Morbidelli et al., 2005; Tsiganis et al., 2005) show that the gas giants in our Solar System can avoid inward migration after the dissipation of the gaseous disk, if they initially were much more closer to each other and on circular orbits. The whole system is encompassed by an outer disk of planetesimals as shown in Fig. 1.1. By scattering planetesimals Uranus, Neptune and Saturn start to migrate outwards while Jupiter migrates inwards.

In case of the terrestrial planets, the growth of the planetary embryos continues and reaches its final stage with the collisions of Mars-sized planetesimals. Near the end of the Earth's formation such a giant impact is thought to have led to the formation of the Moon (Canup & Asphaug, 2001). Isotopic dating using ^{182}Hf yields a formation age of the Moon between 50 and 100 million years (Touboul et al., 2007). Numerical simulations show that the giant impact phase can last up to 100 million years if Jupiter and Saturn were initially on circular orbits as proposed by the Nice model. Additionally, circular initial orbits for the giant planets enable the terrestrial planets to accrete water-rich material from the Main Asteroid Belt, which could explain the existence of water on the terrestrial planets today (O'Brien et al., 2006).

In its T Tauri phase the protosun accretes matter from the surrounding protoplanetary disk and contracts until the core reaches conditions required to ignite hydrogen burning. About 50 million years after its formation, the Sun arrives in a state of hydrostatic equilibrium and enters the main-sequence, where it resides as long as the fusion process can supply sufficient energy to balance the energy loss due to radiation.

The Nice model also explains the present configuration of the Solar System. About 500 million years later, Jupiter and Saturn cross their 2:1 mean motion resonance, their eccentricities increase and lead to a destabilization of the entire system. Due to mutual interactions the outer giants enter the disk of planetesimals causing the Late Heavy Bombardment in the inner Solar System. After another 100 million years the system stabilizes in a configuration close to our present Solar System (cf., Fig. 1.1).

We have evidence from fossil founds that only a few hundred million years later, about 3.8 billion year ago, life emerged on Earth (Mojzsis et al., 1996). In view of this highly dynamic (in fact, chaotic) formation history of our own Solar System, we come back to our initial question, which we now put more precisely: Is there something special about *the evolution of* our Solar System? This question can be answered by studying exoplanetary systems in different configurations and evolutionary states.

1.2. Outline of this work

The work at hand is split into three parts. The first part comprises an introduction to the active field of extrasolar planet reseach and the study of stellar activity in young and solar-like cool stars. It closes with a chapter summarizing practical aspects regarding the analysis of optical high-resolution spectra.

In the second part, I reproduce five publications dealing with different aspects of three landmark extrasolar planetary systems. The first chapter is dedicated to the TrES-2 exoplanetary system. The nearly grazing transit of its hot Jupiter and the low level of stellar variability of the evolved host star make this system particularly suited to study long-term changes of the orbital geometry of the planet. The studies in the second chapter focus on the active planet-hosting stars CoRoT-2A and CoRoT-7A. Both stars show a substantial level of activity, which can be traced through all layers of the stellar atmosphere and has an influence on the evolution of the close-in planets.

The third part provides a synopsis of the results presented in this work. I discuss some open questions and give an outlook on possible future studies.

2. Extrasolar planets

Since the dawn of homo sapiens $200,000$ years ago, the perception of the night sky raised both spiritual awe and scientific curiosity. While the majority of stars appeared fixed on a rotating firmament, there were bright objects that changed their positions on timescales comparable to the human lifetime. The prediction of the positions of these wandering stars or planets (from Greek $\pi\lambda\alpha\nu\acute{\alpha}o\mu\alpha\iota$ - "wandering") and their meaning have since inspired generations of human beings.

2.1. History of the observation of planets

First records of systematic observations of the planets (in its broadest sense including the Sun and the Moon) date back to the Neolithic and Bronze Age. Among the oldest known Neolithic structures is the *Goseck circle* found in Goseck in Saxony-Anhalt, Germany, dating back to the 5th millenium BC. The structure consists of palisade rings with gates in well-defined places and is considered the earliest solar observatory currently known in the world (Bertemes et al., 2004). Only 20 kilometres away from the site the *Nebra sky disk* was found (Meller, 2002). The use of rare materials like gold underlines its religious and cultural significance. Dating back to the Bronze Age, the disk is possibly the oldest astronomical instrument, demonstrating the astronomical knowledge and abilities of the people of the European Bronze Age to observe the yearly course of the Sun.

The first civilization known to systematically record the positions of the planets were the Babylonians in the first and second millennium BC. The Babylonian astronomers realized periodicities in the movement of the planets and applied mathematics to predict their positions. Centuries of astronomical records were found in the form of cuneiform tablets known as the *Enuma Anu Enlil*. The *Tablet of Ammisaduqa*, listing the risings of Venus over 21 years, dates back to the seventh century BC. Besides Venus and Mercury also the outer planets Mars, Jupiter, and Saturn were all identified by Babylonian astronomers (Hunger, 1992). The Enuma Anu Enlil also comprises a compilation of omens and their relation with celestial phenomena, as in Mesopotamian mythology stars and planets were associated with deities. In fact, the Babylonian astrolatry had a strong influence on the Hellenistic world and laid the foundation for Western astrology.

Babylonian astronomers worked strictly empirically. They were mainly concerned with the ephemerides of the planets; their models usually did not involve philosophical speculations and *a priori* assumptions, for example, regarding the geometric structure of the Cosmos. This changed during the first century BC, when the Greeks used their own geometrical and mathematical schemes to predict the positions of the planets. While their geometric models offered a much more comprehensive approach to the diversity of empirical observations, they also allowed for cosmological speculations. For the first time, humankind tackled the question about Earth and its position in the Universe based on astronomical observations.

While most Greek philosophers assumed the Earth to be the center of the Cosmos orbited by celestial bodies, Aristarchos of Samos, a Greek astronomer and mathematician during the third century BC, was the first to think of a heliocentric model of the Solar System. He also realized the implications of his model: Either the stars should show an observable parallax effect as the Earth moves around the Sun or they should be much farther away than was assumed at that time. Since stellar parallaxes are only detectable with telescopes, his speculations, although correct, could not be proven at his time.

A compendium spanning nearly a millenium of astronomical observations together with a complete and comprehensive treatise based astronomical models was given by Claudius Ptolemy, who worked as a librarian in the famous *Ancient Library of Alexandria* in the second century AD. In his *Almagestus* (e.g., Toomer, 1998), Ptolemy rejects the heliocentric models as did most of his predecessors. Due to its completeness and usefulness the Almagest remained the authoritative astronomical "review" for almost thirteen centuries.

With the fall of the Western Roman Empire during the early Middle Ages the ancient scientific texts written in Greek became inaccessible to the Latin-speaking West. The social and scientific development suffered from the loss of a unified cultural context, which in the following centuries was replaced by the Christian Church. However, it was the medieval tradition of scholasticism that established the use of reason in fields like theology, philosophy, and science providing the foundation for the *Scientific Revolution*. The invention of printing and the rediscovery of Greek scientific texts during the Renaissance made the ancient knowledge widely available and allowed to share new ideas.

In 1543 Nicolaus Copernicus, mathematician, astronomer, and Catholic cleric published his epochal work *De revolutionibus orbium coelestium* presenting a heliocentric model (Copernicus, 1543). Copernicus demonstrated that the observed motions of celestial objects can be explained without putting the Earth at rest in the center of the Universe. His model was elaborated and expanded by Johannes Kepler, who formulated the fundamental laws of planetary motion in his works *Astronomia nova* and *Harmonices Mundi* (Kepler, 1609, 1619). Following Kepler's prediction, Pierre Gassendi observed the first transit of Mercury in 1631, and Jeremiah Horrocks studied the Venus transit in 1639. Kepler's works and systematic astronomical observations by Galileo Galilei using his improved telescope provided the foundations for Isaac Newton's theory of gravitation (Newton, 1687). While Kepler's laws of planetary motion were only empirical observations without a fundamental understanding of the physical principles behind the three laws, Newton's theory showed that planets move in ellipses due to the force of gravity.

While the two-body problem had been solved by Newton, the mutual gravitational interactions of three bodies remained a central topic in mathematical physics. In 1772 Joseph-Louis Lagrange attempted to solve the three-body problem analytically leading to the discovery of Lagrangian points. He further deleveloped analytical mechanics and applied perturbation theory to celestial mechanics to determine secular and periodic variations of the orbital elements of the planets (Lagrange, 1811).

After the discovery of Uranus by Herschel & Watson (1781), astronomers of the 19th century used the methods of perturbation theory and celestial mechanics to predict the orbits of planets, comets, and asteroids in the Solar System. Indepently of each other Adams (1846) and Le Verrier (1846) attributed irregularities of Uranus' orbit to the gravitational attraction of another perturbing body. In the same year, Galle (1846) discovered planet Neptune within 1° of the position predicted by Adams and Le Verrier. Thus, Neptune became the first planet to be predicted mathematically before being directly observed.

Le Verrier was also the first to report that the slow precession of Mercury's orbit could not be completely explained by perturbations due to the known planets alone (Le Verrier, 1859). He speculated that another planet might exist in an orbit even closer to the Sun; other explanations included a slight oblateness of the Sun. Mercury's anomalous precession was eventually explained by Einstein's general theory of relativity in his famous paper *Die Grundlage der allgemeinen Relativitätstheorie* (Einstein, 1916). Sixty years later, Hulse & Taylor (1975) discovered the first binary pulsar, whose orbit evolution not only requires general relativity, but, in fact, provides indirect evidence for the existence of gravitational radiation (Weisberg & Taylor, 2005)—a discovery that led to the 1993 Nobel Prize in Physics.

2.2. Hunting extrasolar planets

Within the last 20 years the search for extrasolar planetary systems has become a main impetus for astrophysical research. This section deals with the most important methods that are used to discover and study extrasolar planetary systems and introduces ground- and space-based missions dedicated to the detection of exoplanets. Although still young, the field of exoplanetary research already allows for an historical approach, highlighting the mutual inspirations of different lines of research and fallacies encountered on the way to a total number of nearly 800 extrasolar planets discovered so far (Schneider, 2012).

2.2.1. Astrometry

The heliocentric hypothesis raised by the Scientic Revolution waited for its observational confirmation until the beginning of the 19th century, when Bessel (1838) used astrometric measurements to determine the parallax of 61 Cygni to be 0.3 arcsec proving that the parallax of distant stars is indeed greater than zero.

According to Newton's theory of gravity, planet and star both orbit the barycenter of the system. The motion of a star due to the gravitational influence of a planet thus provides an indirect method to detect the planet. In principle, precise astrometric measurements should therefore allow to detect signatures of planets orbiting the star. However, for a Jupiter mass planeqt in a 1 AU orbit around a nearby (10 pc), solar-like star the apparent motion of the star in the sky is on the order of 10^{-7} arcsec. Such a degree of precision is difficult to achieve even with the largest and most advanced telescopes. As a result, astrometric methods produced only a small number of disputed detections; so far, no such planet has been confirmed.

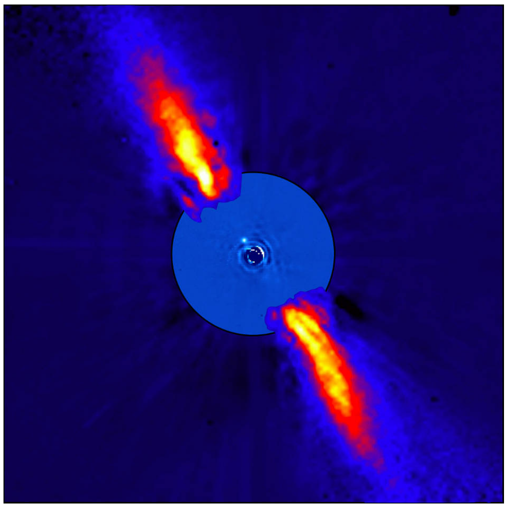

Figure 2.1.: Composite image of β Pictoris in near infrared after subtraction of the stellar halo. The outer part observed with the ESO 3.6 m telescope shows a circumstellar disk, the inner part reveals thermal emission from the young, hot planet imaged with NACO/VLT (Credit: ESO/A.-M. Lagrange et al.).

2.2.2. Pulsar timing

Since the discovery of the first pulsar LGM-1 by Bell & Hewish (1967) the study of these highly magnetized, rotating neutron stars became an important branch of astronomy. The hypothesis that the regular millisecond pulses facilitating the detection of LGM-1 were signs of an extraterrestrial civilization was soon discarded. However, the immense regularity and timing precision of the pulsar measurements paved the way for the first unambiguous detection of two extrasolar planets: Wolszczan & Frail (1992) reported the detection of millisecond changes in the light travel times due the reflex motion of the pulsar PSR B1257+12, which were interpreted as being caused by two orbiting planets in the terrestrial mass regime. The signal discovered by Wolszczan & Frail provided strong evidence for the existence of planets in orbit around other stars and marks the starting point of a 20 year long journey to find the first Earth-like planet orbiting a solar-like star.

2.2.3. Direct Imaging

In a sense, direct imaging is the oldest technique to detect planets. Indeed, the method proved valuable for our understanding of the formation of planetary systems. Planets form in cicumstellar disks, which result from the gravitational collapse of an interstellar gas cloud. Such a circumstellar disk has been observed optically around the fourth-magnitude star β Pictoris (Smith & Terrile, 1984, see Fig. 2.1).

The detection of extrasolar planets via direct imaging is challenging due to the immense brightness contrast between the star and its planet and the small angular separation between them. The planet reflects star light depending on its albedo and shows intrinsic thermal emission; the method thus works best for young planets emitting infrared radiation in large orbits. Several direct imaging techniques like coronography and nulling interferometry have been developed, which allow to disentangle the planetary and stellar emission. In recent years, the field saw a rapid development due to instrumental improvements, e.g., in adaptive optics correction, so that 31 extrasolar planets have been imaged so far (Schneider, 2012). One of the most spectacular findings was the detection of a planet around the A4-type star Fomalhaut, whose orbit coincides with the inner edge of the debris disk surrounding the star (Kalas et al., 2008). However, recent results by Janson et al. (2012) indicate, that the planet interpretation could be erroneous.

2.2.4. The radial-velocity method

The starting point of a new era of exoplanet research was set with the first succesful application of the long-known radial-velocity method. Struve (1952) proposed the use of powerful spectrographs to detect distant planets. He described how a large Jupiter-like planet causes its parent star to wobble slightly as the two objects orbit around their common center of mass. The continuous change of the host star's orbital radial velocity, v_{rad}, leads to small Doppler shifts of the spectrum according to

$$\frac{\Delta\lambda}{\lambda} = \frac{v_{\mathrm{rad}}}{\mathrm{c}} \tag{2.1}$$

with the velocity of light, c.

Assuming the planet to orbit its host star in a circular orbit, the radial velocity varies sinusoidally with the orbital period, P. The radial-velocity semi-amplitude, K, is related to the exoplanet's mass, M_p, and the mass of the host star, M_s, according to

$$K = 28.4\ \mathrm{m\,s^{-1}} \left(\frac{M_p \sin i}{M_J}\right) \times \left(\frac{M_s}{M_\odot}\right)^{-2/3} \left(\frac{P}{\mathrm{years}}\right)^{-1/3} \tag{2.2}$$

where i denotes the inclination of the planetary orbit, and M_J and $M_\odot$ are masses of Jupiter and the Sun, respectively. Struve foresaw that such a periodic variation could be detectable with the most sensitive spectrographs as displacements in the spectral lines only if these extrasolar Jovian planets are on very close-in orbits around their host stars—much unlike the situation in our own Solar System.

The first published discovery of a planetary radial-velocity signal was reported by Campbell et al. (1988). Their observations suggest a planet orbiting the star γ Cephei. However, their observations were at the very limit of the instrumental capabilities at the time, so that astronomers remained skeptical about this and other similar observations. The major drawback of the radial-velocity method is apparent from Eq. 2.2: The measurement only yields an estimate of the projected planet mass, $M_p \sin i$. The true mass depends on an estimate of the inclination of the planet's orbit. If such an estimate is not available, the method can only yield a lower limit on the planetary mass. Therefore, it was assumed that most of the planet candidates were instead brown dwarfs like the object found by Latham et al. (1989), who detected a companion of minimum mass 11 M_J around HD 114762.

The findings by Campbell et al. were confirmed 15 years later by Hatzes et al. (2003). In the mean-

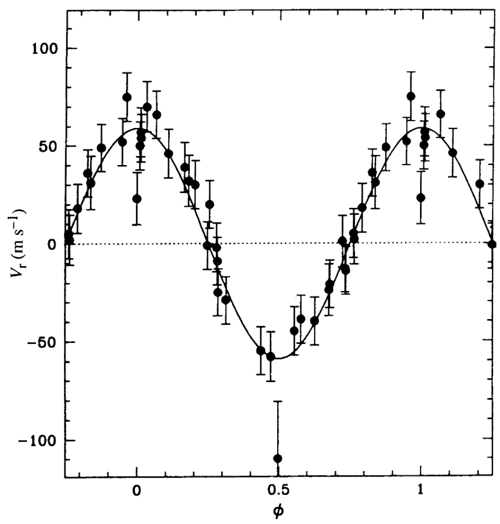

Figure 2.2.: Radial-velocity curve of 51 Pegasi. The overall motion of the system is subtracted. The continuous line is a model for an object with $M_p \sin i = 0.47\ M_J$ in a 4.2 d circular orbit. Figure taken from Mayor & Queloz (1995).

time, Mayor & Queloz (1995) detected an extrasolar planet of only $M_p \sin i = 0.468\ M_J$ around 51 Pegasi (see Fig. 2.2). The planet—nicknamed *Bellerophon* after the hero of Greek mythology, who rode the untamed, winged horse Pegasus to kill the Chimera—became the first of a long series of discoveries of large, close-in planets, which are today known as *hot Jupiters*.

To obtain precise radial-velocity measurements, small wavelength shifts must be measured with high accuracy. The spectral resolving power of a spectrograph is given by

$$R = \frac{\lambda}{\Delta\lambda}, \tag{2.3}$$

which for high-resolution spectrographs is on the order of 100,000. Combining this relation with Eq. 2.1 yields a resolvable radial-velocity shift of 3 $\mathrm{km\,s^{-1}}$, which is several orders of magnitude larger than the typical signal (cf. Eq. 2.2). The method thus requires subpixel accuracy, which can only be obtained if a multitude of spectral lines is considered and the spectrum has sufficiently high signal-to-noise ratio.

Besides a stable optical configuration of the involved instruments, high-precision RV measurements require an accurate wavelength calibration realized by using superimposed absorption line spectra (e.g., using an Iodine gas cell) or by additional calibration spectra obtained from a ThAr lamp (Marcy & Butler, 1992; Butler et al., 1996). It is also possible to use telluric lines due to the Earth's atmosphere as simultaneous reference spectrum (Griffin & Griffin, 1973). These lines, which are due to gases like water vapour, oxygen, or carbon dioxide are imprinted on all ground-based spectral data and can be used to attain a precision on the order of 10 $\mathrm{m\,s^{-1}}$ limited by variations of the atmospheric conditions (Snellen, 2004; Figueira et al., 2010).

Alternatively, the calibration spectrum is fed to the spectrograph via a second fibre and recorded simultaneously with the science spectrum. The radial velocity is then computed by cross-correlating the stellar spectrum with a synthetic template (Zucker, 2003) and correcting it for the instrumental drift as measured with the second calibration fibre. The HARPS spectrograph, working according to this principle, reaches a precision better than 1 $\mathrm{m\,s^{-1}}$ (Lovis et al., 2006). It paved the way for the detection of planets with only a few Earth-masses, the so-called *super-earths* (Vogt et al., 2010).

The detectability of a planetary radial-velocity signature in the stellar spectrum strongly depends on the properties of the observed star. While early-type stars have only few absorption lines, late-type stars tend to be faint and show substantial activity, like starspots, introducing additional radial-velocity scatter (Hatzes, 1999; Desort et al., 2007; Huber et al., 2009b). Activity-induced radial-velocity jitter can be reduced for cool M dwarfs using near-infrared spectra, where the temperature contrast between the spot and the photosphere is lower (Reiners et al., 2010). This approach is pursued by the CARMENES project (Quirrenbach et al., 2010), a combined optical/near-infrared spectrograph at the German-Spanish Calar Alto Astronomical Observatory.

2.2.5. The transit technique

The unanticipated fact that many Jovian exoplanets were found to have very short periods stimulated the search for planets transiting the disk of their host star, a technique which astronomers had long considered inappriate to detect extrasolar planetary systems. Their scepticism was not without reason, since the detection of an exoplanetary transit requires continuous and well-calibrated photometric observations and relies on the fortunate instance that the stellar system is seen close to edge-on. Hence, planetary transits were seen as low probability events, both geometrically and temporally.

The detection of a large number of hot Jupiters using the radial-velocity method showed that the observation of planetary transits is worthwhile even with ground-based equipment. Charbonneau et al. (2000) detected the first transit of an extrasolar planet in HD 209458, a hot Jupiter of 1.3 R_J in an 0.046 AU orbit around a G0-type dwarf. In concert with radial-velocity measurements the mass of the planet could be determined to be 0.69 M_J (Henry et al., 2000). The light curve is shown in Fig. 2.3, which also illustrates the principle of the transit method: The nominal flux level of the star temporarily decreases, as the planet occults a fraction of the stellar surface during its transit in front of the stellar disk. Neglecting limb darkening, the depth of the transit is given by the ratio of the sky-projected area of the planet and the star,

$$\frac{\Delta I}{I} = \left(\frac{R_p}{R_s}\right)^2 , \tag{2.4}$$

where R_p and R_s denote the planetary and stellar radii. The light curve of HD 209458 shows transits with a depth of around 1.5 % lasting for around 3 hours and recurring repeatedly at intervals given by the orbital period, P. Because such dips in the light curve can be mimicked for example by grazing binaries or eclipsing binaries in front of a background star, transit measurements require confirmation by radial-velocity measurements.

The early studies on HD 209458 and its planet (named *Osiris*) were corroborated by the follow-up paper by Brown et al. (2001), who used the Hubble Space Telescope to obtain the first space-based transit light curve. Their photometric data is shown in Fig. 2.4. The data confirm the system parameters derived in earlier studies and demonstrate the supremacy of space-based photometric transit studies.

To systematically search for transits in a large number of stars, several wide-field transit search programs

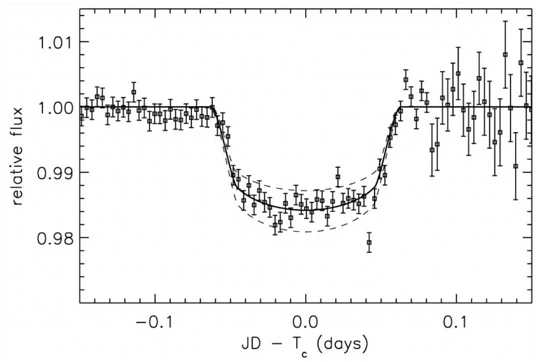

Figure 2.3.: First transit of an exoplanet around HD 209458. The continuous line shows a transit model for a planet of 1.27 R_J (dashed: scaled by $\pm 10\,\%$) with inclination of 87.1° and semimajor axis of 0.047 AU. Figure taken from Charbonneau et al. (2000).

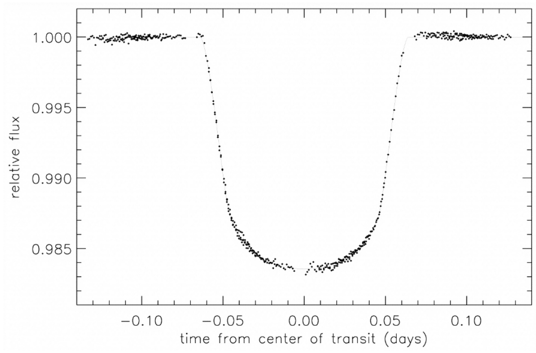

Figure 2.4.: Four transit light curves of HD 209458b obtained with the Hubble Space Telescope phase-folded on the orbital period of 3.5 d. The noise is on the order of 10^{-4} for each 60 s integration. Figure taken from Brown et al. (2001).

have been iniated: The Hungarian Automated Telescope Network (HATNet; Bakos et al., 2002), the Trans-atlantic Exoplanet Survey (TrES; Alonso et al., 2004), the Wide Angle Search for Planets (SuperWASP; Pollacco et al., 2006), the XO Project (McCullough et al., 2006), and only recently the Qatar Exoplanet Survey (Alsubai et al., 2011). All these ground-based surveys aim at covering the entire sky to provide a compilation of all detectable transiting extrasolar giant planets down to a limiting magnitude of about 15 mag.

It is immediately clear from Eq. 2.4, that the detection of Earth-sized planets via the transit method requires relative photometric accuracies of 10^{-5}. Furthermore, the host star has to be monitored continuously over much longer time scales. This is beyond the abilities of ground-based surveys, which are prone to atmospheric disturbances, weather conditions, and the day and night cycle. Therefore, the next logical step was the development of space-based photometers, that can monitor the brightness of thousands of stars with unprecedented time coverage, accuracy, and temporal cadence.

2.2.6. The CoRoT and Kepler missions

The study of transiting extrasolar planets around solar-like stars has been revolutionized with the advent of two space-based missions, CoRoT and Kepler, providing long-term photometric data of a large number of stars. Both missions are dedicated to the study of asteroseismology and the search for extrasolar planets.

The CoRoT mission

The CoRoT space telescope (Fig 2.5, Auvergne et al., 2009) is a project led by the French CNES and ESA launched in December 2006. CoRoT is the first space telescope dedicated to the detection of extrasolar planetary systems and asteroseismological measurements of oscillations in solar-like stars. It is sched-

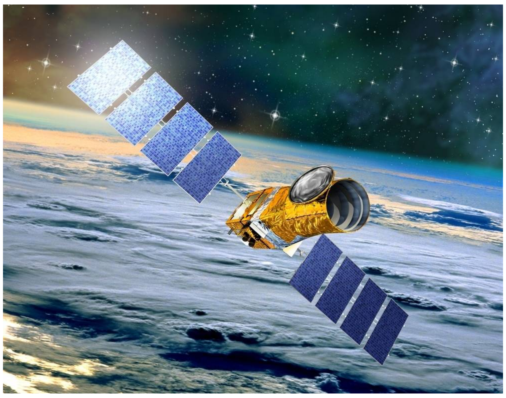

Figure 2.5.: Artist's view of the CoRoT space telescope (Credit: CNES/Octobre 2005/Illus. D. Ducros).

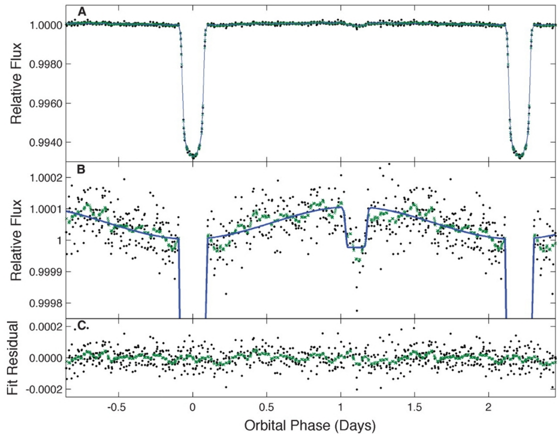

Figure 2.6.: Phase-folded light curve of HAT-P-7b comprising 10 d of Kepler data. Besides the primary transit, the light curve also reveals stellar light reflected from the planet and the secondary transit. Figure taken from Borucki et al. (2009)

uled to operate at least until 2013. The telescope consists of an optical telescope with a diameter of 27 cm and four CCD detectors, two of which are used for the search of exoplanets. A prism in front of these CCDs disperses the light into a small spectrum providing color information in three spectral bands.

CoRoT has been placed in a polar low-Earth orbit and observes perpendicular to its own orbit to avoid Earth occultations. In order to avoid the Sun entering its field of view, CoRoT observes only two areas directed towards the galactic center and anticenter for half a year. In these fields, CoRoT monitors the brightness of 10,000 stars with visual magnitudes ranging from 11 to 16, simultaneously providing up to 150 days of uninterrupted photometric data at a temporal cadence of up to 32 s. After each of these *long runs* the pointing of the telescope is slightly changed, so that no field is observed twice.

CoRoT reaches noise levels down to 0.1 mmag on timescales of 2 hours for targets of 12th magnitude. Its observed performance therefore suffices to detect transits of super-earth planets in short period (< 3 d) orbits around bright stars (Aigrain et al., 2009).

The Kepler mission

The Kepler space telescope (Koch et al., 2010; Borucki et al., 2010) was launched by NASA in March 2009, its foremost mission being the detection of Earth-sized planets in the habitable zone around solar-like stars. Further mission goals are to provide estimates of the frequency of extrasolar planets in our Galaxy and to characterize these worlds with unprecedented accuracy. To accomplish this task the spacecraft is equipped with a photometer consisting of a 1.4 m primary mirror, a 0.95 m aperture, and 42 CCD detectors. Its wide field of view of 115 square degress allows to simultaneously monitor the brightness of 150,000 stars.

The Kepler spacecraft was placed into an Earth-trailing orbit with an orbital period of 372.5 days and points to a field in the constellations of Cygnus, Lyra, and Draco well off the ecliptic. Kepler thus provides continous photometry of a large number of stars over the whole time of observation, which is currently planned to be at least 3.5 years. Most light curves are binned on board to a sampling of 29.4 min to reduce the required data telemetry. Only a small number of up to 512 stars is observed at a shorter cadence of 58.8 s. The noise level for stars of 12th magnitude is typically on the order of $10 - 20$ ppm and is dominated by intrinsic stellar noise (Gilliland et al., 2010, 2011).

An example of the superior quality of the Kepler data is provided by Fig. 2.6 showing the first ten days of Kepler photometry of the transiting hot Jupiter HAT-P-7b, which clearly displays phase variations of light emitted by the planet Borucki et al. (2009).

2.2.7. The Rossiter-McLaughlin effect

A transiting extrasolar planet leaves a characteristic imprint on the spectroscopically inferred radial-velocity variation of the host star, which can be analysed using time-resolved spectroscopy obtained during the transit event. The idea dates back to 1893, when Holt (1893) speculated on the possibility to measure stellar rotation in spectra of partially eclipsing binary systems. While the spectral lines of both stars are broadened in a symmetrical way due to the stellar rotation, their mutual occultations break this symmetry. Two decades later, Schlesinger (1910) found indications of anomalous radial-velocity shifts of eclipsing binary systems during eclipse, which were later confirmed by

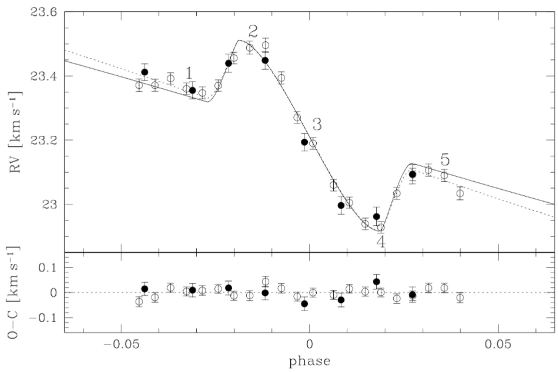

Figure 2.7.: Rossiter-McLaughlin effect for CoRoT-2 obtained with HARPS (circles) and SOPHIE (dots). The solid line shows the best-fit model indicating $\lambda = 7.2°$. Figure taken from Bouchy et al. (2008).

Rossiter (1924) and McLaughlin (1924). The Rossiter-McLaughlin effect originates in the occultation of different parts of a rotating stellar surface. While stellar rotation causes symmetric Doppler broadening of the spectral lines, the occultation of individual fractions of the stellar surface during a transit leads to an asymmetry in the lines profiles. This deformation is usually detected as an anomalous variation of the inferred radial velocity.

With the confirmation of the first transiting extrasolar planets using the radial-velocity technique it became clear, that the Rossiter-McLaughlin effect could be of tremendous use for the study of exoplanetary systems, where the planet acts as nearly perfect black shutter (Schneider, 2000). The first spectroscopic transit was then observed by Queloz et al. (2000) in HD 209458.

The Rossiter-McLaughlin effect allows measurements of the angle λ between the sky-projected spin axis of the star and the sky-projected orbital plane normal of the transiting planet, which can be used to constrain the true obliquity of the stellar spin axis with respect to the planetary orbit (Winn et al., 2005). Figure 2.7 shows an example measurement for the transiting exoplanetary system CoRoT-2.

Since the Rossiter-McLaughlin effect scales with the stellar rotation velocity, its amplitude is much larger for rapidly rotating stars, so that in some cases it can even exceed the orbital radial-velocity amplitude (Anderson et al., 2010). It was expected that planets should orbit the star in the same direction as the star is spinning. Surprisingly, quite a number of extrasolar planetary systems were found to show indications for strong spin-orbit misalignment, some of them even displaying configurations with a retrograde planetary orbit (Hébrard et al., 2008; Triaud et al., 2010). There is an ongoing effort to construct evolutionary scenarios, that are able to explain these findings. While the discussion is far from settled, the current paradigm is that the formation of planetary systems with hot Jupiters is governed by the combined action of tidal processes and few-body gravitational dynamics that yield substantial disk migration (Winn et al., 2010; Morton & Johnson, 2011).

The characteristics of the Rossiter-McLaughlin effect depend on various parameters like the alignment of the planetary orbit and the stellar rotation axis, the ratio of stellar and planetary radius, and the structure of both the planetary and the stellar atmosphere. Analytical models of the effect are based on the estimation of the first moment of distorted spectral lines and have been presented by Ohta et al. (2005) and Giménez (2006). Although they are commonly applied in modeling, these models may not exactly reproduce observational results which are typically obtained by cross-correlation techniques (e.g., Triaud et al., 2009; Hirano et al., 2010).

The presence of spots can introduce spurious signatures in the line profiles that directly affect the shape of the radial-velocity curve—a single spot rotating with the stellar disk could even mimick an activity-induced Rossiter-McLaughlin effect (e.g., Huber et al., 2009b). Furthermore, the Rossiter-McLaughlin effect caused by the planetary transit can be considerably distorted by surface inhomogenities, resulting in incorrectly determined parameters. In fact, activity-induced radial-velocity jitter could be used for studies of stellar activity, for example, using simultanously obtained photometric and spectroscopic measurements to disentangle the effects caused by the presence of activity-related surface features and the planetary signal (Huber, 2010).

There are several other interesting applications of the Rossiter-McLaughlin effect (see Albrecht, 2011, for a compilation). For example, strong absorption due to optically thick spectral lines in the planetary atmosphere could yield a wavelength-dependent size of the planet, which should in principle result in measurable deviations of the Rossiter-McLaughlin effect (Snellen, 2004; Dreizler et al., 2009). In Sect. 6.3 of this thesis, we use the Rossiter-McLaughlin effect observed in the chromospheric emission line cores of the Ca II H and K lines to reconstruct the structure and extent of the chromosphere of the planet-hosting star CoRoT-2A.

2.2.8. The brown dwarf desert

The hunt for exoplanetary systems has always been biased towards finding giant Jupiter-like planets. It comes as no suprise that quite a number of the largest objects turned out to be brown dwarfs, substellar objects exceeding the limiting mass for deuterium fusion.

To formally distinguish both classes of objects, the International Astronomical Union's working group on extrasolar planets has released a working definition for extrasolar planets (Boss, 2001): Exoplanets are defined to have masses below the limiting mass for thermonuclear fusion of deuterium (currently calculated to be 13 Jupiter masses for objects of solar metallicity).

Facing this definition it is interesting to note that the mass distribution of extrasolar planets and brown dwarfs reveals a deficit in the frequency of brown dwarf companions relative to the number of less massive planetary or more massive stellar companions to solar-like host stars (Marcy & Butler, 2000).

The presence of this gap cannot be explained by an observational bias. It is possibly related to the formation scenario of close-in substellar objects, which, shortly after their collapse, tend to migrate inwards and eventually become consumed by the star (Grether & Lineweaver, 2006). Such a mass-dependent migration mechanism could further explain the large number of hot Jupiters found in close orbits.

2.3. Transit modeling

The detailed shape of the transit, especially in combination with radial velocity measurements, is a treasure trove for the study of extrasolar planets: The transit profile is described by four physical parameter, namely the inclination, i, the semi-major axis in stellar radii, a/R_s, the radius ratio, R_p/R_s, and the time of transit minimum, T_0. Observing two consecutive transits, the period, P, of the orbit can be determined. Models describing the transit shape therefore include a free scaling constant (in this case the stellar radius, R_s), which has to be fixed using additional observations or stellar model calculations. In combination with radial-velocity measurements, we can obtain the mass and, therefore, density and composition of the planet[1].

The papers reproduced in Sects. 5.2, 5.3, and 6.3 make extensive use of transit modeling. In the following, the most important aspects of the models and fitting methods are outlined.

2.3.1. Analytical and semi-analytical models

Several analytical and semi-analytical models describing the transit profile based on geometrical considerations have been derived (Mandel & Agol, 2002; Pál, 2008). These models assume a parametrized limb-darkening law for the star, and both bodies to be perfect spheres. While the models can be used to describe circular as well as eccentric orbits (Kipping, 2008), the inclusion of planetary oblateness (Barnes & Fortney, 2003) or ring structures (Barnes & Fortney, 2004) requires a numerical treatment. The advantage

[1] In fact, under suitable conditions, a complete high-resolution light curve including primary transit, secondary transit, and the overall phase shape between the occultations can be used to constrain the planet's mass (Mislis et al., 2012).

of analytical models is their computational efficiency when used in a fitting scheme to derive the best set of parameters. Furthermore, they allow to study the intrinsic correlations of the parameters.

2.3.2. Stellar activity

The light curves of active stars can show substantial rotational modulation due to starspots. Since the occultation of spots leads to a relative increase of the flux within the transit, stellar activity directly affects the estimates of stellar parameters derived by transit modeling.

Czesla et al. (2009) show that the relative light loss during the transit, the *transit equivalent width*, correlates with the level of local out-of-transit flux. An increase in the total surface fraction covered by spots yields larger bumps in the transit profile thereby reducing the transit equivalent width. It is thus important to correctly normalize the transit profiles to a common reference level and to construct an unperturbed transit profile, which is then used for the derivation of the parameters. Czesla et al. (2009) find that these effects cannot be neglected when the planetary parameters are to be accurate up to a few percent.

2.3.3. Limb darkening

The variation of specific intensity over the stellar disk is an important diagnostic of the physical structure of the stellar atmosphere. In the optical, stellar photospheres typically exhibit a monotonically decreasing brightness profile from the center to the limb.

As it is usually impossible to directly observe the center-to-limb variation of other stars, limb darkening is represented by simple analytical expressions whose coefficients are determined by matching the intensities emerging from synthetic atmosphere models. Numerous profile forms have been proposed including linear, quadratic, square-root, logarithmic, and four-coefficient nonlinear presciptions (Claret & Bloemen, 2011). According to Claret & Bloemen, the four-coefficient law gives the most accurate representation of plane-parallel model atmospheres. Adopting this model, the specific stellar intensity is described by

$$\frac{I}{I_0} = 1 - \sum_{k=1}^{4} a_k (1 - \mu^{\frac{k}{2}}), \qquad (2.5)$$

where $\mu = \cos\theta$, with θ denoting the angle between the stellar surface normal vector and the line-of-sight. The a_k are the limb-darkening coefficients.

Spherically symmetric atmosphere models can also be approximated by Eq. 2.5, at least in the case for solar-like stars, whereas simpler limb-darkening laws do not produce accurate fits to the computed models (Claret & Hauschildt, 2003). The strongest deviations occur very close to the stellar limb, where spherical models display a sudden decrease in intensity as there is less material near the limb. These sphericity effects become especially important for giant stars with surface gravities $\log g \lesssim 3.5$ (Orosz & Hauschildt, 2000; Neilson & Lester, 2011).

Most analytical transit models use the quadratic limb-darkening law (Mandel & Agol, 2002; Pál, 2008) or the four-coefficient model given by Eq. 2.5 (Mandel & Agol, 2002). The use of just two coefficients rather than four is preferable from a parameter fitting perspective. However, already a quadratic limb-darkening law introduces strong correlations with the remaining transit parameters. Therefore, most efforts to model planetary transits keep the limb darkening parameters fixed at their theoretically computed values.

From an observational point of view, the information on the global limb darkening encoded in the transit light curve depends on the parts of the stellar surface that are occulted by the planet (i.e., the *impact parameter*, $b = a/R_s \cos i$), and how well these parts allow to extrapolate to unocculted parts of the surface. Howarth (2011) shows that the system geometry itself introduces a systematic bias into the determination of limb-darkening coefficients from the transit light curve, which depends on the impact parameter. He therefore advises against directly comparing the fit results to model atmosphere predictions. Instead, Howarth proposes to obtain synthetic light curves from the model atmospheres, which are then fitted to yield comparable results for the limb-darkening coefficients.

2.3.4. Bayesian statistics

The analysis of observational data with the help of models is inference from incomplete information, i.e., a combination of deductive and inductive reasoning, which should be described by probability theory. The classical "frequentist" approach heavily relies on the idea of independent repetitions of random experiments and excludes prior information—this limits its applicability to special cases, where its stringent conditions are fulfilled.

Bayesian hypothesis testing and parameter estimation, which derives from an extended form of Aristotelian logic (Jaynes, 2003), allows to include a priori information and thus encompasses the fundamental concept of learning. In Bayesian statistics a probability is assigned to a hypothesis, while in the frequentist view, the hypothesis is tested to be true or false. Thus, the Bayesian concept of probability measures the plausibility of a proposition, whereas the frequentist concept of a limiting relative frequency is only valid after an infinite number of repetitions of a random experiment.

Given the data, $\mathbf{x}$, a model, H, and a set of parameters, $\boldsymbol{\theta}$, the frequentist approach restricts attention to the sampling distribution of the data, $p(\mathbf{x}|\boldsymbol{\theta}, H)$. The Bayesian statistician asks for the probability distribution for the parameters, $p(\boldsymbol{\theta}|\mathbf{x}, H)$, given the model, the data, and any prior information, the so-called *posterior* probability distribution. The posterior is related to the *prior* probability distribution for the parameters, $p(\boldsymbol{\theta}|H)$, according to Bayes' Theorem

$$p(\boldsymbol{\theta}|\mathbf{x}, H) = p(\boldsymbol{\theta}|H)\frac{p(\mathbf{x}|\boldsymbol{\theta}, H)}{p(\mathbf{x}|H)}, \quad (2.6)$$

where $p(\mathbf{x}|\boldsymbol{\theta}, H)$ for fixed data is called the *likelihood* function of the parameters. The normalization factor is the *prior predictive.*

While the posterior probability distribution summarizes our (incomplete) knowledge about the parameters, it can be characterized using some mode of the posterior. A typical choice is the mean, $E[\theta|\mathbf{x}, H]$, and the credibility interval, R, containing a specified probability mass of the posterior,

$$E[\theta|\mathbf{x}, H] = \int \theta p(\theta|\mathbf{x}, H), \qquad \int_R p(\theta|\mathbf{x}, H) d\theta = C, \tag{2.7}$$

where C is the probability content (e.g., $C = 95\,\%$), and R includes the region of highest probability density (HPD).

Metropolis-Hastings Markov Chain Monte Carlo sampling

Bayesian analysis involves the computation of multi-dimensional integrals, which can be done efficiently using Monte Carlo methods. Assume we had a method, that simulates a random sample from the posterior distribution. Then the posterior can be approximated by a histogram of these random draws, while the posterior mean is approximated as the sample mean.

As is evident from Eq. 2.6, the posterior is proportional to the joint probability $p(\boldsymbol{\theta}|H)p(\mathbf{x}|\boldsymbol{\theta}, H) = q(\boldsymbol{\theta}|\mathbf{x}, H)$. In the Laplace approximation this joint probability is approximated using a multivariate normal distribution centered on the mode with a covariance matrix determined by the curvature at the mode. This distribution is used as proposal distribution for a Markov Chain Monte Carlo (MCMC) method, which draws random samples from $q(\boldsymbol{\theta}|\mathbf{x}, H)$ using a random-walk Metropolis-Hastings algorithm.

The Metropolis-Hastings algorithm is a prescription designed to draw random samples, which are distributed according to the target distribution. It starts with a point $\boldsymbol{\theta}^0$ in the parameter space, for which the posterior is larger than zero. For each step in the chain it then performs the following operations: It draws a new parameter point $\boldsymbol{\theta}^*$ from a proposal distribution defined by the previous iteration and evaluates the probability ratio

$$r = \frac{p(\boldsymbol{\theta}^*|\mathbf{x}, H)g(\boldsymbol{\theta}^*|\boldsymbol{\theta}^{t-1})}{p(\boldsymbol{\theta}^{t-1}|\mathbf{x}, H)g(\boldsymbol{\theta}^{t-1}|\boldsymbol{\theta}^*)} \tag{2.8}$$

where $g(\boldsymbol{\theta}^*|\boldsymbol{\theta}^{t-1})$ is the proposal distribution. A typical choice for g is a multivariate normal distribution centered on $\boldsymbol{\theta}^{t-1}$ with a covariance derived from the normal approximation to the posterior.

The proposed step to $\boldsymbol{\theta}^*$ is accepted with probability $\min(r, 1)$, otherwise the chain retains the previous state. As the Metroplis-Hasting algorithm involves the computation of posterior probability ratios, it only relies on the unnormalized posterior $q(\boldsymbol{\theta}|\mathbf{x}, H)$. Remarkably, the distribution of the output $\boldsymbol{\theta}^t$ converges on the target distribution under general conditions and the choice of the initial proposal distribution only affects the speed of convergence (Tierney, 1994). Details about MCMC and the Metropolis-Hastings algorithm can be found in most standard texts on Bayesian statistics (e.g., Gelman et al., 2004).

2.3.5. The PyAstronomy fitting framework

The model fitting as well as the Markov-Chain Monte Carlo (MCMC) calculations performed in the context of this work make extensive use of routines of our PyAstronomy collection of astronomy related Python packages. PyAstronomy includes most routines developed in the course of this work and is publicly available online[2]. The core components have been developed by Stefan Czesla, who has the leading role in this project, however I also contributed to parts of the implementation and documentation of the code.

The core of PyAstromomy's fitting framework is the `OneDFit` class, which provides a interface to fitting and sampling algorithms implemented in the PyMC (Patil et al., 2010) and SciPy (Jones et al., 2001) packages. `OneDFit` provides convenient parameter management via the `Params` class, but does not implement a particular model itself. Mathematical fitting functions and physical models are defined via inheritance from the `OneDFit` base class and are collected in the `funcFit` and `modelSuite` subpackages, respectively. It is further possible to combine different models with basic arithmetic operations, calculate overbinned models to simulate the effects of finite bin size using `turnIntoRebin`, and perform simultaneous fits of two related models defined on different axes using the `syncFit` class.

Further subpackages provide routines for timing analysis (the `pyTiming` module), detection algorithms and profile analysis for spectral lines (the `yARES` module), easy access to databases (`keplerAccess`, `tellurLines`, and `constants`), and interpolation on data grids (`tableData`). Finally, the `pyasl` subpackage comprises Python implementations of some routines from the "IDL Astronomy User's Library" (AstroLib).

[2]See `http://www.hs.uni-hamburg.de/DE/Ins/Per/Czesla/PyA/PyA/index.html` for a documentation, download and installation instructions. PyAstronomy and all its submodules, if not explicitly stated otherwise, are distributed under the MIT license.

2.4. Time-dependent transit variations

The photometrically observed planetary transit turned out to be a conceptually simple yet powerful technique for the analysis of exoplanetary systems. In fact, deviations from the expected shape of the transit light curve bear physical implications themselves.

Transit timing variations can be classified according to the observables mediating the detection of time-dependent changes in the system parameters. The most important observables are the time of transit minimum and the duration of the transit event. Timing variations can occur on different timescales, namely periodic orbit-to-orbit variations or long-term secular[3] changes.

2.4.1. Variations in time of transit minimum

Similar to the discovery of Neptune, an additional object in the system can reveal itself by its gravitational influence on the orbital elements of the transiting planet. Most notably, a perturber is expected to induce short-term periodic variations in the times of transit minimum (Holman & Murray, 2005; Agol et al., 2005). These short-term variations of the mid-transit time with amplitudes on timescales of seconds and minutes are usually referred to as transit

[3]Here, the term "secular" refers to the original meaning of the Latin word *saeculum*, describing a long period of time (*Webster's encyclopedic dictionary*, 1989).

timing variations (TTVs). Perturbing objects in mean motion rensonances can even induce TTV amplitudes on the order of hours (e.g., Holman et al., 2010).

While TTVs provide a method to detect and study further unseen planets, moons or Trojan bodies in the system, they can also be caused by other effects. For close (< 10 pc) exoplanetary systems, parallax effects can result in measurable TTV amplitudes on the order of seconds. In the case of eccentric orbits, TTVs can be caused by apsidal precession (Jordán & Bakos, 2008). Furthermore, the presence of large spotted regions on the star can mimick the presence of TTVs as noted by Alonso et al. (2008) in the case of the active planet host star CoRoT-2A. Other causes for TTV signatures are variations in the stellar quadrupole moment driven by the stellar activity cycle, light travel time, and tidal effects (Watson & Marsh, 2010).

The detection of TTVs in ground-based measurements requires a sufficiently long baseline and good phase coverage of the planetary orbit. Furthermore, to reach an accuracy better than 1 min in the time stamps, the adopted time standard has to be a carefully chosen and clearly stated (Eastman et al., 2010).

The search for additional planets by TTVs has been a major field in ground-based exoplanet research during the last years, albeit with limited success: So far, TTVs have been detected in WASP-3b (Maciejewski et al., 2010), WASP-10b (Maciejewski et al., 2011), OGLE-111b (Díaz et al., 2008, but see contradicting results by Adams et al., 2010), WASP-5b (Fukui et al., 2011, but see Hoyer et al., 2012), and HAT-P-13 (Pál et al., 2011, but see Fulton et al., 2011).

The observational situation changed dramatically with the advent of space-based observatories like Kepler, which monitor their targets over time spans of years. Only one year after the start of the mission, the first TTV signatures were found in several planetary systems.

Holman et al. (2010) detected TTVs due to the mutual gravitational interactions between the two Saturn-like transiting planets Kepler-9b and Kepler-9c with amplitudes of 4 and 39 minutes. Shortly after, the spectacular Kepler-11 system was found to host six transiting planets showing TTVs of amplitudes as large as tens of minutes produced by the gravitational perturbations between the planets (Lissauer et al., 2011). Recently, Ballard et al. (2011) reported the detection of variations in the transit timing of the super-earth Kepler-19b due to the presence of an additional Jovian mass perturber. From the analysis of the first three quarters of Kepler data, Ford et al. (2011) conclude that Kepler will provide a large number of additional TTV detections in the coming years.

2.4.2. Variations in transit duration

Due to the complex shape of transit egress and ingress there are various definitions of the transit duration. For circular orbits the transit duration, defined as the total duration from first to fourth contact, can be expressed in a simple expression following Seager & Mallén-Ornelas (2003),

$$t_T = \frac{P}{\pi} \arcsin \frac{\sqrt{(1+\frac{R_p}{R_s})^2 - (\frac{a}{R_s}\cos i)^2}}{\frac{a}{R_s}\sin i}, \tag{2.9}$$

where P, a, and i denote the orbital period, radius, and inclination, respectively, while R_s and R_p refer to the stellar and planetary radii. There is currently no single exact equation in the case of eccentric orbits, however, several approximations can be found in the literature (Tingley & Sackett, 2005; Kipping, 2010).

Periodic short-term variations in the transit duration could be caused by exomoons (Kipping, 2009). Secular variation can result from apsidal precession (e.g., due to stellar oblateness or general relativistic effects; Jordán & Bakos, 2008), nodal regression (e.g., due to an additional perturbing planet; Miralda-Escudé, 2002), infalling planets, and changes in eccentricity via the Kozai mechanism (Kipping, 2009).

In Sects. 5.2 and 5.3 of this thesis, we will discuss ground-based observations indicating long-term variations in the orbital inclination of the transiting exoplanet TrES-2b, which we explain as being due to nodal regression. However, our subsequent analysis of the first four quartes of Kepler photometry of this system in Sect. 5.3 rules out the previously detected inclination change.

3. Solar and stellar activity

Stars like our Sun are luminous, self-gravitating gas balls made up basically of hydrogen and helium, which are stabilized by the generation of energy via nuclear fusion. However, a large number of observable phenomena, collectively referred to as activity and mostly related to magnetic fields, cannot be explained in this simple picture. In this chapter, I outline the phenomenology of magnetic activity in solar and stellar atmospheres and explain the underlying concepts of the solar dynamo. The most important diagnostics of magnetic activity in optical and X-ray astronomy are introduced. Finally, I point out the relevance of stellar activity in exoplanetary systems with close-in Jovian planets for the evolution of the system and summarize the observational status quo.

3.1. Solar activity and dynamo action

Early studies of stellar activity focused on our Sun for an obvious reason: The Sun is the only star being close enough to be resolved in great detail. This section presents an overview of solar magnetic activity. Furthermore, a summary of our current understanding regarding the structure of the Sun and the formation of its magnetic fields is given.

3.1.1. Sunspots and solar cycles

While the Sun is usually perceived by the human eye as a luminous, perfect disk in the sky and thus has been an object of veneration in many cultures, watchful observers like Chinese astronomers noticed the presence of dark spots on the solar disk more than two millenia ago. Reports on the detection of sunspots can be traced throughout the history, however, they were mostly interpreted as planetary transits. In fact, Galilei (1613) was the first, who interpreted sunspots as features on the solar surface, its *photosphere*, and their motion as a consequence of the rotation of the Sun.

Systematic observations then showed that sunspots have typical lifetimes between days and two months and occur as groups at preferred latitudes revealing an average period of 11 years. This *Schwabe cycle*, named after its discoverer, shows clear maxima, during which the number of sunspots is high, followed by phases with less or even no sunspots. The occurence of sunspot groups is not randomly distributed over the solar disk. Instead, with beginning of a cycle sunspots occur preferentially around latitudes of $\pm 30°$. As the cycle progresses, sunspots occur successively closer to the solar equator and disappear at the equator as the first spots of the next cycle appear at higher latitudes. This gives rise to Fig. 3.1 showing the famous *butterfly diagram* of the solar cycle.

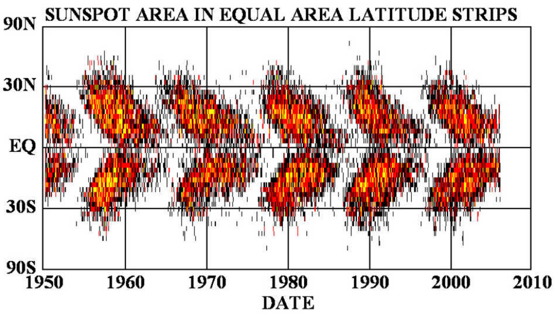

Figure 3.1.: Butterfly diagram of the Sun showing the latitude and area (color-coded) covered by sunspots over the last 60 years (Credit: NASA/NSSTC D. Hathaway).

While the surface fraction covered by sunspots increases towards the activity maximum, the total solar irradiance varies accordingly but in the opposite way: The Sun emits more energy at the solar activity maximum, when there is a large number of sunspots on the surface. This is due to bright, but very small features on the surface called faculae occuring together with the sunspots. The contribution due to faculae overcompensates the reduced emission due to the sunspots.

Strong solar activity is accompanied by a higher level of high energy cosmic radiation, which then produces larger amounts of isotopes like ^{14}C and ^{10}Be in the Earth's atmosphere. Using abundance measurements of radioactive isotopes, the solar cycle can be traced back over centuries as the relative abundance of these isotopes is preserved in trees and polar ice-cores (Weiss & Thompson, 2009). As is evident from these data, the solar cycle is not invariable but can show periods of prolonged sunspot minima. Such a period occured from about 1645 to 1715, when sunspots became exceedingly rare, as noted by solar observers of the time. Those spots that were seen were almost all in the Sun's southern hemisphere. This period, which is only the latest of the grand minima that have occurred in solar activity over time, is known as the Maunder Minimum (Eddy, 1976). The Maunder Minimum temporally coincides with the Little Ice Age, during which Europe and North America were subject to unusually cold winters[1].

Faculae, granules, and enhanced network

Sunspots (Fig. 3.2) are the most obvious features visible on the solar photosphere. However, detailed images of the photosphere reveal even more subtle structures. The photosphere is covered with *granules*, small cellular features on top of convection cells, where plasma rises up from the solar interior. Granules have diameters of about 1000 km and typical lifetimes on the order of 20 minutes. While there is unambigous evidence for their convective origin, this is less clear for higher-scale granulation patterns namely mesogranulation and supergranulation with cell sizes up to 30,000 km and 20 hr lifetime (Rast, 2003, and references therein).

Faculae are bright features seen in visible light near the limb of the Sun, which are more numerous but much smaller than sunspots and occur preferentially close to active regions. They are part of even smaller, magnetically active structures forming the enhanced *photospheric*

[1] Recent observations with NASA's Solar Radiation and Climate Experiment show that variations in solar ultraviolet irradiance may be larger than previously thought and could indeed be correlated to local climate changes, which have only little effect on the global temperature (Ineson et al., 2011)

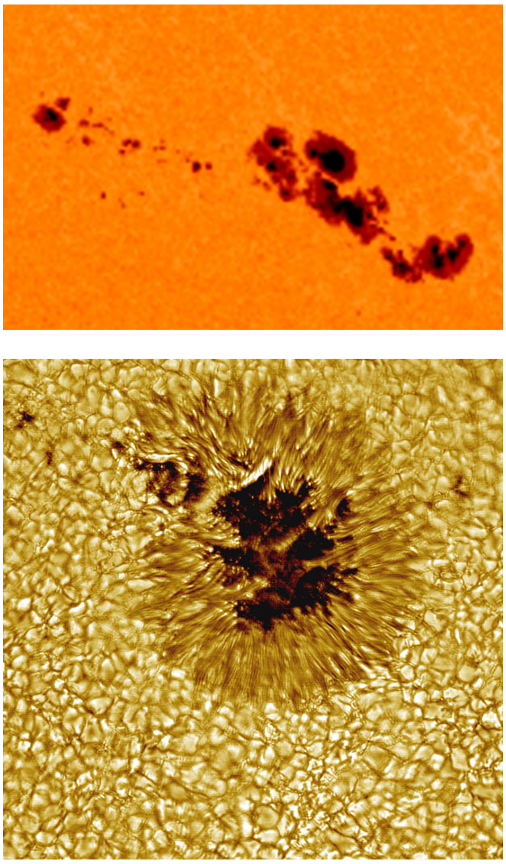

Figure 3.2.: Upper panel: Large sunspot group. (Credit: SOHO/ESA&NASA). Lower panel: Close-up of sunspot and granules (Credit: Vacuum Tower Telescope/NSO/NOAO)

network. The contrast between facular emission and the quiet-Sun photosphere is known to increase from the solar disk's center outwards towards the limb (Chapman & Ziegler, 1996). According to the "hot wall" model, faculae emit through the sides of a cylindrical flux tube, so that the maximum contrast should be located somewhere between the limb and the center depending on the viewing angle, whereas material protruding the photosphere ("hot cloud") would have its highest contrast at the limb. Despite numerous efforts during the last decades to precisely measure the facular center-to-limb variation, there is currently no consistent picture of the exact behavior close to the limb (cf. Berger et al., 2007, and references therein).

Sunspots and magnetic fields

In 1908 Hale demonstrated that sunspots possess a magnetic field. In fact, the magnetic fields, which reach typical strengths of $2-3$ kG, were found to be responsible for the formation of sunspots: The strong magnetic fields in sunspots inhibit the convective motions, which are the dominant energy transport mechanism in the outer 30 % by radius of the Sun, the so-called convection zone. The convective motions of the plasma transport heat from the interior to the solar surface. Strong magnetic fields cause sunspots to be 2000 K cooler compared with the surrounding photosphere and hence darker. However, the detailed structure of a sunspot is rather complex with a dark inner region known as umbra and a surrounding region called the penumbra which exhibits a dynamic filamentary structure and can be shared by several spots in the same group (Fig. 3.2).

Detailed measurements of the magnetic polarization of sunspots by Hale et al. (1919) led to the discovery that sunspots occur in bipolar pairs consisting of a leading spot and a trailing spot. Furthermore, the polarities are reversed for sunspot pairs on opposite hemispheres and the polarities reverse in successive solar cyles—a systematic effect that became known as as Hale's law. It reveals that the apparent 11-year cycle is in fact a magnetic cycle of about 22 years. Another finding known as Joy's law is that the line joining

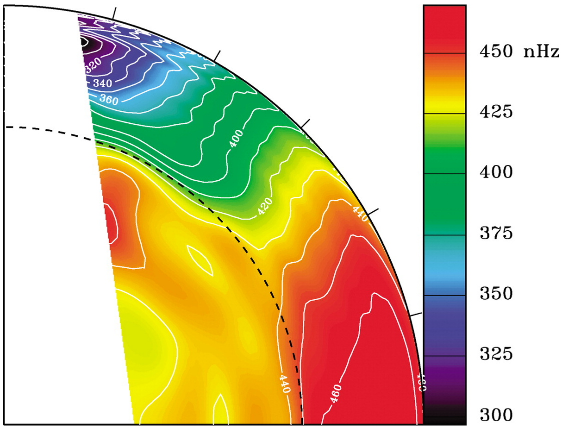

Figure 3.3.: Internal rotation of the Sun obtained with MDI/SOHO. The rotation frequency $\Omega/2\pi$ is given in nHz. The dashed line indicates the tachocline. Figure taken from Thompson et al. (2003).

leading and trailing spots is typically inclined at an angle of about 4° to the equator.

Finally, sunspots occur in larger magnetic complexes called active regions, which usually recur at the same longitudinal position on the Sun. Active regions are associated with large magnetic structures reaching out into the chromosphere and corona of the Sun, where they can give rise to coronal mass ejections and flares caused by magnetic reconnection.

3.1.2. The solar interior inferred from helioseismology

Energy is generated by nuclear fusion in the inner core of the Sun. This energy is transported outwards from 0.25 to 0.7 solar radii by radiative transport. However, solar model calculations indicate that above this inner *radiative zone* the required temperature gradients are too steep to be stable. The remaining part of the solar interior is therefore governed by convective heat transport. This picture was observationally confirmed by helioseismology, which measures characteristic frequencies of global oscillation modes on the Sun. These modes are mediated by acoustic waves generated by turbulent motions in the upper part of the convection zone.

Christensen-Dalsgaard et al. (1991) demonstrate that the base of the convection zone is located at a fractional radius of 0.713 ± 0.003. From the motion of spots on the surface and Doppler spectroscopy, it has long been known that the surface rotation period at the solar equator is about 25 days, increasing with latitude to more than a month at high latitudes. Helioseismology has shown that this differential rotation persists through the whole convection zone. However, beneath the base of the convection zone the solution is consistent with a nearly uniformly rotating radiative interior (see Fig. 3.3). The base of the convection zone is thus a region of shear flow known as the *tachocline* (e.g., Thompson et al., 2003). Even if helioseismology has revealed many details about the interior of our Sun, the rotation of the inner, energy-generating core is still uncertain.

3.1.3. The solar dynamo

The existence of sunspots clearly indicates the presence of strong magnetic fields on the Sun. These magnetic fields are thought to be generated by the solar dynamo. While the detailed operation mechanism of this dynamo process is unknown, it is likely that differential rotation of the solar plasma is an important ingredient. The equations that govern the generation of magnetic fields in the solar interior derive from Maxwell's equations of electrodynamics together with the continuity equation for mass conservation and Euler's equation for fluid mechanics including magnetic forces and gravity. This yields a theoretical framework known as magnetohydrodynamics (MHD). The key equation of MHD is the induction equation

$$\partial_t \mathbf{B} = \nabla \times (\mathbf{u} \times \mathbf{B}) + \eta \nabla^2 \mathbf{B} \tag{3.1}$$

describing the temporal change of the magnetic field, $\mathbf{B}$, in the presence of velocity fields, $\mathbf{u}$, and diffusion of the magnetic field $\eta \nabla^2 \mathbf{B}$, where η denotes magnetic diffusivity.

It is, however, impossible to directly solve these equations in the parameter regimes that occur in stellar interiors with the current computational resources, because the flows that drive the dynamo are extremely turbulent with a large range of spatial and temporal scales interacting in a highly nonlinear manner (Jones et al., 2010).

The dynamics of the global magnetic field is conveniently expressed in terms of its toroidal and poloidal parts, viz. $\mathbf{B} = B_\phi \mathbf{e}_\phi + \nabla \times (A\mathbf{e}_\phi)$, where $A(r, \theta)$ is the vector potential. Assume the presence of a seed magnetic potential $\mathbf{A}$, which may be a relic of a magnetized interstellar cloud that gravitationally contracted to form our Sun. The presence of differential rotation $\mathbf{u}_\phi(r, \theta)$ then leads to the generation of a toroidal field with opposite polarity in the two hemispheres from the poloidal seed field. This is the well-known Ω-effect.

As demonstrated by Cowling (1933) in his famous anti-dynamo theorem, there is no flow that could sustain the axisymmetric field, so that the poloidal field would ultimately decay. Two decades later, Parker (1955a) argued

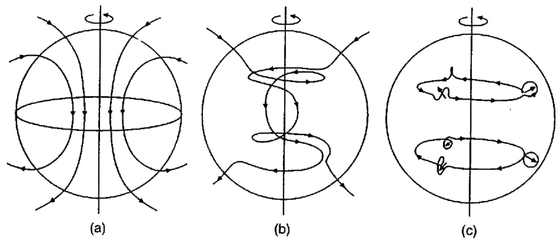

Figure 3.4.: Working principle of the $\alpha\Omega$-dynamo. Poloidal magnetic field (a) is converted into a toroidal field (b) via differential rotation. The α-effect then replenishes the poloidal field (c) by twisting rising flux tubes. Figure taken from Russell (1999).

that non-axisymmetric small-scale magnetic fields could be produced by turbulent convective motions in the solar interior. The net electromotive force resulting from the interaction of small-scale flows and magnetic fields would then be capable of regenerating the large-scale poloidal field from the toroidal field. This can be seen from the formulation of mean-field theory. Magnetic and velocity fields are split into mean and fluctuating parts,

$$\mathbf{B} = \overline{\mathbf{B}} + \mathbf{B}', \mathbf{u} = \overline{\mathbf{u}} + \mathbf{u}', \tag{3.2}$$

so that the means of the fluctuating parts vanish, but products of fluctating quantities can have a non-zero average. Inserting this into the induction equation yields the mean-field induction equation

$$\partial_t \overline{\mathbf{B}} = \nabla \times (\overline{\mathbf{u}} \times \overline{\mathbf{B}}) + \nabla \times (\overline{\mathbf{u}' \times \mathbf{B}'}) + \eta \nabla^2 \overline{\mathbf{B}}. \tag{3.3}$$

Given a suitable configuration, the product of the fluctuating parts yields a non-zero average corresponding to an electromotive force EMF $= \overline{\mathbf{u}' \times \mathbf{B}'}$, which then creates poloidal from toroidal field to close the dynamo loop (Fig. 3.4).

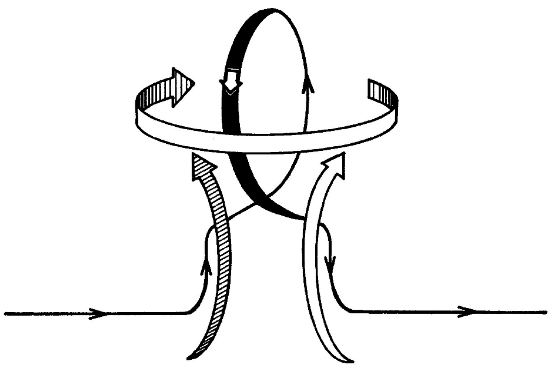

Figure 3.5.: The Parker loop mechanism. Rising plasma with positive helicity lifts up a line of magnetic field and twists it. Figure taken from Parker (1970)

The specific process that leads to the occurence of a non-zero EMF depends on the averaging method and assumptions. A standard approach is to assume that the turbulence is a random superposition of waves $\mathbf{u}' = \Re[\mathbf{u} \exp i(\mathbf{k} \cdot \mathbf{x} - \omega t)]$ and isotropic. This results in an EMF, which is proportional to a factor α, that depends on the average helicity, i.e., the product of velocity and vorticity of the flow, $H = \overline{\mathbf{u}' \cdot \nabla \times \mathbf{u}'}$. For example, a fluid element that rises and thereby rotates produces helicity. The interplay of solar rotation and convection then yields the required asymmetry to obtain a non-zero net α-effect (Steenbeck & Krause, 1969).

The existence of sunspots can be explained with the Parker loop mechanism (Parker, 1955b) illustrated in Fig. 3.5: The toroidal magnetic fields produced at the bottom of the convection zone provide additional pressure to the gas. In an isothermal ideal gas, this leads to a reduced density in the flux tube. Due to the resulting buoyancy, the magnetic flux tube rises through the outer convection zone eventually reaching the solar surface. As an azimuthal loop of magnetic field lines penetrates the photosphere a sunspot pair is created. The systematic tilt of sunspots (Joy's law) is due to the rising loop of flux being rotated by a small angle due to the Coriolis force.

Unfortunately, numerical simulations support neither the isotropy nor the assumptions underlying mean-field theory (cf. Jones et al., 2010), while the inclusion of non-linear effects typically acts to suppress the α-effect (an effect known as *α-quenching*; Vainshtein & Cattaneo, 1992). Today's computing power is still insufficient to treat the full astrophysical parameter regime.

Depending on the relative importance of shear due to differential rotation and turbulent diffusion the mean-field equations yield different kinds of exponentially growing dynamo waves known as α^2-dynamo and $\alpha\Omega$-dynamo. These modes grow exponentially and saturate eventually due to α-quenching. However, the strong fields required to lift the Ω-loops inevitably cause catastrophic α-quenching. Therefore, Parker (1993) suggested to spatially separate both mechanisms, so that Ω operates in the strong field regions near the tachocline, while α can operate in the weak-field region in the convection zone. This model became known as *interface dynamo*. A similar concept underlies the *flux-transport dynamos*, where poloidal flux is transported back to the tachocline by meridional circulations, which indeed can be observed on the Sun (Wang et al., 1991).

3.1.4. The chromosphere

Total solar eclipses reveal the presence of an outer solar atmosphere, which is

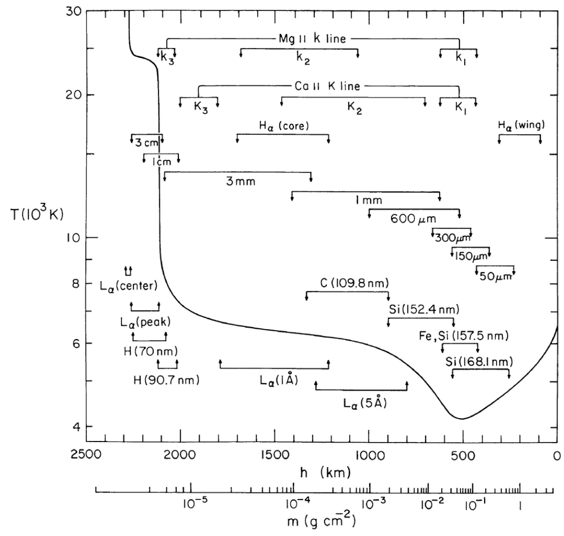

Figure 3.7.: Height-of-formation graph of the classical VAL3C model. The continuous line shows the temperature stratification of the quiet Sun's atmosphere. Figure taken from Vernazza et al. (1981).

otherwise outshone by the brilliance of the photosphere. Expeditions to solar eclipses during the 18th and 19th century revealed "red flames" protruding the limb of the lunar disk—in fact, it comes as a strange fortune, that the apparent angular size of the Moon matches that of our Sun quite exactly in our times. The reddish glow of the observed ring of emission soon led to the idea of a thin spherical shell surrounding the photosphere of the Sun, which was then dubbed chromosphere.

Detailed observations found the chromosphere to be quite heterogeneous showing *prominences* and *spicules*, tightly collimated jets of plasma streaming upward through the chromosphere with lifetimes of several minutes (Roberts, 1945). If seen on the disk, spicules are also known as *mottles* or *fibrils* (see Fig. 3.6). Spicules are bright in Hα, giving the chromosphere its pink color, while the larger and hotter macrospicules are also prominent in extreme ultraviolet images. *Plages* are bright regions in the chromosphere, which are usually found close to photospheric sunspots. They closely map the faculae in the photosphere below, which are, however, spatially less extended. In close analogy to the photosphere, plages are linked to interconnected patches, the *chromospheric network*. While plages and faculae are intimately related, their physical connection is still unclear. Coronal shock waves are accompanied by chromospheric *Moreton waves*. These are fast-mode magnetohydrodynamic waves propagating at speeds between 10^2 and 10^3 km s^{-1}, which are visible in Hα (Moreton, 1960; Uchida et al., 1973).

With the dawn of high-resolution spectroscopy numerous emission features of high-temperature ionized species were found, indicating a strong rise in temperature. Based on many complementary observations Vernazza et al. (1981) developed semi-empirical models, that represent a complete, self-consistent numerical simulation of the radiation from a plane-parallel star. Their VAL3C models, which were later updated by FAL models (Fontenla et al., 2006), present a consistent temperature stratification (cf. Fig 3.7): Declining from 6500 K to 4400 K with increasing altitude through the several hundred kilometers thick photosphere, the temperature shows a slow rise through the entire chromosphere up to around 20,000 K followed by a sharp increase in the narrow transition region up to 2 MK in the corona. Figure 3.7 further shows the formation heights of many important spectral line diagnostics according to the VAL3C models. Clearly, the

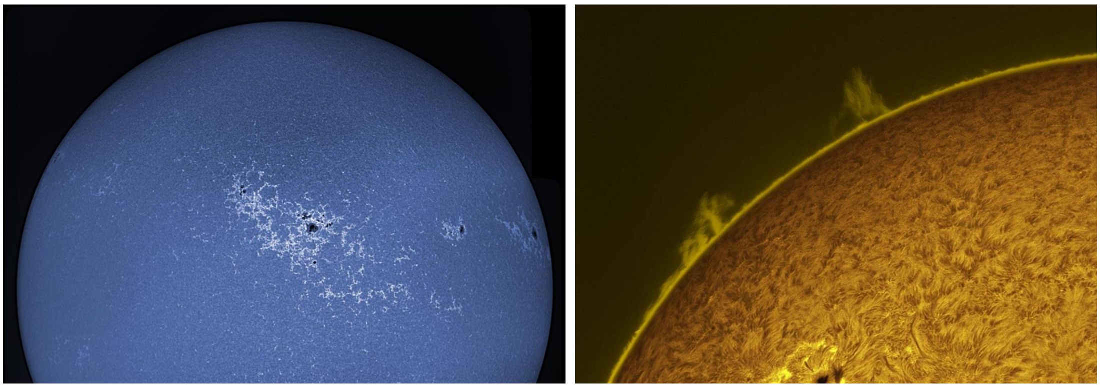

Figure 3.6.: Left: Solar chromospheric plages in the light of the Ca II K-line. Right: Prominences and fibrils in Hα. Both images were obtained by Chris Schur using a Lunt 60 mm Ca K and a Coronado 40 mm Hα filter (Credit: C. Schur, `www.schursastrophotography.com`).

prominent line cores of Mg II, Ca II, and Hα are dominantly formed in the chromosphere. However, the VAL3C models should not be regarded as representing the actual situation in the Sun; quoting Rutten (2007):

> "Let us regard VAL3C [...] as interesting stars with sun-like photospheres but chromospheres that exist only computationally."

Chromospheric activity

Flash spectra of the chromosphere taken during total solar eclipse (Fig. 3.8) reveal a number of emission lines originating in the chromosphere. Back in the late 19th century, most of these lines had been recognized to correspond to the prominent Fraunhofer absorption lines known from the photosphere, namely the H and K lines of singly-ionized calcium and the hydrogen Balmer lines. The emission reversals in these lines indicate departures from radiative equilibrium, however, the "coronal green line" at 5303 Å remained a mystery until it was discovered that the line is emitted by highly ionised iron at temperatures well in excess of one million Kelvin (Grotrian, 1939; Edlén, 1942). The temperature rise throughout the outer solar atmosphere is incompatible with thermal processes alone and points towards the existence of additional heating mechanisms beyond simple equilibrium transfer of radiation. These additional physical processes are generally referred to as *activity*.

So far, there is no quantitative understanding of the heating of the outer solar atmosphere. The main difficulty is to set up a physical process acting as energy carrier, that can efficiently dissipate the transported energy in the higher atmospheric layers. Several heating mechanisms have been proposed that can be classified into hydrodynamic and magnetic heating mechanisms: Hydrodynamic heating relies on rising convective cells that generate outward propagating acoustic waves, which than dissipate their energy via shock processes. Magnetic heating on the other hand is mediated by strong magnetic fields that can induce MHD waves; alternatively,

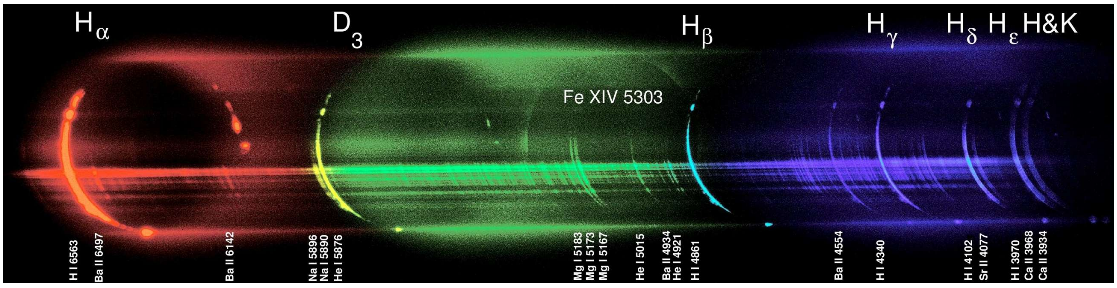

Figure 3.8.: Flash spectrum taken during total Solar eclipse in 1999 showing the most prominent chromospheric emission lines. Credit: EurAstro Team Szeged I, M. Rudolf, A. Jakoblich, F. Michlmayer, C. Ortega (`http://www.eurastro.de/webpages/mrspect.htm`)

the energy stored in the magnetic field can be released by magnetic reconnection (cf. Erdélyi & Ballai, 2007, for a review). The heating process results in a higher ionization fraction of hydrogen releasing large numbers of electrons, which then enable collisional radiative cooling through strong resonance lines of abundant species like Ca II and Hα.

A dynamical view of the chromosphere

The layered view of the solar chromoshere as a homogeneous, spheroidal shell in the solar atmosphere has to be revised. Infrared observations reveal the presence of strong rotation-vibrational emission of carbon monoxide reaching hundreds of kilometers into the chromosphere. This indicates comparably cool gas of 3700 K coexisting with much hotter surrounding gas (Ayres & Testerman, 1981). From recent satellite imagery of chromospheric and coronal emission Rutten (2007) develops a dynamical view of the chromosphere, which he defines as the mass of fibrils observed in Hα. Darker Hα fibrils span large cells forming magnetic canopies, whose relatively cool interiors are pervaded by acoustic shocks. Other fibrils appear as bright upright straws opening up into the hot coronal plasma. The chromosphere appears as a thin and inhomogeneously warped dynamic interface, which is variable on short and long timescales. The detailed physical mechanisms leading to the observed properties of the solar chromosphere have not been settled yet (e.g., Ayres, 2002; Hall, 2008). This dynamic picture of a strcutured chromosphere is also confirmed by recent two- and three-dimensional magnetohydrodynamic simulations of chromospheric features using the Oslo Staggered Code (e.g., Leenaarts et al., 2007; Martínez-Sykora et al., 2011), which present the complexity of the highly dynamic outer atmospheric layers of the Sun (cf. Fig. 3.9).

Center-to-limb variation

The center-to-limb variation of the quiet solar chromosphere is difficult to measure due to the presence of plages and other varying features. Images of the Sun obtained in narrow filter bands, so-called spectroheliograms, show that the quiet Ca II K and Mg II k emission decreases towards the solar limb (Brandt & Steinegger, 1998; Morrill & Korendyke, 2008). Limb-brightening of the chromosphere can be

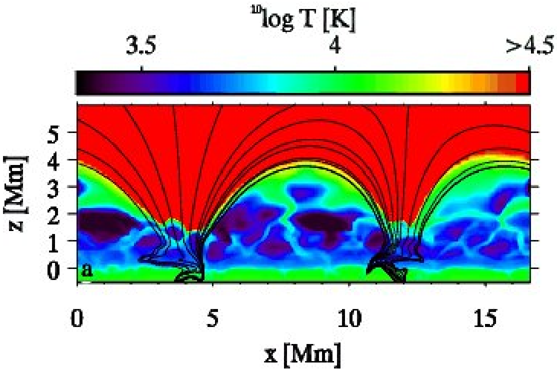

Figure 3.9.: Snapshot of the 2D Oslo MHD simulation showing the gas temperature (color-coded) and magnetic field lines (black) extending into the corona. The chromopshere is pervaded by shocks and reaches heights of 2–4 Mm depending on the magnetic field configuration. Figure taken from Leenaarts et al. (2007).

observed in sub-millimeter wavelengths (Bastian et al., 1993).

Chromospheric prominences and spicules clearly protrude the photospheric solar limb. The largest solar prominences such as the "Grand Daddy Prominence" extend up to heights of 112 000 km above the limb as measured in Hα emission (Pettit, 1946). Steady Ca II H and K emission reaching up to 5000 km above the solar limb was observed by Beck & Rezaei (2011), who also measured the change of the H and K emission line profile with varying height. Their images clearly display that the chromosphere extends beyond the photospheric radius—even for less active stars like our Sun.

The extent of chromospheres of other active stars can be studied only under fortunate circumstances, e.g., if resolved images are available (e.g., Lobel et al., 2004) or in eclipsing binary systems (e.g., Eaton, 1993). In Sect. 6.3, the chromosphere of the active planet-host star CoRoT-2A is studied using the Rossiter-McLaughlin effect in chromospheric emission lines.

3.1.5. The X-ray Sun

From the detection of the one million Kelvin hot gas in the solar corona in the 1930s (Grotrian, 1939; Edlén, 1942), the Sun was expected to be a source of high-energy radiation with photon energies ranging from hundreds of electron Volt (eV) up to hundreds of keV, known as X-rays. X-rays are produced by material heated to temperatures of millions of Kelvin and particles accelerated to relativistic velocities. In air at ground level, X-ray radiation has a mean free path of only a few meters. It is therefore impossible to directly detect X-rays of cosmic origin from the ground. The speculations regarding the nature of the solar corona were confirmed in 1949 with the detection of the solar corona during a rocket flight (Burnight, 1949).

The era of modern X-ray astronomy started with the launch of the X-ray satellites UHURU and EINSTEIN in 1970 and 1978. Both mission revealed that X-rays are found for a large number of stars throughout the Hertzsprung-Russel diagram. In 1990 the German ROSAT mission was launched and provided an all-sky survey with more than 100, 000 source detections. Since these early times of X-ray astronomy, an armada of satellite observatories dedicated to solar and extrasolar high-energy radiation contributed to our understanding of the solar corona and a plethora of high-energy processes throughout the Universe. Today, the two main X-ray missions are ESA's XMM Newton and NASA's Chandra X-ray observatory, both launched in 1999. The Chan-

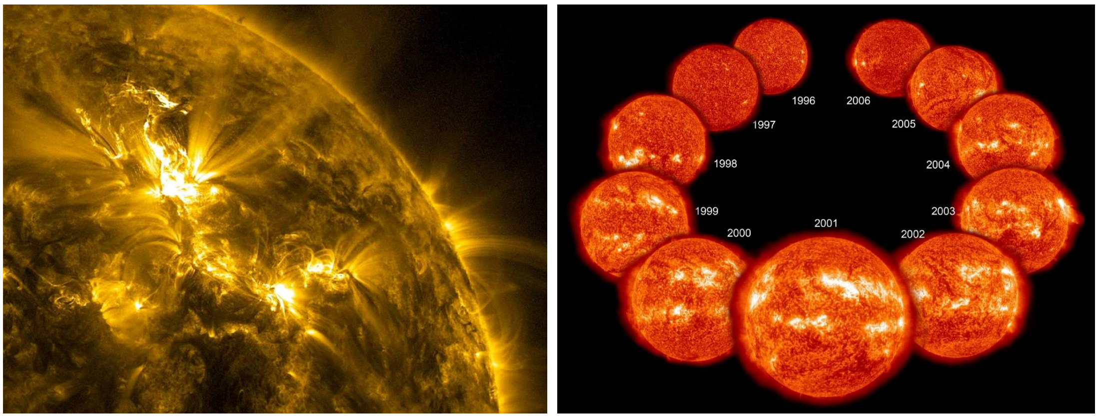

Figure 3.10.: Left: Flare eruption and magnetic loops observed with SDO (Credit: SDO/NASA). Right: The solar corona as seen with SOHO in the extreme UV light following an entire solar activity cycle (Credit: SOHO/ESA&NASA).

dra telescope and its working principle will be introduced in Sect. 3.2.4.

The solar corona has been studied extensively by numerous space telescopes in extreme ultraviolett (EUV) light (e.g., SOHO, TRACE, SDO) and X-rays (e.g., Yohkoh, Hinode). Their ornamental imagery reveal a highly dynamic picture of the outer atmosphere of the Sun: Closed magnetic *coronal loops* are the basic structures of the solar corona. These loops vary in shape and size and are fed by hot and dense plasma originating in the photosphere (see Fig. 3.10). Coronal loops have lifetimes between seconds and days and contribute to the Sun's quiescent X-ray emission. Large regions which are comparably dark in X-rays are called *coronal holes*. They result from open unipolar field lines reaching out into interplanetary space and are typically found at the polar region during solar minimum. Coronal loops of modest height can brighten up on timescales of minutes causing X-ray *flares*. Flares are related to sudden changes of the magnetic field configuration via magnetic reconnection releasing an enormous amount of energy on a timescale of hours. Finally, the 11 year activity cycle of the Sun is clearly visible in the soft X-ray regime as can be seen in Fig. 3.10.

The advent of space-based UV and X-ray observatories led to the discovery of tight correlations between the chromosphere and corona suggesting that these are intimately connected: While magnetic fields rooted in the photosphere are governed by the plasma motion, they in turn dominate the plasma motions in the higher atmospheric layers. Thus, properties of the plasma motion in the photosphere are sustained in the chromosphere and the corona.

3.2. Stellar activity

The work at hand deals with signatures of stellar activity in solar-like planet-hosting stars in different evolutionary states. While the Sun provides a natural starting point for all our investigations and will certainly remain the best-studied star in the Universe (at least, in the near future), improved observational techniques allow astronomers to

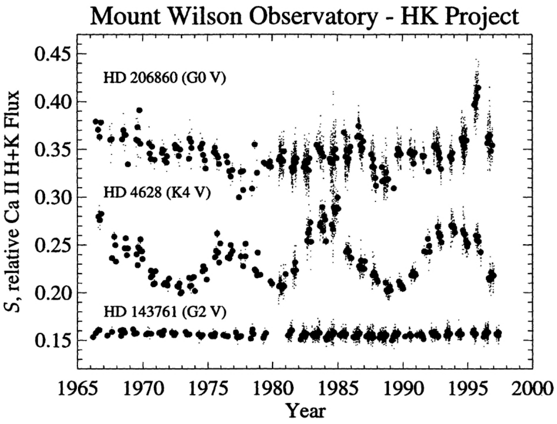

Figure 3.11.: Different actvity patterns for three stars observed in the Mt. Wilson HK program as evidenced by the relative flux observed in Ca II H and K emission line cores. Figure taken from Baliunas et al. (1998).

study signs of magnetic activity in a large number of stars. Some of the main efforts and results will be outlined in the following.

3.2.1. Chromspheric emission reversal

One of the most important indicators for stellar activity is the chromospheric emission reversal in the Ca II H and K lines. Stellar Ca II H and K emission has been studied systematically since early works by Wilson & Bappu (1957). These early studies demonstrated that chromospheric activity signatures can also be observed in the spectra of many other late-type stars. In close analogy to the activity cycles observed on the Sun, it was expected that these stars should show activity modulations with periods over several years. In 1966 Wilson started the Mt. Wilson HK program searching for such long-term trends. The campaign revealed a large variety in activity levels with regular cycles and irregular variation Baliunas et al. (1995, see Fig. 3.11).

The ubiquitous detection of Ca II H and K emission suggests that magnetic activity is a universal phenomenon in late-type main-sequence stars. One of the many important results of these studies is a relation between the rotation velocity of a star and its level of magnetic activity: The faster the star rotates, the more active it is. This can be understood in terms of the stellar dynamo, which weakens for slower rotation (Noyes et al., 1984). Another closely related correlation indicates a decreasing level of stellar activity for older stars. This relationship between chromospheric emission and age, the so-called *chromospheric age*, served as the leading age indicator for long time (Soderblom et al., 1991; Donahue, 1998).

However, both relations are aspects of the more fundamental activity-rotation-age paradigm (e.g., Skumanich, 1972), which explains the decrease of activity for older stars as the result of a steady angular momentum loss during stellar evolution. According to this paradigm, main-sequence stars begin their life as fast rotators with rotation periods of less than one day. During their evolution they drive strong magnetized stellar winds yielding a mass outflow along the large-scale open magnetic field lines. This phenomenon, known as magetic braking, thus weakens the stellar dynamo reducing magnetic activity.

This would make rotation the most fundamental property which together with stellar mass would be responsible for the behavior of all other activity indicators. Jointly taking into account both parameters, Barnes (2003, 2007) devise a method to determine the *gy-*

rochronological age. From his analysis of cluster and field stars, Barnes finds that there are basically two categories of rotating solar-type stars, he calls C- and I-type stars. Following his simple model, C-type stars have a convection zone maintaining a turbulent dynamo that creates a small-scale magnetic field. This field cannot mediate a coupling between the inner radiative zone (if any) and the exterior, so that these stars show an exponential spindown of the outer convection zone. In I-type stars, a strong dynamo develops at the interface between convective and radiative zones creating a large-scale field which couples the inner radiative zone and the exterior to the surface convective zone—these stars show the Skumanich-style spindown. Treating these two regimes separately, Barnes obtains a tight relationship between the rotation period of a star and its age and color. With space-based photometric missions like CoRoT and Kepler stellar rotation can be measured directly and at very high precision. Further, the technique avoids the necessity to obtain a distance estimate of a field star, which is required for dating based on isochrones.

3.2.2. Starspots

Starspots are expected to appear on the photospheres of all solar-like stars with outer convection zones and magnetic field. During the last decades the field of starspot research saw significant progress due to improved diagnostic techniques, some of which are outlined in following.

Because of its large size and relative proximity Betelgeuse was the first object from which direct images could be obtained (Gilliland & Dupree, 1996). Direct imaging is, however, only feasible in a very limited number of cases.

Kron (1947) was the first, who tried to infer the presence of stellar spots from the morphology of stellar light curves. The modeling of the observed light curve based on analytical or numerical schemes became known as *light-curve inversion* (e.g., Eker, 1994, and references therein).

Spots on the rotating stellar surface lead to an observable distortion of the spectral line profiles, which can be used to reconstruct an image of the stellar surface. This technique is called *Doppler imaging* (e.g., Vogt & Penrod, 1983). Doppler imaging has high demands regarding spectral resolution and phase coverage and is therefore applicable only in the case of bright, fast rotating stars. For both methods the reconstruction of the stellar surface is an ill-posed, inverse problem, so that additional regularization methods are required to obtain a unique solution. While light-curve inversion is observationally less demanding, it completely lacks latitudinal information on the spot position. As shown by Huber et al. (2009b), the strong degeneracy between different models may be slightly lifted in the case of simultaneously observed radial-velocity data.

An approach applicable in stellar systems with a transiting extrasolar planet is *planetary eclipse mapping*. This method relies on high-precision transit light curves as delivered by recent space-based observatories like CoRoT and Kepler. During the transit, the planet occults different parts of the stellar disk, but also starspots located at latitudes beneath the planetary path. The occultation of a spot on the stellar surface can then be observed as a relative increase in brightness during the

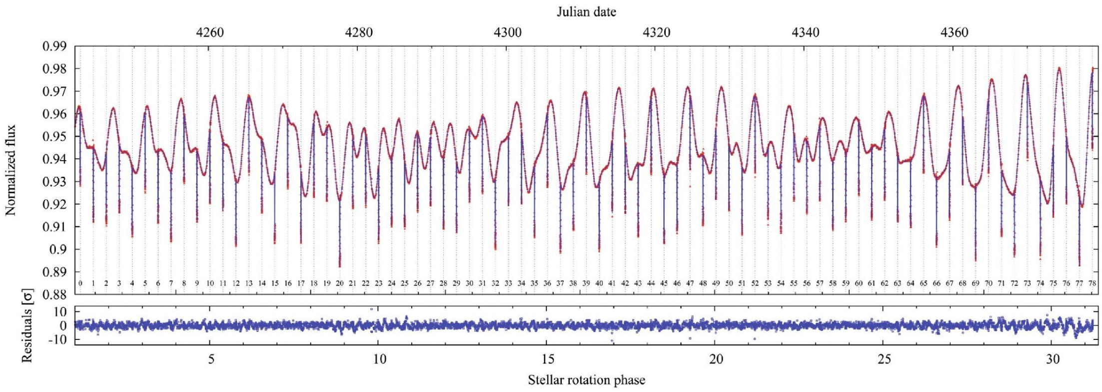

Figure 3.12.: Light curve of CoRoT-2A obtained with the CoRoT space telescope. The light curve shows pronounced variability due to starspots and regularly recurring transits. The surface reconstruction by Huber et al. (2010), which also reproduces the shape of each transit, is indistinguishable from the data. Figure taken from Huber et al. (2010).

transit (e.g., Wolter et al., 2009). This technique thus partly recovers latitudinal information. It has been applied succesfully by Huber et al. (2009a, 2010) in the case of the exoplanetary system CoRoT-2. With 152 days of space-based photometry available, this system is ideally suited for planetary eclipse mapping: Its hot Jupiter is in a close orbit transiting its host star every 1.74 days, which is about three times the stellar rotation period. Furthermore, the host star shows an exceptional degree of activity as evidenced by its light curve, which is modulated with an amplitude of 6 % (see Fig. 3.12). Fitting the global light curve and all transits simultaneously, Huber et al. (2009a, 2010) are able to consistenly reconstruct the surface brightness distribution of CoRoT-2A and its evolution over the course of the observation. The authors find strong indications for two active longitudes, where most spots can be found, separated by 180°. Their results can be interpreted in terms of differential rotation or the flip-flop phenomenon, which we discuss below.

The technique of *magnetic Doppler imaging* uses Zeeman splitting of photosperic lines caused by magnetic fields, which shows up as additional line broadening in unpolarized light. Spectropolarimetric observations can resolve this broadening as being due to contributions of different polarization. Magnetic Doppler imaging can therefore be used to reconstruct a magnetic map of the stellar surface (Donati et al., 1997; Piskunov & Kochukhov, 2002). Clearly, also this method is prone to non-uniqueness.

The observational status quo

Starspots have been studied in a few hundreds (Strassmeier, 2009) of binary systems of different types (BY Dra-, W UMa-, RS CVn-, Algol-type) and single stars (T Tau, FK Com, and solar-type stars). In contrast to the Sun, where spots typically cover always less than 1 % of the visible disk, some stars show enormous starspots covering up to

50 % of the stellar surface (O'Neal et al., 1996). While most young solar-type stars show typical variability at the percent level (Radick et al., 1982), photometric amplitudes up to 0.63 mag were observed in a light curve of the RS CVn star II Peg (Tas & Evren, 2000). However, spot coverage does not directly translate into spot sizes and the smallest spot sizes are usually determined by the resolution of the adopted method. The actual size distribution of starspots is therefore unknown.

In many cases Doppler images show a pronounced concentration of spots in the polar region. Because such a polar spot does not contribute to the modulation of the light curve, the reality of these features has long been doubted but is currently mostly accepted (Rice, 2002). The lifetimes of single stellar spots cannot be reliably determined, as observations do not distinguish between single spots and groups of spots conglomerating to active regions. Observations by Hatzes (1995) suggest that an active region on V410 Tau has survived on the stellar surface for about 20 years. Thus, active regions seem to be relatively long-lived features on stellar photospheres. Long-term observations indicate that active regions occur on preferred active longitudes, which are typically located on opposite hemispheres (e.g., Korhonen et al., 2002; Berdyugina et al., 2002). These active longitudes, which apparently also exist on the Sun (Berdyugina & Usoskin, 2003), alternately change their activity level on a timescale of years, an effect known as *flip-flop* phenomenon.

While there is a large body of phenomenological evidence for the existence of starspots and active regions for many stars, the physical origin of these observed properties remains an active field of research.

3.2.3. Stars in X-rays

The first detection of *stellar* X-ray emission is attributed to Catura et al. (1975), who report an X-ray signal from the stellar system Capella. In analogy to the Sun, the X-ray emission was explained by the presence of thin and hot coronal plasma with temperatures of one million Kelvin or more (Mewe et al., 1975).

X-ray emitting stars were soon found to be distributed over the whole Hertzsprung-Russel diagram. The main focus of this work are cool, solar-like stars, that have outer convection zones driving a solar-like dynamo. The X-ray emission of these stars is similar to solar emission in many respects. A detailed review on coronal X-ray emission is beyond the scope of this introduction. I refer to the review by Güdel (2004) for further details on this subject.

A stellar coronal spectrum differs from photospheric optical spectra, because the corona consists of hot, mostly optically thin plasma, which is collisionally ionized. Low-resolution stellar X-ray spectra can be characterized by one or two thermal componenents with temperatures between $1-5$ MK and a specific plasma metallicity. The level of X-ray activity is measured in terms of the quantity $\log L_X/L_{\rm bol}$ relating the X-ray luminosity of a star to its bolometric luminosity. For stellar coronae this ratio typically lies in the range from -7 to -3 for energies between 0.2 and 10 keV, whereas the solar value of $\log L_X/L_{\rm bol}$ varies between -7 and -6 depending on the solar cycle (Judge et al., 2003).

One of the most important findings is that similar stars can largely differ in their X-ray emission and that there is a clear correlation between their X-ray activity, age, and rotation as evidenced by chromospheric activity indicators (cf. Sect. 3.2.1): The X-ray luminosities of stars decay with increasing age roughly proportional to $t^{-1/2}$ (Guedel et al., 1997; Maggio et al., 1987). As suggested above, this decay is linked to the slowing of the rotation rate with stellar age.

X-ray activity cycles, as detected for the Sun and a large number of stars in chromospheric activity indicators, have been found only for a small number of stars (Hempelmann et al., 2006; Robrade et al., 2007; Favata et al., 2008).

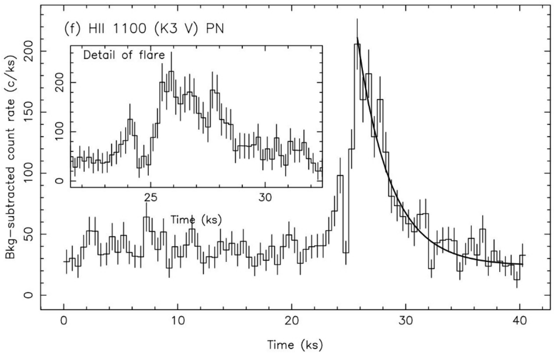

Figure 3.13.: Background-subtracted XMM-Newton light curve of Pleiades member H II 1100. Is the flare occulted by a Jovian planet? Figure taken from Briggs & Pye (2003).

Coronal structure inferred from eclipses

Close binary stars are on average more active than single stars because the rotation periods of the two stars are tidally locked to the orbital period. The rapid rotation then is accompanied by a higher level of magnetic activity. In principle, X-ray eclipses in these binary systems provide the possibility to resolve extent, structure, and location of coronal emission and mass ejections. This kind of coronal eclipse mapping has been accomplished in several cases.

Ottmann (1994) used the offset of the X-ray eclipse relative to the optical first contact in the eclipsing binary system Algol to determine the height of the corona of the active K star component. Further studies detected a signature of flares via X-ray eclipses (Schmitt & Favata, 1999; Schmitt et al., 2003). Using ROSAT observations, Schmitt & Kürster (1993) were able to spatially resolve coronal X-ray emission from the secondary component of the eclipsing binary system α Coronae Borealis, which consists of a G5 star being regularly eclipsed by its X-ray dark A-type companion. Modeling the shape of the eclipse light curve it was possible to reconstruct the X-ray brightness distribution of the G star (Güdel et al., 2003).

Briggs & Pye (2003) detected an eye-catching sudden drop during a flare occurring on the active Pleiades member H II 1100 (see Fig. 3.13). The authors carefully rule out instrumental causes and argue that the dip could be caused by a rising flare being eclipsed by another object. Given the involved timescales the observed dip would be consistent with a transiting Jovian planet in close orbit around the star. So far, however, this hypothesis lacks confirmation.

The observation of increased activity in binary systems led to the idea that stars with close-in Jovian planets should exhibit similar signs of activity due to mutual interactions. In turn, the planet allows to study the corona of its host star via "coronal eclipse mapping", an approach we will pursue further in Sects. 6.2 and 6.3.

3.2.4. The Chandra observatory

The observation of cosmic X-ray sources poses several challenges for mission design and the construction of an X-ray telescope. Since the Earth's atmosphere absorbs X-rays, the detection of X-rays requires rocket experiments or space-based instrumentation. Further, X-ray radiation behaves different from optical light in several respects. Conventional mirrors used in optical telescopes are completely inappropriate to reflect X-rays, because they would simply be absorbed by the mirror. Therefore, X-ray telescopes work with total reflection of X-rays after grazing incidence on parabolic and hyperbolic metallic surfaces, a principle proposed by Wolter (1952). As the wavelength of X-rays of about 1 Å is comparable to the size of an atom, these metallic mirrors require a very precise optical surface. Because of these high demands regarding the production and polishing of the mirrors, the first observatory equipped with a Wolter-type telescope was launched not until 1978, nearly three decades after Wolter's studies. Since the first X-ray telescopes the mirror quality has continuously improved; modern X-ray telescopes like Chandra provide an angular resolution of up to 0.5 arcsecond.

The Chandra X-ray Observatory is a space-based X-ray telesope launched by NASA in July 1999. The spacecraft was placed in an eccentric orbit at high altitudes mostly beyond Earth's radiaton belts, so that it can observe continuously for up to 55 hours of its 64 hour orbital period. Its High Resolution Mirror Assembly consists of four sets of nested, grazing incidence mirror pairs providing an aperture of 1.2 m. Chandra is equipped with two focal plane instruments, the Advanced CCD Imaging Spectrometer (ACIS) and the High Resolution Camera (HRC). This work relies on data obtained with the ACIS instrument, a set of CCDs operating in the range of $0.2 - 10$ keV providing a spectral resolution on the order of 0.1 keV. Additionally, two transmission gratings (HETGS/LETGS) provide the possibility for high-resolution spectroscopy.

3.3. The role of stellar activity in exoplanetary systems

The most prominent example of magnetic interactions between a planet and its host star on Earth is evidenced by polar lights. They are caused by charged particles from the solar corona that are trapped within Earth's magnetosphere. These particles are injected into the ionospheric current system trough Birkeland currents and accelerated towards the geomagnetic poles, where they ionize oxygen and nitrogen atoms in the upper atmosphere. Human eye can witness their colorful recombination emission as aurora.

Another interesting case is the Jupiter-Io system, which constitutes a miniature stellar system. As shown in Fig. 3.14, Jupiter shows auroral lights at the footprints of a large current system connecting the magnetospheres of Jupiter and Io (Bigg, 1964; Goldreich & Lynden-Bell, 1969). Exoplanets orbiting their host stars at very

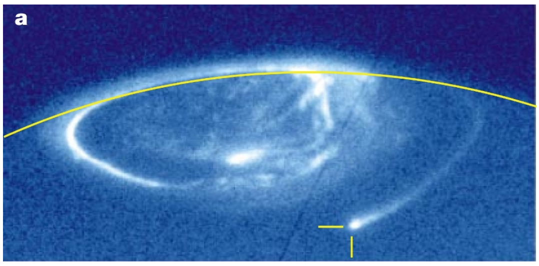

Figure 3.14.: UV images of Jupiter's polar cap obtained with the HST/STIS instrument. Tick marks point to emission from the magnetic footprints of Io. Figure taken from Clarke et al. (2002).

close distances are expected to show much stronger mutual interactions.

3.3.1. Star-planet interactions

While the Solar System planets on their part are unlikely to have any significant influence on the Sun, this could be different for large Jovian planets in close vicinity to their host stars. It is known, that binary star systems are generally more active than single stars as evidenced for example by their X-ray emission (Siarkowski et al., 1996; Getman et al., 2011).

Mutual interaction between star and planet could be mediated by tidal or magnetic effects. Gravitational interaction due to close-in ($d \leq 0.1$ AU) hot Jovian planets can cause tidal bulges on the star with typical heights up to 10 % of the photospheric scale height. This yields enhanced coronal activity via increased turbulence (Cuntz et al., 2000). Magnetic interaction could be due to reconnection events between planetary and stellar magnetic field lines (Lanza, 2008, 2009). As the planet triggers the reconnection of stellar magnetic field lines, this would result in stellar flares preferentially occuring beneath the planet. Alternative scenarios comprise the planet's magnetosphere preventing the expansion of coronal magnetic field structures (Cohen et al., 2009) or a Jupiter-Io-like interaction (Schmitt, 2009).

Star-planet interaction should manifest itself in enhanced chromospheric and coronal X-ray emission modulated with the planetary rotation period. Observing such signatures is, however, difficult since all cool stars show a certain level of intrinsic variability causing both short-term and long-term activity changes.

Indications for *chromospheric* activity enhancement have been found for some stars (Shkolnik et al., 2005), but could not be confirmed in later observations (Poppenhaeger et al., 2011). Canto Martins et al. (2011a) find no indications for enhanced chromospheric Ca II emission analyzing a sample of 74 planet-bearing stars.

The observational results in X-rays regarding a planet-induced increase of stellar activity are even less encouraging. While Kashyap et al. (2008) and Scharf (2010) detect an increase in coronal activity of a large sample of planet-bearing stars compared to stars without planets, Poppenhaeger et al. (2010) find no such trend in their volume-limited nearly complete sample that cannot be explained by observational biases and selection effects. Another noteworthy case is the first detected hot Jupiter, 51 Peg b, which is found to be in an exceptionally low state of X-ray activity comparable to the solar Maunder minimum (Poppenhäger et al., 2009).

So far, there is no unambiguous evidence for planet-induced enhancement of stellar X-ray activity. The direct influence of the planet on stellar activity appears to be negligible compared to intrinsic stellar variability. However, high-energy emission due to stellar activity might, conversely, have a significant influence on the planet.

3.3.2. Evaporating atmospheres

Hot Jupiters are observed to have systematically lower masses than extrasolar planets at larger distances from their stars (Zucker & Mazeh, 2002). This correlation may be a result of their formation history: Once the planet has formed and the stellar disk disappeared, close-in hot Jupiters are immersed in an enormous high-energy radiation field due to coronal emission from the host star. The ionizing radiation can have a significant influence on the structure and evolution of the planetary atmosphere heating it up to temperatures of more than $10,000$ K by X-rays and extreme ultraviolet (EUV, 100-912 Å) radiation. At these high temperatures the thermal energy per atom or molecule exceeds its gravitational potential energy, so that they may experience hydrodynamic blow-off.

Schneider et al. (1998) estimate the extent of the planetary exosphere and find that atmospheres of hot Jovian exoplanets can exceed the Roche lobe, leading to evaporation of planetary material and the formation of a comet-like tail through interaction with the stellar wind. Indeed, extended atmospheres of extrasolar planets were found for HD 209458b (Vidal-Madjar et al., 2003), HD 189733b (Lecavelier Des Etangs et al., 2010), and WASP-12b (Fossati et al., 2010).

Several evaporation scenarios are discussed in the literature (e.g., Lammer et al., 2003; Lecavelier des Etangs et al., 2004). The usual assumption is that the atmosphere is composed of hydrogen and that all available energy goes into hydrodynamic escape (Watson et al., 1981). The mass loss of the atmosphere is calculated by balancing the evaporation losses with the planet's gravity.

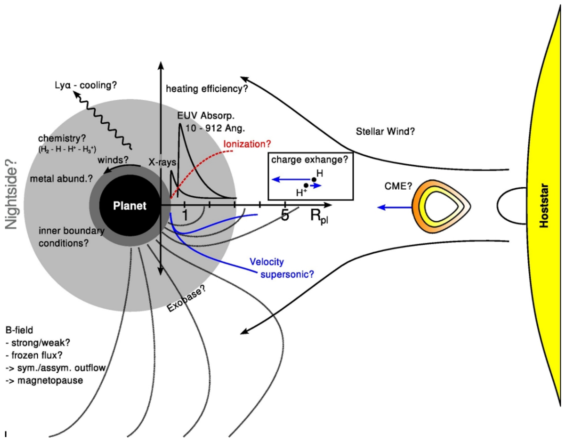

Figure 3.15.: Sketch illustrating the complex interplay of heating and cooling mechanisms important for planetary evaporation simulations. Figure courtesy of M. Salz.

While the energy-limited approach assumes that a particle must be moved to infinity to escape the gravitational potential of a planet, the particle must in fact only reach the edge of the Roche lobe increasing the mass loss rate by a factor of $1/K$ where $K \leq 1$ (Erkaev et al., 2007). Hydrodynamical simulations of thermal mass loss (e.g., Murray-Clay et al., 2009) include a multitude of heating and cooling effects yielding a complex picture of the planetary exosphere (Fig. 3.15). However, the bottom line is that indeed most of the EUV and X-ray radiation contributes to the evaporation of the atmosphere.

A convenient expression for the mass loss taking roche lobe overflow into account is given by Sanz-Forcada et al. (2011), viz.

$$\dot{M} = \frac{\pi R_p^3 F_{\mathrm{XUV}}}{GKM_p}, \tag{3.4}$$

where F_{XUV} is the sum of the stellar X-ray and EUV flux at the planetary orbit, G is the gravitational constant, R_p is the radius and M_p the mass of the planet (all in cgs units). Introducing the mean density ρ of the planet and neglecting Roche lobe overflow a lower limit on the mass loss is given by

$$\dot{M} = \frac{3F_{\mathrm{XUV}}}{4G\rho}. \tag{3.5}$$

From their analysis of a large sample of planetary systems Sanz-Forcada et al. (2010) come to the conclusion that accumulated effects of mass loss due to stellar high-energy illumination indeed has a detectable influence on the observed mass distribution of exoplanets. It gives rise to an erosion line, below which the authors find the large majority of the planets in their sample.

On the other hand, a study by Leitzinger et al. (2011) shows that the close-in rocky planets CoRoT-7b and Kepler-10b are unlikely to be remnants of thermally evaporated hydrogen-rich gas giants, but have already started their life as super-earth, at least following the current paradigm of thermal planetary evaporation.

It is however possible that additional non-thermal escape processes like internal magnetic fields or the influence of coronal mass ejections (Khodachenko et al., 2007) are important factors in the modeling of planetary evaporation. Furthermore, current models do not take into account the effect of X-rays, which penetrate deeper into the atmosphere than EUV radiation, where they lead to ionization of heavy elements yielding increased heating (Cecchi-Pestellini et al., 2006, 2009).

Studies by Knutson et al. (2010) suggest that chromospheric activity has an observable influence on the dayside emission spectra of hot Jupiters. The authors find a correlation between activity measured using Ca II H and K emission and the presence of a thermal inversion in the atmospheric structure of the planet, which seems to be present only for inactive host stars. Interestingly, the hot Jupiter around the most active star in their sample, CoRoT-2b, has an unusual spectrum, which is well-described neither by inverted nor non-inverted atmosphere models.

The impact of high-energy radiation on the atmospheres of the two hot Jupiters CoRoT-2b and CoRoT-7b will be studied in detail in Sects. 6.2 and 6.4 of this work.

4. Analysis of high-resolution spectroscopy of solar-like stars

Deriving accurate stellar parameters from a given spectrum is the bread-and-butter business of a stellar spectroscopist. The first part of this chapter summarizes different methods to determine the fundamental photospheric characteristics like effective temperature, surface gravity, and metallicity of solar-like stars from an observational perspective. Details on the underlying framework of radiative transfer can be found in Mihalas (1978) or Gray (1992). The next part focuses on further parameters like age and distance. The chapter closes with a short review of chromospheric activity indicators in the spectra of late-type stars.

4.1. Basics of stellar line formation

Spectral lines are not infinitesimally narrow but have a finite width. The characteristic profile of the line is determined by a multitude of processes, that in turn allow to probe the physical conditions in the stellar atmosphere under which the line was formed. I will outline some of the most important broadening mechanisms of spectral lines following Tatum (2004).

The most fundamental mechanism is *natural broadening* by *radiation damping*. An electron immersed in the time-dependent electromagentic field of a light wave will be forced to oscillate and thus starts to radiate. In the classical description, the loss of energy results in damped harmonic oscillations. The full quantum mechanical treatment accounts for the finite lifetimes of different energy levels due to Heisenberg's principle of uncertainty. In a next step, the single oscillator is replaced by a slab of gas containing a number of oscillators per unit volume. This gives rise to the combination ϖf of statistical weight, ϖ, and oscillator strength, f, of the energy level under consideration. In the case of an optically thin gas the absorption line profile can then be described by a Lorentz profile being characterized by a narrow core, skirted by extensive wings.

The motion of atoms in a hot gas introduces another broadening mechanism known as *thermal broadening*. The random motions induced by a certain temperature result in Doppler shifts of the wavelength of the observed radiation. The distribution of the resulting wavelength shifts is proportional to Maxwell's distribution of velocities at a given temperature, T, and mass of the species. The profile emerging from this process is a Gaussian or Doppler profile, which compared to the Lorentzian profile is dominated by the core and lacks extensive wings.

The stellar atmosphere is a highly dynamic and turbulent system with different scales being involved. Assume turbulent cells of gas moving in random directions with velocities according to Maxwell's distribution. If these cells are small compared to the optical depth, an observer sees many of these cells contributing to the Gaussian velocity distribution. This is the realm of *microturbulence*, which can be approximated by a Gaussian velocity distribution of width ξ. Microturbulence thus contributes to the Doppler broadening of the line profile. However, from an observational point of view it is still possible to separate both contributions, because the thermal broadening varies with the mass of the emitting or absorbing atom while microturbulence is determined by the mass of the gas cells. In the *macroturbulence* limit the size of the turbulent cells is no longer small compared with the optical depth, so that it results in non-thermal broadening without changing the equivalent width. Solar granulation suggests to describe the macroturbulence velocity, ζ, as superposition of velocity fields in either radial and or tangential direction following a Gaussian distribution.

Pressure broadening (also known as *collisional broadening*) subsumes all line broadening effects due to the presence of nearby particles that affect the radiation process of the emitting atom. For stars on or above the main sequence collisions between atoms are frequent and their duration is small compared to the intercollision time. Such collisions interrupt the emission process thereby increasing the uncertainty in energy. The intercollision times are assumed to be distributed according to a Poisson distribution. The resulting broadening effect can be described by a Lorentzian profile with a damping constant determined by the mean time between two collisions depending on both the density and the temperature of the gas.

At the moment of collision the presence of an electromagentic field due to other particles shifts the energy levels in the emitting atom. The shape of the resulting line profile is determined by the functional dependence of the perturbing force on the distance from the perturbing particle. If an atom is approached by an electron or an ion the lines will be broadened by the Stark effect. In the case of interactions between two atoms of the same species dipole coupling results in resonance broadening, while interactions with neutral particles are mediated by van der Waals forces.

A non-local broadening effect is *self-absorption.* Light emitted at a particular point in the stellar atmosphere can be absorbed as it travels through the outer layers of the atmosphere. As the re-absorption probability depends on the wavelength with photons at the line center having the highest absorption probability, this process will lead to line broadening or even self-reversal of the line core.

Further broadening mechanisms include *rotational broadening* due to the rotation of the star, where the light from the receding limb is redshifted and light from the approaching limb is blueshifted, and *instrumental broadening* due to the finite resolution of the spectrograph.

In a stellar atmosphere these broadening agents all act in concert and contribute to the observed line profile. Assuming all effects to be independent, the resulting line profile is the convolution of the constituent profiles. While the convolution of Gaussian profiles remains a Gaussian and the convolution of Lorentzian profiles remains a

Lorentzian, the convolution of a Gaussian and a Lorentzian profile yields the *Voigt profile*, which is the general description of a spectral line profile.

4.2. Stellar parameters inferred from strong lines

The profile of a spectral line contains a wealth of information on the physical processes accompanying its formation. Strong lines which are well-resolved provide useful diagnostics of the fundamental stellar parameters governing the broadening processes.

4.2.1. Effective temperature from Balmer lines

One of the most important parameters in stellar astrophysics is the effective temperature of a star. It is defined as the temperature of a black body with the same luminosity as the star. The effective temperature, $T_{\rm eff}$, relates the stellar luminosity, L, to the stellar radius, R, according to the Stefan-Boltzmann law,

$$L = 4\pi\sigma R^2 T_{\rm eff}^4, \quad \sigma = \frac{2\pi^5 \mathrm{k}^4}{15\mathrm{c}^2\mathrm{h}^3}, \qquad (4.1)$$

where k and h denote Boltzmann's and Planck's constant and c is the velocity of light. The effective temperature is a parameter that is difficult to measure with high accuracy; on the other hand, the degree of accuracy of the measurement directly propagates into the estimation of the remaining stellar parameters like surface gravity or metallicity.

There are several methods to determine the effective temperature based on photometric or spectroscopic measurements. Photometric methods are usually based on the calibration of multi-band color indices (e.g., Nordström et al., 2004). Spectroscopically, the effective temperature of a star can be determined from continuum features in the stellar spectrum. Popular temperature indicators are for example the slope of the Paschen continuum, which can be approximated by the $B-V$ color index, or the Balmer jump defined as a change in the continuum height at 3647 Å due to hydrogen bound-free absorption. Other temperature indicators rely on single spectral lines, the most prominent example being the hydrogen Balmer lines.

The wings of the Balmer lines show substantial pressure broadening, which is due to the linear Stark effect and resonance broadening (Struve, 1929; Gehren, 1981; Barklem, 2008). For solar-like stars with effective temperatures below 8000 K, the curvature of the Balmer line wings is sensitive to changes in effective temperature (Fuhrmann et al., 1993, 1994). Using only Hα at 6563 Å an accuracy of ± 50 K is possible. Furthermore, the other lines of the Balmer series can provide independent confirmation of the Hα results. The dependence on parametes like surface gravity and metallicity is comparably low. For broad hydrogen lines it becomes exceedingly difficult to measure equivalent widths. Therefore one usually uses synthetic spectra to fit the line profile directly. In the case of chromospheric activity the Balmer lines show substantial emission leading to a fill-in of the line core. However, if the chromospheric contamination is not too strong the line wings remain unaffected and yield consistent results (Fuhrmann, 2004).

4.2.2. Surface gravity from the Mg Ib triplet

The second fundamental parameter describing the stellar photosphere is the surface gravity. The gravitational acceleration, g, at the surface of a star of mass M and radius R is given by

$$g = g_\odot \frac{M/M_\odot}{(R/R_\odot)^2} \tag{4.2}$$

where the quantities $g_\odot$, $M_\odot$, and $R_\odot$ refer to the corresponding solar values. The surface acceleration is typically referred to as surface gravity parameter and is expressed on a logarithmic scale in units of the decimal exponent (*dex*). The surface gravity is the acceleration due to gravity experienced by a test particle close to the stellar surface and is thus a measure of the pressure at the surface of the star.

In late-type stars several strong, pressure-broadened lines provide the possibility to derive the surface gravity parameter. A useful tracer of the surface gravity is the Mg Ib triplet with lines at 5167 Å, 5172 Å, and 5183 Å (Fuhrmann et al., 1997). The Mg Ib triplet has well-known atomic parameters and its lines populate a spectral region where the continuum is well defined. Furthermore, the use of more than one line provides additional consistency checks.

Several other lines also show strong pressure-broadened wings. These are Ca II H and K, the Na I D doublet (5890 Å, 5896 Å), a number of strong Ca I lines, e.g. at 6122 Å, 6162 Å, and 6439 Å (Bruntt et al., 2010), and the Ca II infrared triplet (Smith & Drake, 1987). For solar-like stars some of these broad lines show significant blending and in some cases also contamination by telluric lines. In most cases, it is thus advisable to fit the line wings with synthetic spectra instead of trying to compute an equivalent width.

4.3. Chemical abundance analysis

The fundamental stellar parameters can also be determined as a byproduct in a spectroscopic abundance analysis by measuring the equivalent widths of a large number of stellar absorption lines. The underlying concepts of this approach are discussed in standard texts of stellar atmospheres (e.g., Gray, 1992). In the following some aspects and assumptions of spectroscopic abundance analysis are reviewed and the main line of thought is outlined.

4.3.1. Equivalent widths

The depth and shape of spectral lines encode a plethora of information on physical quantities and processes that led to the formation of the line. A suitable measure of the strength of a line is the equivalent width (EW) defined as

$$W = \int \frac{F_c - F_\lambda}{F_c} \, \mathrm{d}\lambda \tag{4.3}$$

where F_c and F_λ denote the continuum flux and the flux in the line, respectively. The EW is the width of a perfectly black, rectangular absorption line with an area equal to the area in the spectral line. It measures the line flux removed from the spectrum relative to the continuum and thus yields the number of absorbing atoms in an optically thin gas.

While the ability to resolve the line profile depends on the resolving power of the spectrograph, the shape of a spectral line itself depends on the detailed physical conditions within the star, broadening effects as detailed above, and instrumental distortions. For moderate spectral resolutions ($\lambda/\Delta\lambda \lesssim 50,000$) and faint targets the EW is a convenient choice, because it does not require to exactly trace the line profile.

4.3.2. Curve of growth approach

The theory of curves of growth has a long history dating back more than 80 years (Unsöld et al., 1930). The following is a short review of the conceptual basics to acquaint the reader with the spectroscopic parlance.

The *curve of growth* is a graph showing the monotonic increase of the EW of an absorption line with the abundance of the absorbing species (Fig. 4.1). In an optically thin gas, the EW of weak lines (EW < 80 mÅ for solar-like stars) is linearly proportional to the number of atoms, N, in the initial level of the line. The line width is dominated by thermal broadening. Increasing the number of absorbing atoms drives the line towards the saturated regime. After the line saturates, the Doppler wings barely change, so that the EW increases roughly as $\sqrt{\ln N}$. Eventually, for even larger abundances the strong wings due to pressure broadening start to add to the EW, so that the EW increases again ($\propto \sqrt{N}$), although more slowly than during the optically thin stage. While the third stage of the curve of growth is scarcely evident in case of a Gaussian-shaped line profile, the second stage is missing for a pure Lorentzian profile. The classic three-stage curve of growth is exhibited for a Voigt profile in which the Gaussian and Lorentzian contributions are comparable.

The derivation of chemical abundances from an observed spectrum relies on the construction of partial curves of growth using the EWs of a large number of spectral lines pertaining to the element under consideration. Given a model for the photosphere of a star with known temperature and pressure the curve of growth of a single line with specified excitation potential and oscillator strength can be calculated by varying the abundance of the element under consideration. The curves of growth then yield EWs, that are required to match the measured ones. This is done on a line-by-line basis until, ideally, all measured EWs are reproduced.

From the observational point of view the star has a fixed abundance. The curve of growth can then be constructed from a large number of lines of the species being considered with different excitation potentials and oscillator strengths. By comparing the shape of the observed curve of growth with one of the theoretical curves, it is possible to deduce the Gaussian and Lorentzian contributions of the measured lines to deduce the temperature and the pressure. As described above, the Gaussian component includes both a thermal and a microturbulent component, whereas the Lorentzian contribution includes radiation damping and pressure broadening. While the microturbulence can be assumed to be the same for all elements given a homogeneous and isothermal atmosphere, this is less clear for the radiation damping component, which can vary from line to line. However, in the case of main-sequence stars the pressure broadening component is typically much greater than the radiation damp-

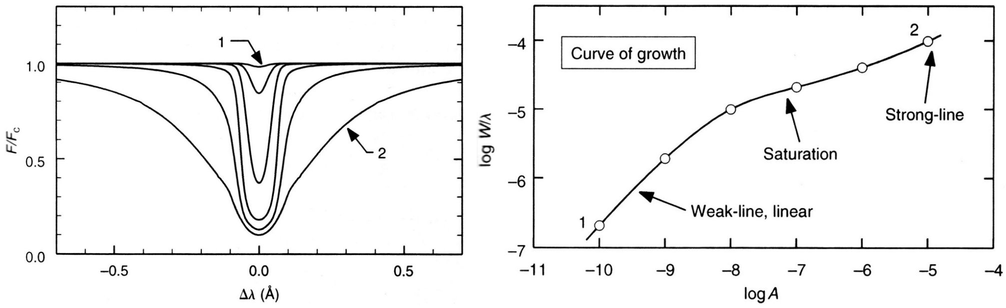

Figure 4.1.: Left: Synthetic line profile of Fe I at 6065 Å for different iron abundances, A, as specified in the right panel. Right: Three-stage curve of growth showing the relation between reduced equivalent width, W/λ, and abundance, A. The dots correspond to the profiles shown in the left panel. Figures taken from Gray (1992).

ing component, so that this effect can be neglected.

4.3.3. Differential analysis

The abundance of an element X with respect to hydrogen is expressed on a scale in which the logarithm of the abundance of hydrogen is set equal to 12,

$$\log A(\mathrm{X}) = \log \frac{N_\mathrm{X}}{N_\mathrm{H}} + 12, \qquad (4.4)$$

with N denoting the number of particles. For solar-like stars it is advantageous to determine abundances strictly differential to the Sun, because the problem of uncertain ϖf values can be circumvented. In a differential analysis, all abundances are related to solar abundances, viz.

$$[\mathrm{X/H}] = \log \frac{A(\mathrm{X})}{A_\odot(\mathrm{X})}. \qquad (4.5)$$

This approach requires that the spectra are obtained under similar instrumental conditions and that the EWs are measured using the same technique. Further the differential approach only works for stars that do not strongly deviate from the Sun. It is hardly possible to give an exact criterium, however, according to Fuhrmann (1998, 2004) the method yields reliable results for dwarf and subgiant stars with spectral types ranging from late-F to early-K.

4.3.4. Line selection

In spectroscopic abundance analyses of solar-like stars physical parameters are typically inferred from measuring the equivalent widths of a large number of iron lines and enforcing balance constraints on abundances derived from neutral (Fe I) and ionized (Fe II) lines. The first step in such an analysis therefore is to compile a suitable set of lines that are used in the analysis. Such a line list includes the wavelength, excitation potential, oscillator strength, and the EW of the line as measured in a solar spectrum.

Abundance measurements are usually based on a large number of weak spectral lines. For solar-like stars the lines should have EWs between 10 and 200 mÅ to allow a reliable measurement (Sousa et al., 2008), while in the case of young and active stars EWs should be smaller than 60 mÅ to avoid the influence of chromospheric effects

(Fuhrmann, 2004). In principle, as many lines as possible should be used in the analysis; these lines should cover a broad range of excitation potentials up to 8 eV. In the case of Fe I, the excitation potential should be larger than 2 eV to avoid strong non-LTE effects. The spectral lines should be isolated lines unaffected by blends. Line lists should always be cross-checked with other lists of stable lines. Additionally, Bubar & King (2010) suggest to minimize the correlation of excitation potential with reduced equivalent width, which results from higher excitation potential lines being predominantly formed in hotter and therefore deeper layers of the stellar atmosphere, so that these lines may be weaker.

4.3.5. Model atmospheres and MOOG

The main reasoning in spectroscopic abundance analysis is as follows: After having measured the EWs of a large number of spectral lines contained in the previously compiled line list, the starting point is a guess for the fundamental parameters describing the photospheric properties of the star. In particular, one guesses the effective temperature, surface gravity, microturbulence velocity, and metallicity.

These quantities are used to generate a model atmosphere providing the physical parameters within the stellar atmosphere that directly enter the calculation of the theoretical curves of growth. For late-type stars such model atmosphers are provided for example by Castelli & Kurucz (2004). These are one-dimensional plane-parallel model atmospheres that divide the photosphere into a number of layers of certain mass depth, with defined temperature, gas pressure, electron density, Rosseland mean absorption coefficient, radiation pressure, and microturbulent velocity. The most essential assumption underlying the atmosphere models is local thermal equilibrium (LTE), i.e., the equation of radiative transfer is solved assuming that the radiation can be modeled by a blackbody source function and the properties of a small volume of gas are characterized by the thermodynamic equilibrium values determined from the local pressure and temperature.

The measured EWs and the model atmosphere are used as input to the MOOG spectral analysis tool (Sneden, 1973). MOOG uses the physical parameters provided by the model atmosphere to solve the basic equations of stellar line formation in LTE for the lines and their atomic parameters as specified in the line list. It then uses the curve of growth approach to compute EWs for a given abundance. The `abfind` subroutine then fits the abundances to yield EWs that agree with the measured ones.

As the stellar parameters are usually not known *a priori*, the derived abundances for neutral and ionized lines will display characteristic correlations and systematic imbalances. Enforcing a number of balance constraints then allows to converge to the correct solution (in the sense, that the parameter set minimizing the intrinsic correlations is considered to be the true one). The constraints, which are motivated in the following, can be summarized in a simple recipe:

(1) Adjust T_{eff} to minimize correlations between iron abundance and excitation potential.

(2) Adjust $\log g$ so that the abundance inferred from Fe II lines matches the abundance inferred from Fe I lines.

(3) Adjust ξ to minimize correlations between iron abundance and reduced EW.

As the physical parameters are correlated with each other, these balance constraints have to be implemented in an iterative scheme.

4.3.6. Excitation balance

Under the assumption of local thermodynamic equilibrium the number N_i of populated energy levels with statistical weight ϖ_i and excitation potential χ_i is Boltzmann-distributed,

$$\frac{N_i}{\sum_i N_i} = \frac{\varpi_i \exp\left(-\frac{\chi_i}{\mathrm{k}T}\right)}{Z},$$
$$Z = \sum_i \varpi_i \exp\left(-\frac{\chi_i}{\mathrm{k}T}\right), \tag{4.6}$$

where k is Boltzmann's constant and Z is the partition function. The excitation temperature, T, is derived spectroscopically and interpreted as effective temperature, T_{eff}, of the photosphere.

Given a first guess for the stellar parameters and the measured EWs, MOOG uses the equation of LTE line formation to compute expected abundances for each measured line by fitting the line's measured EW. According to Eq. 4.6, the number of excited atoms depends on their respective excitation potential for an assumed value for T_{eff}. If the initial guess for T_{eff} is correct, lines with different excitation potentials yield consistent results for T_{eff}. An underestimation of T_{eff} results in a lower number of excited atoms, so that MOOG predicts lower EWs for lines with high excitation potential. Consequently, larger abundances are needed to yield theoretical EWs that are compatible with the measured EWs. Accordingly, an overestimation of T_{eff} will yield lower abundances for lines with high excitation potentials. Therefore, the value for T_{eff} yielding consistent results can be obtained by minimizing the correlation between abundance and excitation potential. From this consideration one simultaneously obtains effective temperature and Fe I abundance.

4.3.7. Ionization balance

Given the effective temperature and Fe I abundance of the star, it is possible to derive the surface gravity, $\log g$, of the star. Again, one provides an inital guess for the surface gravity. In thermodynamic equilibrium collisions of the atoms in a gas of temperature T lead to ionization of a certain fraction of the atoms. For collision-dominated plasmas the degree of ionization is given by Saha's equation,

$$\frac{N_1}{N_0} = \frac{2}{\Lambda^3}\frac{\mathrm{k}T}{P_e}\frac{Z_1}{Z_0}\exp\left(-\frac{I}{\mathrm{k}T}\right),$$
$$\Lambda = \sqrt{\frac{\mathrm{h}^2}{2\pi \mathrm{m}_e \mathrm{k}T}}, \tag{4.7}$$

where Λ is the thermal de Broglie wavelength of the electron with h denoting Planck's constant and m_e, the electron mass, P_e, the electron pressure, I, the ionization energy, and Z_1/Z_0 is the ratio of the partition functions for ions and neutral atoms.

As the temperature T is fixed by excitation balance, the only remaining free quantity is the surface gravity, $\log g$, which directly affects the electron pressure. Assume the guess for $\log g$ to be overestimated. Then the electron pressure is larger, thereby reducing the number of ions and free electrons in the plasma according to Eq. 4.7. A lower number of available electrons yields a lower continuous absorption coefficient κ, which for solar-like stars is dominated by bound-free transitions of the negative hydrogen ion (Gray, 1992, p. 135) such that $\kappa \propto P_e$. In solar-type stars, Fe is mostly ionized, i.e., the upper ionization level in Eq. 4.7 is approximately given by the (constant) total number of Fe atoms, while the number of Fe I atoms varies as $N_0 \propto P_e$. Under the Eddington approximation and considering only weak lines, the line profile varies as the quotient of line absorption coefficient and continuous absorption coefficient, l_ν/κ_ν. number of absorbing atoms, Fe II lines are pressure indicators while Fe I lines are insensitive to pressure, because in the latter case both dividend and divisor scale proportional to P_e. An overestimate of $\log g$ thus yields lower EWs for the Fe II lines, so that a higher Fe abundance is required to match the observed EWs. Fixing temperature and Fe I abundance in Eq. 4.7, it is therefore possible to obtain an estimate of $\log g$ by requiring the lines of Fe II to yield the same abundance as derived from the Fe I lines.

4.3.8. Equivalent width balance

The microturbulent velocity, ξ, represents non-thermal motions on scales smaller than the mean free path of photons in the stellar atmosphere. Microturbulence can redistribute photons contributing to different parts of the line profile. In case of saturated lines, microturbulence acts to desaturate the lines yielding broader wings, thereby increasing their EWs. Microturbulence is usually treated as an additional isotropic Gaussian broadening component. Typical microturbulent velocities for solar-like stars are $1 - 3\ \mathrm{km\,s^{-1}}$.

Assume that temperature and surface gravity are already known from the previous steps. Then ξ can be established using the condition that lines of different EW should yield the same abundances. Assume the first guess for ξ to be an overestimate. Then the increase in microturbulence yields larger EWs for strong saturated lines, which *per se* would have been insensitive to slight abundance changes. However, mediated by microturbulence these lines desaturate yielding larger EWs. To reproduce the measured EWs, stronger lines therefore need less absorbing atoms; the abundance derived from stronger lines is lower than from weak lines. Hence, ξ can be determined by minimizing the correlation between abundances and EWs. In practice, one typically uses reduced EWs, i.e., the EW of a line divided by its respective wavelength λ, as Doppler shifts are a linear function of wavelength.

4.3.9. Error estimates and limitations

Using standard spectroscopic abundance analyses, T_{eff} can be determined up to ± 100 K. Typical uncertainties of $\log g$ are on the order of ± 0.1 dex, while the best possible abundance measurements (for the Sun and other very bright stars) reach an accuracy of 0.05 dex. Without further independent indicators, it is usually impossible to obtain better results. Formal errors are derived from the scatter of the observed correlations. Typically, the parameters T_{eff} and ξ are varied until Pearson's correlation coefficient reports a significant correlation at the 1σ-level. The corresponding limiting values then provide estimates of the parameter errors. The uncertainty in $\log g$ is based on the uncertainties of the abundances derived from Fe I and II lines. As however the abundances depend again on the stellar parameters including $\log g$, the uncertainties of the stellar parameters have to be propagated accordingly (Bubar & King, 2010).

At effective temperatures below 5000 K the abundance analysis is complicated by severe line blends and the lower number of available Fe II lines. For temperatures above 6000 K most Fe is ionized and non-LTE effects start to become important for Fe I lines, so that $\log g$ is systematically underestimated (Fuhrmann et al., 1997). Methods based on Fe I/II excitation and ionization balance can, thus, be used for T_{eff} in the $5000-6000$ K range.

4.4. Line-ratios of metal lines as temperature indicator

In solar-type stars the lines of neutral metals are not sensitive to pressure (cf., Sect. 4.3.7). Line-depth or equivalent-width ratios of these lines therefore provide a useful temperature diagnostic. To avoid strong effects due to mictroturbulence, line-ratio methods use weak lines, which must be carefully chosen to avoid blending effects. Particularly useful are line ratios of spectral lines belonging to metallic species with different temperature sensitivity.

If the spectral data have sufficient resolution to resolve individual line profiles and a signal-to-noise ratios of several hundred, one can use single *line-depth ratios* as a precise temperature indicator. A prominent example is the depth ratio of V I at 6252 Å and Fe I 6253 Å (Gray & Johanson, 1991; Gray, 1994). As rotational broadening and macroturbulence affect all lines simultaneously, these effects have a minor influence on the line-depth ratio. Using this method an accuracy of ± 10 K can be reached.

A similar method based on the comparison of *equivalent width ratios* of spectral lines was proposed by Sousa et al. (2007), who calibrated their method using 451 FGK dwarf stars. The authors provide an empirical relation between effective temperature and the EW ratio for a set of 433 pairs of spectral lines (Sousa et al., 2010a). This method can also be used in the case of medium spectral resolution and lower signal-to-noise ratios. The authors argue that the use of EWs instead of line-depth ratios is advantageous or at least equivalent, because the EW should contain more information than the line depth, while normalization problems and line blends affect both quantities.

4.5. Age estimates from lithium

There are several indicators of stellar age, some of them being empirical, some being strongly model-dependent. Examples of model-dependent indicators are the kinematics of very young moving groups, comparison to theoretically computed isochrone calculations, and core density diagnostics using asteroseismology. Empirical indicators are the depletion of lithium, the stellar spin-down with age, and the decay of activity. Most of these indicators are only valid if applied to an ensemble of stars. Details on these indicators can be found in the excellent review by Soderblom (2010).

The abundance of lithium is a valuable indicator of the stellar structure and evolution and, thus, can provide an estimate of the stellar age. Captured within a star, the element is depleted by Li burning during the early phases of stellar evolution, because the existence of deep convection zones during this evolutionary stage allows to efficiently interchange material between the stellar surface and the interior (Pinsonneault, 1994). Following the standard models, Li depletion begins later and lasts longer in lower-mass stars. The rate of Li depletion drops as soon as the star develops a larger radiative core. The importance of additional extra mixing processes is still a matter of debate, so that the details of the Li depletion mechanism remain elusive (Canto Martins et al., 2011b). Detailed empirical studies of Li abundances in pre-main sequence stars and young stellar clusters allow a calibration of the relation between Li abundance and the stellar age (e.g., Soderblom et al., 1993, which is part of a decalogy of papers dedicated to the evolution of the lithium abundances of solar-type stars).

Interestingly, Israelian et al. (2009) report indications for a systematically higher Li depletion in planet host stars when compared with single stars for which no planets have been detected so far. These findings were corroborated by Sousa et al. (2010b), who used stellar evolutionary models to show that differences in stellar age or mass are not responsible for the observed correlation. This would mean that the observed Li depletion is indeed linked to the formation and evolution of exoplanetary systems. However, later results by Baumann et al. (2010) and Ghezzi et al. (2010) suggest, that their findings are due to selection biases and that there is no evidence for a relation between the depletion of Li and the presence of a planet.

4.6. Distance estimates from spectral data

There are several methods that can be used to determine the distance of stars in our Galaxy. The trigonometric parallax is the most fundamental distance measurement technique for stars. The Hipparcos satellite measured trigonometric parallaxes for more than 100, 000 stars down to visual magnitudes around 12 mag in the solar neighborhood (Perryman et al., 1997). Within the next years, the Gaia mission (Jordan, 2008) is expected to provide parallaxes for about one billion stars down to 20th magnitude, thereby dramatically increasing the volume with available distance data. Until then, however, we have to revert to alternative methods to determine the distances to otherwise well-observed stars.

The use of standard candles like RR Lyrae and Cepheid variables, which can provide accurate distance estimates, is limited to a small number of stars that are part of a population comprising such standard candles.

4.6.1. The spectroscopic parallax

In most cases, it is possible to deduce the luminosity of a star from its colors or spectroscopically inferred stellar parameters. This photometric (or spectroscopic) distance is derived from the apparent magnitude of the star (see Jurić et al., 2008, for an *in extenso* use of this technique). The difference between apparent magnitude V and absolute magnitude M_V is related to the distance d in parsecs of an object according to

$$V - M_V = 5 \log d - 5 + A_V \tag{4.8}$$

and is therefore known as the distance modulus. Here the extinction A_V accounts for scattered and absorbed radiation between the object and the observer, e.g., due to interstellar absorption.

An interesting alternative to obtain the distance modulus is the use of the Wilson-Bappu effect relating the measured width of chromospheric emission in the Ca II K line core to the absolute visual magnitude, M_V, of the star (Wilson & Bappu, 1957).

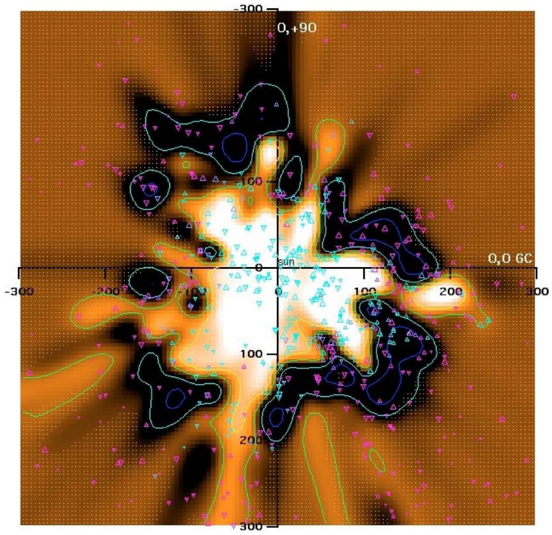

Figure 4.2.: Spatial distribution of interstellar Na I absorption within 300 pc of the Sun projected onto the galactic plane. Triangles indicate the position of stars used to construct the map. The colorscale indicates values of Na I volume density (dark=high) on a logarithmic scale. Figure taken from Welsh et al. (2010).

4.6.2. Interstellar absorption

A complementary approach is the use of absorption features caused by the interstellar medium. The Sun is situated within a region of low density, hot gas known as Local Cavity. This region extends to roughly 100 pc and is surrounded by a "wall" of higher density gas clouds (e.g., Cox & Reynolds, 1987). While the Local Cavity contains many diffuse cloudlets with a complex velocity structure, beyond it the density distribution of the gas becomes fairly uniform. Thus, absorption features caused by the interstellar medium can be used as distance indicator.

The most dominant absorption features are the Na I D lines and the H and K lines of Ca II. Strömgren (1948) utilizes a curve-of-growth approach to compute the column densities of the absorbing species from EW ratios of line doublets. As the density distribution of Ca II and Na I is fairly uniform in the interstellar medium beyond the Local Cavity, the derived column can directly be converted into a distance estimate (Megier et al., 2005). This has also been confirmed empirically by Megier et al. (2009), who provide a relation between the EWs of interstellar Ca II lines and the distances to early-type stars within 1 kpc calibrated with 262 stars with measured Hipparcos parallaxes. Welsh et al. (2010) compiled a catalog of interstellar Na absorption lines and provide a map of the local interstellar medium, which provides a contiguous, three-dimensional view of the dominant structures within the Local Cavity (Fig. 4.2).

In X-ray spectroscopy the attenuation due to interstellar hydrogen and heavier elements is usually incorporated into the spectral model (Morrison & McCammon, 1983). Given the mean gas density of the interstellar medium in the galactic plane of roughly $n(\mathrm{H\ I} + \mathrm{H_2}) = 1.15\ \mathrm{cm}^{-3}$ (Bohlin et al., 1978), the hydrogen column density inferred from the spectral fit provides another rough distance estimate. The fact that the distribution of hydrogen in the interstellar medium is correlated to the distribution of interstellar Na I (Ferlet et al., 1985) provides an additional check of consistency between both spectral regimes.

4.7. Proxies for stellar activity

As described in Chapter 3, stellar activity can be observed as non-thermal emission from the upper layers of the stellar atmosphere. The total flux from these layers is typically much weaker than the photospheric flux. Therefore, stellar activity is best observed in wavelength regimes with less or no photospheric contribution like in X-rays or in the cores of strong photospheric absorption lines in optical spectra. In the context of the work at hand, normalized flux indices related to chromospheric Ca II emission are of special importance. The detailed connection between these diagnostics and stellar activity is, however, subtle and critically depends on the complex dynamics of the chromosphere (see Rutten, 2010).

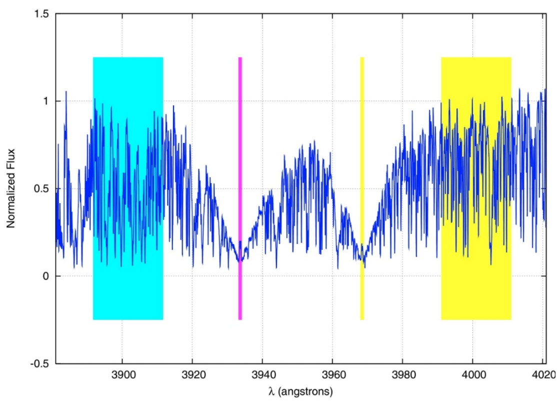

Figure 4.3.: Ca II H and K line profile for TrES-1. Line core and continuum bands used in the computation of the S-index, a relative measure of the chromospheric flux in the line cores. Figure taken from Melo et al. (2006).

4.7.1. The Mount Wilson S index

Probably the most popular chromospheric diagnostic is the Mt. Wilson chromospheric flux index (S_{MW}; Vaughan et al., 1978; Baliunas et al., 1998) used in the famous Mt. Wilson HK project. The S-index is defined as the ratio of the sum of the chromospheric fluxes measured in two approximately 1 Å wide wavelength intervals centered on the Ca II H and K emission line cores relative to the flux measured in two nearby 20 Å wide continuum windows (see Fig. 4.3). The original definition of S_{MW} was related to the filters used with the Mt. Wilson Observatory HKP spectrometers. It is common practice to calibrate measurements obtained with another instrument to the Mt. Wilson scale (e.g., Melo et al., 2006, for a calibration with respect to the VLT/UVES spectrograph). As the photospheric continuum decreases for cooler stars, an ad-

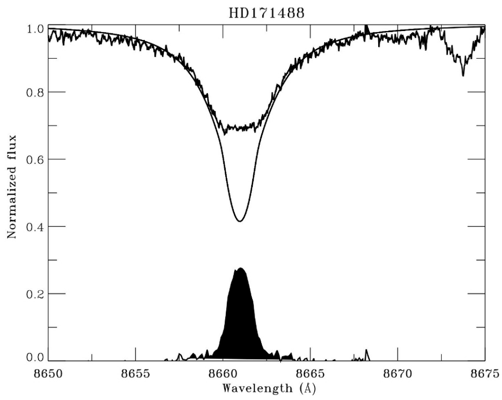

Figure 4.4.: Chromospheric activity in HD 171488 measured using the Ca IRT. The plot shows the observed spectrum (thick) and a synthetic model (thin). Their difference yields the residual EW, ΔW_{IRT} (filled). Figure taken from Busà et al. (2007).

ditional correction term depending on the $B-V$ color index has to be applied to the calibrated index (Rutten, 1984). Further, the expected photospheric contribution in the line cores should be subtracted following the prescription of (Noyes et al., 1984).

The corrected S-index, typically denoted as R'_{HK}, is interpreted as a measure of magnetic activity and can be related to stellar rotation and age (see Sect. 3.2.1, for details).

4.7.2. The Ca IRT triplet

Chromospheric activity can also be measured in the Ca II infrared triplet (IRT) at 8498 Å, 8542 Å, and 8662 Å (see e.g., Linsky et al., 1979). In contrast to photographic plates, modern CCD detectors are sensitive in the near infrared, so that the Ca IRT provides another accessible diagnostic of chomospheric activity. While the photospheric continuum around the IRT is well-defined, the photospheric background within the lines is much larger and must be accurately modeled to correctly assess the chromospheric contribution to the line profile. Andretta et al. (2005) proposed the activity indicator R_{IRT} defined as the difference between the central line depths of the observed spectrum and a rotationally-broadened non-LTE model. In addition, the total EW of the residual line profiles, ΔW_{IRT}, provides a useful indicator of the chromospheric excess emission (Busà et al., 2007). As shown by Busà et al., the $\log R'_{\mathrm{HK}}$ activity index and ΔW_{IRT} display an almost linear correlation, however, with a large scatter.

Part II.

Scientific contributions

5. Orbital dynamics of the transiting extrasolar system TrES-2

The transiting Jovian planet TrES-2b discovered by O'Donovan et al. (2006) offers an outstanding opportunity to search for changes in its orbital parameters. The planet orbits its host star, an old G0V star with about solar radius and mass, in a close-in orbit (0.035 AU). Together with its large inclination of about 84° the orbit geometry yields a nearly grazing transit, making the shape and timing of the transit sensitive to small variations of the orbital parameters. Since May 2009, TrES-2 is one of the main short-cadence targets of the Kepler telescope and, therefore, among the photometrically best-studied planetary systems known today.

As each paper in this work lists several authors, I will provide an overview of my contributions, especially in cases where I am not listed as first author.

5.1. My contributions

The initial discovery of the change in the orbital geometry of the TrES-2 system goes back to results obtained by Mislis & Schmitt (2009), who found first indications for a secular change in the orbital inclination in their ground-based data obtained with the Oskar-Lühning-Teleskop (OLT) in Hamburg. To corroborate these results Dimitris Mislis obtained additional photometric data with the BUSCA instrument at Calar Alto Observatory and the OLT in Hamburg. Dimitris had already finished his data reduction and parts of the analysis for Mislis et al. (2010), when I joined in to provide an interpretation of his results in terms of secular changes in the orbital parameters. During the work several parts of the introduction and analysis had to be adapted, so that, while Dimitris provided the major part of the data analysis (§2 and §3 of the paper), I also have a share in these parts. My main contributions are the interpretation of the results and the model calculations presented in §4. I also wrote major parts of the introduction and the abstract. All results were reached in close cooperation with my supervisor Jürgen Schmitt. This work is presented in Sect. 5.2 of my thesis.

Shortly after the publication of our results in Mislis et al. (2010), several studies provided additional transit data and searched for indications for the proposed inclination change (Rabus et al., 2009; Raetz et al., 2009; Scuderi et al., 2010; Raetz et al., 2011; Christiansen et al., 2011). However, these studies were unable to conclusively confirm or reject the proposed inclination change, because the uncertainties in the system parameters itself were too large. Further complications were the detection of a third light in the system (Daemgen et al., 2009) and different fitting approaches making it difficult to compare the results.

The definite answer regarding the proposed inclination change had to await the availability of the first quarters of photometric data obtained with the Kepler telescope. Kipping & Bakos (2011) presented the first analysis based on two quarters of Kepler data. However, their baseline comprising 18 transits remained too short to support or exclude the proposed inclination change. The issue has finally been resolved in our publication contained in Sect. 5.3 (Schröter et al., 2012), which provides an analysis of all available ground-based data together with four quarters of space-based Kepler photometry of TrES-2 in a consistent approach. The major contribution to this work was provided by myself, again supported by Jürgen Schmitt.

Of course, the other coauthors also provided contributions to the work, which I, however, will not describe in detail here.

A&A 510, A107 (2010)
DOI: 10.1051/0004-6361/200912910

Astronomy & Astrophysics

Multi-band transit observations of the TrES-2b exoplanet*

D. Mislis[1], S. Schröter[1], J. H. M. M. Schmitt[1], O. Cordes[2], and K. Reif[2]

[1] Hamburger Sternwarte, Gojenbergsweg 112, 21029 Hamburg, Germany
e-mail: mdimitri@hs.uni-hamburg.de
[2] Argelander-Institut für Astronomie, Auf dem Hügel 71, 53121 Bonn, Germany

Received 17 July 2009 / Accepted 14 December 2009

ABSTRACT

We present a new data set of transit observations of the TrES-2b exoplanet taken in spring 2009, using the 1.2 m Oskar-Lühning telescope (OLT) of Hamburg Observatory and the 2.2 m telescope at Calar Alto Observatory using BUSCA (Bonn University Simultaneous CAmera). Both the new OLT data, taken with the same instrumental setup as our data taken in 2008, as well as the simultaneously recorded multicolor BUSCA data confirm the low inclination values reported previously, and in fact suggest that the TrES-2b exoplanet has already passed the first inclination threshold ($i_{\min,1} = 83.417°$) and is not eclipsing the full stellar surface any longer. Using the multi-band BUSCA data we demonstrate that the multicolor light curves can be consistently fitted with a given set of limb darkening coefficients without the need to adjust these coefficients, and further, we can demonstrate that wavelength dependent stellar radius changes must be small as expected from theory. Our new observations provide further evidence for a change of the orbit inclination of the transiting extrasolar planet TrES-2b reported previously. We examine in detail possible causes for this inclination change and argue that the observed change should be interpreted as nodal regression. While the assumption of an oblate host star requires an unreasonably large second harmonic coefficient, the existence of a third body in the form of an additional planet would provide a very natural explanation for the observed secular orbit change. Given the lack of clearly observed short-term variations of transit timing and our observed secular nodal regression rate, we predict a period between approximately 50 and 100 days for a putative perturbing planet of Jovian mass. Such an object should be detectable with present-day radial velocity (RV) techniques, but would escape detection through transit timing variations.

Key words. planetary systems – techniques: photometric – stars: individual: TrES-2b

1. Introduction

As of now more than 400 extrasolar planets have been detected around solar-like stars. In quite a few cases several planets have been detected to orbit a given star, demonstrating the existence of extrasolar planet systems in analogy to our solar system. Just as the planets in our solar system interact gravitationally, the same must apply to extrasolar planet systems. Gravitational interactions are important for the understanding of the long-term dynamical stability of planetary systems. The solar system has been around for more than four billion years, and the understanding of its dynamical stability over that period of time is still a challenge Simon et al. (1994). In analogy, extrasolar planet systems must be dynamically stable over similarly long time scales, and most stability studies of extrasolar planet systems have been directed towards an understanding of exactly those long time scales. Less attention has been paid to secular and short-term perturbations of the orbit, since such effects are quite difficult to detect observationally. Miralda-Escudé (2002) gives a detailed discussion on what secular effects might be derivable from extrasolar planet transits; in spectroscopic binaries the orbit inclination i can only be deduced in conjunction with the companion mass, and therefore the detection of an orbit inclination change is virtually impossible. Short-term transit timing variations (TTVs) have been studied by a number of authors (Holman & Murray 2005; Agol et al. 2005), however, a detection of such effects has remained elusive so far. In principle, a detection of orbit change would be extremely interesting since it would open up entirely new diagnostic possibilities of the masses and orbit geometries of these systems; also, in analogy to the discovery of Neptune, new planets could in fact be indirectly detected.

The lightcurve of a transiting extrasolar planet with known period allows very accurate determinations of the radii of star and planet (relative to the semi-major axis) and the inclination of the orbital plane of the planet with respect to the line of sight towards the observer. Clearly, one does not expect the sizes of host star and planet to vary on short time scales, however, the presence of a third body can change the orientation of the orbit plane and, hence, lead to a change in the observed inclination with respect to the celestial plane. The TrES-2 exoplanet is particularly interesting in this context. It orbits its host star once in 2.47 days, which itself is very much solar-like with parameters consistent with solar parameters; its age is considerable and, correspondingly, the star rotates quite slowly. Its close-in planet with a size of 1.2 $R_{\rm Jup}$ is among the most massive known transiting extrasolar planets (Holman et al. 2007; Sozzetti et al. 2007).

What makes the TrES-2 exoplanet orbits even more interesting, is the fact that an apparent inclination change has been reported by some of us in a previous paper (Mislis & Schmitt 2009, henceforth called Paper I). The authors carefully measured several transits observed in 2006 and 2008. Assuming a circular orbit with constant period P, the duration of an extrasolar planet transit in front of its host star depends only on the stellar and planetary radii, $R_{\rm s}$ and $R_{\rm p}$, and on the inclination i of the orbit plane w.r.t. the sky plane. A linear best fit to the currently available inclination measurements yields an apparent

* Photometric transit data are only available in electronic form at the CDS via anonymous ftp to
cdsarc.u-strasbg.fr (130.79.128.5) or via
http://cdsweb.u-strasbg.fr/cgi-bin/qcat?J/A+A/510/A107

A&A 510, A107 (2010)

Table 1. Observation summary.

Date	Instrument	Filter	Airmass	Seeing
11/04/2009	*OLT*	*I*	1.7877–1.0712	2.94″
28/05/2009	*BUSCA*	*v*, *b*, *y*, *I*	1.8827–1.0453	3.09″

inclination decrease of 5.1×10^{-4} deg/day. The transit modeling both by Holman et al. (2007) and Mislis & Schmitt (2009) shows the transit of TrES-2b in front of its host star to be "grazing". In fact, according to the latest modeling the planet occults only a portion of the host star and transits are expected to disappear in the time frame 2020–2025, if the observed linear trend continues. This "grazing" viewing geometry is particularly suitable for the detection of orbital changes, since relatively small changes in apparent inclination translate into relatively large changes in eclipse duration. At the same time, a search for possible TTVs by Rabus et al. (2009) has been negative; while Rabus et al. (2009) derive a period wobble of 57 s for TrES-2, the statistical quality of their data is such that no unique periods for TTVs can be identified.

The purpose of this paper is to present new transit observations of the TrES-2 exoplanet system obtained in 2009, which are described in the first part (Sect. 2) and analysed (Sect. 3). In the second part (Sect. 4) of our paper we present a quantitatively analysis of what kind of gravitational effects can be responsible for the observed orbit changes of TrES-2b and are consistent with all observational data of the TrES-2 system.

2. Observations and data reduction

We observed two transits of TrES-2 using the ephemeris suggested by O'Donovan et al. (2006) and by Holman et al. (2007) from $T_c(E) = 2\,453\,957.6358[\text{HJD}] + E \cdot (2.47063$ days), using the 1.2 m Oskar Lühning telescope (OLT) at Hamburg Observatory and Calar Alto Observatory 2.2 m telescope with BUSCA.

The OLT data were taken on 11 April 2009 using a $3K \times 3K$ CCD with a $10' \times 10'$ FOV and an I-band filter as in our previous observing run (Paper I). The readout noise and the gain were 16.37 e^- and 1.33 e^-/ADU respectively. With the OLT we used 60-s exposures which provided an effective time resolution of 1.17 min. During the observation, the airmass value ranged from 1.7877 to 1.0712 and the seeing was typically 2.94″.

The Calar Alto data were taken on 28 May 2009 using BUSCA and the 2.2 m telescope. BUSCA is designed to perform simultaneous observations in four individual bands with a FOV of $11' \times 11'$. Therefore it has four individual 4K × 4K CCD systems which cover the ultra-violet, the blue-green, the yellow-red and the near-infrared part of the spectrum (channel a–d respectively). For this run we used the Strömgren filters v (chn. a), b (chn. b), and y (chn. c), and a Cousins-*I* filter for the near-infrared (chn. d). The readout-noise for these four detectors are 9.09 e^-, 3.50 e^-, 3.72 e^-, and 3.86 e^- respectively for the a, b, c, and d channels. The gain values for the same channels are 1.347 e^-/ADU, 1.761 e^-/ADU, 1.733 e^-/ADU, and 1.731 e^-/ADU respectively. The airmass value ranged from 1.8827 to 1.0453 and the seeing was 3.09″. For the BUSCA observations we took 30 s exposure yielding an effective time resolution of 1.63 min. In Table 1 we summarize the relevant observation details.

For the data reduction, we used *Starlink* and *DaoPhot* software routines, and the *MATCH* code. We perform the normal reduction tasks, bias subtraction, dark correction, and flat fielding on the individual data sets before applying aperture photometry on on all images. For TrES-2, we selected the aperture photometry mode using apertures centered on the target star, check stars, and sky background. Typical sky brightness values for the 11 April and for the 28 May were 89 and 98 ADUs, respectively, i.e., values at a level 0.008% and 0.006% of the star's flux, respectively (for *I*-filter). For the relative photometry we used the star U1350-10220179 as a reference star to test and calibrate the light curve. For the data analysis presented in this paper we did not use additional check stars, but note that we already checked this star for constancy in the Paper I. To estimate the magnitude errors, we followed Howell & Everett (2001) and the same procedure as described in our first paper (Paper I) to obtain better relative results. Our final relative photometry is presented in Table 2, which is available in its entirety in machine-readable form in the electronic version of this paper.

Table 2. Relative photometry data.

HJD	RelativeFlux	Uncertainty	Flag
2 454 933.44031	0.99172	0.0037	*OLT – I*
2 454 933.44091	0.99204	0.0038	*OLT – I*
2 454 933.44221	1.00514	0.0039	*OLT – I*
2 454 933.44281	1.00314	0.0038	*OLT – I*
2 454 933.44341	0.99458	0.0035	*OLT – I*
2 454 933.44401	0.99745	0.0037	*OLT – I*

Notes. Relative photometry vs. time; note that the complete table is available only electronically at the CDS. The time stamps refer to the Heliocentric Julian Date (HJD) at the middle of each exposure. The "Flag" column refers to the telescope and filter.

3. Model analysis and results

In our model analysis we proceeded in exactly the same fashion as described in Paper I. Note that the assumption of circularity appears to apply very well to TrES-2b (O'Donovan et al. 2009; O'Donovan et al. 2006); the assumption of constant period and hence constant semi-major axis will be adressed in Sect. 4. For our modelling we specifically assumed the values $R_s = 1.003 R_{\rm o}$, $R_p = 1.222\, R_J$, $P = 2.470621$ days, $\alpha = 0.0367$ AU for the radii of star and planet, their period and the orbit radius respectively. All limb darkening coefficients were taken from Claret (2004), and for the OLT data we used the same values as in Paper I, viz., $u_1 = 0.318$ and $u_2 = 0.295$ for the *I* filter, as denoted by S1 in Table 3.

3.1. OLT data and modeling

Our new OLT data from 11 April 2009 were taken with the same instrumental setup as our previous data taken on 18 September 2008. The final transit light curve with the best fit model is shown in Fig. 1, the reduced light curve data are provided in Table 1. Keeping the planetary and stellar radii and the limb darkening coefficients fixed (at the above values), we determine the best fit inclination and the central transit time T_c with our transit model using the χ^2 method; the thus obtained fit results are listed in Table 3. The errors in the derived fit parameters are assessed with a bootstrap method explained in detail in Paper I, however, we do not use random residuals for the new model, but we circularly shift the residuals after the model substraction to produce new light curves for the bootstrapped data following

Table 3. Individual values of duration, inclination, χ^2 values and limb darkening coefficients from five light curve fits.

T_c time [HJD]	Duration	Errors	Inclin.	Errors	χ^2value	LDL
3989.7529 ± 0.00069	110.308	0.432	83.59	0.019	432.1	
3994.6939 ± 0.00066	109.230	0.448	83.56	0.019	296.8	
4041.6358 ± 0.00070	109.025	0.430	83.55	0.019	290.6	
4607.4036 ± 0.00072	106.620	0.883	83.44	0.036	179.1	
4728.4640 ± 0.00071	106.112	0.870	83.43	0.036	190.1	
4933.5274 ± 0.00076	105.077	0.964	83.38	0.039	296.1	$S1$
4980.4675 ± 0.00068	105.056	0.848	83.38	0.034	181.7	$S1$
4980.4679 ± 0.00090	104.748	1.076	83.37	0.043	202.2	$S2$
4980.4667 ± 0.00082	103.832	1.021	83.33	0.041	186.0	$S3$
4980.4678 ± 0.00100	104.363	1.194	83.35	0.048	195.0	$S4$
4980.4675 ± 0.00060	104.522		83.36	0.030		

Notes. Units for duration and errors are minutes and for inclination errors are degrees. The OLT light curve has 268 points, the I-filter light curve has 198, the y-filter light curve has 208, the b-filter light curve 198 and the v-filter light curve 162 points respectively.

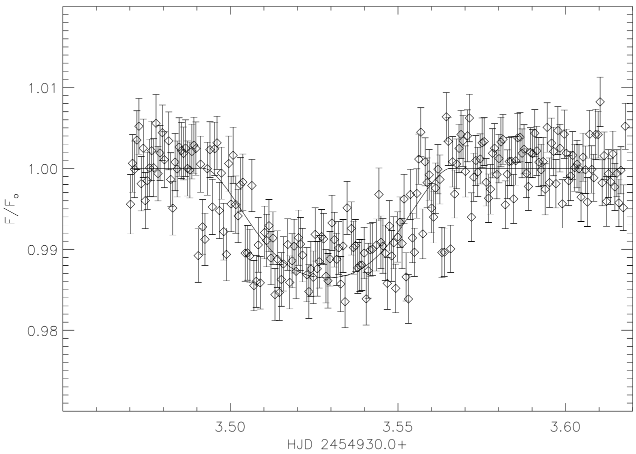

Fig. 1. Observed TrES-2 light curves and model fits for the light curve taken with the 1.2 m OLT at Hamburg Observatory taken in April 2009.

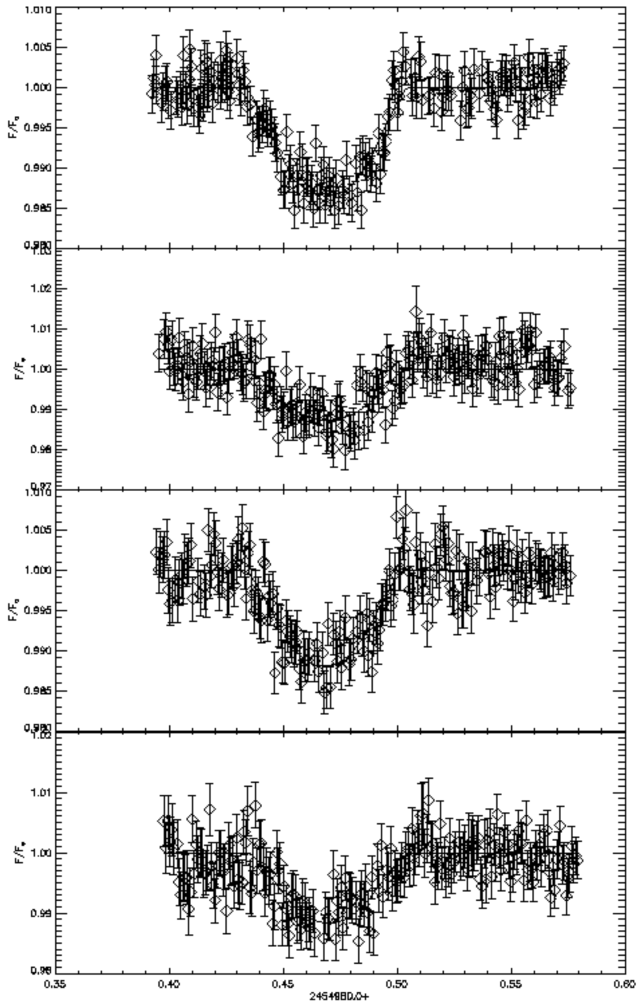

Fig. 2. Four light curves and corresponding model fits taken in May 2009 with the 2.2 m telescope at Calar Alto using BUSCA.

Alonso et al. (2008). In Table 3 we also provide corrected central times and errors for those transists already reported in Paper I, since due to some typos and mistakes the numbers quoted for central time and their error are unreliable (five first lines of Table 3). In Fig. 3 we plot the thus obtained inclination angle distribution for epoch April 2009 (solid curve) compared to that obtained in September 2008 (dashed curve). While the best fit inclination of $i = 83.38°$ differs from that measured in September 2008 ($i = 83.42°$), the errors are clearly so large that we cannot claim a reduction in inclination from our OLT data (taken with the same instrumental setup, i.e., in September 2008 and April 2009) alone, however, is clearly consistent with such a reduction.

3.2. BUSCA data and modeling

Our BUSCA data have the great advantage of providing simultaneously measured multicolor data, which allows us to demonstrate that limb darkening is correctly modelled and does not affect the fitted inclinations and stellar radii. The limb darkening coefficients used for the analysis of the BUSCA data were also taken from Claret (2004); we specifically used $u_1 = 0.318$ and $u_2 = 0.295$ for the I filter (S1), i.e., the same values as for the OLT, $u_1 = 0.4501$ and $u_2 = 0.286$ for the y filter (S2), $u_1 = 0.5758$ and $u_2 = 0.235$ for the b filter (S3), $u_1 = 0.7371$ and $u_2 = 0.1117$ for the v filter (S4) respectively. The data reduction and analysis was performed in exactly the same fashion as for the OLT data, we also used the same comparison star U1350-10220179; the reduced light curve data are also provided in Table 2. The modelling of multicolor data for extrasolar planet transits needs some explanation. In our modelling the host star's radius is assumed to be wavelength independent. Since stars do not have solid surfaces, the question arises how much the stellar radius R_* does actually change with the wavelength. This issue has been extensively studied in the solar context, where the limb of the Sun can be directly observed as a function of wavelength (Neckel 1995). Basically the photospheric height at an optical depth of unity is determined by the ratio between pressure and the absorption coefficient, and for the Sun, Neckel (1995) derives a maximal radius change of 0.12 arcsec between 3000 and 10 000 Å, which corresponds to about 100 km. If we assume similar photospheric parameters in the TrES-2 host star, which appears reasonable since TrES-2 is a G0V star, we deduce a wavelength-dependent radius change on the order of 100 km, which is far below a percent of the planetary radius and thus not detectable. Therefore in our multi-band data modelling we can

A&A 510, A107 (2010)

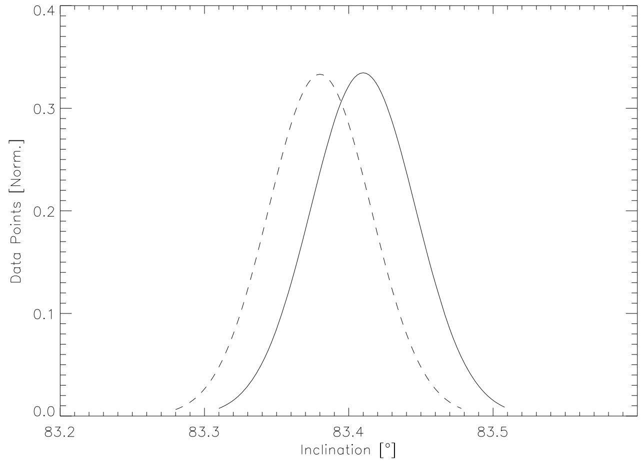

Fig. 3. Inclination distribution for the OLT data using 1000 Monte Carlo simulations for the September 2008 (solid curve) and April 2009 (dashed curve); see the text for details.

safely fix the radius of the star and the radius of the planet in a wavelength-independent fashion.

We thus kept the stellar and planetary fixed at the above values, treated all BUSCA channels as independent observations and fitted the light curves – as usual – by adjusting inclination and central transit time. The filter light curves are shown together with the so obtained model fits in Fig. 2, the model fit parameters are again summarized in Table 3. We emphasize that we obtain good and consistent fits for all light curves with the chosen set of limb darkening coefficients, thus demonstrating our capability to correctly model multicolor light curves.

Since the BUSCA data are recorded simultaneously, it is clear that the light curves in the four BUSCA channels must actually be described by the same values of inclination and transit duration. We therefore simultaneously fit all the four light curves, leaving free as fit parameters only the central time T_c and inclination i. With this approach we find an average inclination of $i = 83.36° \pm 0.03°$, which is consistent with our spring OLT data and also suggests that the inclination in spring 2009 has further decreased as compared to our 2008 data.

3.3. Joint modeling

Using all our data we can check whether our assumption of the wavelength-independence of the radius is consistent with the observations. For this consistency test we kept the inclination value fixed at $i = 83.36°$ and fitted only the radius of the star R_s and T_c. The errors on R_s were again assessed by a Monte Carlo simulation as described in Paper I and the distribution of the thus derived stellar radius values R_s is shown in Fig. 4; as apparent from Fig. 4, all BUSCA channels are consistent with the same stellar radius as – of course – expected from theory since any pulsations of a main-sequence star are not expected to lead to any observable radius changes.

The crucial issue about the TrES-2 exoplanet is of course the constancy or variability of its orbit inclination. Our new BUSCA and OLT data clearly support a further decrease in orbit inclination and hence decrease in transit duration. In order to demonstrate the magnitude of the effect, we performed one more sequence of fits, this time keeping all physical parameters fixed and fitting only the central transit times T_c using 1000 Monte Carlo realisations and studying the resulting distribution in χ^2; for the inclination we assumed for, first, the value $i = 83.57°$ (as derived by Holman et al. for their 2006 data) and the value $i = 83.36°$ (this paper for the 2009 data). The fit results (in terms of obtained χ^2 values) are summarised in Table 4, which shows that for all (independent) data sets the lower inclination values yield smaller χ^2-values; for some filter pairs the thus obtained improvement is extremely significant.

Table 4. χ^2 tests for two different inclination values and the χ^2 errors after 1000 Monte Carlo simulations.

Inclination [°]	OLT	$B-I$	$B-y$	$B-b$	$B-v$
83.57(Holman)	304.9	199.4	207.8	216.0	206.3
σ_{χ^2} (Holman)	16.12	14.04	16.16	21.05	14.26
83.36 (this paper)	213.8	173.44	164.3	180.0	131.1
σ_{χ^2} (this paper)	11.96	11.11	9.96	12.01	8.77

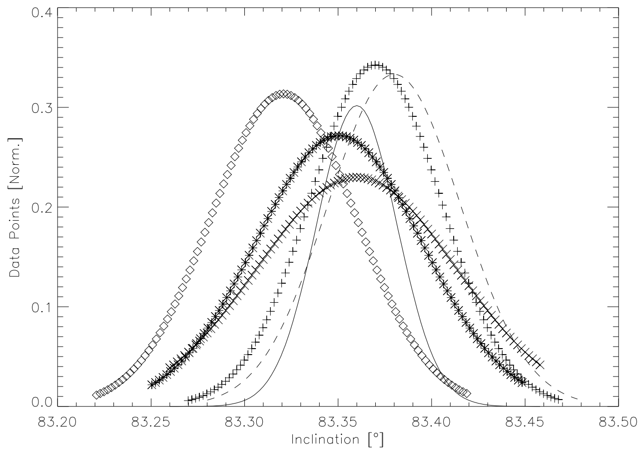

Fig. 4. Inclination distribution derived 1000 Monte Carlo simulations for the multi-band BUSCA observations data in the I (crosses), y (stars), b (diamonds) and v (×-symbol) filter bands; the mean inclination distribution from the four BUSCA lightcurves is shown as solid line, the inclination distribution derived from the OLT data taken in April 2009 is also shown for comparison (dashed line).

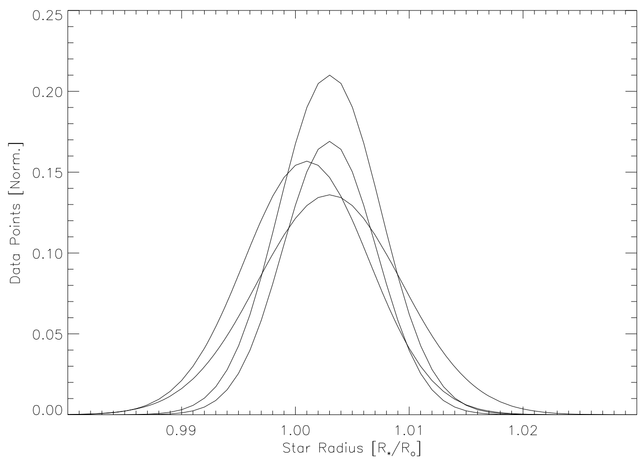

Fig. 5. Stellar radius distribution (R_*), derived from 1000 Monte Carlo simulations in four different filters (from higher to lower peak, I, y, b and v filter respectively). The overlap of the curves shows that all colors can be explained with the same stellar radius as suggested by theory (see Neckel 1995).

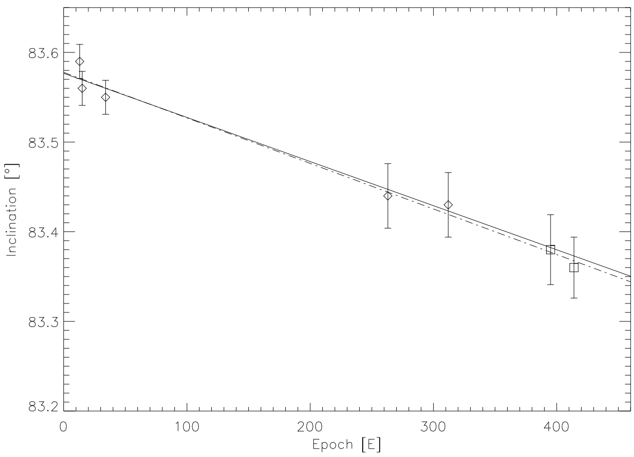

Fig. 6. Epoch versus inclination together with a linear fit to the currently available data; the diamond points are those taken in 2006 by Holman et al. (2007), and those taken in 2008 and reported in Paper I. The square points are derived from our new observations taken in April and May 2009. The solid lines showing two linear fits, from the first paper (dashed line) and the fit from the present paper (solid line).

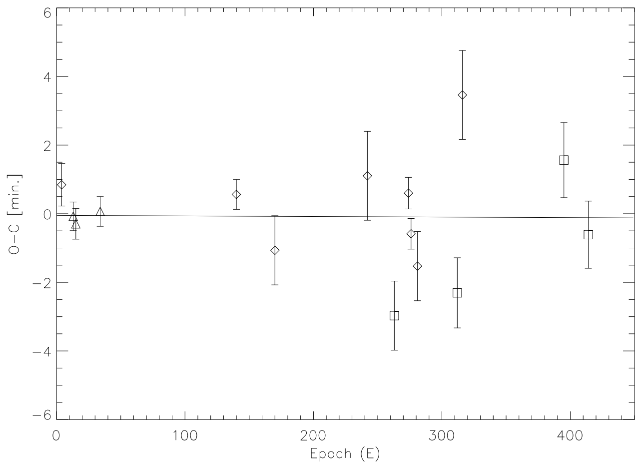

Fig. 7. O–C values versus epoch including the transits observed by Holman et al., Rabus et al. and our data denoted by triangles, squares and diamonds respectively.

3.4. Inclination changes

In Fig. 6 we plot all our current inclination vs. epoch data together with a linear fit to all data; a formal regression analysis yields for the time evolution of the inclination ($i = i_o + a \cdot (Epoch)$, $i_o = 83.5778$, $a = 0.00051$). In Paper I we noted the inclination decrease and predicted inclination values below the first transit threshold ($i_{\min,1} < 83.417°$) after October 2008. Both the new OLT data set and all BUSCA channel observations yield inclinations below the first transit threshold. While the error in a given transit light curve is typically on the order of 0.04° for i, we consider it quite unlikely that 5 independent measurements all yield only downward excursions. We therefore consider the decrease in inclination between fall 2008 and spring 2009 as significant, conclude that the inclination in the TrES-2 system is very likely below the first transit threshold, and predict the inclinations to decrease further; also, the transit depths should become more and more shallow since the exoplanet eclipses less and less stellar surface.

3.5. Period changes

The observed change in orbit inclination is in marked contrast to the period of TrES-2b. While possible TTVs in TrES-2b have been studied by Rabus et al. (2009) we investigate the long-term stability of the period of TrES-2b. From our seven transit measurements (plus five more data points of Rabus et al. 2009) spanning about ~400 eclipses we created a new O–C diagram (cf., Fig. 7); note that we refrained from using the transit times dicussed by Raetz et al. (2009), since these transits were taken with rather inhomogeneous instruments and sometimes only partial transit coverage. For our fit we used a modified epoch equation $HJD_c = HJD_o + E \cdot P$, where we set $P = P_o + \dot{P}(t - HJD_o)$ and explicitly allow a non-constant period P. We apply a χ^2 fit to find the best fit values for $\dot{P}$, P_o, and HJD_o. With this approach we find a best fit period change of $\dot{P} = 5 \times 10^{-9}$, however, carrying out the same analysis keeping a fixed period shows that the fit improvement due to the introduction of a non-zero $\dot{P}$ is insignificant. We then find as best fit values $P_o = 2.47061$ and $HJD_o = 2453957.6350$ conforming to the values derived by Rabus et al. (2009). Thus, the period of TrES-2b is constant, and any possible period change over the last three years must be less than about 1 s.

4. Theoretical implications of observed inclination change

The results of our data presented in the preceding sections strenghten our confidence that the observed inclination changes do in fact correspond to a real physical phenomenon. Assuming now the reality of the observed inclination change of $\Delta i \sim 0.075°/\mathrm{yr}$, given the constancy of the period and the absence of TTVs at a level of ≈100 s we discuss in the following a physical scenario consistent with these observational findings. We specifically argue that the apparent inclination change should be interpreted as a nodal regression and then proceed to examine an oblate host star and the existence of an additional perturbing object in the system as possible causes for the change of the orbital parameters of Tres-2b.

4.1. Inclination change or nodal regression?

It is important to realize that the reported apparent change of inclination refers to the orientation of the TrES-2 orbit plane with respect to the observer's tangential plane. It is well known that the z-component of angular momentum for orbits in an azimuthally symmetric potential is constant, resulting in a constant value of inclination. An oblate star (cf., Sect. 4.2) or the averaged potential of a third body (cf., Sect. 4.3) naturally lead to such potentials, thus yielding orbits precessing at (more or less) constant inclination as also realized by Miralda-Escudé (2002). Such a precession would cause an apparent inclination change, however, physically this would have to be interpreted as nodal regression at fixed orbit inclination. To interpret the observations, one has to relate the rate of nodal regression to the rate of apparent inclination change.

Consider a (massless) planet of radius R_p orbiting a star of radius R_* at some distance d. Let the planet's orbit lie in a plane with a fixed inclination i relative to the x-y plane, which we take as invariant plane. Let an observer be located in the x-z plane with some elevation γ, reckoned from the positive x-axis. The

A&A 510, A107 (2010)

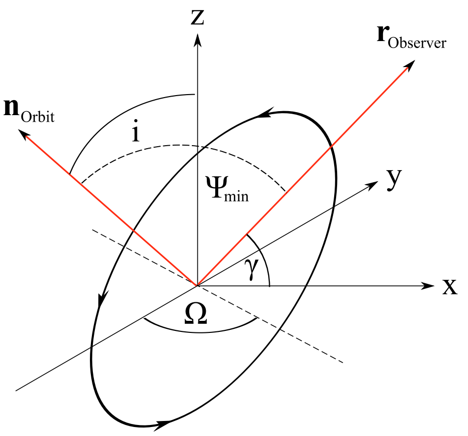

Fig. 8. System geometry (see text for details): the orbit plane with normal vector $\boldsymbol{n}_{\mathrm{Orbit}}$ is inclined relative to the x-y plane by an inclination i, the observer (towards $\boldsymbol{r}_{\mathrm{Observer}}$) is within the x-z plane.

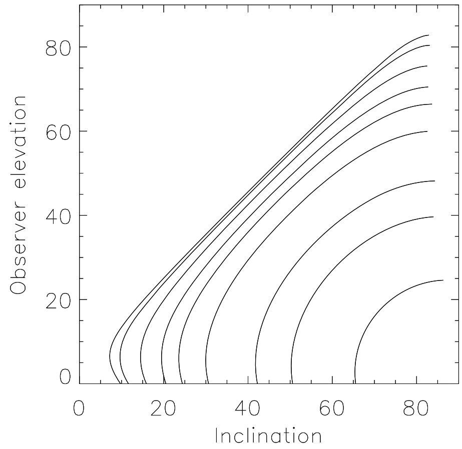

Fig. 9. Linear coefficient of Eq. (3) between nodal regression and observed inclination change as a function of view geometry (cf., Eq. (3)), computed for $i_{\mathrm{obs}} = 83.38°$ as applicable for TrES-2; the plotted contour levels denote values of 1.1, 1.3, 1.5, 2., 2.5, 5., 4., 6., 8. *from right bottom up*.

line of the ascending node in the x-y plane is denoted by the angle Ω, with $\Omega = 0$ implying the ascending node pointed along the negative y-axis (see Fig. 8). Let in the thus defined geometry the angle Ψ denote the angle between planet and observer as seen from the central star. For each system configuration defined by the angles (γ, i, Ω) there is a minimal angle Ψ_{min} between orbit normal and observer obtained in each planetary orbit, which can be computed from

$$\cos\Psi_{\mathrm{min}} = \boldsymbol{n}_{\mathrm{Orbit}} \cdot \boldsymbol{r}_{\mathrm{Observer}} = -\cos\gamma\sin i\cos\Omega + \sin\gamma\cos i. \quad (1)$$

A transit takes place when

$$|\cos\Psi_{\mathrm{min}}| \leq (R_p + R_*)/d, \quad (2)$$

and from the geometry it is clear that the observed inclination i_{obs}, i.e., the parameter that can be derived from a transit light curve is identical to Ψ_{min}. Setting then $\Psi_{\mathrm{min}} = i_{\mathrm{obs}}$ and differentiating Eq. (1) with respect to time we obtain

$$\frac{\mathrm{d}i_{\mathrm{obs}}}{\mathrm{d}t} = -\frac{\sin\Omega\cos\gamma\sin i}{\sin i_{\mathrm{obs}}}\frac{\mathrm{d}\Omega}{\mathrm{d}t}\,. \quad (3)$$

Equation (3) relates the nodal regression of the orbit to its corresponding observed apparent rate of inclination change $\mathrm{d}i_{\mathrm{obs}}/\mathrm{d}t$, given the fixed inclination i relative to the x-y plane. Since transit observations yield very precise values of i_{obs}, the required ascending node Ω and its rate of change can be computed, once the orbit geometry through the angles γ and i_{obs} is specified. In Fig. 9 we show a contour plot of the linear coefficient of Eq. (3) between nodal regression and observed inclination change as a function of orbit geometry. Note that the apparent change of inclination due to the nodal regression does vanish for $i = 0$. Physically it is clear that a perturbing planet in a coplanar orbit cannot exercise a torque and therefore cannot cause the observed inclination variation. We will therefore always assume $i \neq 0$ in the following.

4.2. Oblate host star

We first consider the possibility that the TrES-2 host star is oblate. The motion of a planet around an oblate host star is equivalent to that of an artifical satellite orbiting the Earth, a problem intensely studied over the last decades and well understood Connon Smith (2005). The potential $U(r, \phi)$ of an axisymmetric body of mass M and radius R can be expressed as a power series involving the so-called harmonic coefficients. In second order one approximates the potential $U(r, \phi)$ as

$$U(r, \phi) = \frac{GM}{r}\left[1 - J_2\left(\frac{R}{r}\right)^2 \frac{1}{2}\left(3\sin^2\phi - 1\right)\right], \quad (4)$$

where r is the radial distance from the body's center, ϕ is latitude above the equator and G denotes the gravitational constant. Clearly, the perturbing term in the potential is proportional to J_2 and a perturbation calculation yields as first order secular perturbation the angular velocity of the ascending node as

$$\frac{\mathrm{d}\Omega}{\mathrm{d}t} = -\frac{3}{2}\frac{J_2 R^2}{(1-e^2)^2}\cos i\left(\frac{2\pi}{P}\right)^{7/3}\frac{1}{(GM_{\mathrm{total}})^{2/3}}, \quad (5)$$

where e and i denote the eccentricity and inclination of the orbiting body, P its period, M_{total} the sum of the masses of planet and host star and the validity of Kepler's third law has been assumed.

Interpreting the observed inclination change as nodal regression due to an oblate host star, we can compute a lower bound on the required harmonic coefficient J_2 assuming $e = 0$. Therefore, we combine Eqs. (3) and (5) to obtain an expression for J_2. Excluding pathological cases like $i, \Omega = 0$ and $\gamma = \pi/2$ and neglecting the planetary mass in Eq. (5) we find for any given set of parameters (Ω, γ, i)

$$J_2 \geq J_2^{\mathrm{min}} = \frac{2}{3}\frac{\mathrm{d}i_{\mathrm{obs}}}{\mathrm{d}t}\left(\frac{P}{2\pi}\right)^{7/3}\frac{(GM_{\mathrm{host}})^{2/3}}{R^2}\sin i_{\mathrm{obs}}, \quad (6)$$

where M_{host} denotes the mass of the host star. Mass, radius, inclination and period of the TrES-2 system are well known, and using the measured nodal regression we find $J_{2,\mathrm{TrES-2}} \approx 1.4 \times 10^{-4}$, i.e., a value smaller than that of the Earth ($J_{2,\oplus} = 0.00108$) by an order of magnitude, but considerably larger than that of the Sun, which is usually taken as $J_{2,\odot} \approx 3\text{–}6 \times 10^{-7}$ Rozelot et al. (2001). Since the host star of TrES-2 is a slow rotator very similar to the Sun Sozzetti et al. (2007), we expect similarly small J_2 values in contrast to our requirements. We therefore conclude that oblateness of the host star cannot be the cause for the observed orbit variations.

4.3. Perturbation by a third body

An alternative possibility to explain the observed orbit variations of the TrES-2 exoplanet would be the interaction with other planets in the system. Let us therefore assume the existence of such an additional perturbing planet of mass m_p, circling its host star of mass m_0 with period P_p at distance r_p located further out compared to the known transiting TrES-2 exoplanet. This three-body problem has been considered in past in the context of triple systems (Khaliullin et al. 1991; Li 2006) and the problem of artificial Earth satellites, whose orbits are perturbed by the Moon. In lowest order, the perturbing gravitational potential R_2 onto the inner planet with mass m and distance r is given by the expression

$$R_2 = \frac{m_p}{m_p + m_o}\left(\frac{2\pi a}{P_p}\right)^2\left(\frac{a_p}{r_p}\right)^3\left(\frac{r}{a}\right)^2\frac{3\cos^2 S - 1}{2}, \quad (7)$$

where the angle S denotes the elongation between the perturbed and perturbing planet as seen from the host star, a and a_p denote their respective semi-major axes and the validity of Kepler's third law has been assumed. Note that in this approach the perturbed body is assumed to be massless, implying that its perturbations onto the perturbing body are ignored. Next one needs to insert the orbital elements of the two bodies and, since we are interested only in secular variations, average over both the periods of the perturbed and perturbing planet. This is the so-called double-averaging method (Broucke 2003), which, however, in more or less the same form has also been applied by Li (2006) and Kovalevsky (1967). Denoting by e the eccentricity of the perturbed planet, by ω the longitude of the periastron and by i the angle between the two orbital planes, one obtains after some lengthy computation (see Kovalevsky 1967)

$$R_2 = \frac{m_p}{m_p + m_o}\left(\frac{\pi a}{2P_p}\right)^2 \times K_0(i, e, \omega), \quad (8)$$

with the auxiliary function $K_0(i, e, \omega)$ given by

$$K_0(e, i, \omega) = \left(6\cos^2 i - 2\right) + e^2\left(9\cos^2 i - 3\right) + 15e^2\sin^2 i\cos 2\omega.$$

The partial derivatives of R_2 with respect to the orbital elements are needed in the so-called Lagrangian planetary equations to derive the variations of the orbital elements of the perturbed body. One specifically finds for the motion of the ascending node

$$\frac{d\Omega}{dt} = \frac{m_p}{m_p + m_o}\frac{3\pi}{4}\frac{P}{P_p^2}\frac{\cos i}{\sqrt{1-e^2}} \times K_1(e, \omega), \quad (9)$$

where the auxiliary function $K_1(e, \omega)$ is defined through

$$K_1(e, \omega) = 5e^2\cos 2\omega - 3e^2 - 2 \quad (10)$$

and for the rate of change of inclination

$$\frac{di}{dt} = -e^2\frac{m_p}{m_p + m_o}\frac{15\pi}{8}\frac{P}{P_p^2}\frac{1}{\sqrt{1-e^2}}\sin(2i)\sin(2\omega). \quad (11)$$

As is obvious from Eq. (11), the rate of change of inclination in low eccentricity systems is very small and we therefore set $e = 0$. Assuming next a near coplanar geometry, i.e., setting $\cos i \approx 1$, we can simplify Eq. (9) as

$$\frac{d\Omega}{dt} = -\frac{m_p}{m_p + m_o}\frac{3\pi}{2}\frac{P}{P_p^2}\cdot \quad (12)$$

If we assume a host star mass and interpret the observed inclination change as the rate of nodal regression via Eq. (3), Eq. (12) relates the unknown planet mass m_p to its orbital period P_p.

4.3.1. Sanity check: application to the solar system

The use of Eq. (12) involves several simplifications. Thus, it is legitimate to ask, if we are justified in expecting Eq. (12) to describe reality. As a sanity check we apply Eq. (12) to our solar system. Consider first the motion of the Moon around the Earth, i.e., P = 27.3 d, which is perturbed by the Sun, i.e., P_p = 365.25 d. Since for that case our nomenclature requires $m_p \gg m_o$ and $i \sim 5.1°$, we find from Eq. (12) a time of 17.83 years for the nodes to complete a full circle, which agrees well with the canonical value of 18.6 years for the lunar orbit. In the lunar case it is clear that the Sun with its large mass and close proximity (compared to Jupiter) is by far the largest perturber of the Earth-Moon two-body system and this situation is exactly the situation described by theory.

Consider next the the perturbations caused by the outer planets of our solar system. Considering, for example, Venus, we can compute the perturbations caused by the planets Earth, Mars, Jupiter, Saturn and Uranus. Since the perturbation strength scales by the ratio $m_p P_p^{-2}$, we can set this value to unity for the Earth and compute values of 0.03, 2.26, 0.11 and 0.002 for Mars through Uranus respectively. So clearly, Venus is perturbed by several planets, but the perturbations by Jupiter are strongest. We therefore expect that our simple approach is not appropriate. We further note that among the outer solar system planets long period perturbations and resonances occur, which are not described by Eq. (12). If we nevertheless compute the nodal regression for Venus caused by Jupiter using Eq. (12), we find a nodal regression of 0.1°/cty for Venus, and 0.3°/cty for Mars. Using the orbital elements computed by Simon et al. (1994) and calculating the nodal regressions of Venus and Mars in the orbit plane of Jupiter we find values smaller than the true values, but at least, they computed values in the right order of magnitude and do not lead to an overprediction of the expected effects.

4.3.2. Sanity check: application to V 907 Sco

From archival studies Lacy et al. (1999) report the existence of transient eclipses in the triple star V 907 Sco. According to Lacy et al. (1999) this system is composed out of a short-period (P_{short} = 3.78 days) binary containing two main sequence stars of spectral type ~A0 and mass ratio 0.9, orbited by a lower mass third companion (P_{long} = 99.3 days), of spectral type mid-K or possibly even a white dwarf. The close binary system showed eclipses from the earliest reported observations in 1899 until about 1918, when the eclipses stopped; eclipses reappeared in 1963 and were observed until about 1986. Interpreting the appearance of eclipses due to nodal regression, Lacy et al. (1999) derive a nodal period of 68 years for V 907 Sco. Using Eq. (12) and assuming a mass of 2 $M_\odot$ for the host (m_o) and a mass of 0.5 $M_\odot$ for the companion (m_p), we compute a nodal regression period of 47.6 years, which agrees well with the nodal period estimated by Lacy et al. (1999). We therefore conclude that Eq. (12) also provides a reasonable description of the transient eclipse observations of V 907 Sco.

4.3.3. Application to TrES 2

Applying now Eq. (12) to the TrES-2 exoplanet we express the period of the (unknown) perturbing planet as a function of its also unknown mass through

$$P_p = \sqrt{\frac{m_p}{m_p + m_o}\frac{3\pi P}{2}\frac{1}{d\Omega/dt}}\cdot \quad (13)$$

A&A 510, A107 (2010)

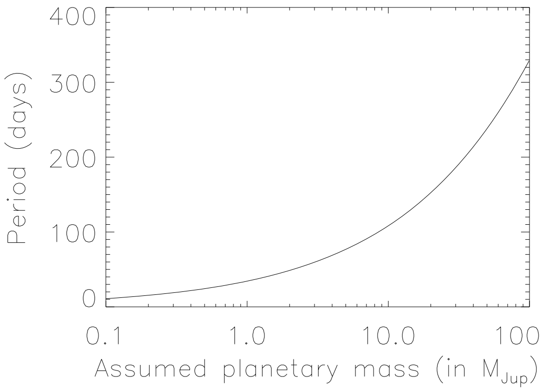

Fig. 10. Period of hypothesized second planet vs. mass assuming a linear coefficient of unity in Eq. (3) and near coplanarity.

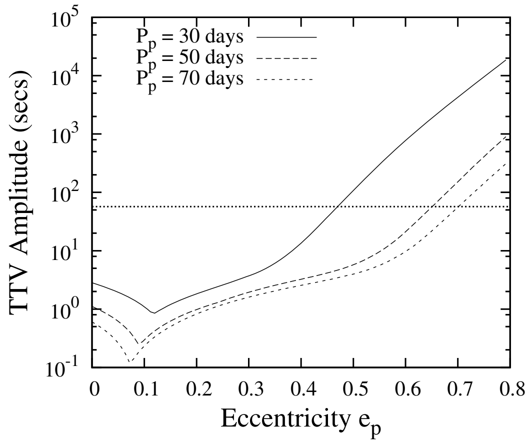

Fig. 11. Amplitude of expected Transit Timing Variations (TTVs) in the TrES-2 system. The perturber is assumed to have $m_p = 1\ M_{Jup}$. Its eccentricity e_p and period P_p are varied within plausible ranges. The orbit of TrES-2 is assumed to be circular. The vertical dotted line marks the best fitting TTV signal found by Rabus et al. (2009) of 57 s.

Since the host star mass and the nodal regression are known, the perturbing mass is the only remaining unknown; we note that Eq. (13) should be correct, as long as there is only one dominant perturber in the system with a low-eccentricity orbit sufficiently far away from the known close-in transiting planet. In Fig. 10 we plot the expected perturber period P_p as a function of m_p (in Jupiter masses) for $m_o = 1\ M_\odot$ and the measured rate of nodal regression assuming a linear coefficient of unity in Eq. (3). Assuming ad hoc a mass of about one Jupiter mass for this perturber and taking into account that a factor of a few is likely (cf., Fig. 9), we find that periods of 50 to 100 days are required to explain the observed nodal regression in TrES-2. Such an additional planet should be relatively easily detectable with RV studies. Daemgen et al. (2009) report the presence of a faint companion about one arcsec away from TrES-2. Assuming this companion to be physical, a spectral type between K4.5 and K6, a mass of about 0.67 $M_\odot$ at a distance of 230 AU with a period of 3900 years follow. Computing with these numbers the maximally expected nodal regression from Eq. (12), one finds values a couple of orders of magnitude below the observed values. We thus conclude that this object cannot be the cause of the observed orbit variations. On the other hand, this companion, again if physical, makes TrES-2 particularly interesting because it provides another cases of a planet/planetary system in a binary system, and eventually the orbit planes of binary system and the planet(s) can be derived.

4.4. Transit timing variations by a putative perturber

A perturbing second planet capable of causing fast nodal precession on the transiting planet is also expected to induce short-term periodic variations of its orbital elements. In addition to the secular precession of the node of the orbit we would thus expect to see short-term transit timing variations (TTVs), periodic variations of the mid-transit times (Holman & Murray 2005; Agol et al. 2005). Just as nodal regression, the TTV signal can be used to find and characterize planetary companions of transiting exoplanets. Rabus et al. (2009) carefully analyzed eight transit light curves of TrES-2 over several years. However, they were unable to detect any statistically significant TTV amplitudes in the TrES-2b light curves above about 50 s; cf. their Fig. 10. Therefore, the existence of perturbing objects leading to TTVs on the scale of up to about 50 s are consistent with actual observations. Putting it differently, the orbital parameters of any perturbing object causing the nodal precession of the orbit should yield a TTV amplitude below that and hence remain undetectable in the presently existing data.

To analyze the mutual gravitational influence of a perturbing second planet in the system on TrES-2, we have to treat the classical three-body problem of celestial mechanics. Instead of direct N-body integrations of the equations of motion we use an alternative method based on analytic perturbation theory developed and extensively tested by Nesvorný & Morbidelli (2008) and Nesvorný (2009). Outside possible mean-motion resonances their approach allows for a fast computation of the expected TTV amplitude given a combination of system parameters. As input we have to specify the orbital elements and masses of both planets. Consistent with the observations we assume TrES-2 to be in a circular orbit around its host star, while we allow for different eccentricities e_p and periods P_p of the perturber, which we assume to be of Jovian mass; since the TTV amplitudes scale nearly linearly with the perturber mass, we confine our treatment to $m_p = 1\ M_{Jup}$; all other orbital elements are set to zero. This is justified as these parameters in most cases do not lead to a significant amplification of the TTV signal (see Nesvorný 2009, for a detailed discussion of the impact of these orbital elements). The resulting TTV amplitude for different reasonable orbit configurations (given the observed secular node regression as discussed above) of the system of $P_{pert} = 30$, 50 and 70 days is plotted vs. the assumed eccentricity in Fig. 11; the currently available upper limit to any TTV signal derived by Rabus et al. (2009) is also shown. As is obvious from Fig. 11, a Jovian-mass perturber at a distance required to impose the observed secular changes (period of 50–100 days) leads to a TTV signal well below the current detection limit for all eccentricities e_p as long as $e_p \lesssim 0.4$. We therefore conclude that a putative perturbing Jovian-mass planet with a moderate eccentricity and with a period between 30–70 days would not yield any currently detectable TTV signal and would therefore be a valid explanation for the observed inclination change in the TrES-2 system.

5. Conclusions

In summary, our new observations taken in the spring of 2009 confirm the smaller transit durations reported in Paper I and suggest an even further decrease. With our simultaneously taken multicolor BUSCA data we demonstrate that the recorded multicolor lightcurves can be consistently modelled with a reasonable set of limb darkening coefficients, and that there is no need to fit the limb darkening coefficients to any particular light curve. An error in the description of the limb darkening therefore appears thus as an unlikely cause of the observed inclination changes. Also as expected, the obtained stellar radius is independent of the wavelength band used, demonstrating the internal self-consistency of our modelling.

As to the possible causes for the observed apparent orbit inclination change in TrES-2 we argue that the apparent observed inclination change is very likely caused by nodal regression. The assumption of an oblate host star leads to implausibly large J_2 coefficients, we therefore favor an explanation with a third body. We argue that Eq. (12) is a reasonable approximation for the interpration of the observed inclination changes; applying it to the TrES-2 system, we find that a planet of one Jovian mass with periods between 50–100 days would suffice to cause the observed inclination changes, while at the same time yield TTVs with amplitudes well below the currently available upper limits.

The assumption of such an additional planet in the TrES-2 system is entirely plausible. First of all, if it is near coplanar with TrES-2b, it would not cause any eclipses and therefore remain undetected in transit searches. Next, an inspection of the exosolar planet data base maintained at *www.exoplanet.eu* reveals a number of exoplanet systems with properties similar to those postulated for TrES-2, i.e., a close-in planet together with a massive planet further out: In the Gl 581 system there is a 0.02 Jupiter-mass planet with a period of 66 days, and in fact a couple of similarly massive planets further in with periods of 3.1, 5.4 and 12.9 days respectively; in the system HIP 14810 there is a close-in planet with a 6.6 day period and a somewhat lighter planet with a period of 147 days, in the HD 160691 system the close-in planet has a period of 9.6 days and two outer planets with Jupiter masses are known with periods of 310 and 643 days. It is also clear that in these systems nodal regression changes must occur, unless these systems are exactly coplanar, which appears unlikely. Therefore on longer time scales the observed orbit inclination in these systems must change, but only in transiting systems the orbit inclination can be measured with sufficient accuracy. Because of its apparent inclination change TrES-2b is clearly among the more interesting extrasolar planets. If the system continues its behavior in the future the transits of TrES-2b will disappear. Fortunately, within the first data set of the Kepler mission ~30 transits should be covered. From our derived inclination change rate of $\Delta i \sim 0.075^\circ/\mathrm{yr}$ this corresponds to an overall change of $\Delta i \sim 0.015^\circ$ in this first data set, which ought to be detectable given the superior accuracy of the space-based Kepler photometry. As far as the detection of our putative second planet is concerned, RV methods appear to be more promising than a search for TTVs, unless the orbital eccentricities are very large.

Acknowledgements. The paper is based on observations collected with the 2.2 m telescope at the Centro Astronómico Hispano Alemán (CAHA) at Calar Alto (Almería, Spain), operated jointly by the Max-Planck Institut für Astronomie and the Instituto de Astrofísica de Andalucía (CSIC). The authors thank H.Poschmann and the BUSCA team for their tremendous work on the new controller and CCD system. D.M. was supported in the framework of the DFG-funded Research Training Group "Extrasolar Planets and their Host Stars" (DFG 1351/1). S.S. acknowledges DLR support through the grant 50OR0703.

References

Agol, E., Steffen, J., Sari, R., & Clarkson, W. 2005, MNRAS, 359, 567
Alonso, R., Barbieri, M., Rabus, M., et al. 2008, A&A, 487, L5
Broucke, R. A. 2003, J. Guidance Control Dynamics, 26, 27
Claret, A. 2004, A&A, 428, 1001
Connon Smith, R. 2005, The Observatory, 125, 341
Daemgen, S., Hormuth, F., Brandner, W., et al. 2009, A&A, 498, 567
Holman, M. J., & Murray, N. W. 2005, Science, 307, 1288
Holman, M. J., Winn, J. N., Latham, D. W., et al. 2007, ApJ, 664, 1185
Howell, S. B., & Everett, M. E. 2001, in Third Workshop on Photometry, ed. W. J. Borucki, & L. E. Lasher, 1
Khaliullin, K. F., Khodykin, S. A., & Zakharov, A. I. 1991, ApJ, 375, 314
Kovalevsky, J. 1967, in Les Nouvelles Méthodes de la Dynamique Stellaire, 221
Lacy, C. H. S., Helt, B. E., & Vaz, L. P. R. 1999, AJ, 117, 541
Li, L. 2006, AJ, 131, 994
Miralda-Escudé, J. 2002, ApJ, 564, 60
Mislis, D., & Schmitt, J. H. M. M. 2009, A&A, 500, L45
Neckel, H. 1995, Sol. Phys., 156, 7
Nesvorný, D. 2009, ApJ, 701, 1116
Nesvorný, D., & Morbidelli, A. 2008, ApJ, 688, 636
O'Donovan, F. T., Charbonneau, D., Mandushev, G., et al. 2006, ApJ, 651, L61
O'Donovan, F. T., Charbonneau, D., Harrington, J., et al. 2009, in IAU Symp., 253, 536
Rabus, M., Deeg, H. J., Alonso, R., Belmonte, J. A., & Almenara, J. M. 2009, A&A, 508, 1011
Raetz, S., Mugrauer, M., Schmidt, T. O. B., et al. 2009, Astron. Nachr., 330, 459
Rozelot, J. P., Godier, S., & Lefebvre, S. 2001, Sol. Phys., 198, 223
Simon, J. L., Bretagnon, P., Chapront, J., et al. 1994, A&A, 282, 663
Sozzetti, A., Torres, G., Charbonneau, D., et al. 2007, ApJ, 664, 1190

A&A 539, A97 (2012)
DOI: 10.1051/0004-6361/201118536

Astronomy & Astrophysics

A consistent analysis of three years of ground- and space-based photometry of TrES-2⋆

S. Schröter, J. H. M. M. Schmitt, and H. M. Müller

Hamburger Sternwarte, Universität Hamburg, Gojenbergsweg 112, 21029 Hamburg, Germany
e-mail: sschroeter@hs.uni-hamburg.de

Received 28 November 2011 / Accepted 26 January 2012

ABSTRACT

The G0V dwarf TrES-2A, which is transited by a hot Jupiter, is one of the main short-cadence targets of the *Kepler* telescope and, therefore, among the photometrically best-studied planetary systems known today. Given the near-grazing geometry of the planetary orbit, TrES-2 offers an outstanding opportunity to search for changes in its orbital geometry. Our study focuses on the secular change in orbital inclination reported in previous studies. We present a joint analysis of the first four quarters of *Kepler* photometry together with the publicly available ground-based data obtained since the discovery of TrES-2b in 2006. We use a common approach based on the latest information regarding the visual companion of TrES-2A and stellar limb darkening to further refine the orbital parameters. We find that the *Kepler* observations rule out a secular inclination change of previously claimed order as well as variations of the transit timing, however, they also show slight indication for further variability in the inclination which remains marginally significant.

Key words. stars: individual: TrES-2 – planetary systems

1. Introduction

The transiting Jovian planet TrES-2b was originally discovered by O'Donovan et al. (2006), and later extensively observed by Holman et al. (2007) and Sozzetti et al. (2007), who determined more accurate properties for the TrES-2 system. TrES-2A is an old (≈5 Gyr) G0V star with about solar radius and mass, orbited by a close-in (0.035 AU) planet with a mass of 1.2 M_J and a period of 2.47 d. The planet has a radius of 1.24 R_J and a large inclination angle of about 84°, implying a nearly grazing transit. The spectroscopic parameters of the systen determined by Sozzetti et al. (2007) were confirmed and refined by Ammler-von Eiff et al. (2009).

As already pointed out by Holman et al. (2007), TrES-2 offers an outstanding opportunity to search for changes in orbital parameters for several reasons: its large inclination and close-in orbit yield a high impact parameter, making the shape and timing of the transit sensitive to variations of the orbital parameters. Its large radius and short orbital period allow the study of large numbers of deep transits over hundreds of epochs. Additionally, TrES-2 is in the field of view of the *Kepler* telescope, which has already gathered more than 220 days of publicly available photometric data, probably making TrES-2 the photometrically best-studied exoplanetary system to date.

Since its discovery there have been numerous attempts to detect secular changes in the orbital parameters of TrES-2b due to an external perturber. Mislis & Schmitt (2009) combined their own transit observations with the data from Holman et al. (2007) and found these data to be consistent with a decrease in transit duration, suggesting a decrease of about 0.075°/yr in the orbital inclination of the planet, an interpretation corroborated by another series of observations (Mislis et al. 2010). Reverting to secular perturbation theory, Mislis et al. (2010) suggest that a Jovian mass planet with a period between 50 to 100 days can explain the observed inclination changes. On the other hand, Scuderi et al. (2010), in their analysis from data taken in June 2009, find systematically higher values for the inclination of TrES-2b, ruling out any systematic trend. Their analysis also includes 33 days of *Kepler* data comprising multiple transits originally published by Gilliland et al. (2010), which they find to be in agreement with their ground-based observations.

Additional photometric data of TrES-2 are presented by Rabus et al. (2009), who analyze five transits sytematically searching for signatures of transit timing variations. However, they do not find a clear signal and are only able to provide upper constraints on the perturber's mass. Christiansen et al. (2011) obtained nine additional transits from NASA's EPOXI Mission of Opportunity (Deep impact). Comparing their results with earlier measurements, they find a formally significant decrease in the transit duration with time, which however disappears if they exclude the duration measurement by Holman et al. (2007).

A thorough analysis of the first two quarters of *Kepler* data (Q0 and Q1) is presented by Kipping & Bakos (2011b), who do not find any inclination change within the *Kepler* data, obtaining an inclination change of (+0.0019 ± 0.0020)°/cycle. They also reanalyze the data by Holman et al. (2007) fitting the limb-darkening coefficients and compare the measured average transit durations in both data sets. Their results neither support nor exclude the inclination change, largely due to the still very small temporal baseline of 18 cycles. Raetz et al. (2009, 2011) analyze 22 additional transits observed between March 2007 and August 2010, but find no indications of variations in the transit duration. However, their data quality does not suffice to exclude the inclination change proposed by Mislis et al. (2010).

The whole discussion is further complicated by the results of Daemgen et al. (2009), who detected a visual companion to TrES-2A at a separation of 1.089 ± 0.008″ that contaminates

⋆ Appendix A is available in electronic form at http://www.aanda.org

A&A 539, A97 (2012)

the photometric data, and leads to filter-dependent deviations in the orbital parameters if not being accounted for. While Scuderi et al. (2010) already mention the contribution of a third light and estimate its influence on the system parameters, Kipping & Bakos (2011b) were actually the first to include it in their light-curve modeling of the *Kepler* data.

The purpose of this work is to present a joint analysis of all publicly available *Kepler* data of TrES-2 focussing on the apparent change in orbital inclination as proposed by Mislis et al. (2010). We exploit four quarters of *Kepler* photometry and publicly available ground-based transit observations in a joint approach including the latest observational results regarding the TrES-2-system, aiming at a consistent picture of the observational status quo regarding changes in the orbital parameters, especially the inclination of the planet.

2. Light-curve modeling

We fit the transit data with the transit model developed by Mandel & Agol (2002) making use of their `occultquad` and `occultnl` FORTRAN routines[1]. From the transit light curve, we can directly infer the following parameters: the orbital period, P, the time of transit minimum, τ, the radius ratio, $p = R_{\rm p}/R_{\rm s}$, the semi-major axis in stellar radii, $a/R_{\rm s}$, the orbital inclination, i, and the limb-darkening law. For our fits we either assume a quadratic limb darkening with coefficients u_1 and u_2 or a four-parametric non-linear prescription as proposed by Claret & Bloemen (2011, their Eq. (5)), which provides a significantly more accurate representation of model atmosphere intensities (Howarth 2011a). Furthermore, our model includes the contribution of a third light, L_3, given as a fraction of the host-star's luminosity.

We assume a circular orbit fixing $e = 0$, as there are no indications for any non-zero eccentricity (Kipping & Bakos 2011b).

2.1. On the role of limb darkening

There is an ongoing debate on the role of limb darkening in the analysis of planetary transit light curves regarding the question whether the limb-darkening coefficients (LDCs) should be fitted together with the remaining parameters or left fixed during the fit. On the one hand, LDCs are the only quantities in the parameter set describing the transit that can be predicted theoretically, given some basic spectroscopic information of the object. As such they are inherently dependent on the quality of available spectroscopic data and the subtleties of underlying assumptions entering the model calculations itself. Fitting the LDCs therefore assures that the resulting transit parameters are independent of the spectroscopic background model and that the uncertainties of the spectroscopic parameters are readily included into the transit model. Furthermore, the inclusion of LDCs as free parameters in the fitting process leads to considerably larger uncertainties in the remaining model parameters, reflecting the fact, that the LDCs are highly correlated to most parameters.

On the other hand, the data quality of most ground-based measurements is not sufficient to substantially constrain the LDCs. Several fit parameters, especially the LDCs, are known to be mutually correlated, as demonstrated analytically by Pál (2008) and numerically by Southworth (2008) in the specific case of TrES-2. The mutual correlations among the parameters are particularly strong in the case of TrES-2, where the transit is nearly grazing, because TrES-2b only covers the outermost parts of the stellar disk that are dominated by strong limb-darkening effects. The remaining orbital parameters thus depend crucially on the details of the adopted limb darkening resulting in strong correlations with the LDCs. The amount of information on the limb darkening, which can be extracted even from the *Kepler* data, is limited by the fact, that the transit of TrES-2b is nearly grazing, i.e. $\mu \ll 1$. Assuming a quadratic limb-darkening law this approximation yields

$$\frac{I(\mu)}{I_0} = 1 - (u_1 + u_2) + \mu(u_1 + 2u_2) - O(\mu^2). \tag{1}$$

Therefore, to zeroth order we are only sensitive to the sum of the LDCs, i.e. the amount of deducible knowledge on the individual parameter is inherently limited. This introduces a degeneracy between both LDCs due to their strong correlation. While, in principle, it would always be preferable to fit for LDCs, thereby cross-checking spectroscopic results and theoretical modeling, analyses of ground-based observations of TrES-2 cannot afford to refrain from including as much independently obtained information as possible.

Therefore, in a first attempt, we will fit the *Kepler* data without assuming any a priori information on the LDCs (see Sect. 4.1) and compare our results to theoretical predictions. However, comparing the results from the *Kepler* data to several ground-based transit observations requires a common treatment of the data. We therefore eventually use fixed LDCs for all data sets assuming the theoretically predicted values (see Sect. 4.2).

The spectroscopic studies by Sozzetti et al. (2007) and Ammler-von Eiff et al. (2009) concordantly suggest that TrES-2A has an effective temperature of 5800 K, a surface gravity of 4.4, microturbulence velocity of 1 km s^{-1} and solar metallicity (see Table 1). Claret & Bloemen (2011) provide LDCs in several filter bands calculated for a grid of PHOENIX and ATLAS9 model atmospheres, employing two different calculation methods. We linearly interpolated on the data grid to obtain a set of LDCs pertaining to a PHOENIX model closely matching the inferred spectroscopic properties of TrES-2A. Our interpolated LDCs for the different filter bands are summarized in Table 2.

Table 1. Spectroscopic parameters of TrES-2.

	Sozzetti et al. (2007)	Ammler-von Eiff et al. (2009)
$T_{\rm eff}$ (K)	5850 ± 50	5795 ± 73
$\log g$ (cgs)	4.4 ± 0.1	4.30 ± 0.13
$\xi_{\rm T}$ (km s^{-1})	1.00 ± 0.05	0.79 ± 0.12
[M/H]	−0.15 ± 0.10	0.06 ± 0.08

2.2. On the contribution of a third light

Daemgen et al. (2009) report the detection of a faint visual companion of TrES-2A in their ground-based high-resolution images obtained with the *AstraLux* lucky imaging camera at Calar Alto. The angular distance from TrES-2A to this object is only $1.089 \pm 0.009''$. It contaminates all previous published observations and introduces a systematic error in the transit parameters, especially the transit depth. According to Southworth (2010), roughly 5% of third light can be compensated for by decreasing $a/R_{\rm s}$ by 1%, p by 3% and i by 0.1 degrees.

Daemgen et al. (2009) measured magnitude differences in the Sloan Digital Sky Survey (SDSS) z' and i' filters, that can be used to obtain the flux contribution of the third light, L_3. They find $\Delta z' = 3.429 \pm 0.010$ and $\Delta i' = 3.661 \pm 0.016$ resulting in

[1] `http://www.astro.washington.edu/users/agol`

Table 2. Non-linear limb-darkening coefficients obtained by linear interpolation on the tables provided by Claret & Bloemen (2011) based on PHOENIX atmosphere models.

Filter	a_1	a_2	a_3	a_4	L_3
Kepler	0.473[a]	0.192[a]	–	–	0.0276
Kepler	0.801	−0.676	1.053	−0.388	0.0276
Strömgren u	0.910	−1.006	1.388	−0.355	0.0045
Strömgren v	0.863	−0.767	1.872	−0.617	0.0102
Strömgren b	0.698	−1.206	1.572	−0.599	0.0180
Strömgren y	0.758	−0.663	1.203	−0.454	0.0227
Johnson U	1.085	−1.412	1.721	−0.466	0.0053
Johnson B	0.754	−0.937	1.734	−0.641	0.0137
Johnson V	0.742	−0.602	1.134	−0.434	0.0216
Cousins R	0.796	−0.632	0.993	−0.378	0.0294
Cousins I	0.853	−0.746	0.963	−0.363	0.0360
SDSS i'	0.829	−0.688	0.935	−0.354	0.0343[b]
SDSS z'	0.861	−0.807	0.967	−0.360	0.0425[b]

Notes. The last column gives the fraction of flux due to the visual companion detected by Daemgen et al. (2009). [(a)] Interpolated coefficients for a quadratic limb-darkening law. [(b)] Values are based on magnitude differences directly measured by Daemgen et al. (2009).

flux contributions of 0.0425 ± 0.0004 and 0.0343 ± 0.0005 in the z' and i' bands, respectively. We assume that the nearby companion has an effective temperature of 4400 K, surface gravity of 4.5, solar metallicity and microturbulent velocity of 2 km s^{-1} compatible with its spectral type being K4.5 to K6 as derived by Daemgen et al. (2009). We used Gray's SPECTRUM together with a Kurucz atmosphere model to calculate a synthetic spectrum. We then use STScI's *pysynphot*[2] to convolve the spectrum with transmission curves of all standard filter systems, taking into account the high-resolution *Kepler* response function[3] to obtain the throughput in *Kepler*'s broad spectral band. The resulting fractional contributions of third light, L_3, are tabulated in Table 2.

2.3. Fitting approach and error analysis

To obtain adequate errors for the fit parameters and to determine the mutual dependence of the parameters, we explore the parameter space by sampling from the posterior probability distribution using a Markov-chain Monte-Carlo (MCMC) approach.

Typically, the system parameters, especially the LDCs, are prone to substantial correlation effects. These correlations can easily render the sampling process inefficient. It is therefore advisable to use a suitably decorrelated set of LDCs as e.g. proposed by Pál (2008). However, due to the near-grazing system geometry in the case of TrES-2 we expect strong correlations between the whole set of parameters. We therefore chose to use a modification of the usual Metropolis-Hastings sampling algorithm, which is able to adapt to the strong correlation structure. This modification, known as Adaptive Metropolis algorithm (AM; Haario et al. 2001), releases the strict Markov property of the sampling chains by updating the sampling parameters using a multivariate jump distribution whose covariance is tuned during sampling. This tuning is based on all previous samples of the chain, so that AM looses the Markov property. However, the algorithm can be shown to have the correct ergodic properties, i.e. it approaches the correct posterior probability distribution under very general assumptions (Haario et al. 2001; Vihola 2011). We checked that AM yields correct results for simulated data sets with parameters close to TrES-2, and found that this approach showed fast convergence and efficiency.

All MCMC calculations make extensive use of routines of `PyAstronomy`[4], a collection of Python routines providing a convenient interface to fitting and sampling algorithms implemented in the PyMC (Patil et al. 2010) and SciPy (Jones et al. 2001) packages.

3. Data preparation

We retrieved the *Kepler* data of quarters Q0 to Q3 from the NASA Multimission Archive at STScI[5]. Specifically, we use data pertaining to data release 5 (Q0, Q1), data release 7 (Q2), and data release 4 (Q3) as provided by the *Kepler* Data Analysis Working Group[6]. *Kepler* observed TrES-2 in short cadence mode with a sampling of 58.85 s covering 229 days. For our analysis, we use the raw aperture photometry (SAP) flux and the corresponding error as provided in the FITS files. The raw data have been processed using *Kepler*'s photometric analysis (PA) pipeline, which includes barycentric time correction, detection of Argabrightening (a transient increase of background flux possibly due to dust particles) and cosmic ray events, background removal, and the computation of aperture corrected flux. Further, we removed invalid data points and all points marked by the SAP_QUALITY flag. The *Kepler* data provide time stamps in barycentric Julian dates (BJD_{UTC}), which we convert into barycentric dynamical time (BJD_{TDB}) accounting for 34 leap seconds elapsed since 1961.

The data show discontinuities and exponential jumps due to instrumental duty cycles ("pointing tweaks", "safe mode recoveries", and "earth points") and long-term trends ("focus drifts"), which must be corrected beforehand. First, we removed all transits from the light curve including one half of the transit duration on either side and rejected 3σ outliers using a sliding median filter of window size 30 min. We then used the information provided in the data release notes to exclude data points affected by safe mode recoveries and earth points, which are difficult to correct otherwise. Subsequently, we divided the data into chunks covering undisturbed duty cycles. As there are two pointing tweaks occuring during quarter Q2, we subdivided the Q2 data at these tweaks into three chunks covering full duty cycles.

To remove long-term trends due to focus drifts, we followed an approach similar to Kipping & Bakos (2011b) by using the discrete cosine transform (Makhoul 1980) to obtain a smoothed model of the continuum for each data chunk separately. The discrete cosine transform decomposes a signal $x(n)$ into a linear combination of N cosine functions according to

$$y(k) = \sum_{n=0}^{N-1} x(n) \cos\left(\frac{\pi k(2n+1)}{2N}\right), \qquad 0 \le k < N, \tag{2}$$

and provides an efficient way of extracting the low-frequency information within the signal. We applied the discrete cosine transform to each chunk of the light curve removing all but the first l low-frequency terms, where l is the rounded integer value of the length of the chunk divided by the orbital period. The thus cleaned transformed signal was inversely transformed to

[2] http://stsdas.stsci.edu/pysynphot/

[3] http://keplergo.arc.nasa.gov/CalibrationResponse.shtml

[4] http://www.hs.uni-hamburg.de/DE/Ins/Per/Czesla/PyA/PyA/index.html

[5] http://archive.stsci.edu/kepler/

[6] http://archive.stsci.edu/kepler/release_notes

Table 3. Publicly available data of ground-based photometric observations of TrES-2.

Epoch	Filter	Reference
13, 15, 34	z'	Holman et al. (2007)
263	near R	Mislis & Schmitt (2009)
312	I	Mislis & Schmitt (2009)
395	I	Mislis et al. (2010)
414	I, y, b, v	Mislis et al. (2010)
421	I	Scuderi et al. (2010)

Notes. The epoch refers to the first transit of TrES-2b observed by O'Donovan et al. (2006).

obtain a smoothed model of the continuum. Finally, we divided the complete light curve including the transits by the model and extracted the data in a box of half-width 0.06 days around each transit center. We further discard three transits, which occur close to the pointing tweaks, where the continuum flux shows strong distortions.

To check that the results of our study do not depend on the details of the data reduction, we also extracted the un-detrended data directly around each transit center and divided the transit by a third-order polynomial fit to the local continuum (Welsh et al. 2010). We find, that this procedure yields essentially the same results.

The ground-based data covering a total of 8 planetary transits between 2006 and 2009 are used as provided by the authors (see Table 3, for references). The time stamps are specified as Heliocentric Julian Dates (HJD_{UTC}) and are converted into BJD_{TDB} using the webtool by Eastman et al. (2010).

4. Fitting results

Before fitting the *Kepler* data, we use all available data to obtain estimates of the period, P, and the time of transit minimum, τ. As already pointed out by Southworth (2008), P and τ are usually correlated with each other, but uncorrelated with the remaining parameters. Therefore, the period can be determined quite accurately without interference of other parameters. Fitting all publicly available data we obtained

$$\tau_0 = 2\,453\,957.635486^{+0.000069}_{-0.000068}\ \mathrm{BJD_{TDB}}\ \text{and}$$

$$P = 2.470613402^{+0.000000150}_{-0.000000154}\ \mathrm{d},$$

where τ_0 refers to the first transit of TrES-2b observed by O'Donovan et al. (2006) and errors correspond to 68.3% HPD (highest probability density) intervals. The fractional error in P is approximately 10^5 times smaller than the fractional errors in a/R_s and p, and can safely be ignored. We checked that including both parameters with Gaussian priors corresponding to their errors in the MCMC calculations yields negligible changes in the remaining parameters but slows down the MCMC algorithm. In the following, we therefore fix these parameters to their best-fit values.

4.1. Four quarters of Kepler data

In the following, we fit all 81 transits observed by *Kepler* during the first four quarters of observations. To explore the whole parameter space of solutions, we relax the constraints on the parameters as much as possible by imposing uniform prior probability distributions allowing large parameter variations. By fixing the LDCs to their theoretically computed values we would impose strong a priori information on the fitting process. If the LDCs were chosen incorrectly, we would obtain well-constrained model parameters with comparably small credibility intervals, which, however, could be inconsistent. We therefore additionally fitted quadratic LDCs, assuming uniform priors on u_1 and u_2, and performed an MCMC error analysis of the complete set of parameters. Our best-fit solution is determined by those parameter values that minimize the deviance after 10^6 iterations of the sampler. The errors are calculated from 68.3% HPD intervals of the posterior probability distributions for the parameters. Our results are summarized in the upper part of Table 4.

Given their credibility intervals the parameters of our global fit are compatible with those by Southworth (2011) and Kipping & Bakos (2011b). We note a slight discrepancy with the results by Kipping & Bakos (2011b), who obtain a slightly larger radius ratio, p, of 0.1282. A small, possibly systematic discrepancy compared to the values of Kipping & Bakos (2011b) has also been noted by Southworth (2011). Within their 2σ error intervals our LDCs are still consistent with the best-fit solution obtained by Kipping & Bakos (2011b), who found LDCs of $u_1 = 0.52$ and $u_2 = 0.06$. We note that the sum, $u_1 + u_2$, of the LDCs is very well constrained in agreement with our considerations in Sect. 2.1.

As discussed in Howarth (2011b) we cannot directly compare our best-fit LDCs to predictions based on the stellar atmosphere model. This is due to the fact that we are fitting photometric data from a real star, using a simplified model of the stellar limb darkening. The high impact parameter of TrES-2b together with the fitting approach inevitably lead to considerable deviations of the photometrically determined LDCs from model-atmosphere characterizations. Instead, Howarth (2011b) proposes to compare the results from the photometric analysis with the results obtained from *s*ynthetic *p*hotometry based on a given *a*tmosphere *m*odel (termed "SPAM"). Figure 1 shows the result of this consideration. The lowest deviance combination of LDCs after 10^6 MCMC samples is obviously inconsistent if compared directly to the predictions by Claret & Bloemen (2011) based on PHOENIX model atmospheres for TrES-2. However, the SPAM model based on the same model atmosphere is consistent with the best-fit LDCs. This strengthens our confidence in the reliability of the theoretically calculated LDCs.

Note that the simplified prescription of limb darkening used in our model also introduces small, but non-negligible systematic errors in the remaining light curve parameters due to the strong correlations between all parameters. In the following we therefore use the four-parametric, non-linear limb-darkening law proposed by Claret & Bloemen (2011), holding the LDCs fixed at their theoretically expected values to obtain the remaining transit parameters. This, of course, substantially reduces the errors on our parameter estimates because the strong correlations mediated by the limb-darkening treatment diminuish. Our resuls after 10^6 iterations of the MCMC sampler are summarized in the lower part of Table 4.

4.2. Secular change in inclination

The values inferred from the fit to the *Kepler* data are the most robust estimates of the planetary parameters of TrES-2 currently available. In the following, we reanalyze all publicly available photometric data of TrES-2 examining each transit separately to search for secular variations in the orbital inclination.

Table 4. Lowest-deviance parameters for the *Kepler* data after 10^6 MCMC samples compared to the results with fixed limb-darkening coefficients.

Parameter	Value	Error (68.3% HPD)
i (°)	83.874	[83.806, 83.910]
p	0.1257	[0.1240, 0.1265]
a/R_s	7.903	[7.835, 7.937]
u_1	0.19	[−0.10, 0.36]
u_2	0.43	[0.25, 0.75]
$u_1 + u_2$	0.626	[0.605, 0.648]
i (°)	83.9788	[83.9740, 83.9837]
p	0.12759	[0.12755, 0.12762]
a/R_s	7.9899	[7.9856, 7.9943]
a_1, a_2, a_3, a_4	fixed, see Table 2	

Notes. Both fits assume a third light contribution according to Table 2.

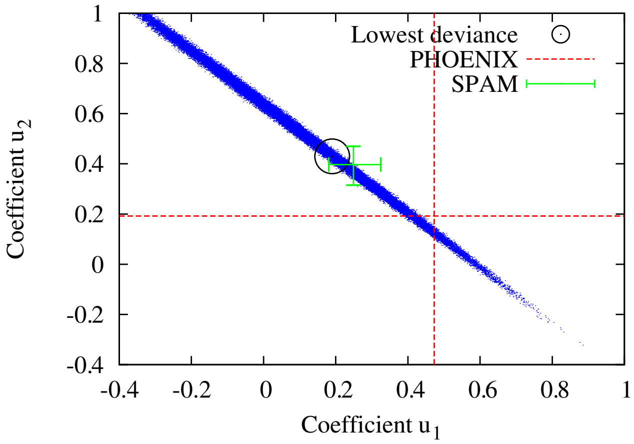

Fig. 1. Correlation between linear and quadratic limb-darkening coefficient resulting from 10^6 MCMC runs. The lowest deviance combination of parameters (circle) is significantly offset from the Claret & Bloemen (2011) model prediction (dashed red) but consistent with the result obtained from fitting synthetic photometry based on the same atmosphere model (SPAM, green).

Secular inclination changes are empirically detectable as changes in transit duration, which is a function of a/R_s, p and i (Seager & Mallén-Ornelas 2003). While each of these parameters may itself exhibit secular changes resulting in changes in the transit duration (Kipping 2010), we focus in the following on changes in the orbital inclination, i, and the time of transit minimum, τ, of each transit. We thereby assume that neither the radius ratio nor the planetary orbit change in size over the course of the observations and that the orbit is circular. However, we still must account for our incomplete knowledge of the true value of a/R_s and p. We therefore leave both parameters free during the MCMC calculations imposing Gaussian priors according to the errors obtained from our global fit. Depending on the instrumental setup of the observations (cf. Table 3) we take into account the expected third light contribution and the LDCs according to Table 2. For each transit we obtain the posterior distributions for both τ and i using 10^4 iterations of the MCMC sampler. We summarize the prior information in Table 5. The errors again correspond to 68.3% HPD intervals.

Concerning the *Kepler* data, Kipping & Bakos (2011b) did not find evidence for parameter changes within the first two quarters. However, the public release of the last two quarters, i.e. quarters Q2 and Q3, provided a substantial enlargement of the data set. We therefore reanalyze the complete Q0 to Q3 set of transits in detail searching for variations of the inclination or transit timing variations (TTVs).

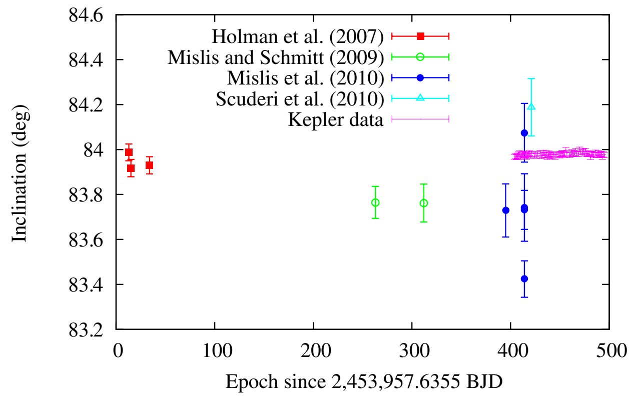

Fig. 2. Inclination versus transit epoch for TrES-2 based on publicly available ground-based data and the *Kepler* observations. Errors are derived from 95.5% HPD intervals corresponding to 2σ errors based on 10^4 MCMC iterations for each transit.

Table 5. Prior information used for the MCMC calculations in Sect. 4.2.

Quantity	Prior	Source
a/R_s	7.9899 ± 0.0043	Table 4
p	0.127585 ± 0.000035	Table 4
τ	uniform	
i	uniform	
a_1, a_2, a_3, a_4	fixed	Table 2
L_3	fixed	Table 2
e	0 (fixed)	

Our results are shown in Fig. 2. The superior quality of the *Kepler* data manifests itself in very small credibility intervals for these observations. While the data by Holman et al. (2007) are fully consistent with the inclination obtained by *Kepler*, we find systematically lower inclinations for the data sets of Mislis & Schmitt (2009) and Mislis et al. (2010). In fact, ignoring the *Kepler* data, the secular inclination change detected by Mislis & Schmitt (2009) is clearly visible.

Note, however, that our common fitting approach based on the results from *Kepler* and including the third light contribution yields best-fit values for the inclinations derived from the ground-based measurements that are closer to the *Kepler* values than those originally obtained by Mislis & Schmitt (2009) and Mislis et al. (2010). Furthermore, our new errors are quite large so that the *Kepler* value lies only just outside of our 3σ error.

We also checked, whether it is possible to completely reconcile the *Kepler* observations with the results by Mislis & Schmitt (2009) and Mislis et al. (2010). Accounting for the possibility of normalization problems during data reduction we introduce an additional normalization constant to our model. Including this constant as another parameter of our MCMC marginally enlarges the uncertainties on the inclinations. We thus do not expect the deviation to stem from simple normalization problems.

Another cause for erroneous results would result from incorrectly taking into account the contribution of the contaminating third light. To fully reconcile the inclinations by Mislis & Schmitt (2009) and Mislis et al. (2010) with the best-fit inclination from the *Kepler* data would require contributions of a third light of 10 to 20% of the total flux, which can be excluded from

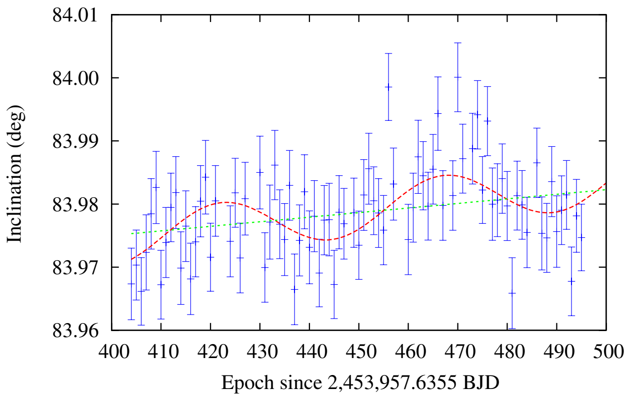

Fig. 3. Inclination versus transit epoch for the *Kepler* observations. Errors are computed from the 68.3% HPD intervals based on 10^4 MCMC iterations for each transit. The best-fitting linear (dotted/green) and sinusoidal models including a linear trend (dashed/red) are overplotted.

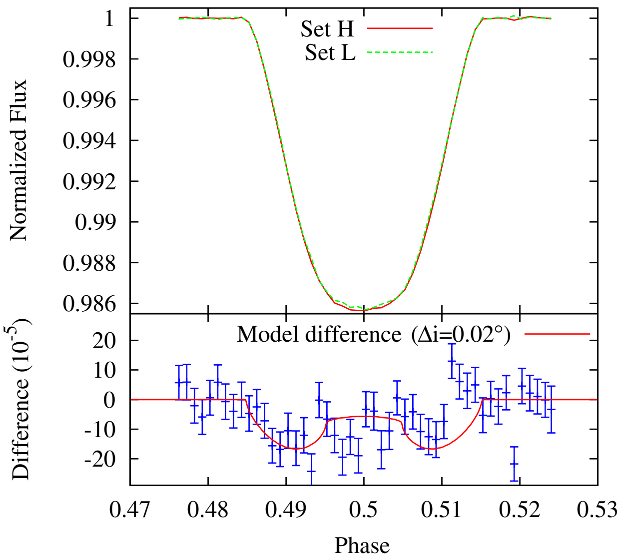

Fig. 4. *Upper panel:* averaged templates of two sets of 10 transits with high (H, solid red) and low (L, dashed green) inclinations, respectively, as expected from the tentative sinusoidal variation of the inclinations obtained by *Kepler*. *Lower panel:* the difference between the two averaged transits. The expected difference for two models pertaining to i = 83.97° and 83.99° is shown for reference (solid red).

the observations by Daemgen et al. (2009). However, assuming a uniform prior for the third light contribution and demanding it to be smaller than 10%, the credibility intervals become substantially larger including the *Kepler* result. We thus conclude, that problems with the flux calibration possibly caused by the reference star are the most likely cause for the observed deviations.

In either case, the *Kepler* data rule out a decrease in inclination of the size expected by Mislis et al. (2010). The exact reason for their systematic deviation remains unclear. The Holman et al. (2007) data are consistent with the first four quarters of *Kepler* data. Note, however, that despite the long available time baseline the errors of the Holman et al. (2007) data points are too large to draw significant conclusions on the presence of other, smaller linear trends.

4.3. Variability in the Kepler data

We now focus on the *Kepler* data searching for small trends or variations, which could still be consistent with the previous ground-based observations. Figure 3 shows an enlarged view of the *Kepler* data; the errors are derived from the 68.3% HPD intervals, so they are equivalent to 1σ errors.

We found a slight linear trend in the *Kepler* data. An MCMC analysis yields a slightly non-zero slope of $(0.8 \pm 0.2) \times 10^{-4}$ °/cycle. This would correspond to a secular inclination change nearly two orders of magnitude smaller than the value by Mislis et al. (2010). Extrapolating this trend back to the epoch of transit observations obtained by Holman et al. (2007), we would expect an inclination of 83.94° ± 0.01° consistent with the measurement errors.

In order to quantify the improvement of the different fits, we calculated the statistic

$$\hat{F} = \frac{\left(\chi_a^2 - \chi_b^2\right)/(\nu_a - \nu_b)}{\chi_b^2/\nu_b} \tag{3}$$

and compared its value to an F-distribution with $\nu_a - \nu_b$ and ν_b degrees of freedom (e.g., Rawlings et al. 1998). We obtain a p-value of 0.004 indicating that the linear trend provides a better description compared to the constant at the 2.8σ level, which we consider as indicative, but not significant evidence for the presence of such a trend.

After subtracting the linear trend from the data, we computed an error-weighted Lomb-Scargle periodogram (Zechmeister & Kürster 2009), which displays a single signal at a period of 45 cycles or 111 days with a false-alarm probability below 10%. Figure 3 shows our best-fit sinusoidal model including a linear trend. An F-test comparing the model to the constant model yields a p-value of 0.015 (or 2.4σ); the test thus indicates the presence of an additional sinusoidal modulation superimposed on the linear trend, which however remains insignificant.

We can also compare the three models using the Bayesian information criterion, BIC = $\chi^2 + k \ln N$ (Schwarz 1978), which penalizes the number k of model parameters given $N = 81$ data points. We obtain BICs of 136.3, 127.6, and 117.0 for the constant, the linear trend, and the sinusoid with linear trend, respectively.

Despite being close to formal significance the signal is easily obliterated by the noise and could be introduced by some subtleties in our analysis. Assuming the sinusoidal model with linear trend to be true, we averaged two sets of 10 transits pertaining to low (around epoch 409, compare Fig. 3) and high (around epoch 470) inclinations, respectively. Subtracting both templates, their difference should exhibit a characteristic signature, which we model by subtracting two model calculations for $i_{\rm L}$ = 83.97° and $i_{\rm H}$ = 83.99°. We show the averaged templates together with their difference and the model in Fig. 4. While during ingress the flux difference shows a decrease following the difference model, the signature during egress is obliterated by the noise. We checked that averaging transits pertaining to epochs close to the zero-crossing points of the sinusoidal model yields no substantial deviation from a constant.

We repeated our analysis using simulated control data to check, whether the signal is introduced by our data reduction or by "phasing effects" due to the *Kepler* cadence (Kipping & Bakos 2011a). However, we could not detect similar signals exceeding the noise. We further changed our data normalization strategy (see Sect. 3), but found the variation of inclination to be

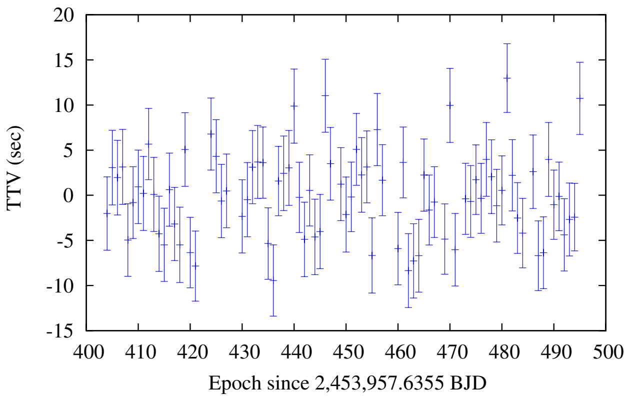

Fig. 5. Transit timing variation (TTV) versus transit epoch for TrES-2b using the best-fit ephemerides. Errors are computed from the 68.3% HPD intervals based on 10^4 MCMC iterations for each transit.

stable against these changes. Analyzing similar *Kepler* targets we found spurious periodicities in some cases, which, however, remained insignificant in the periodogram (at false-alarm probabilities above 10%). In summary, there seem to be some indications for a short-term inclination variation and an underlying secular change in the *Kepler* data of TrES-2. However, the detected signal is merely an indication of inclination changes in the *Kepler* data, because the baseline of space-based observations is still too short to draw significant conclusions on the stability or variability in the inclination (compare Fig. 4).

Turning to the times of transit minimum of the *Kepler* transits, Fig. 5 shows that the transit timing is consistent with being constant over the course of the *Kepler* data. An F-test comparing the constant and a linear model yields a p-value of 0.92; thus, there is no evidence for a linear trend. In the periodogram there is no signal at false-alarm probabilities below 10%. We thus do not see any evidence for TTVs in the *Kepler* data.

The apparent secular change in inclination refers to the orientation of the orbital plane of TrES-2b relative to the observer's tangential plane and, assuming a circular orbit, can be interpreted as nodal regression at fixed orbit inclination. While gravitational perturbation due to an oblate host star is unlikely given that TrES-2A is a slow rotator very similar to the Sun (Mislis et al. 2010), additional bodies in the stellar system could offer a viable explanation for secular changes in the orbital parameters. If we assume our linear trend in inclination to be physical, we can estimate the period of a perturber of specified mass in a circular, coplanar orbit using Eq. (13) in Mislis et al. (2010). We find that a perturbing planet of Jovian mass would be expected at orbital periods between 100 and 300 days. However, a perturbing second planet capable of causing nodal precession of the transiting planet would also be expected to induce short-term periodic variations of its orbital elements (Holman & Murray 2005; Agol et al. 2005). To calculate the amplitude of such TTVs, we use an approach based on analytic perturbation theory developed by Nesvorný & Morbidelli (2008). Outside possible mean-motion resonances additional Jovian mass bodies with periods larger than 100 days would cause a TTV amplitude below 1 s if on a circular orbit. Given the standard deviation of the times of transit minimum of 4.8 s, such a TTV amplitude cannot be ruled out. Thus, the existence of an external perturber in the system still provides an entirely plausible scenario.

5. Summary and conclusion

We presented an analysis of all publicly available photometric data obtained during planetary transits of TrES-2b including four quarters of data obtained with the *Kepler* space telescope. The transits were fitted in a common scheme using theoretically calculated LDCs and taking into account the contribution of a third light.

Fitting quarters Q0 to Q3 of the *Kepler* data, we were able to refine the system parameters determined by Kipping & Bakos (2011b) and Southworth (2011). Our results are compatible with these previous studies, our errors being slightly smaller. Its high impact parameter makes the TrES-2-system sensitive to details of the adopted stellar limb-darkening model because only the covered regions close to the stellar limb are used to extrapolate the limb darkening for the whole stellar disk. Small differences between limb-darkening prescriptions therefore yield significant differences in the resulting best fits. We find that the theoretically calculated LDCs by Claret & Bloemen (2011) provide a correct description of the observed limb darkening if compared with the data via the SPAM approach as advocated by Howarth (2011b).

The data by Mislis & Schmitt (2009) and Mislis et al. (2010) are found to be inconsistent with the remaing data, especially the *Kepler* data. The discrepancy can neither be attributed to errors in the theoretical LDCs nor to the contribution of third light, which the original studies did not account for. The most probable explanations would be subtleties in the data reduction, perhaps due to problems with the reference star, or the presence of time-correlated noise yielding underestimated parameter errors (Carter & Winn 2009).

Excluding the Mislis & Schmitt (2009) and Mislis et al. (2010) data sets, all observations can be reconciled in a consistent picture. The extension of the available *Kepler* data by two additional quarters reveal some hints for systematic variations in the inclination, the marginally significant slope would be consistent with the data by Holman et al. (2007). However, given the available baseline of space-based observations we consider the inclination change as indicative but not significant. Further data, which already have been obtained by the *Kepler* space telescope, will settle this issue in the near future.

Our study shows that space-based and ground-based photometry of TrES-2 can be analyzed in a common scheme yielding consistent results. While space-based photometry offers the possibility to constrain all system parameters at once, with the eventual decommissioning of *Kepler* it will again be up to ground-based measurements to search for long-term changes in the orbital parameters of TrES-2.

Acknowledgements. This paper includes data collected by the *Kepler* mission. Funding for the *Kepler* mission is provided by the NASA Science Mission directorate. The *Kepler* observations were obtained from the Multimission Archive at the Space Telescope Science Institute (MAST). H.M.M. is supported in the framework of the DFG-funded Research Training Group "Extrasolar Planets and their Host Stars" (DFG 1351/2). S.S. acknowledges support from the DLR under grant 50OR0703.

References

Agol, E., Steffen, J., Sari, R., & Clarkson, W. 2005, MNRAS, 359, 567
Ammler-von Eiff, M., Santos, N. C., Sousa, S. G., et al. 2009, A&A, 507, 523
Carter, J. A., & Winn, J. N. 2009, ApJ, 704, 51
Christiansen, J. L., Ballard, S., Charbonneau, D., et al. 2011, ApJ, 726, 94
Claret, A., & Bloemen, S. 2011, A&A, 529, A75
Daemgen, S., Hormuth, F., Brandner, W., et al. 2009, A&A, 498, 567
Eastman, J., Siverd, R., & Gaudi, B. S. 2010, PASP, 122, 935
Gilliland, R. L., Jenkins, J. M., Borucki, W. J., et al. 2010, ApJ, 713, L160
Haario, H., Saksman, E., & Tamminen, J. 2001, Bernoulli, 7, 223

Holman, M. J., & Murray, N. W. 2005, Science, 307, 1288
Holman, M. J., Winn, J. N., Latham, D. W., et al. 2007, ApJ, 664, 1185
Howarth, I. D. 2011a, MNRAS, 413, 1515
Howarth, I. D. 2011b, MNRAS, 418, 1165
Jones, E., Oliphant, T., Peterson, P., et al. 2001, SciPy: Open source scientific tools for Python, http://www.scipy.org
Kipping, D. M. 2010, MNRAS, 407, 301
Kipping, D., & Bakos, G. 2011a, ApJ, 730, 50
Kipping, D., & Bakos, G. 2011b, ApJ, 733, 36
Makhoul, J. 1980, Acoustics, Speech and Signal Processing, IEEE Transactions on, 28, 27
Mandel, K., & Agol, E. 2002, ApJ, 580, L171
Mislis, D., & Schmitt, J. H. M. M. 2009, A&A, 500, L45
Mislis, D., Schröter, S., Schmitt, J. H. M. M., Cordes, O., & Reif, K. 2010, A&A, 510, A107
Nesvorný, D., & Morbidelli, A. 2008, ApJ, 688, 636
O'Donovan, F. T., Charbonneau, D., Mandushev, G., et al. 2006, ApJ, 651, L61
Pál, A. 2008, MNRAS, 390, 281
Patil, A., Huard, D., & Fonnesbeck, C. J. 2010, J. Stat. Software, 35, 1
Raetz, S., Maciejewski, G., Mugrauer, M., et al. 2011, Detection and Dynamics of Transiting Exoplanets, St. Michel l'Observatoire, France, ed. F. Bouchy, R. Díaz & C. Moutou, EPJ Web Conf., 11, 5007
Rabus, M., Deeg, H. J., Alonso, R., Belmonte, J. A., & Almenara, J. M. 2009, A&A, 508, 1011
Raetz, S., Mugrauer, M., Schmidt, T. O. B., et al. 2009, Astron. Nachr., 330, 459
Rawlings, J. O., Pantula, S. G., & Dickey, D. A. 1998, Applied regression analysis, 2nd edn., Springer texts in statistics (New York, NY: Springer)
Schwarz, G. 1978, The Annals of Statistics, 6, 461
Scuderi, L. J., Dittmann, J. A., Males, J. R., Green, E. M., & Close, L. M. 2010, ApJ, 714, 462
Seager, S., & Mallén-Ornelas, G. 2003, ApJ, 585, 1038
Southworth, J. 2008, MNRAS, 386, 1644
Southworth, J. 2010, MNRAS, 408, 1689
Southworth, J. 2011, MNRAS, 417, 2166
Sozzetti, A., Torres, G., Charbonneau, D., et al. 2007, ApJ, 664, 1190
Vihola, M. 2011, Stochastic Processes and their Applications, 121, 2839
Welsh, W. F., Orosz, J. A., Seager, S., et al. 2010, ApJ, 713, L145
Zechmeister, M., & Kürster, M. 2009, A&A, 496, 577

Pages 9 to 10 are available in the electronic edition of the journal at http://www.aanda.org

Appendix A: Results from individual fits

In Table A.1, we show the transit parameters of TrES-2b from individual fits of ground-based and *Kepler* data.

Table A.1. Transit parameters for TrES-2b from individual fits of ground-based and *Kepler* data.

Epoch	τ [$\mathrm{BJD_{TDB}} - 2\,450\,000$ d]	i [deg]	a/R_s	p	Reference
		Publicly available ground-based data			
13	$3989.752878^{+0.000208}_{-0.000233}$	$83.9876^{+0.0171}_{-0.0201}$	$7.9899^{+0.0038}_{-0.0047}$	$0.127585^{+0.000034}_{-0.000035}$	Holman et al. (2007)
15	$3994.694003^{+0.000233}_{-0.000227}$	$83.9174^{+0.0166}_{-0.0219}$	$7.9898^{+0.0042}_{-0.0044}$	$0.127585^{+0.000038}_{-0.000033}$	Holman et al. (2007)
34	$4041.635919^{+0.000213}_{-0.000255}$	$83.9300^{+0.0184}_{-0.0198}$	$7.9893^{+0.0042}_{-0.0041}$	$0.127582^{+0.000039}_{-0.000031}$	Holman et al. (2007)
263	$4607.398143^{+0.000512}_{-0.000574}$	$83.7650^{+0.0378}_{-0.0332}$	$7.9897^{+0.0042}_{-0.0043}$	$0.127585^{+0.000037}_{-0.000034}$	Mislis & Schmitt (2009)
312	$4728.465365^{+0.000596}_{-0.000580}$	$83.7622^{+0.0430}_{-0.0413}$	$7.9895^{+0.0040}_{-0.0042}$	$0.127581^{+0.000036}_{-0.000034}$	Mislis & Schmitt (2009)
395	$4933.527211^{+0.000743}_{-0.000861}$	$83.7291^{+0.0602}_{-0.0579}$	$7.9897^{+0.0039}_{-0.0045}$	$0.127584^{+0.000037}_{-0.000034}$	Mislis et al. (2010)
414	$4980.466843^{+0.000712}_{-0.000717}$	$83.4239^{+0.0455}_{-0.0358}$	$7.9897^{+0.0040}_{-0.0046}$	$0.127583^{+0.000034}_{-0.000036}$	Mislis et al. (2010)
414	$4980.467292^{+0.000552}_{-0.000648}$	$83.7314^{+0.0427}_{-0.0440}$	$7.9896^{+0.0038}_{-0.0048}$	$0.127582^{+0.000034}_{-0.000037}$	Mislis et al. (2010)
414	$4980.467765^{+0.001166}_{-0.001178}$	$84.0745^{+0.0579}_{-0.0726}$	$7.9897^{+0.0039}_{-0.0045}$	$0.127585^{+0.000036}_{-0.000034}$	Mislis et al. (2010)
414	$4980.467504^{+0.001041}_{-0.001389}$	$83.7421^{+0.0780}_{-0.0723}$	$7.9900^{+0.0044}_{-0.0044}$	$0.127585^{+0.000035}_{-0.000037}$	Mislis et al. (2010)
421	$4997.762881^{+0.000642}_{-0.000820}$	$84.1880^{+0.0659}_{-0.0616}$	$7.9900^{+0.0046}_{-0.0040}$	$0.127587^{+0.000037}_{-0.000033}$	Scuderi et al. (2010)
		Kepler data			
404	$4955.763245^{+0.000050}_{-0.000044}$	$83.9673^{+0.0047}_{-0.0066}$	$7.9883^{+0.0044}_{-0.0044}$	$0.127577^{+0.000037}_{-0.000034}$	
405	$4958.233917^{+0.000047}_{-0.000048}$	$83.9703^{+0.0055}_{-0.0056}$	$7.9886^{+0.0044}_{-0.0041}$	$0.127579^{+0.000036}_{-0.000032}$	
406	$4960.704517^{+0.000042}_{-0.000054}$	$83.9662^{+0.0052}_{-0.0055}$	$7.9886^{+0.0039}_{-0.0041}$	$0.127575^{+0.000034}_{-0.000034}$	
407	$4963.175144^{+0.000040}_{-0.000056}$	$83.9723^{+0.0063}_{-0.0056}$	$7.9897^{+0.0042}_{-0.0047}$	$0.127577^{+0.000031}_{-0.000036}$	
408	$4965.645664^{+0.000048}_{-0.000045}$	$83.9784^{+0.0056}_{-0.0056}$	$7.9901^{+0.0046}_{-0.0040}$	$0.127578^{+0.000037}_{-0.000036}$	
409	$4968.116325^{+0.000048}_{-0.000044}$	$83.9826^{+0.0062}_{-0.0052}$	$7.9900^{+0.0046}_{-0.0039}$	$0.127580^{+0.000037}_{-0.000033}$	
410	$4970.586959^{+0.000043}_{-0.000051}$	$83.9672^{+0.0056}_{-0.0053}$	$7.9899^{+0.0040}_{-0.0043}$	$0.127587^{+0.000038}_{-0.000031}$	
411	$4973.057564^{+0.000052}_{-0.000043}$	$83.9739^{+0.0049}_{-0.0062}$	$7.9876^{+0.0047}_{-0.0036}$	$0.127570^{+0.000039}_{-0.000032}$	
412	$4975.528240^{+0.000043}_{-0.000048}$	$83.9795^{+0.0052}_{-0.0056}$	$7.9891^{+0.0037}_{-0.0043}$	$0.127578^{+0.000036}_{-0.000034}$	
413	$4977.998789^{+0.000047}_{-0.000048}$	$83.9818^{+0.0058}_{-0.0056}$	$7.9904^{+0.0049}_{-0.0036}$	$0.127589^{+0.000037}_{-0.000034}$	
414	$4980.469352^{+0.000045}_{-0.000051}$	$83.9698^{+0.0060}_{-0.0055}$	$7.9893^{+0.0041}_{-0.0044}$	$0.127570^{+0.000032}_{-0.000035}$	
415	$4982.939951^{+0.000047}_{-0.000047}$	$83.9765^{+0.0061}_{-0.0051}$	$7.9874^{+0.0037}_{-0.0045}$	$0.127569^{+0.000038}_{-0.000031}$	
416	$4985.410635^{+0.000047}_{-0.000047}$	$83.9681^{+0.0056}_{-0.0057}$	$7.9900^{+0.0037}_{-0.0048}$	$0.127581^{+0.000037}_{-0.000033}$	
417	$4987.881204^{+0.000046}_{-0.000048}$	$83.9740^{+0.0055}_{-0.0056}$	$7.9904^{+0.0038}_{-0.0044}$	$0.127585^{+0.000036}_{-0.000033}$	
418	$4990.351791^{+0.000048}_{-0.000048}$	$83.9804^{+0.0053}_{-0.0060}$	$7.9896^{+0.0042}_{-0.0043}$	$0.127580^{+0.000037}_{-0.000031}$	
419	$4992.822527^{+0.000042}_{-0.000052}$	$83.9843^{+0.0054}_{-0.0062}$	$7.9896^{+0.0048}_{-0.0038}$	$0.127576^{+0.000036}_{-0.000035}$	
420	$4995.293008^{+0.000044}_{-0.000046}$	$83.9716^{+0.0051}_{-0.0057}$	$7.9890^{+0.0041}_{-0.0040}$	$0.127578^{+0.000035}_{-0.000032}$	
421	$4997.763604^{+0.000045}_{-0.000045}$	$83.9805^{+0.0051}_{-0.0062}$	$7.9895^{+0.0039}_{-0.0043}$	$0.127578^{+0.000038}_{-0.000032}$	
424	$5005.175613^{+0.000049}_{-0.000044}$	$83.9741^{+0.0063}_{-0.0049}$	$7.9900^{+0.0041}_{-0.0041}$	$0.127589^{+0.000033}_{-0.000036}$	
425	$5007.646198^{+0.000045}_{-0.000049}$	$83.9818^{+0.0053}_{-0.0056}$	$7.9884^{+0.0043}_{-0.0041}$	$0.127577^{+0.000037}_{-0.000032}$	
426	$5010.116754^{+0.000047}_{-0.000047}$	$83.9715^{+0.0055}_{-0.0056}$	$7.9904^{+0.0043}_{-0.0039}$	$0.127583^{+0.000040}_{-0.000029}$	
427	$5012.587380^{+0.000045}_{-0.000050}$	$83.9809^{+0.0056}_{-0.0059}$	$7.9899^{+0.0045}_{-0.0041}$	$0.127583^{+0.000030}_{-0.000038}$	
430	$5019.999187^{+0.000042}_{-0.000052}$	$83.9850^{+0.0055}_{-0.0060}$	$7.9895^{+0.0048}_{-0.0045}$	$0.127589^{+0.000032}_{-0.000036}$	
431	$5022.469822^{+0.000051}_{-0.000044}$	$83.9700^{+0.0052}_{-0.0058}$	$7.9901^{+0.0039}_{-0.0044}$	$0.127589^{+0.000037}_{-0.000033}$	
432	$5024.940477^{+0.000050}_{-0.000044}$	$83.9771^{+0.0051}_{-0.0067}$	$7.9892^{+0.0043}_{-0.0046}$	$0.127581^{+0.000040}_{-0.000030}$	
433	$5027.411097^{+0.000046}_{-0.000047}$	$83.9862^{+0.0050}_{-0.0060}$	$7.9897^{+0.0041}_{-0.0041}$	$0.127579^{+0.000035}_{-0.000036}$	
434	$5029.881709^{+0.000043}_{-0.000048}$	$83.9768^{+0.0054}_{-0.0055}$	$7.9887^{+0.0040}_{-0.0043}$	$0.127577^{+0.000034}_{-0.000037}$	
435	$5032.352219^{+0.000047}_{-0.000045}$	$83.9744^{+0.0057}_{-0.0058}$	$7.9899^{+0.0041}_{-0.0044}$	$0.127580^{+0.000038}_{-0.000032}$	
436	$5034.822785^{+0.000047}_{-0.000045}$	$83.9830^{+0.0052}_{-0.0058}$	$7.9906^{+0.0039}_{-0.0045}$	$0.127587^{+0.000032}_{-0.000035}$	
437	$5037.293526^{+0.000042}_{-0.000047}$	$83.9665^{+0.0052}_{-0.0060}$	$7.9893^{+0.0041}_{-0.0042}$	$0.127577^{+0.000034}_{-0.000036}$	
438	$5039.764149^{+0.000046}_{-0.000049}$	$83.9742^{+0.0057}_{-0.0056}$	$7.9890^{+0.0044}_{-0.0041}$	$0.127582^{+0.000031}_{-0.000038}$	
439	$5042.234769^{+0.000049}_{-0.000047}$	$83.9819^{+0.0054}_{-0.0063}$	$7.9916^{+0.0042}_{-0.0046}$	$0.127606^{+0.000035}_{-0.000036}$	
440	$5044.705462^{+0.000049}_{-0.000046}$	$83.9731^{+0.0061}_{-0.0054}$	$7.9897^{+0.0041}_{-0.0044}$	$0.127580^{+0.000037}_{-0.000034}$	
441	$5047.175958^{+0.000043}_{-0.000047}$	$83.9781^{+0.0059}_{-0.0054}$	$7.9889^{+0.0038}_{-0.0047}$	$0.127583^{+0.000034}_{-0.000035}$	
442	$5049.646518^{+0.000046}_{-0.000050}$	$83.9691^{+0.0057}_{-0.0050}$	$7.9903^{+0.0039}_{-0.0042}$	$0.127591^{+0.000038}_{-0.000032}$	
443	$5052.117194^{+0.000045}_{-0.000046}$	$83.9774^{+0.0063}_{-0.0047}$	$7.9902^{+0.0035}_{-0.0047}$	$0.127588^{+0.000031}_{-0.000038}$	
444	$5054.587747^{+0.000051}_{-0.000046}$	$83.9775^{+0.0058}_{-0.0057}$	$7.9885^{+0.0044}_{-0.0042}$	$0.127581^{+0.000040}_{-0.000030}$	
445	$5057.058368^{+0.000046}_{-0.000049}$	$83.9673^{+0.0055}_{-0.0054}$	$7.9890^{+0.0044}_{-0.0039}$	$0.127581^{+0.000037}_{-0.000034}$	

A&A 539, A97 (2012)

Table A.1. continued.

Epoch	τ [$\mathrm{BJD_{TDB}} - 2\,450\,000$ d]	i [deg]	a/R_s	p	Reference
446	$5059.529155^{+0.000044}_{-0.000049}$	$83.9787^{+0.0056}_{-0.0060}$	$7.9890^{+0.0042}_{-0.0045}$	$0.127580^{+0.000036}_{-0.000033}$	
447	$5061.999681^{+0.000048}_{-0.000045}$	$83.9769^{+0.0054}_{-0.0057}$	$7.9895^{+0.0043}_{-0.0042}$	$0.127576^{+0.000036}_{-0.000035}$	
449	$5066.940882^{+0.000048}_{-0.000045}$	$83.9786^{+0.0050}_{-0.0060}$	$7.9902^{+0.0043}_{-0.0041}$	$0.127589^{+0.000034}_{-0.000036}$	
450	$5069.411456^{+0.000046}_{-0.000050}$	$83.9735^{+0.0050}_{-0.0058}$	$7.9896^{+0.0042}_{-0.0041}$	$0.127583^{+0.000033}_{-0.000036}$	
451	$5071.882092^{+0.000045}_{-0.000044}$	$83.9814^{+0.0051}_{-0.0061}$	$7.9900^{+0.0048}_{-0.0038}$	$0.127587^{+0.000033}_{-0.000035}$	
452	$5074.352766^{+0.000044}_{-0.000048}$	$83.9856^{+0.0058}_{-0.0054}$	$7.9910^{+0.0040}_{-0.0046}$	$0.127591^{+0.000034}_{-0.000033}$	
453	$5076.823347^{+0.000047}_{-0.000048}$	$83.9805^{+0.0058}_{-0.0050}$	$7.9896^{+0.0045}_{-0.0035}$	$0.127578^{+0.000037}_{-0.000032}$	
454	$5079.293970^{+0.000049}_{-0.000043}$	$83.9786^{+0.0051}_{-0.0058}$	$7.9904^{+0.0042}_{-0.0042}$	$0.127581^{+0.000039}_{-0.000029}$	
455	$5081.764470^{+0.000043}_{-0.000054}$	$83.9759^{+0.0051}_{-0.0059}$	$7.9892^{+0.0044}_{-0.0038}$	$0.127581^{+0.000035}_{-0.000035}$	
456	$5084.235245^{+0.000045}_{-0.000048}$	$83.9985^{+0.0058}_{-0.0048}$	$7.9907^{+0.0037}_{-0.0043}$	$0.127594^{+0.000036}_{-0.000032}$	
457	$5086.705793^{+0.000048}_{-0.000044}$	$83.9832^{+0.0053}_{-0.0061}$	$7.9902^{+0.0045}_{-0.0040}$	$0.127581^{+0.000035}_{-0.000034}$	
460	$5094.117546^{+0.000046}_{-0.000047}$	$83.9744^{+0.0065}_{-0.0046}$	$7.9914^{+0.0041}_{-0.0043}$	$0.127594^{+0.000037}_{-0.000033}$	
461	$5096.588269^{+0.000042}_{-0.000049}$	$83.9794^{+0.0057}_{-0.0052}$	$7.9904^{+0.0042}_{-0.0039}$	$0.127585^{+0.000032}_{-0.000038}$	
462	$5099.058744^{+0.000049}_{-0.000046}$	$83.9875^{+0.0059}_{-0.0057}$	$7.9908^{+0.0042}_{-0.0048}$	$0.127593^{+0.000037}_{-0.000034}$	
463	$5101.529370^{+0.000051}_{-0.000044}$	$83.9845^{+0.0058}_{-0.0051}$	$7.9903^{+0.0043}_{-0.0043}$	$0.127599^{+0.000037}_{-0.000032}$	
464	$5103.999990^{+0.000048}_{-0.000045}$	$83.9797^{+0.0050}_{-0.0058}$	$7.9895^{+0.0043}_{-0.0041}$	$0.127592^{+0.000037}_{-0.000033}$	
465	$5106.470706^{+0.000049}_{-0.000043}$	$83.9855^{+0.0049}_{-0.0061}$	$7.9899^{+0.0044}_{-0.0041}$	$0.127586^{+0.000035}_{-0.000035}$	
466	$5108.941275^{+0.000046}_{-0.000044}$	$83.9943^{+0.0056}_{-0.0061}$	$7.9897^{+0.0048}_{-0.0037}$	$0.127581^{+0.000038}_{-0.000030}$	
467	$5111.411898^{+0.000042}_{-0.000048}$	$83.9798^{+0.0051}_{-0.0059}$	$7.9896^{+0.0041}_{-0.0044}$	$0.127585^{+0.000035}_{-0.000037}$	
469	$5116.353078^{+0.000042}_{-0.000048}$	$83.9814^{+0.0062}_{-0.0049}$	$7.9907^{+0.0046}_{-0.0039}$	$0.127591^{+0.000035}_{-0.000033}$	
470	$5118.823862^{+0.000046}_{-0.000049}$	$84.0001^{+0.0058}_{-0.0051}$	$7.9922^{+0.0047}_{-0.0038}$	$0.127599^{+0.000033}_{-0.000038}$	
471	$5121.294291^{+0.000047}_{-0.000046}$	$83.9872^{+0.0053}_{-0.0056}$	$7.9899^{+0.0040}_{-0.0046}$	$0.127590^{+0.000032}_{-0.000036}$	
473	$5126.235583^{+0.000044}_{-0.000047}$	$83.9888^{+0.0052}_{-0.0061}$	$7.9893^{+0.0043}_{-0.0040}$	$0.127586^{+0.000035}_{-0.000037}$	
474	$5128.706192^{+0.000046}_{-0.000046}$	$83.9941^{+0.0051}_{-0.0058}$	$7.9910^{+0.0044}_{-0.0036}$	$0.127586^{+0.000037}_{-0.000033}$	
475	$5131.176834^{+0.000042}_{-0.000047}$	$83.9822^{+0.0061}_{-0.0045}$	$7.9911^{+0.0040}_{-0.0039}$	$0.127592^{+0.000034}_{-0.000035}$	
476	$5133.647423^{+0.000042}_{-0.000048}$	$83.9931^{+0.0052}_{-0.0058}$	$7.9909^{+0.0041}_{-0.0041}$	$0.127593^{+0.000033}_{-0.000035}$	
477	$5136.118086^{+0.000043}_{-0.000052}$	$83.9800^{+0.0055}_{-0.0059}$	$7.9907^{+0.0042}_{-0.0046}$	$0.127592^{+0.000029}_{-0.000043}$	
478	$5138.588677^{+0.000048}_{-0.000047}$	$83.9806^{+0.0055}_{-0.0060}$	$7.9928^{+0.0040}_{-0.0049}$	$0.127603^{+0.000035}_{-0.000035}$	
479	$5141.059254^{+0.000044}_{-0.000049}$	$83.9840^{+0.0060}_{-0.0050}$	$7.9905^{+0.0041}_{-0.0043}$	$0.127588^{+0.000038}_{-0.000031}$	
480	$5143.529887^{+0.000045}_{-0.000043}$	$83.9797^{+0.0061}_{-0.0049}$	$7.9888^{+0.0043}_{-0.0041}$	$0.127577^{+0.000036}_{-0.000034}$	
481	$5146.000644^{+0.000042}_{-0.000046}$	$83.9659^{+0.0053}_{-0.0059}$	$7.9895^{+0.0038}_{-0.0047}$	$0.127580^{+0.000033}_{-0.000036}$	
482	$5148.471133^{+0.000046}_{-0.000046}$	$83.9813^{+0.0052}_{-0.0057}$	$7.9898^{+0.0043}_{-0.0043}$	$0.127584^{+0.000036}_{-0.000033}$	
483	$5150.941691^{+0.000043}_{-0.000047}$	$83.9799^{+0.0054}_{-0.0055}$	$7.9899^{+0.0042}_{-0.0039}$	$0.127591^{+0.000034}_{-0.000037}$	
484	$5153.412285^{+0.000044}_{-0.000045}$	$83.9755^{+0.0049}_{-0.0062}$	$7.9902^{+0.0040}_{-0.0042}$	$0.127583^{+0.000035}_{-0.000036}$	
486	$5158.353590^{+0.000045}_{-0.000049}$	$83.9865^{+0.0057}_{-0.0053}$	$7.9909^{+0.0043}_{-0.0040}$	$0.127592^{+0.000034}_{-0.000034}$	
487	$5160.824096^{+0.000046}_{-0.000043}$	$83.9753^{+0.0054}_{-0.0062}$	$7.9909^{+0.0047}_{-0.0040}$	$0.127592^{+0.000035}_{-0.000035}$	
488	$5163.294713^{+0.000041}_{-0.000051}$	$83.9746^{+0.0056}_{-0.0054}$	$7.9907^{+0.0042}_{-0.0042}$	$0.127587^{+0.000032}_{-0.000037}$	
489	$5165.765446^{+0.000051}_{-0.000044}$	$83.9836^{+0.0058}_{-0.0053}$	$7.9897^{+0.0047}_{-0.0036}$	$0.127587^{+0.000032}_{-0.000035}$	
490	$5168.236001^{+0.000042}_{-0.000047}$	$83.9756^{+0.0056}_{-0.0058}$	$7.9913^{+0.0041}_{-0.0045}$	$0.127593^{+0.000031}_{-0.000036}$	
491	$5170.706625^{+0.000045}_{-0.000043}$	$83.9790^{+0.0048}_{-0.0061}$	$7.9905^{+0.0046}_{-0.0038}$	$0.127590^{+0.000036}_{-0.000032}$	
492	$5173.177189^{+0.000049}_{-0.000043}$	$83.9814^{+0.0057}_{-0.0052}$	$7.9907^{+0.0039}_{-0.0044}$	$0.127598^{+0.000034}_{-0.000035}$	
493	$5175.647822^{+0.000043}_{-0.000051}$	$83.9678^{+0.0050}_{-0.0059}$	$7.9901^{+0.0042}_{-0.0039}$	$0.127581^{+0.000033}_{-0.000036}$	
494	$5178.118439^{+0.000039}_{-0.000048}$	$83.9781^{+0.0060}_{-0.0055}$	$7.9907^{+0.0048}_{-0.0043}$	$0.127598^{+0.000034}_{-0.000036}$	
495	$5180.589204^{+0.000040}_{-0.000053}$	$83.9747^{+0.0048}_{-0.0057}$	$7.9892^{+0.0043}_{-0.0037}$	$0.127582^{+0.000035}_{-0.000036}$	

Notes. Epoch refers to the first transit of TrES-2b observed by O'Donovan et al. (2006). For the MCMC analysis, we fix the limb-darkening coefficients corresponding to the filter band (cf. Table 2) and use prior information as described in Table 5.

6. Chromospheric and coronal stellar activity in extrasolar planetary systems

On the following pages, I reproduce two publications on CoRoT-2 (Schröter et al., 2011; Czesla et al., 2012), which have been published in *Astronomy & Astrophysics*, and one publication on CoRoT-7 (Poppenhaeger et al., 2012), which is accepted for publication in the same journal. The works focus on the active host stars of both planetary systems and study amongst others, the relationship between stellar high-energy radiation and the close-in extrasolar planets.

6.1. My contributions

The transit light curves of CoRoT-2 show pronounced rotational modulation due to starspots. Since the occultation of spots leads to a relative increase of the flux within the transit, stellar activity directly affects the estimates of stellar parameters derived by transit modeling. Czesla et al. (2009) found that these effects cannot be neglected when the planetary parameters are to be accurate up to a few percent.

During the early phases of my doctoral studies, I participated in the preparation of Czesla et al. (2009), so I will outline my contributions here. S. Czesla and I developed a reduction pipeline for CoRoT light curves used in the analysis to correct the photometry for instrumental jumps, artifacts, periodic noise, and long-term trends. We further set up a transit fitting code based on the analytic transit model by Pál (2008). Additionally, I provided some of the statistical considerations in §3.3 of the paper. However, since I am not a main author, Czesla et al. (2009) is not included in this PhD thesis.

The publications reproduced in Sects. 6.2 and 6.3 of this thesis (Schröter et al., 2011; Czesla et al., 2012) are based on observational data obtained by Klaus F. Huber with the UVES spectrograph at the Very Large Telescope. Both works on CoRoT-2 are the result of a collective effort. Therefore, I will not attribute individual sections exclusively to me. The major contributions to Schröter et al. (2011) and Czesla et al. (2012) were provided by Stefan Czesla and myself. Both works are prepared and written in close cooperation with Stefan, who is also (co)author of both papers. Stefan and I provided approximately equal contributions to Schröter et al. (2011). The initial idea for Czesla et al. (2012) was contributed by Stefan, who proposed to use the chromospheric Rossiter-McLaughlin effect as a tool to resolve chromospheric emission regions. However, both of us have an equal share in every part of the work. Of course, the other coauthors also provided contributions, which I, however, will not outline in detail here.

The third paper in this chapter (Poppenhaeger et al., 2012) is the result of a collaboration initiated by Katja Poppenhaeger. She discovered the unpublished XMM-Newton X-ray data of CoRoT-7 originally proposed for observation by Vinay Kashyap. Katja provided the reduction and analysis of the X-ray data. Sairam Lalitha contributed the discussion of the UV light curve obtained with XMM's Optical Monitor. Stefan Czesla and I reduced 46 archival optical VLT/UVES spectra of CoRoT-7. My main contribution is the analysis of the optical spectra searching for interstellar absorption and signatures for absorption due to the planetary atmosphere during primary transit. I wrote the corresponding parts of the results section (§3) of the paper and contributed to the discussion of planetary evaporation in §4.

A&A 532, A3 (2011)
DOI: 10.1051/0004-6361/201116961

Astronomy & Astrophysics

The corona and companion of CoRoT-2a. Insights from X-rays and optical spectroscopy⋆

S. Schröter, S. Czesla, U. Wolter, H. M. Müller, K. F. Huber, and J. H. M. M. Schmitt

Hamburger Sternwarte, Universität Hamburg, Gojenbergsweg 112, 21029 Hamburg, Germany
e-mail: sschroeter@hs.uni-hamburg.de

Received 25 March 2011 / Accepted 23 May 2011

ABSTRACT

CoRoT-2 is one of the most unusual planetary systems known to date. Its host star is exceptionally active, showing a pronounced, regular pattern of optical variability caused by magnetic activity. The transiting hot Jupiter, CoRoT-2b, shows one of the largest known radius anomalies. We analyze the properties and activity of CoRoT-2a in the optical and X-ray regime by means of a high-quality UVES spectrum and a 15 ks *Chandra* exposure both obtained during planetary transits. The UVES data are analyzed using various complementary methods of high-resolution stellar spectroscopy. We characterize the photosphere of the host star by deriving accurate stellar parameters such as effective temperature, surface gravity, and abundances. Signatures of stellar activity, Li abundance, and interstellar absorption are investigated to provide constraints on the age and distance of CoRoT-2. Furthermore, our UVES data confirm the presence of a late-type stellar companion to CoRoT-2a that is gravitationally bound to the system. The *Chandra* data provide a clear detection of coronal X-ray emission from CoRoT-2a, for which we obtain an X-ray luminosity of 1.9×10^{29} erg s^{-1}. The potential stellar companion remains undetected in X-rays. Our results indicate that the distance to the CoRoT-2 system is ≈270 pc, and the most likely age lies between 100 and 300 Ma. Our X-ray observations show that the planet is immersed in an intense field of high-energy radiation. Surprisingly, CoRoT-2a's likely coeval stellar companion, which we find to be of late-K spectral type, remains X-ray dark. Yet, as a potential third body in the system, the companion could account for CoRoT-2b's slightly eccentric orbit.

Key words. stars: individual: CoRoT-2a – stars: fundamental parameters – planetary systems – stars: late-type – X-rays: stars

1. Introduction

The CoRoT-2 system stands out of the plethora of known exoplanet systems both for its exceptionally active host star and its unusually inflated planet. The hot Jupiter CoRoT-2b is the second transiting planet discovered by the space-based CoRoT mission (Alonso et al. 2008); its planetary nature was confirmed by spectroscopic follow-up observations with SOPHIE and HARPS (Bouchy et al. 2008). The planet orbits its host star every 1.74 days. Given its mass of 3.31 M_J and large radius of 1.465 R_J (Alonso et al. 2008), CoRoT-2b appears to be anomalously inflated in comparison to current evolutionary models (Guillot & Havel 2011). A spectral analysis showed that its host star, CoRoT-2a, is a G7 dwarf with solar composition. Its spectrum shows strong Li I absorption and emission-line cores in Ca II H and K, indicating that CoRoT-2a is a young and active star (Bouchy et al. 2008). CoRoT-2a has a close visual companion, 2MASS J19270636+0122577, separated by about 4″. Photometric magnitudes from the optical to the infrared concordantly suggest that this object is a late-K or early-M type star located at the same distance as CoRoT-2 (Alonso et al. 2008; Gillon et al. 2010). Thus, CoRoT-2a and its visual companion possibly form a physical pair.

The continuous photometric data of CoRoT-2a provided by the CoRoT telescope span 152 days. CoRoT-2a's light curve shows a distinct pattern of variability caused by starspots. In several studies, the light curve was used to reconstruct the surface brightness distribution of CoRoT-2a: Lanza et al. (2009) applied a light-curve inversion technique and found that most spots are concentrated in two active longitudes of alternating strength located on opposite hemispheres. Moreover, it was demonstrated that starspots influence the profiles of transit light-curves and that this effect cannot be neglected in transit modeling (Wolter et al. 2009; Czesla et al. 2009). Because the latitudinal band eclipsed by the planet is accurately known (Bouchy et al. 2008), it is even feasible to study the spot coverage on the surface section recurrently eclipsed by the planet (Huber et al. 2009; Silva-Valio et al. 2010; Huber et al. 2010).

Secondary eclipses of CoRoT-2b were observed in the optical with CoRoT (Alonso et al. 2009; Snellen et al. 2010), in the infrared with Spitzer (Gillon et al. 2010; Deming et al. 2011), and from the ground (Alonso et al. 2010). While atmospheric models (Fortney et al. 2008) suggest the presence of a stratospheric thermal-inversion layer in CoRoT-2b caused by the strong irradiation, the observational situation remains inconclusive (e.g., Deming et al. 2011). The observed emission of the planet is currently incompatible with any kind of standard atmosphere model, and more sophisticated approaches including, for example, substantial carbon monoxide mass loss or additional substructure in the atmosphere may be needed to explain the observations (see Deming et al. 2011, for a discussion); the substantial activity of the host star adds another complicating factor to the picture (e.g., Knutson et al. 2010).

Using KECK/HIRES data, Knutson et al. (2010) searched for a relation between stellar activity as manifested by chromospheric emission in the Ca II H and K line cores and the emission spectra of hot Jovians. Among their sample of planet host-stars,

⋆ Based on observations obtained with UVES at the ESO VLT Kueyen telescope (program ID 385.D-0426) and the *Chandra* X-ray Observatory (obs. ID 10989).

CoRoT-2a stands out as being the most active as measured by its $\log R'_{\mathrm{HK}}$ index. Ammler-von Eiff et al. (2009) reanalyzed the archival UVES data presented in Bouchy et al. (2008) (program 080.C-0661D) and determined precise estimates of CoRoT-2a's spectral properties such as effective temperature and iron abundance. In August 2009, Gillon et al. (2010) obtained and analyzed a new UVES spectrum (program 083.C-0174C). The authors provide a more detailed discussion of the Li absorption line and derive an age between 30 and 316 Ma for CoRoT-2a. Additionally, they find evidence for a slight eccentricity of 0.014 ± 0.008 for the planetary orbit, which they attribute to the youth of the system, if not caused by CoRoT-2a's potential stellar companion.

Guillot & Havel (2011) investigated the matter of CoRoT-2a's anomalously inflated planet on theoretical grounds by simultaneously modeling the planetary and stellar evolution including stellar activity. The authors' models favor two classes of solutions: either a young system with a star on the pre-main sequence (30−40 Ma) or a much older system (>100 Ma) with a main-sequence star. The authors discuss several effects that could have led to the anomalously large radius of CoRoT-2b. While they argue that the influence of starspots is minor, either the presence of additional infrared opacity sources in the planetary atmosphere that reduces the rate of heat loss during the planet's evolution or a recent interaction with a third body in the system that leaves the planet in an eccentric orbit could account for the observed radius anomaly.

In this work, we present a new UVES spectrum of CoRoT-2a and its visual companion, which we analyzed in detail to refine the spectroscopic parameters and chromospheric activity indicators. We especially aim at deriving several independent estimates of the age and the distance of the CoRoT-2 system. First, we present the results of our analysis of the high-resolution UVES spectrum of CoRoT-2a and our low-quality spectrum of its visual companion. Second, we present our analysis of the first X-ray observation of CoRoT-2a. We proceed by discussing the physical implications of our findings (Sect. 4) and, finally, we present our conclusions.

2. Optical spectroscopy with UVES

2.1. Observations

On June 7, 2010, we acquired 24 high-resolution spectra of CoRoT-2a with the UVES spectrograph (Dekker et al. 2000) mounted at the VLT Kueyen telescope (program ID 385.D-0426(A)). The instrument was set up in "Dichroic 2" mode with a slit width of 0.7″. We used the cross-disperser #4 with a central wavelength of 7600 Å providing a wavelength coverage of 3800−5000 Å on the blue arm and 5700−9500 Å on the red arm. Around 7600 Å a section of 100 Å is missing because of the gap between the two detectors. Because no overbinning was applied during CCD read-out, we reach a spectral resolving power of about 60 000.

In this set-up, we obtained 24 individual spectra with exposure times of 800 s each. The observations were scheduled to cover a full planetary transit of CoRoT-2b including a reasonable time span before and after the actual transit event. Owing to worsening seeing conditions, the last 13 observations were carried out using the image slicer to reduce light losses. Additionally, we used an archived UVES spectrum obtained on Oct. 13, 2007 in the framework of the program 080.C-0661(D) for comparison.

To reduce the UVES echelle data, we applied the UVES pipeline in version 4.7.8 with its associated standard recipes and the REDUCE package developed by Piskunov & Valenti (2002). Our analysis is based on the REDUCE spectra unless stated otherwise. Background-sky subtraction for exposures taken with the image slicer is difficult because there is hardly any sky area left on the detector that could be used to extract the background. Indeed, the UVES pipeline does currently not apply any such subtraction for exposures taken with the image slicer. The 24 individual UVES spectra were combined and yielded a high-resolution spectrum of CoRoT-2a with a signal-to-noise ratio (SNR) of about 200 at 6500 Å. Although sky emission-lines are present in the spectrum, they did not affect our analysis.

2.2. Analysis of optical data

The stellar spectrum conveys information about the physical conditions in the stellar atmosphere. The parameters of primary interest in our analysis were the effective temperature, elemental abundances, surface gravity, and microturbulence velocity. Unfortunately, those parameters cannot be determined independently from the observed stellar spectrum, but they are highly correlated. Several techniques are commonly used in spectroscopic analyses, and the results depend on the underlying assumptions and implementation. Systematic errors can originate in the data reduction process or in differences in the adopted atomic data. As a consequence, error bars based on purely statistical considerations usually underestimate the true uncertainty. Therefore, we applied a number of independent analyses to corroborate the validity of our parameter and error estimates. In the following analysis, we concentrate on the time-averaged UVES spectrum of CoRoT-2a. An analysis of the temporally resolved properties will be presented in another context.

2.3. Elemental abundances via excitation/ionization balance

In our high-resolution UVES spectrum of CoRoT-2a, we measured equivalent widths (EWs) of lines of neutral (Fe I) and ionized iron (Fe II) and several other metals (Na, Mg, Al, Si, Ca, Ti, V, Cr, Mn, Co, Ni, and Ba). Our selection of lines is based on the line lists provided by Sousa et al. (2008) and Bubar & King (2010), out of which we compiled a list of iron lines without severe blends with excitation potentials below 5 eV and EWs between 10 and 200 mÅ. Our resulting line list comprises 212 Fe I lines, 26 Fe II lines, and 162 lines of other metals.

To measure the EWs of a large number of spectral lines, Sousa et al. (2007) developed the ARES[1] code. This algorithm detects spectral lines by evaluating numerical derivatives of the spectrum. For the following analysis, we set up our own implementation of the ARES algorithm, extending it at several points, for example, by a low-pass Fourier filter to suppress noise effects and an estimation of the local continuum. Our tool runs semi-automatically, allowing the user to interactively improve the fit result by visual inspection where desired. The normalization of the spectrum is made manually by comparing the observed to a synthetic spectrum to identify regions of undisturbed continuum, which are then used as nodes for a linear (or cubic) spline fit.

The EWs thus obtained were used as input for the 2010 version of MOOG[2] (Sneden 1973) together with ATLAS plane-parallel model atmospheres[3] (Kurucz 1993). We used MOOG

[1] See http://www.astro.up.pt/~sousasag/ares/
[2] See http://www.as.utexas.edu/~chris/moog.html
[3] See http://kurucz.harvard.edu/grids.html

Table 1. Stellar parameters and iron abundance of CoRoT-2a determined from the analysis of Fe I and II lines, the Sousa et al. (2007) line-ratio technique, and SME line profile fitting.

Stellar parameters	$T_{\rm eff}$ [K]	$\log g$ (cgs)	ξ_t [km s^{-1}]	[Fe/H]	N(Fe I, Fe II)	Source
Excitation/ionization balance	5598 ± 34	4.47 ± 0.14	1.75 ± 0.04	0.04 ± 0.02	212, 26	this work (Sect. 2.3)
Excitation/ionization balance	5608 ± 37	4.71 ± 0.20	1.49 ± 0.06	0.07 ± 0.04	26, 9	Ammler-von Eiff et al. (2009)
Fe I and II lines	5625 ± 120	4.3 ± 0.2	0.0 ± 0.1			Bouchy et al. (2008)
Line ratio calibration	5513 ± 111					this work (Sect. 2.4)
SME global fit	5475 ± 44	4.62 ± 0.06	1.52	-0.06 ± 0.03		this work (Sect. 2.5)
Hα λ6563	5510^{+90}_{-70}					this work (Sect. 2.5)
Hα λ6563	5450 ± 120					Bouchy et al. (2008)
Ca I λ6122, λ6162, λ6439		4.49 ± 0.14				this work (Sect. 2.5)
Na D λ5890, λ5896		4.53 ± 0.18				this work (Sect. 2.5)

to derive the effective temperature by minimizing the correlation between iron abundance and excitation potential, whereas the microturbulence velocity was obtained by removing the correlation with reduced EW, i.e., the EW normalized by the central wavelength of the line. The surface gravity is derived by minimizing the difference between the resulting Fe I and Fe II abundances.

To account for possible errors in the atomic line parameters, the spectroscopic analysis proceeds differentially to the Sun. Therefore, we measured each EW in both a lunar UVES spectrum provided by the ESO Quality Control and Data Processing Group[4] and the stellar spectrum and subsequently subtracted the solar abundance from the resulting stellar abundance. We used the freely available PYSPEC[5] Python interface to MOOG by Bubar for our differential spectroscopic analysis (for details, see Bubar & King 2010). The abundances of the other metals were derived in the same way, but keeping the input stellar atmosphere model fixed.

We present our results in Table 1. The listed errors on effective temperature and microturbulent velocity are estimated by investigating the correlation of the iron abundance with excitation potential and reduced EW, respectively, as measured by Spearman's rank correlation coefficient. In particular, the parameters were varied until a 1σ correlation was found, and the associated values were then used as an estimator of the reasonable parameter range. The error on $\log g$ was propagated based on the errors of the remaining parameters as detailed in Bubar & King (2010). Our spectral parameters agree well with earlier results obtained by Bouchy et al. (2008) and Ammler-von Eiff et al. (2009) from the analysis of Fe I and II lines.

The inferred elemental abundances are summarized in Table 2. Neither for Ni nor for Ti I and II did we find any strong correlations of abundance with excitation potential or EW given the atmospheric model derived from the Fe I and II lines. This indicates that the stellar parameters were indeed correctly chosen. Within the errors the elemental abundances are compatible with the solar values. The overabundance of Ba II is a result of the lines being blended with Fe lines. We therefore redetermined the Ba II abundance via line synthesis and obtained a value of $+0.13 \pm 0.09$ dex, which better agrees with the remaining elemental abundances.

2.4. Effective temperature via line ratios

Comparing spectral lines with different temperature sensitivity with each other provides a valuable temperature diagnostic.

[4] See http://www.eso.org/observing/dfo/quality/

[5] See http://www.pas.rochester.edu/~ebubar/speclink.html

Table 2. Elemental abundances for CoRoT-2a relative to the Sun with the number of lines N(X) used for each element.

Elem.	[X/H]	N(X)	Elem.	[X/H]	N(X)
Mg I	-0.16 ± 0.13	4	Mn I	$+0.05 \pm 0.15$	5
Si I	-0.05 ± 0.11	17	Co I	-0.13 ± 0.10	4
Ca I	$+0.12 \pm 0.10$	14	Ni I	-0.10 ± 0.10	38
Ti I	$+0.05 \pm 0.14$	25	Na I	-0.03 ± 0.04	2
Ti II	-0.02 ± 0.15	13	Al I	$+0.01 \pm 0.10$	4
V I	$+0.05 \pm 0.10$	12	Ba II	$+0.25 \pm 0.05$	3
Cr I	$+0.03 \pm 0.27$	18	Ba II^{a}	$+0.13 \pm 0.09$	
Cr II	$+0.05 \pm 0.16$	3	Li I^{b}	$+1.55 \pm 0.38$	

Notes. $^{(a)}$ See discussion in Sect. 2.3. $^{(b)}$ See discussion in Sect. 2.6.

Particularly useful is comparing the EWs of spectral lines belonging to metallic species. A line-ratio technique based on such a comparison was proposed by Sousa et al. (2007), who also calibrated their method using 451 FGK dwarf stars (Sousa et al. 2010). The authors determine an empirical relation between effective temperature and the EW ratio for a set of 433 pairs of spectral lines and incorporated their results into the "Teff_LR Code" code, which is an extension to the ARES code; both are freely available.

We used the relations published in Sousa et al. (2007, 2010) and obtained a value of $T_{\rm eff} = 5513 \pm 111$ K for CoRoT-2a's effective temperature, using 322 metallic lines and 22 independent line ratios. Although somewhat lower, this value is consistent with previous estimates (cf. Table 1). As a cross-check, we determined the solar effective temperature using the same set of lines in the UVES solar spectrum and found the resulting value of 5784 ± 152 K to agree well with the literature (Cox 2000, p. 341).

2.5. Synthetic spectra fitting via SME

As an alternative to the modeling of line EWs, the stellar parameters can also be obtained by directly fitting the profile of spectral lines using synthetic spectra. This approach is implemented in the "Spectroscopy Made Easy" (SME) package (version 2.1; Valenti & Piskunov 1996). This interpolates on a Kurucz grid of stellar atmospheres and employs a VALD[6] (Piskunov et al. 1995) line list to compute a synthesized spectrum for each set of stellar parameters. The observed spectrum is fitted by minimizing the residuals via a non-linear least-squares algorithm.

We used SME to determine the stellar parameters first in a global fit and second by fitting individual lines sensitive to $T_{\rm eff}$ and $\log g$. Currently, it is not feasible to compute a reliable error

[6] See http://www.astro.uu.se/~vald/php/vald.php

estimate for a global fit due to the large computational effort of calculating synthetic spectra. From the analysis of a set of 1040 FGK stars, however, Valenti & Fischer (2005) derived typical errors of 44 K in $T_{\rm eff}$, 0.06 dex in $\log g$, and 0.03 dex in metallicity, which we adopt below. For the analysis of single line profiles, we usually fixed all parameters at their best-fit values and obtained the error by computing the 90% confidence interval ($\Delta\chi^2 = 2.71$).

An approximation of the effective temperature can be obtained by investigating the Hα line profile. The wings of the prominent Hα line at a nominal wavelength of 6563 Å are sensitive to a wide range of effective temperatures of G- and F-type stars (e.g. Fuhrmann 2004), while remaining reasonably unaffected by the surface gravity, $\log g$, and the metallicity.

However, active late-type stars are known to show strong contributions of chromospheric emission in the Balmer lines, which can even extend into the wings of the line profiles (e.g., Montes et al. 1997). This can interfere with the determination of the effective temperature. We independently analyzed the line wings of Hα and Hβ. Consistent results for the temperatures deduced from both Balmer lines indicate that the wings of Hα are not strongly affected by chromospheric activity (Fuhrmann 2004; König et al. 2005).

A visual inspection of the symmetry of the Hα line profile suggested that the UVES pipeline, in this respect, provided a superior result, so that we rely on the pipeline spectra during this analysis. We note, however, that in any case a manual rectification of the spectrum is necessary. Hence, this method is prone to considerable uncertainties. We used SME to fit synthetic spectra to the observed Hα and Hβ line profiles excluding the line cores and found an effective temperature $T_{\rm eff}$ of 5510^{+90}_{-70} K and 5520^{+80}_{-90} K, respectively. This is consistent with the result of 5450 ± 120 K derived from the analysis of the Hα line observed with HARPS (Bouchy et al. 2008). The good agreement between the Balmer line estimates indicates that the chromospheric contribution remains small.

Several pressure-broadened spectral lines can be used to determine the surface gravity of late-type stars. Examples of these lines are the Mg ɪb triplet (Fuhrmann 1998), the Na ɪ D doublet, and the Ca ɪ lines at 6122, 6162, and 6439 Å (e.g., Bruntt et al. 2010). Because of the gap between the two detectors, the spectrum does not contain any Mg ɪb lines. We therefore concentrated on the Na and Ca lines. With SME, we iteratively fitted synthetic spectra to the three Ca ɪ lines and the Na D line, leaving only $\log g$ as a free parameter. The resulting value from the Ca ɪ lines (4.49 ± 0.14) was found to be consistent with the value derived from Na D (4.53 ± 0.18).

2.6. The age of CoRoT-2a as determined by Li ɪ

The abundance of lithium is a valuable indicator of the stellar age. The element is depleted by lithium burning primarily during the early phases of stellar evolution, when the existence of deep convection zones allows for the interchange of material between the stellar interior and the surface (e.g., Pinsonneault 1994).

CoRoT-2a shows a strong Li line at ≈6708 Å, for which we determined an EW of 139 ± 1 mÅ. We used SME to fit synthetic spectra with all remaining stellar parameters kept fixed and derived an abundance of $A_{\rm Li} = +2.6 \pm 0.3$. This value confirms the result of Gillon et al. (2010), who found $A_{\rm Li} = +2.8$. According to Sestito & Randich (2005), this Li content is typically found in G-type stars of $T_{\rm eff} = 5600$ K at an age between 100 and 250 Ma.

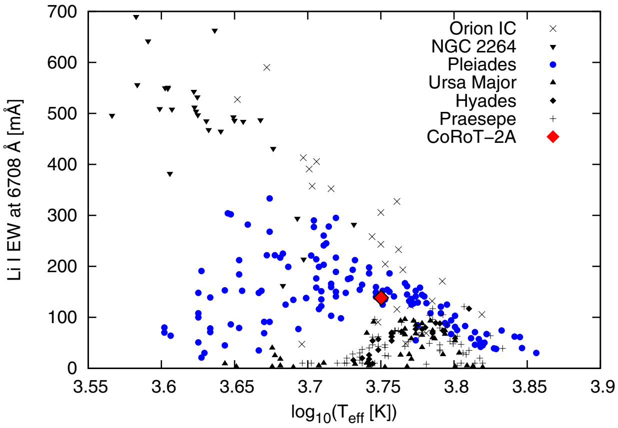

Fig. 1. Li ɪ EW vs. effective temperature for CoRoT-2a and a sample of open stellar clusters with different ages.

In Fig. 1 we show effective temperature versus Li ɪ line EW for the open stellar clusters Orion IC (10 Ma), NGC 2264 (10 Ma), Pleiades (100 Ma), Ursa Major (300 Ma), Hyades (660 Ma), and Praesepe (660 Ma) (King 1993; Soderblom et al. 1990, 1993a,b,c, 1999), additionally, the location of CoRoT-2a is marked in the diagram. The clusters are of different age, so that putting CoRoT-2a in the context of the cluster properties provides an indication of its age. The Li ɪ EW of CoRoT-2a is best compatible with those in the Pleiades, indicating an age of about 100 Ma. This finding is consistent with the numbers derived by Guillot & Havel (2011) from evolutionary modeling and also the age estimates given by Gillon et al. (2010), who derive an age between 30 and 316 Ma.

2.7. Activity indicators

Active stars are known to show strong emission in the Ca ɪɪ H and K line cores at 3934.8 and 3969.7 Å (see Linsky 1980, for a profound discussion). This is also true for CoRoT-2a; we show its Ca ɪɪ H and K lines in Fig. 2.

In late-type stars the width, W_0, of the emission cores seen in the Ca ɪɪ H and K lines is mainly sensitive to the value of $\log g$, and, hence, to the mass and radius of the star, but insensitive to the effective temperature and metallicity. If calibrated appropriately, the width can be used as a rough estimator of the absolute luminosity of a star (Wilson & Bappu 1957). We used the recent calibration of Pace et al. (2003) together with CoRoT-2a's apparent magnitude corrected for interstellar extinction (see Sect. 4.3) to obtain a distance estimate for the CoRoT-2 system. Pace et al. find no significant effect of rotational and instrumental broadening within their sample, which comprises stars with $v \sin i < 14$ km s^{-1}. Neglecting broadening effects, we obtained a distance estimate of 190^{-50}_{+60} pc. When both broadening mechanisms were taken into account by a quadratic correction to W_0 as described by Pace et al., the distance estimate reduced to 140^{+50}_{-40} pc, which is lower but still compatible, given the errors.

The Wilson chromospheric flux index ($S_{\rm MW}$; Vaughan et al. 1978; Baliunas et al. 1998) is a popular measure of chromospheric activity. To estimate $S_{\rm MW}$ from our spectra, we used the calibration procedure for UVES spectra described by Melo et al. (2006). These authors defined a proper index $S_{\rm US}$ and

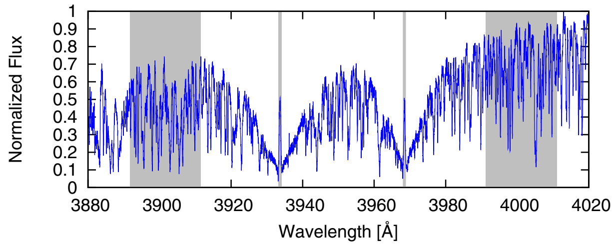

Fig. 2. Region of CoRoT-2a's spectrum containing the Ca II H and K lines. Gray shades indicate the bands defined by Melo et al. (2006) for the definition of $\log R'_{\rm HK}$. See text for details.

determined the following relation between their index and the Wilson index:

$$S_{\rm US} = 0.06111 \times S_{\rm MW} - 0.00341$$

(see Eq. (1) in Melo et al. 2006). Inverting this relation, we obtained an $S_{\rm MW}$ index of 0.479. We proceeded by correcting our $S_{\rm MW}$ index for the color dependence (Rutten 1984) and subtracted the expected photospheric contribution to the flux in the line cores (Noyes et al. 1984). Using a value of 0.854 for the $B-V$ color of CoRoT-2a from the SIMBAD database[7], we obtained an emission ratio of $\log R'_{\rm HK} = -4.458 \pm 0.051$, which agrees well with the results of Gillon et al. (2010) (−4.471 ± 0.0629) and Knutson et al. (2010) (−4.331).

The central part of the Ca II H and K emission core does not show the double-horned structure usually observed in the line cores of solar-like stars. We found no sign of self-reversal in the central part of the line core. According to Ayres (1979), strong chromospheric heating through stellar activity leads to a decrease of the wavelength separation between the two K_2 peaks of the emission core, so that the central K_3 dip is easily obliterated by instrumental, macroscopic, and microscopic broadening effects. The lack of a detectable self-reversal is, therefore, an indicator of strong chromospheric heating itself. Because chromospheric heating causes an increase in the wavelength separation of the two K_1 minima that approximately counterbalances the mutual approach of the K_2 peaks, the Wilson-Bappu width, W_0, remains basically insensitive to stellar activity.

Chromospheric activity can also be measured in the Ca II infrared triplet (IRT) at 8498, 8542, and 8662 Å (see e.g., Andretta et al. 2005; Busà et al. 2007). To correctly assess the chromospheric contribution to the line profile, the line forming process within the photosphere must be accurately modeled. Andretta et al. (2005) proposed the activity indicator $R_{\rm IRT}$ defined as the difference between the central line depths (or central depressions) of the observed spectrum and a rotationally-broadened NLTE model. We calculated the central depression, $R_{\rm IRT}$, and $\Delta W_{\rm IRT}$, i.e., the EW of the residual line profile and the corresponding error estimates following the approach detailed in Busà et al. (2007). In our calculations, we used LTE models synthesized via SME, which, according to Andretta et al., suffice to approximate the photospheric spectrum for main-sequence stars of solar metallicity. The parameters thus obtained are summarized in Table 3. The CoRoT-2a Ca IRT along with our synthetic templates are shown in Fig. 3, which also indicates the residuals. Busà et al. found a relationship between the $\log R'_{\rm HK}$ activity index and $R_{\rm IRT}$, however, with a large scatter. Given our value of $\log R'_{\rm HK} = 4.46$, the relation predicts a value of 0.25 for $R_{\rm IRT}$, which reasonably agrees with our results.

[7] See http://simbad.u-strasbg.fr/simbad/

Table 3. Central depression (CD), $R_{\rm IRT}$ and residual equivalent width $\Delta W_{\rm IRT}$ for the lines of the Ca II infrared triplet in CoRoT-2a.

λ [Å]	$CD_{\rm obs}$	$R_{\rm IRT}$	$\Delta W_{\rm IRT}$ [mÅ]
8498	0.266 ± 0.009	0.342 ± 0.009	237.6 ± 1.6
8542	0.361 ± 0.006	0.297 ± 0.006	63.1 ± 0.6
8662	0.413 ± 0.014	0.256 ± 0.014	171.4 ± 2.1

2.8. Interstellar absorption features

Analyzing the emission line cores of the Ca II H and K complex, we found narrow K_4 (see e.g., Reimers 1977, for designation) and H_4 absorption features close to both central chromospheric emission peaks (Fig. 4). We therefore attribute the features to Ca II absorption and determine a barycentric velocity of −15 km s^{-1}, corresponding to a relative velocity of about +40 km s^{-1} with respect to CoRoT-2a.

Separately considering our 24 UVES spectra observed within 6 h and the archived UVES spectrum taken about three years earlier in 2007, we found no intrinsic variability of this feature. The EW of the Ca II K_4 absorption feature is 65 mÅ, slightly higher than the corresponding EW of the Ca II H_4 feature with 53 mÅ. These blue shifted absorption features of ionized material may be caused by wind absorption as observed in giant stars (e.g., Reimers 1977) or, alternatively, by the interstellar medium.

While Ca H_4 and K_4 features caused by wind absorption are observed in giant stars rather than dwarfs such as CoRoT-2a, the narrowness of the features is surprising if they are attributed to interstellar absorption. Often, multiple interstellar clouds are found in the line of sight, giving rise to a more diffuse absorption feature. Indeed, the width of the Ca H_4 and K_4 features is comparable to that of telluric lines in our spectrum. However, considering the temporal stability, we argue in favor of interstellar absorption as the origin of the Ca H_4 and K_4 features.

The Sun is situated within a region pervaded by hot, ionized plasma of low density known as the Local Cavity that reaches a radius of about 100 pc (e.g., Cox & Reynolds 1987; Sfeir et al. 1999). This cavity contains many diffuse clouds with a complex velocity structure, which typically give rise to Ca II absorption features with EWs of a few mÅ (Lallement & Bertin 1992). The density distribution of Ca II is fairly uniform in the interstellar medium beyond the Local Cavity, so that the EW of interstellar Ca II H and K absorption can be used as a distance indicator for sufficiently distant objects (Megier et al. 2005, 2009; Welsh et al. 2010). Using Eqs. (1) and (2) in Megier et al. (2005), we translated the EWs of both Ca II absorption features into distance estimates of 274 pc for the Ca II K_4 feature and 256 pc for the Ca II H_4 feature.

We note that our spectrum of CoRoT-2a also shows two strong, nearly saturated Na I absorption lines with the same radial velocity shift within the blue wing of the Na I D doublet. These broad absorption features have EWs of 270 mÅ (D_2) and 230 mÅ (D_1), which is again compatible with interstellar absorption and a distance of 340 ± 180 pc and 320 ± 140 pc, respectively (Welsh et al. 2010). Additional interstellar absorption lines of K I at 7698.974 Å or molecules such as CH could not be detected.

In summary, we estimate a distance of 270 ± 120 pc for CoRoT-2a, based on interstellar absorption; the error was estimated from the standard deviation of the distances of the stars with K_4 EWs in a ±5 mÅ band around our measured EW (cf., Fig. 5).

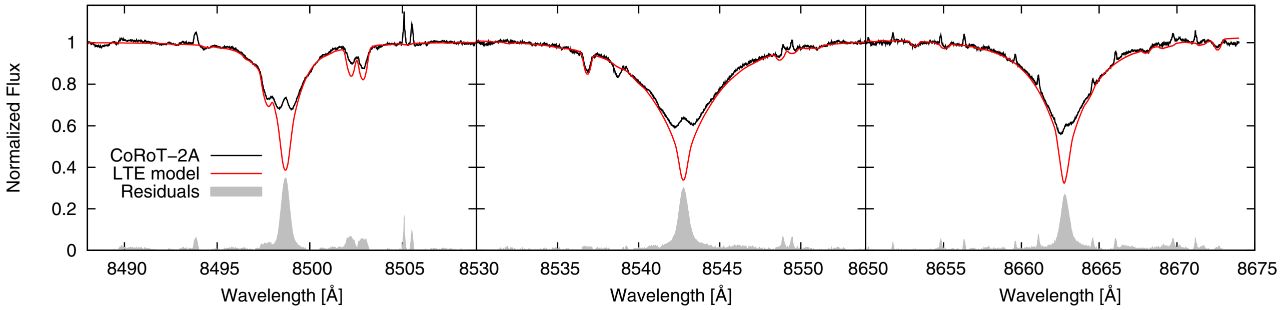

Fig. 3. Ca II infrared triplet in the spectrum of CoRoT-2a (black), which is used as activity diagnostic. The activity indicators are calculated relative to an LTE synthetic spectrum (red) based on the residuals (gray) as outlined in Busà et al. (2007). The small emission features result from sky emission (cf., Sect. 2.1).

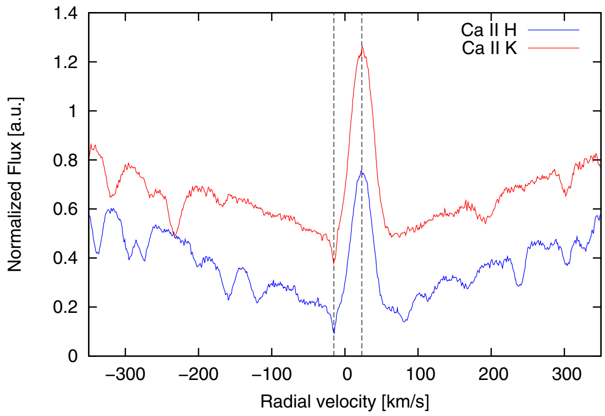

Fig. 4. Emission line cores of the Ca II H and K lines clearly showing the H_4 and K_4 absorption features. The spectrum of CoRoT-2a is shifted in radial velocity by 23.2 km s^{-1}, while the absorption features show a barycentric velocity shift of -15 km s^{-1}.

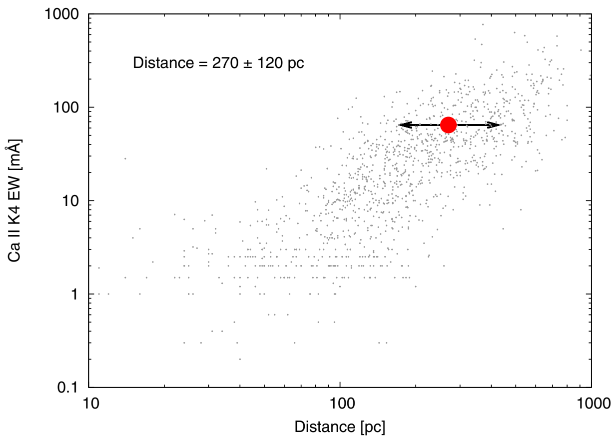

Fig. 5. Equivalent width of the interstellar Ca II K_4 absorption line versus distance for stars within 800 pc (catalog data compiled by Welsh et al. 2010). The measured Ca II K_4 absorption of CoRoT-2a is consistent with a distance of roughly 300 pc.

2.9. Evidence for a gravitationally bound companion

CoRoT-2a has a close neighbor, 2MASS J19270636+0122577, about 4″ in southeast direction. Alonso et al. (2008) found that the color of this visual companion is consistent with a late-K or early-M type star located at the same distance as CoRoT-2a. During five of our 24 UVES observations this nearby neighbor was placed inside the slit along with CoRoT-2a, which we used to obtain a low SNR spectrum of the companion. The separation of the two objects allowed us to separately extract the spectra using the UVES pipeline.

Because the companion is ≈3.5 mag fainter than CoRoT-2a in the visual band, the resulting spectrum has an SNR of no more than 10−20 depending on wavelength. It is dominated by absorption lines from neutral and singly-ionized metals. In particular, we find strong absorption in Ca I and Mg II, whereas the Ca II lines are comparably weak. Furthermore, we find a relatively weak Hα line and distinct edges caused by titanium oxide (TiO) absorption.

The TiO bands are a valuable indicator of stellar effective temperature if the metallicity is known, while they are less sensitive to surface gravity (Milone & Barbuy 1994). To obtain an estimate of the effective temperature, we compared the coadded companion spectrum to synthetic spectra calculated with SPECTRUM[8] (Gray & Corbally 1994) using line lists containing the TiO and ZrO lines compiled by Plez (1998)[9].

Assuming solar metallicity, we set up a Markov-Chain Monte-Carlo (MCMC) framework to find an estimate of the effective temperature and the associated error. We used uniform priors on the stellar parameters and allowed for an additional normalization constant accounting for inadequacies during blaze correction and continuum normalization. We focused on the strongest TiO band with its bandhead at 7054 Å and analyzed the three absorption edges individually. The resulting three 95% credibility intervals for $T_{\rm eff}$ consistently yield an effective temperature between 3900 and 4100 K (see Fig. 6). The surface gravity was found to be $\log g = 4.9 \pm 0.1$, which is very close to our imposed upper bound of $\log g = 5$ and does not seem to be well constrained.

We tried to use SME to fit synthetic spectra to several spectral lines known to be sensitive to the stellar parameters. Our efforts were, however, strongly hampered by the low SNR of the spectral data owing to the faintness of the companion. From the analysis of the Na I doublet at 5890 Å, the Ca I lines at 6122, 6162, and 6439 Å, and a set of 137 single Fe lines, we found the stellar spectrum to be best described by effective temperatures

[8] See http://www1.appstate.edu/dept/physics/spectrum

[9] See http://www.graal.univ-montp2.fr/hosted/plez

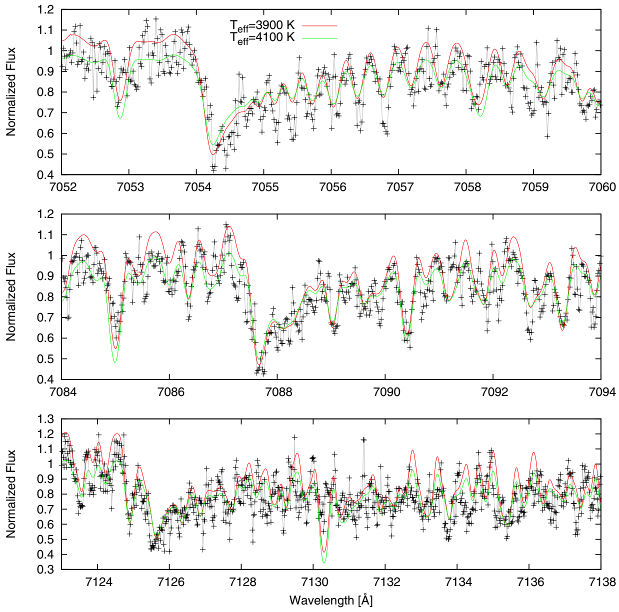

Fig. 6. Part of the companion spectrum showing the temperature-sensitive TiO band at 7050−7200 Å. The red/green lines are synthetic spectra for $T_{\rm eff} = 3900$ K and 4100 K, respectively, computed for solar metallicity and $\log g = 4.9$.

around 4000 K and a surface gravity between 4.6 and 4.9. Unfortunately, the quality of the spectrum made an analysis of the Hα line impossible. The set of Fe I lines was also used to quantify the effect of rotational line broadening. Neglecting additional line broadening effects, we obtained an upper limit of 10 km s^{-1} on $\upsilon \sin i$ at a confidence level of 90%.

These findings are compatible with the companion being a K9 star (Cox 2000, p. 388, Table 15.7). Our results are in line with those of Alonso et al. (2008) and Gillon et al. (2010), who found the photometric magnitudes measured in optical (Exodat), near-infrared (2MASS), and infrared (*Spitzer*) filter bands to be consistent with a late-K or early-M type companion star.

To find the radial velocity of the visual companion, we cross-correlated our five companion spectra with a template spectrum corresponding to our best-fit stellar parameters. The radial velocity was estimated independently in our five companion spectra, and corrected for the wavelength drift visible in the telluric lines. The resulting average radial velocity amounts to 23.9 ± 0.4 km s^{-1}, a value close to CoRoT-2a's radial velocity of 23.245 ± 0.010 km s^{-1}, which we determined accordingly. We note that it is also independent of the details of the chosen spectral model. Given the apparent distance in the sky of 4″ and a distance of about 270 pc the projected distance between CoRoT-2a and the companion amounts to about 1100 AU. Because CoRoT-2a is basically solar-like in mass, Kepler's third law yields a lower bound for the orbital period of 40 000 a, which gives an orbital velocity of up to 0.9 km s^{-1}. Thus, the radial velocity found for the visual companion of CoRoT-2a is compatible with the hypothesis of a gravitationally bound companion.

To check for relative sky motions of CoRoT-2a and 2MASS J19270636+0122577, we inspected the photographic data available from the Digitized Sky Survey. We checked the digitized plates of the Palomar Observatory Sky Surveys from 1951, 1983, and 1991 and the HST Guide Star Catalogue from 1980, but found no indications for a relative transversal motion. This finding corroborates the hypothesis that 2MASS J19270636+0122577 and CoRoT-2a are gravitationally bound and form a wide binary system.

The parameters derived for the companion are summarized in Table 4.

Table 4. Stellar parameters of 2MASS J19270636+0122577.

Parameter	Value	Lines
$T_{\rm eff}$ [K]	[3900, 4100] (95% cred.)	TiO 7050−7200 Å
$\upsilon \sin i$ [km s^{-1}]	<10 (90% CL)	137 Fe I lines
RV [km s^{-1}]	23.9 ± 0.4	

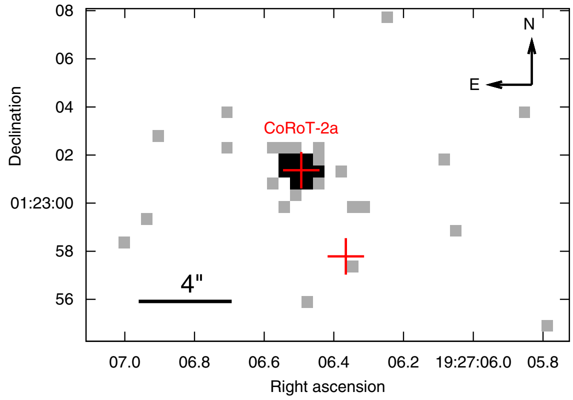

Fig. 7. X-ray image (0.5″/bin) of the surrounding of CoRoT-2a for energies above 0.3 keV. The nominal 2MASS positions of CoRoT-2a and 2MASS J19270636+0122577 are marked with red crosses.

3. Analysis of the *Chandra* X-ray data

3.1. Observations

CoRoT-2a was observed by *Chandra* using the ACIS-S detector on June 24, 2010 for about 15 ks (Obs.-ID 10989). In the reduction and analysis process, we used the standard software package CIAO in version 4.2. To obtain the best possible timing, the tool `axbary` was used to apply a barycentric correction to the photon arrival times.

3.2. Detection and spectral analysis

In a first step, we screened the X-ray image for photons in the 0.3−4 keV energy band. This step reduces the background contamination and focuses our analysis on the energy band, in which stellar coronal emission is expected to dominate. We show parts of the resulting X-ray image in Fig. 7.

In a second step, we counted all photons within a 2″ radius circular region centered on the nominal position of CoRoT-2a. In this region, we found 87 photons with an expected background contribution of ≈3 photons, deduced from nearby source-free regions.

Finally, we carried out a spectral analysis of the source photons. Using XSPEC v12.5 Arnaud (1996), we fitted the ACIS spectrum with an absorbed, thermal APEC (e.g., Smith et al. 2001) model. Because the abundances are not well constrained by the fit, we fixed them at their solar values for the rest of the analysis, which is in accordance with our optical estimates (cf. Sect. 2.3). For the depth of the absorbing column, the fit provides a value of $\approx 10^{21}$ cm^{-2}, which is well compatible

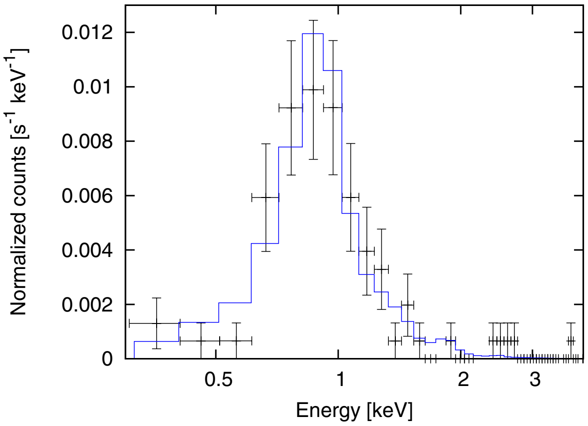

Fig. 8. ACIS-S spectrum of CoRoT-2a with applied spectral model.

Table 5. Spectral-fit results for CoRoT-2a derived from *Chandra* ACIS-S data.

Parameter	Value (90% conf.)
N_H [10^{22} cm^{-2}]	<0.2
T [keV]	0.74 (0.57–0.83)
T [10^6 K]	8.6 (6.6–9.6)
f_X [10^{-14} erg cm^{-2} s^{-1}]	2.1 (0.8–2.9)
L_X (at 270 pc) [10^{29} erg s^{-1}]	1.9 (0.7–2.5)[a]

Notes. [(a)] An error of ±120 pc on the distance estimate translates into a larger conf. interval for L_X of $(0.2–5.2) \times 10^{29}$ erg s^{-1}.

with a canonical density of 1 particle per cm^3 for the interstellar medium and a distance of ≈270 pc (see Sect. 2.8) for CoRoT-2a.

Figure 8 shows the X-ray spectrum and our best-fit model; the fit results are summarized in Table 5. From our best-fit model, we obtain an X-ray luminosity of $L_X = 1.9 \times 10^{29}$ erg s^{-1} in the 0.3–4 keV band, corresponding to an activity level of $\log_{10} L_X/L_{bol} \approx -4.2$, which indicates that CoRoT-2a is an active star also by X-ray standards.

3.3. X-ray light curve and transit

To investigate the X-ray variability of CoRoT-2a, we constructed background-subtracted light curves with various binnings. A barycentric time-correction was applied to all light curves to obtain time stamps, which can be easily reconciled with planetary ephemerides given in the literature. Figure 9 presents the light curve of CoRoT-2a, which shows no indications of strong short-term variability like flares, and, therefore, we argue in favor of quiescent emission.

The ephemerides of CoRoT-2b were derived by Alonso et al. (2008) using the CoRoT data. The transit duration is 8208 s, during which the relative flux deficit in the optical reaches 3%. Our *Chandra* observation completely covers one planetary transit (epoch 651 with respect to the ephemerides from Alonso et al. 2008). The ingress begins 6538 s after the start of the observation and the egress is finished shortly before the observation ends (cf., Fig. 9).

Our analysis showed that the source count rate, if anything, increased by 17% during the eclipse. Similarly, the hardness ratio $HR = (H-S)/(H+S)$ with $S = 0.3-1$ keV and $H = 1-4$ keV (lower panel in Fig. 9) remains unaffected. On the one hand,

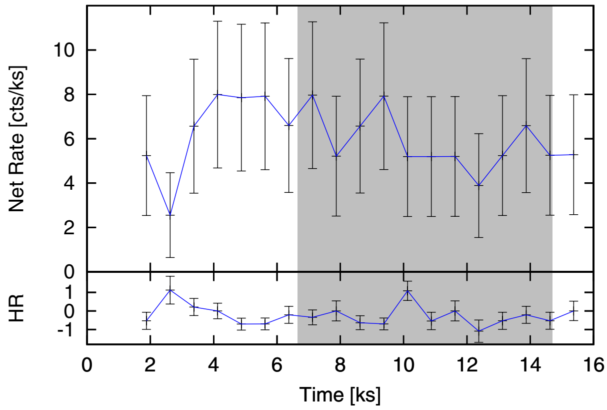

Fig. 9. Light curve of CoRoT-2a in the 0.3–4 keV band and hardness ratio $(H-S)/(H+S)$ for 0.3–1 and 1–4 keV bands (750 s binning). The shaded area corresponds to the transit in visual wavelengths.

given 82 source counts in 15 ks, detecting a 3% drop in brightness as observed in the optical seems to be out of reach in X-rays. On the other hand, the sources of X-ray emission are believed to be distributed much more inhomogeneously across the stellar surface than those of optical light. We conclude that either the planet did not eclipse a strong concentration of X-ray emitting material in this particular case, the emission is distributed homogeneously, or concentrated at higher latitudes avoided by the planetary disk.

3.4. The companion in X-rays

To check whether CoRoT-2a's potentially physical companion, 2MASS J19270636+0122577, is an X-ray source, we collected the photons within a circle of 1″ radius centered on the star's 2MASS position. According to our modeling, this region contains 93% of the *Chandra* point spread function (PSF) at 1 keV. A single photon with an energy of 1.1 keV was detected in this region. Because 99% of CoRoT-2a's PSF are confined to a distance of 4″ and less from CoRoT-2a, the detected photon is unlikely to stem from that source. From nearby source-free regions, we estimated the rate of background-counts with energies of 1.1±0.1 keV, where the 0.1 keV range accounts for *Chandra*'s energy resolution, to be 2×10^{-4} cts s^{-1} within the encircled region centered on the companion.

The detected photon may, consequently, be associated with an X-ray source at the companion's position. To derive an upper limit on the X-ray flux of the companion, we determined the count rate yielding one or less detected photons with a probability of 95%. Consulting Poisson statistics, the limiting count rate amounts to 0.36 cts in 15 ks or 2.4×10^{-5} cts s^{-1}. Assuming that the source has a 1 keV thermal spectrum, a distance of 270 pc (cf. Sect. 2.8), and neglecting absorption, we used WebPIMMS[10] to convert the count rate into an upper limit of $L_X < 9 \times 10^{26}$ erg s^{-1} for the companion's X-ray luminosity.

4. Discussion

We presented new X-ray and optical data of the active planet host-star CoRoT-2a. Below, we discuss the impact of our findings on our understanding of the CoRoT-2 system.

[10] http://heasarc.gsfc.nasa.gov/Tools/w3pimms.html

4.1. CoRoT-2a's atmosphere and activity

We studied the photosphere of CoRoT-2a applying different techniques of spectroscopic analysis to determine the stellar effective temperature, surface gravity, metallicity, and microturbulence velocity. First, we measured the EW of 238 Fe I and II lines and determined the entire set of parameters by imposing excitation and ionization balance. Second, we redetermined the parameters by directly fitting several sensitive spectral lines and found consistent results, which are, moreover, in line with previously published values (Ammler-von Eiff et al. 2009; Bouchy et al. 2008). With an effective temperature of 5598 ± 34 K and a surface gravity of $\log g = 4.47 \pm 0,14$, CoRoT-2a is a star of spectral type G6–G7 (Cox 2000, p. 151, Table 7.5) with slightly increased metallicity compared to the Sun. We compared the stellar parameters to those predicted by theoretical isochrone calculations for pre-main and main-sequence stars (Siess et al. 2000). Assuming that CoRoT-2a is close to the zero-age main sequence, these models favor a spectral type of G7 given the observed values of effective temperature and metallicity.

The fact that CoRoT-2a is a highly active star became first obvious in the photometry observed by the CoRoT observatory. The light curve shows pronounced rotational variability caused by active regions that cover a substantial fraction of the stellar photosphere (e.g., Wolter et al. 2009; Czesla et al. 2009; Huber et al. 2009, 2010). This high level of activity, mainly diagnosed by photospheric spots, is expected to be also detectable in chromospheric lines excited by enhanced chromospheric heating.

Indeed, CoRoT-2a shows strong chromospheric emission-line cores in its Ca II H and K lines as well as in the Ca IRT lines. We quantified the strength of the emission by determining the Wilson S-index and a $\log R'_{\rm HK}$ value of 4.458 ± 0.051. Our results agree well with those reported by Knutson et al. (2010) and place CoRoT-2a among the most active known planet host-stars. Furthermore, we studied the Ca IRT and derived a value of 0.298 ± 0.006 for the $R_{\rm IRT}$ index, which again demonstrates that CoRoT-2a is a highly active star.

The presence of starspots and strong chromospheric heating suggests that coronal heating is substantial as well. Indeed, our 15 ks *Chandra* observation yields a clear detection of coronal X-ray emission characterized by a thermal spectrum with a temperature of 1 keV. Combining CoRoT-2a's X-ray luminosity of 1.9×10^{29} erg s^{-1} with its spectral type of G7, we derived an activity level of $\log L_{\rm X}/L_{\rm bol} \approx -4.2$, showing that CoRoT-2a is a very active star also by X-ray standards. Although optical studies (Lanza et al. 2009; Huber et al. 2010) suggested a large inhomogeneity in the distribution of active regions, which is very likely also true for the distribution of X-ray emission across the stellar disk, an X-ray transit could neither be detected in the X-ray count rate nor in the hardness ratio. This indicates that either no prominent source of X-ray emission was occulted during this particular transit or that the emission is distributed too homogeneously to cause an X-ray transit detectable with *Chandra*. In any case, we emphasize that our *Chandra* snapshot covers no more than 4% of CoRoT-2a's rotation period and a virtually negligible fraction of the optically observed "beating pattern" (e.g., Alonso et al. 2008) with a period of ≈50 d, so that it remains insufficient to obtain a representative picture of CoRoT-2a's corona.

4.2. The age of CoRoT-2

One of the key quantities needed to understand the evolution not only of the CoRoT-2 system but of all planetary systems is their age. Based on our analysis, we applied several techniques to estimate the age of CoRoT-2a.

From the EW of the lithium line at 6708 Å in the spectrum of CoRoT-2a, we inferred an age comparable with that of the Pleiades, i.e., ≈100 Ma. Furthermore, we derived a Li abundance of $A_{\rm Li} = +2.6$ dex, which suggests an age between 100 and 250 Ma. Applying the relation provided by Donahue (1998, Eq. (1)), we used the strength of the Ca II H and K emission-line cores measured by the $\log R'_{\rm HK}$ index to estimate a "chromospheric age" of 670^{+200}_{-280} Ma for CoRoT-2a. The coronal activity provides another age estimate. Using the relation between X-ray luminosity and age for late-F to early-M dwarfs presented in Sanz-Forcada et al. (2010), we calculated an age of 230^{+200}_{-40} Ma. An additional estimate can be obtained from gyrochronology. Using the relation presented by Barnes (2007), we determined an age of 76 ± 7 Ma for CoRoT-2a. However, Barnes note that gyrochronology tends to underestimate the stellar age if $(B-V) > 0.6$, which is true for CoRoT-2a, owing to the sparseness of the open cluster sample used for calibration in case of blue stars.

Guillot & Havel (2011) modeled the evolution of the star, CoRoT-2a, and its planet simultaneously and found two classes of solutions reproducing the observed properties of the CoRoT-2 system: first, a solution in which CoRoT-2a is a very young star with an age of 30 to 40 Ma and second, a solution with a more evolved main-sequence host-star with an age of 130 to 500 Ma. None of the above age indicators, not even the gyrochronological age estimate, favors the solution with a very young host-star, rendering this class of evolutionary scenarios found by Guillot & Havel (2011) unlikely.

In summary, we conclude that combining our outcomes with published results both observational and theoretical favors an age between 100 and 300 Ma for CoRoT-2a. This suggests that CoRoT-2a is a young main-sequence star that has already left the zero-age main sequence, which for a G7 star of solar mass is situated at an age of 30 Ma (Siess et al. 2000).

4.3. Distance to CoRoT-2a

Photometric colors are often used for a rough spectral classification. The magnitudes provided by SIMBAD yield a $B-V$ color index of 0.854 mag for CoRoT-2a. Comparing this value with the color index expected for a G7 star of age 200 Ma with slightly increased metallicity ($Z = 0.01$) (Siess et al. 2000), we calculated a color excess of $E(B-V) = 0.15$ mag. Thus, CoRoT-2a appears redder than expected; we attribute this to interstellar extinction.

Combining the $B-V$ color excess with the relation given by Bohlin et al. (1978)

$$\langle N(\text{H I} + \text{H II})/E(B-V)\rangle = 5.8 \times 10^{21}\ \text{cm}^{-2}\ \text{mag}^{-1},$$

we obtain a column density of 9×10^{20} cm^{-2}, which is consistent with the upper limit of 2×10^{21} cm^{-2} derived from our X-ray observations. Converting the EWs of the interstellar Na D absorption lines into a column density of 8×10^{12} cm^{-2} via the line-ratio method (Strömgren 1948), we obtained another consistent estimate of $\approx 10^{21}$ cm^{-2} for the hydrogen column density (Ferlet et al. 1985). Assuming a density of one particle per cm^3 for the interstellar medium, the hydrogen column density inferred from the color excess directly translates into a distance estimate of 290 pc, which is consistent with our previous estimate of 270 pc.

According to our spectroscopic analysis, CoRoT-2a can be classified as a G7-type dwarf and, according to the evolutionary model, should have an absolute visual brightness of 5.1 mag. Assuming a value of $R = 3.1$ (Schultz & Wiemer 1975) for the ratio of total visual extinction, A_V, and $E(B-V)$, we derive $A_V = 0.48$ mag for CoRoT-2a. Combining this with the apparent visual brightness of 12.57 mag, we derived an extinction-corrected spectroscopic parallax of 250 pc.

In Sect. 2.7 we estimated the distance to the CoRoT-2 system from the Wilson-Bappu width of the Ca II H and K emission line cores and obtained 140^{+50}_{-40} to 190^{+60}_{-50} pc depending on the details of the calibration. We further determined the distance from the presence of interstellar Ca and Na absorption features in the spectrum and obtained 270 ± 120 pc based on the interstellar absorption column (Sect. 2.8). In summary, we argue in favor of a distance of ≈270 pc as the most likely value.

4.4. X-rays eroding CoRoT-2b

Because CoRoT-2b orbits its host star at a distance of only 0.03 AU, it is immersed in an enormous high-energy radiation field. According to CoRoT-2a's X-ray luminosity, the X-ray flux at the distance of CoRoT-2b's orbit amounts to 8.5×10^4 erg cm^{-2} s^{-1}, which is five orders of magnitude larger than the solar X-ray flux received by Earth. This amount of ionizing radiation can have a significant influence on the structure and evolution of the planetary atmosphere. Schneider et al. (1998) found that the extent of the atmospheres of hot Jovian exoplanets can exceed the Roche lobe, leading to evaporation of planetary material by an interaction with the stellar wind. Indeed, extended atmospheres of extrasolar planets were found for HD 209458b (Vidal-Madjar et al. 2003; Linsky et al. 2010) and HD 189733b (Lecavelier Des Etangs et al. 2010).

Sanz-Forcada et al. (2010) analyzed a sample of planetary systems. The authors come to the conclusion that erosion triggered by stellar high-energy illumination has a detectable influence on the observed mass distribution of exoplanets. This gives rise to an "erosion line", below which Sanz-Forcada et al. (2010) find the large majority of the planets in their sample. To estimate the mass loss induced by the X-ray and extreme-UV (EUV) irradiation, we used Eq. (2) from Sanz-Forcada et al. (2011), viz.

$$\dot{M} = \frac{3F_{\rm XUV}}{4G\rho},$$

where $F_{\rm XUV}$ is the sum of the stellar X-ray and EUV flux at the planetary orbit, G is the gravitational constant, and ρ is the density of the planet (all in cgs units). Because there are no EUV data of CoRoT-2a available, we use Eq. (3) from Sanz-Forcada et al. (2011), which provides a relation between X-ray and EUV luminosity calibrated with their sample of objects, to obtain an estimate of 4.3×10^5 erg cm^{-2} s^{-1} for the expected EUV flux at the distance of CoRoT-2b. Substituting the parameters for CoRoT-2b (Alonso et al. 2008, Table 1), we obtained a mass-loss rate of 4.5×10^{12} g s^{-1} or 7.3×10^{-2} $M_{\rm J}$ Ga^{-1} for the planet. Given the uncertainties, this value remains a coarse estimate, but places CoRoT-2b clearly above the erosion line, which, according to Sanz-Forcada et al., may be explained by the youth of the system. We note, however, that by using different assumptions for the extent of CoRoT-2b's atmosphere (Sanz-Forcada et al. 2010, Eq. (1)), the mass-loss rate may be increased by up to one order of magnitude. Moreover, the effects leading to planetary mass loss are not yet well understood.

4.5. The companion – a puzzling genesis

An important consequence of our analysis is that the CoRoT-2 system may extend far beyond the planetary orbit. CoRoT-2a's visual companion, 2MASS J19270636+0122577, may actually also be a physical companion, forming a wide binary pair with CoRoT-2a.

We obtained and analyzed the first low-SNR UVES spectrum of the companion. Alonso et al. (2008) already noticed that the companion may be a late-K or early-M-type star at about the same distance as CoRoT-2a. We measured the companion's radial velocity and found a value of 23.9 ± 0.4 km s^{-1}, which is close to CoRoT-2a's radial velocity. By modeling the TiO bands present in the spectrum, we determined an effective temperature between 3900 and 4100 K. Wide lines of Ca I were used to infer a surface gravity of $\log g = 4.74$. Consulting the evolutionary tracks of Siess et al. (2000) at an estimated age of 200 Ma, we find that the companion is likely to be a star of spectral type K9, which is gravitationally bound to CoRoT-2a. This would make CoRoT-2 one of about 40 known binary systems harboring an exoplanet (Mugrauer & Neuhäuser 2009).

If this hypothesis withstands further observational tests, it would challenge our understanding of the CoRoT-2 system, in particular, the age of the system. From the *Chandra* data we derived an upper limit of 9×10^{26} erg s^{-1} for the X-ray luminosity of the companion, and the Siess et al. evolutionary tracks suggest an absolute bolometric luminosity of 6.8 mag. Combining these numbers, we obtain $\log L_{\rm X}/L_{\rm bol} < -5.8$, making the companion a star much less active than CoRoT-2a. From our spectral analysis, we concluded that CoRoT-2a has an age between 100 and 300 Ma. Assuming that the companion is physically bound and has the same age as CoRoT-2a, we would expect an X-ray flux significantly higher than observed in our *Chandra* pointing. From the study of X-ray emission of members of the Pleiades cluster, Micela et al. (1996) find typical X-ray luminosities for K-stars of $\log L_{\rm X} = 29.4$ erg s^{-1}, which is more than two orders of magnitude above our upper limit for the companion. We therefore conclude that either the companion has never been an active X-ray source, which seems unusual for a young late-type star, or that the activity of the companion has already dropped to a moderate level. Given the upper limit for the X-ray luminosity, the companion may be an evolved K-type star similar to those found in the solar neighborhood (Schmitt et al. 1995). This also agrees with the upper limit on its rotational velocity of $v \sin i < 10$ km s^{-1}; neglecting the unknown inclination, this would be a value typical for K-type stars on the main-sequence (Cox 2000, p. 389, Table 15.8).

We speculate that the CoRoT-2 system, if bound, should be old enough to let the K-star become sufficiently inactive, while the G-star CoRoT-2a remained more active, maybe through an interaction with its close-in planet. This hypothesis is backed by the recent results presented by Brown et al. (2011), who reported on a discrepancy between different age estimations of the host stars of the planetary systems WASP-18 and WASP-19. Both stars harbor a close-in hot Jupiter and appear to be older than attested by their gyrochronological age. Brown et al. (2011) suggested that an inward migration of the hot Jupiters has caused a spin-up of their host stars via tidal interaction. Alternatively, or even additionally, interactions between the planetary and stellar magnetic fields may have reduced the stellar angular-momentum loss as proposed by Lanza (2010). The CoRoT-2 system is among the planetary systems with the shortest orbital periods and should, therefore, be susceptible to these effects.

4.6. On the dynamics including the companion

A gravitationally bound stellar companion influences the dynamics of the CoRoT-2 system. In particular, it slightly disturbs the planetary orbit. Indeed, Gillon et al. (2010) find a temporal offset of the secondary eclipse, which can be attributed to a slight orbit eccentricity or another interacting body. Because transit timing variations larger than 10 s are excluded by the CoRoT light curve (Alonso et al. 2009), Gillon et al. conclude that the planetary orbit has an eccentricity of ~0.014. Given the present eccentricity of the orbit, the anomalous radius of the planet can be explained by evolutionary scenarios if the models include a third planetary body in the system. Guillot & Havel (2011) propose two possible scenarios, which would result in a relatively recent (~20 Ma) start of the circularization process of the orbit. One requires a planetary encounter and the other is based on the Kozai interaction with a distant body. Our findings clearly favor the latter scenario.

5. Conclusion

The CoRoT-2 system may be a key to a more profound understanding of the early evolution of planetary systems. We studied new optical and X-ray data. Our analysis showed that magnetic activity can be traced through all layers of the stellar atmosphere from the photosphere to the corona and provided new evidence, helping to answer questions about the age, distance, and evolution of the system. A detailed analysis of several age indicators showed that an age between 100 and 300 Ma is most likely. Furthermore, we were able to provide an estimate of 270 pc for the distance of CoRoT-2a, but with a large uncertainty.

Beyond answering questions, our analysis also raised new problems. Most notably, the true nature of 2MASS J19270636+0122577, the optical and potentially physical stellar companion of CoRoT-2a, remains doubtful. The apparent presence of a gravitationally bound and, therefore, most likely coeval K-type stellar companion, which, nonetheless, shows no detectable activity, would challenge our picture of the CoRoT-2 system. Either the companion is old enough to have already become inactive, or CoRoT-2a appears to be younger than it actually is. A third body would have a substantial impact on the evolutionary dynamics of the whole system. It may account for the eccentricity of the planetary orbit and may even be responsible for the observed anomalously large radius of CoRoT-2b.

Acknowledgements. This work has made use of observational data obtained with UVES at the ESO Very Large Telescope, Paranal, Chile, and the *Chandra* X-ray Observatory. We acknowledge use of the VALD and NIST atomic line databases, DSS, and SIMBAD. We are indebted to Nikolai Piskunov (University of Uppsala) for making SME available to us. We are thankful to Eric J. Bubar (University of Rochester) for providing us with his MSPAWN and PYSPEC routines. We are grateful to Richard O. Gray (Appalachian State University) for making his SPECTRUM line synthesis code publicly available. We thank Matthias Ammler-von Eiff (Georg-August-Universität Göttingen) for sharing his insight with us. S.S. acknowledges support from the DLR under grant 50OR0703. S.C. and U.W. acknowledge support from the DLR under grant 50OR0105. H.M.M. and K.F.H. are supported in the framework of the DFG-funded Research Training Group "Extrasolar Planets and their Host Stars" (DFG 1351/1).

References

Alonso, R., Auvergne, M., Baglin, A., et al. 2008, A&A, 482, L21
Alonso, R., Aigrain, S., Pont, F., Mazeh, T., & The CoRoT Exoplanet Science Team 2009, in IAU Symp., 253, 91
Alonso, R., Deeg, H. J., Kabath, P., & Rabus, M. 2010, AJ, 139, 1481
Ammler-von Eiff, M., Santos, N. C., Sousa, S. G., et al. 2009, A&A, 507, 523
Andretta, V., Busà, I., Gomez, M. T., & Terranegra, L. 2005, A&A, 430, 669
Arnaud, K. A. 1996, in Astronomical Data Analysis Software and Systems V, ed. G. H. Jacoby, & J. Barnes, ASP Conf. Ser., 101, 17
Ayres, T. R. 1979, ApJ, 228, 509
Baliunas, S. L., Donahue, R. A., Soon, W., & Henry, G. W. 1998, in Cool Stars, Stellar Systems, and the Sun, ed. R. A. Donahue, & J. A. Bookbinder, ASP Conf. Ser., 154, 153
Barnes, S. A. 2007, ApJ, 669, 1167
Bohlin, R. C., Savage, B. D., & Drake, J. F. 1978, ApJ, 224, 132
Bouchy, F., Queloz, D., Deleuil, M., et al. 2008, A&A, 482, L25
Brown, D. J. A., Collier Cameron, A., Hall, C., Hebb, L., & Smalley, B. 2011, MNRAS, in press [arXiv:1103.3599]
Bruntt, H., Deleuil, M., Fridlund, M., et al. 2010, A&A, 519, A51
Bubar, E. J., & King, J. R. 2010, AJ, 140, 293
Busà, I., Aznar Cuadrado, R., Terranegra, L., Andretta, V., & Gomez, M. T. 2007, A&A, 466, 1089
Cox, A. N. 2000, Allen's astrophysical quantities, ed. A. N. Cox,
Cox, D. P., & Reynolds, R. J. 1987, ARA&A, 25, 303
Czesla, S., Huber, K. F., Wolter, U., Schröter, S., & Schmitt, J. H. M. M. 2009, A&A, 505, 1277
Dekker, H., D'Odorico, S., Kaufer, A., Delabre, B., & Kotzlowski, H. 2000, in SPIE 4008, ed. M. Iye, & A. F. Moorwood, 534
Deming, D., Knutson, H., Agol, E., et al. 2011, ApJ, 726, 95
Donahue, R. A. 1998, in Cool Stars, Stellar Systems, and the Sun, ed. R. A. Donahue, & J. A. Bookbinder, ASP Conf. Ser., 154, 1235
Ferlet, R., Vidal-Madjar, A., & Gry, C. 1985, ApJ, 298, 838
Fortney, J. J., Lodders, K., Marley, M. S., & Freedman, R. S. 2008, ApJ, 678, 1419
Fuhrmann, K. 1998, A&A, 330, 626
Fuhrmann, K. 2004, Astron. Nachr., 325, 3
Gillon, M., Lanotte, A. A., Barman, T., et al. 2010, A&A, 511, A3
Gray, R. O., & Corbally, C. J. 1994, AJ, 107, 742
Guillot, T., & Havel, M. 2011, A&A, 527, A20
Huber, K. F., Czesla, S., Wolter, U., & Schmitt, J. H. M. M. 2009, A&A, 508, 901
Huber, K. F., Czesla, S., Wolter, U., & Schmitt, J. H. M. M. 2010, A&A, 514, A39
King, J. R. 1993, AJ, 105, 1087
Knutson, H. A., Howard, A. W., & Isaacson, H. 2010, ApJ, 720, 1569
König, B., Guenther, E. W., Woitas, J., & Hatzes, A. P. 2005, A&A, 435, 215
Kurucz, R. L. 1993, SYNTHE spectrum synthesis programs and line data, ed. R. L. Kurucz
Lallement, R., & Bertin, P. 1992, A&A, 266, 479
Lanza, A. F. 2010, A&A, 512, A77
Lanza, A. F., Pagano, I., Leto, G., et al. 2009, A&A, 493, 193
Lecavelier Des Etangs, A., Ehrenreich, D., Vidal-Madjar, A., et al. 2010, A&A, 514, A72
Linsky, J. L. 1980, ARA&A, 18, 439
Linsky, J. L., Yang, H., France, K., et al. 2010, ApJ, 717, 1291
Megier, A., Strobel, A., Bondar, A., et al. 2005, ApJ, 634, 451
Megier, A., Strobel, A., Galazutdinov, G. A., & Krełowski, J. 2009, A&A, 507, 833
Melo, C., Santos, N. C., Pont, F., et al. 2006, A&A, 460, 251
Micela, G., Sciortino, S., Kashyap, V., Harnden, Jr., F. R., & Rosner, R. 1996, ApJS, 102, 75
Milone, A., & Barbuy, B. 1994, A&AS, 108, 449
Montes, D., Fernandez-Figueroa, M. J., de Castro, E., & Sanz-Forcada, J. 1997, A&AS, 125, 263
Mugrauer, M., & Neuhäuser, R. 2009, A&A, 494, 373
Noyes, R. W., Weiss, N. O., & Vaughan, A. H. 1984, ApJ, 287, 769
Pace, G., Pasquini, L., & Ortolani, S. 2003, A&A, 401, 997
Pinsonneault, M. H. 1994, in Cool Stars, Stellar Systems, and the Sun, ed. J.-P. Caillault, ASP Conf. Ser., 64, 254
Piskunov, N. E., & Valenti, J. A. 2002, A&A, 385, 1095
Piskunov, N. E., Kupka, F., Ryabchikova, T. A., Weiss, W. W., & Jeffery, C. S. 1995, A&AS, 112, 525
Plez, B. 1998, A&A, 337, 495
Reimers, D. 1977, A&A, 57, 395
Rutten, R. G. M. 1984, A&A, 130, 353
Sanz-Forcada, J., Ribas, I., Micela, G., et al. 2010, A&A, 511, L8
Sanz-Forcada, J., Micela, G., Ribas, I., et al. 2011, A&A, in press [arXiv:1105.0550]
Schmitt, J. H. M. M., Fleming, T. A., & Giampapa, M. S. 1995, ApJ, 450, 392
Schneider, J., Rauer, H., Lasota, J. P., Bonazzola, S., & Chassefiere, E. 1998, in Brown Dwarfs and Extrasolar Planets, ed. R. Rebolo, E. L. Martin, & M. R. Zapatero Osorio, ASP Conf. Ser., 134, 241
Schultz, G. V., & Wiemer, W. 1975, A&A, 43, 133

Sestito, P., & Randich, S. 2005, A&A, 442, 615
Sfeir, D. M., Lallement, R., Crifo, F., & Welsh, B. Y. 1999, A&A, 346, 785
Siess, L., Dufour, E., & Forestini, M. 2000, A&A, 358, 593
Silva-Valio, A., Lanza, A. F., Alonso, R., & Barge, P. 2010, A&A, 510, A25
Smith, R. K., Brickhouse, N. S., Liedahl, D. A., & Raymond, J. C. 2001, ApJ, 556, L91
Sneden, C. A. 1973, Ph.D. thesis, University of Texas at Austin
Snellen, I. A. G., de Mooij, E. J. W., & Burrows, A. 2010, A&A, 513, A76
Soderblom, D. R., Oey, M. S., Johnson, D. R. H., & Stone, R. P. S. 1990, AJ, 99, 595
Soderblom, D. R., Fedele, S. B., Jones, B. F., Stauffer, J. R., & Prosser, C. F. 1993a, AJ, 106, 1080
Soderblom, D. R., Jones, B. F., Balachandran, S., et al. 1993b, AJ, 106, 1059
Soderblom, D. R., Pilachowski, C. A., Fedele, S. B., & Jones, B. F. 1993c, AJ, 105, 2299
Soderblom, D. R., King, J. R., Siess, L., Jones, B. F., & Fischer, D. 1999, AJ, 118, 1301
Sousa, S. G., Santos, N. C., Israelian, G., Mayor, M., & Monteiro, M. J. P. F. G. 2007, A&A, 469, 783
Sousa, S. G., Santos, N. C., Mayor, M., et al. 2008, A&A, 487, 373
Sousa, S. G., Alapini, A., Israelian, G., & Santos, N. C. 2010, A&A, 512, A13
Strömgren, B. 1948, ApJ, 108, 242
Valenti, J. A., & Fischer, D. A. 2005, ApJS, 159, 141
Valenti, J. A., & Piskunov, N. 1996, A&AS, 118, 595
Vaughan, A. H., Preston, G. W., & Wilson, O. C. 1978, PASP, 90, 267
Vidal-Madjar, A., Lecavelier des Etangs, A., Désert, J., et al. 2003, Nature, 422, 143
Welsh, B. Y., Lallement, R., Vergely, J., & Raimond, S. 2010, A&A, 510, A54
Wilson, O. C., & Bappu, M. K. V. 1957, ApJ, 125, 661
Wolter, U., Schmitt, J. H. M. M., Huber, K. F., et al. 2009, A&A, 504, 561

A&A 539, A150 (2012)
DOI: 10.1051/0004-6361/201118042

Astronomy & Astrophysics

The extended chromosphere of CoRoT-2A★

Discovery and analysis of the chromospheric Rossiter-McLaughlin effect

S. Czesla[1], S. Schröter[1], U. Wolter[1], C. von Essen[1], K. F. Huber[1], J. H. M. M. Schmitt[1], D. E. Reichart[2], and J. P. Moore[2]

[1] Hamburger Sternwarte, Universität Hamburg, Gojenbergsweg 112, 21029 Hamburg, Germany
e-mail: stefan.czesla@hs.uni-hamburg.de
[2] Department of Physics and Astronomy, University of North Carolina, Chapel Hill, CB 3255, Phillips Hall, Chapel Hill, NC 27599-3255, USA

Received 7 September 2011 / Accepted 16 January 2012

ABSTRACT

The young G7V dwarf CoRoT-2A is transited by a hot Jupiter and among the most active planet host-stars known to date. We report on the first detection of a chromospheric Rossiter-McLaughlin effect observed in the Ca II H and K emission-line cores. In Ca II H and K, the transit lasts 15% longer than that observed in visual photometry, indicating that chromospheric emission extends 100 000 km beyond the photosphere. Our analysis is based on a time series of high-resolution UVES spectra obtained during a planetary transit and simultaneously obtained photometry observed with one of the PROMPT telescopes. The chromospheric Rossiter-McLaughlin effect provides a new tool to spatially resolve the chromospheres of active planet host-stars.

Key words. stars: individual: CoRoT-2A – planetary systems – stars: late-type

1. Introduction

The G7V dwarf CoRoT-2A is one of the most active planet host-stars known to date. Every 1.74 d, the star is transited by the unusually inflated hot Jupiter CoRoT-2b (Alonso et al. 2008; Bouchy et al. 2008). CoRoT-2A is young (100–300 Ma) and has basically solar metallicity (Schröter et al. 2011). It shows a high level of magnetic activity as diagnosed from the amplitude of its photometric variation, strong chromospheric emission lines, and coronal X-ray emission (Alonso et al. 2008; Knutson et al. 2010; Schröter et al. 2011). Furthermore, Schröter et al. (2011) provided strong evidence that CoRoT-2A's optical neighbor, 2MASS J19270636+0122577, is a true physical companion of spectral type K9, as earlier hypothesized by Alonso et al. (2008), making CoRoT-2 a wide binary system with at least one planet.

The CoRoT-2 system has been subject to a multitude of photometric and spectroscopic studies. To name but a few: Alonso et al. (2008) reported the discovery of CoRoT-2b and first radial velocity (RV) measurements, later refined by Bouchy et al. (2008); Gillon et al. (2010) studied the secondary transit observed with Spitzer's IRAC instrument and Snellen et al. (2010) analyzed the secondary transit as observed by CoRoT; Lanza et al. (2009), Czesla et al. (2009), and Huber et al. (2009, 2010) used light-curve inversion techniques to recover CoRoT-2A's surface; finally, Ammler-von Eiff et al. (2009) and Schröter et al. (2011) investigated the spectral properties, activity, and X-ray emission of the system.

During a transit, the planet occults different parts of the rotating stellar surface, which leads to the Rossiter-McLaughlin effect (RME). The occultation introduces asymmetries into the rotationally broadened line profile, which result in an apparent radial velocity (RV) shift of the stellar spectrum. The RME, first observed in eclipsing binary stars (Schlesinger 1910; Rossiter 1924; McLaughlin 1924), has become a standard tool to analyze the geometry of exoplanetary systems (e.g., Fabrycky & Winn 2009). Analytical models of this effect, based on the first moment of spectral lines, have been presented by Ohta et al. (2005) and Giménez (2006) and are commonly applied to modeling, although they may not exactly reproduce the results obtained by cross-correlation techniques (e.g., Triaud et al. 2009; Hirano et al. 2010).

The RME has widely been used to measure the projected rotation velocity of planet host-stars and the alignment of their rotation axis relative to the planetary orbit (e.g., Bouchy et al. 2008). Snellen (2004) and Dreizler et al. (2009) proposed the use of the RME to probe the planetary atmosphere by analyzing the differences between measurements in various spectral lines showing potentially large absorption due to the planet's exosphere. In contrast to narrow-band photometry, the differential RME measurement does not rely on accurate photometric calibration (Snellen 2004).

The applicability of the RME is not limited to the study of the planetary orbit and atmosphere, but can be extended to the study of the *stellar* atmosphere. By confining the RME measurement to spectral lines originating in individual layers of the stellar atmosphere, the properties of these layers can be separately analyzed. In this paper, we demonstrate the feasibility of this approach for the stellar chromosphere. While the apparent surface brightness of the photosphere decreases toward the limb, the optically thin chromosphere and corona show limb-brightening (Wolter & Schmitt 2005). Narrow-band transit light-curves of limb-brightened emission lines are expected to display characteristic profiles (Assef et al. 2009; Schlawin et al. 2010), which

★ Based on observations obtained with UVES at the ESO VLT Kueyen telescope (program ID 385.D-0426).

also applies to the RME derived from chromospheric emission lines. Therefore, the RME observed in chromospheric emission lines allows us to probe the spatial structure of the chromosphere, including both the chromospheric center-to-limb variation and inhomogeneities due to active regions. These measurements can be used to study the chromospheres of active planet host-stars and examine whether faculae dominate over spots on the surfaces of young, active stars, as found by Radick et al. (1998).

In this paper, we present time-resolved transit spectroscopy of CoRoT-2A obtained with the UVES spectrograph and simultaneous photometry obtained with the "Panchromatic Robotic Optical Monitoring and Polarimetry Telescopes" (PROMPT, Reichart et al. 2005). We refine the wavelength calibration of the spectra and discuss the RME observed in photospheric lines. In Sect. 3.3, we report the first detection of the prolonged RME in the chromospheric emission-line cores of Ca II H and K, before closing with a discussion of our findings.

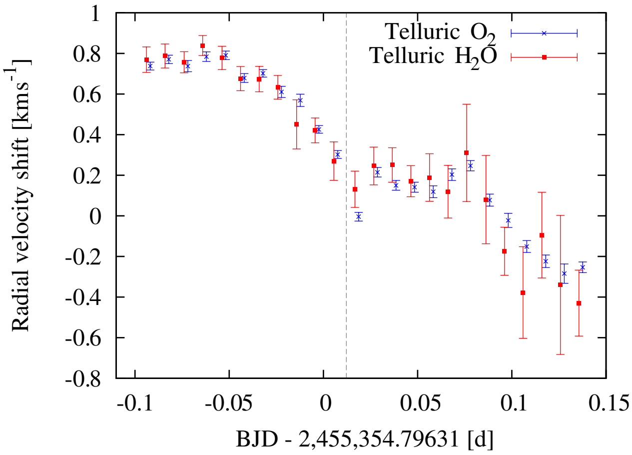

Fig. 1. Time-dependent drift of the UVES wavelength calibration determined from 64 isolated H_2O (red) and O_2 (blue) telluric absorption lines (small temporal displacement for clarity). The dashed line indicates the insertion of the image slicer.

2. Observation

We acquired 24 high-resolution spectra of CoRoT-2A using the UVES spectrograph (Dekker et al. 2000) mounted at the VLT Kueyen. The observations were obtained on June 7, 2010, under program-ID 385.D-0426(A) and cover a full planetary transit of CoRoT-2b, including one hour before and two hours after the actual transit; the spectra have individual exposure times of 800 s.

The UVES spectrograph was set up in *dichroic 2* mode with a slit width of 0.7 arcsec. For the selected setup, UVES provides a wavelength coverage of 3800–9000 Å with gaps at 5000–5700 Å and 7500–7680 Å at a resolving power of about 60 000. Owing to the worsening seeing conditions during the second half of the night, we inserted the image slicer into the light path to reduce light losses during exposures Nos. 12–24. To reduce the UVES echelle data, we applied the REDUCE package developed by Piskunov & Valenti (2002); for a more detailed discussion of the data and the reduction, we refer the reader to Schröter et al. (2011).

The transit observed with UVES was simultaneously followed by one of the six 0.41 m Ritchey-Chrétien telescopes belonging to the PROMPT observatory (Reichart et al. 2005) located at the "Cerro Tololo Inter-American Observatory" (CTIO) in Chile. The telescope is equipped with an "Apogee Alta U47" detector with a $1k \times 1k$ pixel array with a gain of 4.91 electrons/ADU and a read-out noise of 10 electrons.

A total of 528 science frames were taken with a fixed exposure time of 30 s. No filter was used in the observations. We calibrated all science frames using a master bias, but refrained from applying a sky-flat correction, because the sky-flat exposures showed a strong illumination gradient from the center to the periphery, possibly caused by the projected shadow of the shutter. The following reduction was carried out using standard routines from the IRAF *daophot* package for image processing.

3. Analysis

We present an analysis of the temporal evolution of the observed spectra including a detailed presentation of the wavelength calibration, which is crucial to our analysis. All line profile and model fits as well as the Markov-chain Monte Carlo (MCMC) calculations make extensive use of routines of our PyAstronomy[1] collection of Python packages, which provide a convenient interface to fitting and sampling algorithms implemented in the PyMC (Patil et al. 2010) and SciPy (Jones et al. 2001) packages.

3.1. Refining the wavelength calibration using telluric standards

Our wavelength calibration was obtained using Th-Ar lamp spectra. Since those spectra are not taken simultaneously with the science spectra, they cannot account for instrumental wavelength drifts produced, for example, by environmental effects. To obtain a more accurate, time-dependent wavelength calibration, we exploited telluric absorption lines. The power of this technique has already been demonstrated, for instance, by Snellen (2004), who used atmospheric H_2O lines in a UVES spectrum to show that a precision of ~5–10 m s^{-1} can be attained, and by Figueira et al. (2010), who found that the accuracy obtained by using atmospheric features can compete with that reached with gas-cell methods on timescales of days.

To obtain an absolute wavelength calibration, we determined the wavelengths of the strong atmospheric lines of H_2O and O_2. Telluric absorption lines of H_2O are present around 6500 Å and in the 6900–7400 Å region, while those pertaining to O_2 populate the regions 6200–6300, 6800–6950, and 7650–7700 Å.

We selected the 64 strongest, isolated telluric lines (27 H_2O, 37 O_2) and fitted them with Gaussians. The best-fit wavelengths were then compared with the spectral atlas of telluric absorption lines provided by the "high-resolution transmission molecular absorption database" (HITRAN[2]; Rothman et al. 2009). The sample standard deviation between observed and nominal wavelengths was used as an error estimate. Errors were determined for H_2O and O_2 separately and found to be larger for the H_2O lines, which predominantly populate the wavelength band beyond 7000 Å, where the signal-to-noise (S/N) ratio decreases.

In Fig. 1, we show the thus obtained apparent RV shift of the 24 spectra. Clearly, the difference between nominal and

[1] http://www.hs.uni-hamburg.de/DE/Ins/Per/Czesla/PyA/PyA/index.html

[2] http://www.cfa.harvard.edu/hitran

observed wavelength of the telluric lines follows a systematic, time-dependent trend. The blue shift corresponds to a drifting of approximately 1 km s^{-1} in five hours. The drift is neither linear nor monotonic, but shows a humpy behavior. Most notably, there is a sudden jump of 0.2 km s^{-1} after the 12th observation. We find no wavelength-dependence of the trend in the 6200−7700 Å range covered by telluric lines.

This telluric drift may be caused by instrumental and atmospheric effects. As an evolving velocity field in the atmosphere gives rise to a Doppler shift, it induces a wavelength-proportional line shift. To check whether this is the case, we determined the apparent shift of telluric lines in seven echelle orders. Our analysis suggests that the drift of telluric lines does not show the characteristics of a Doppler shift, but is dominated by a displacement of the spectrum on the detector (about 0.1 CCD pixels at 6700 Å).

The telluric line drift may be the result of a changing dispersion relation caused by a variation in the ambient conditions. The ambient pressure and temperature reported in the FITS headers, indeed, follow a pattern reminiscent of the telluric line drift. Figure 2 shows both quantities as a function of time. Ambient pressure and temperature are both strongly correlated with the telluric drift pattern yielding Pearson correlation coefficients of 0.92 and 0.80, corresponding to shifts of 1.38 km s^{-1}/hPa and 1.12 km s^{-1}/°C. According to the ESO UVES User Manual (Kaufer et al. 2011) and the ESO Quality Control Group (2005), variations in temperature yield shifts of typically 0.35 pixels/°C (0.5 km s^{-1}/°C) in dispersion direction and changes in the ambient pressure cause typical shifts of 0.05 pixels/hPa (0.1 km s^{-1}/hPa). Given the environmental conditions during the night (see Fig. 2), temperature variations dominate the instrumental drift.

Although the observed drift in our spectra is larger than that inferred from the UVES manual, we identify the ambient conditions as the likely dominating cause of the apparent drift. This conclusion is in line with the results of Reiners (2009), who analyze similar differential velocity drifts.

3.2. Photospheric Rossiter-McLaughlin effect and optical photometry

Below, we present a joint analysis of the photospheric Rossiter-McLaughlin effect derived from the UVES spectra and simultaneously obtained optical photometry.

3.2.1. Analysis of PROMT data

The photometry was obtained using PROMPT. To reduce these data, we carried out the usual CCD data reduction steps. We identified USNO-B1.0-0913-0447626 as the most well-suited comparison star and obtained the differential light curve for CoRoT-2A along with several control light-curves using other comparison stars. To obtain the light curves, we extracted the photons from circular apertures centered on the individual stars. The local sky level was measured within an annulus surrounding the aperture. In the case of CoRoT-2A, the aperture also comprised its bona-fide physical companion, 2MASS J19270636+0122577. The resulting light curve was normalized using a linear fit to the out-of-transit points and is shown in the lower panel of Fig. 4.

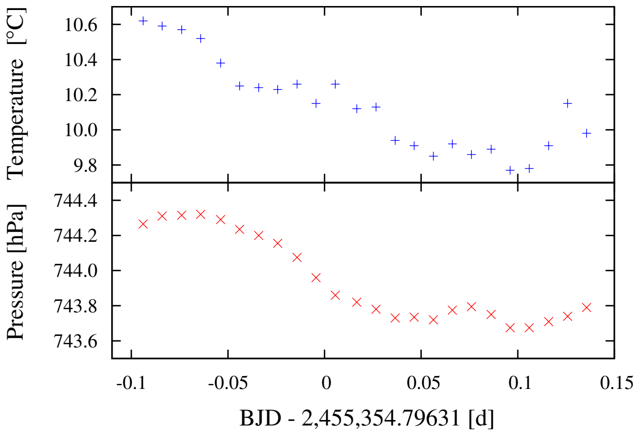

Fig. 2. Time dependence of ambient pressure and temperature during the UVES observations.

3.2.2. Measurement of the photospheric Rossiter-McLaughlin effect

We determined the radial-velocity shift of the stellar spectrum obtained with UVES by cross-correlating it with a synthetic template of CoRoT-2A according to the prescription by Zucker (2003). The template was calculated with the SPECTRUM stellar synthesis code (Gray & Corbally 1994) and is based on Kurucz model atmospheres (Kurucz 1993). The stellar parameters were adopted from Schröter et al. (2011).

Before cross-correlating them, the observed spectra were continuum-normalized. To define the continuum, we manually specified an appropriate number of supporting points for a piecewise linear fit, chosen by comparing the spectra with the template. We then calculated the cross-correlation function for different parts of the spectrum that show no contamination by telluric absorption lines. While the blue parts of the spectra are most convenient from that point of view, they completely lack telluric lines that could be used to correct for the systematic instrumental drift described in Sect. 3.1. We, therefore, computed the cross-correlation in the 5700−7500 Å range and subsequently subtracted the instrumental drift inferred from the telluric lines. The result is shown in Fig. 3 along with a quadratic fit to the out-of-transit points used in the modeling.

3.2.3. Joint modeling of photometry and Rossiter-McLaughlin effect

In our modeling, we apply the analytical RME curves presented by Ohta et al. (2005) and the transit model developed by Pál (2008). In addition to the RME model, we take into account the orbital reflex motion of the host star using a sinusoidal curve. In our approach, we neglect the slightly non-zero ($e = 0.0143^{+0.0077}_{-0.0076}$) eccentricity determined by Gillon et al. (2010), whose influence on our model is small.

The transit model has the following parameters: the orbital period, P, the mid-transit time, T_0, the radius ratio, r_p/R_s, the semi-major axis in stellar radii, a/R_s, the orbital inclination, i, the linear stellar limb-darkening coefficient, ϵ, and the contribution of third light, L_3, given as a fraction of the host-star's luminosity.

The RME model of Ohta et al. (2005) encompasses, apart from the third light contribution, all parameters used in the transit model. In addition, it includes the sky-projected stellar

A&A 539, A150 (2012)

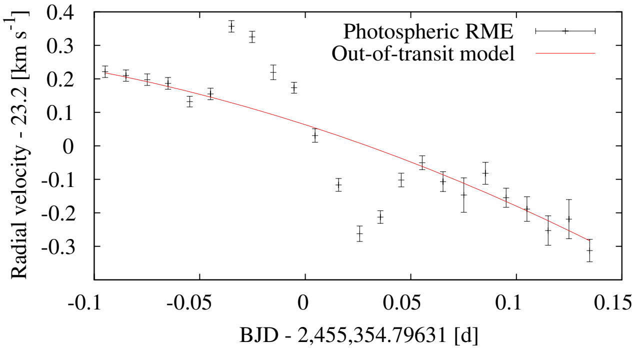

Fig. 3. The photospheric Rossiter-McLaughlin effect observed with UVES and a quadratic out-of-transit model.

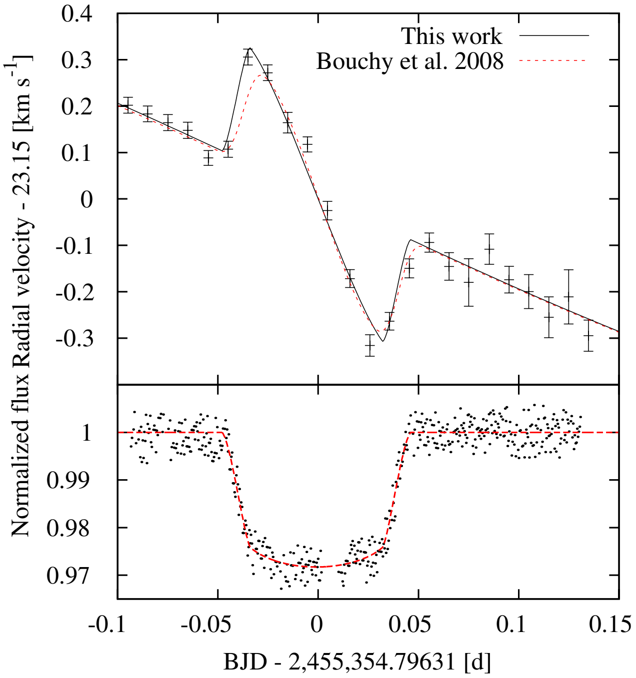

Fig. 4. *Upper panel*: photospheric Rossiter-McLaughlin effect of CoRoT-2A determined in the 5700–7500 Å band, our most likely model (solid), and the model given by Bouchy et al. (2008) (dashed). *Lower panel*: transit simultaneously observed with PROMPT and most likely model from our joint transit+RME fit.

rotational velocity, $\upsilon\sin(I_s)$, and the sky-projected angle between stellar spin axis and planetary orbit normal, λ. Furthermore, we characterize the stellar reflex motion using a sine with RV semi-amplitude, K, and an RV zero point, V_0. In the computation of the RV curve, we used an "overbinned" model to account for the finite (800 s) integration time per spectrum. In particular, each observed bin was divided into 15 model bins, which were finally averaged and compared to the observation.

In an active star such as CoRoT-2A, stellar activity could affect the measured RV curve (Albrecht et al. 2011; Bouchy et al. 2008). Additionally, systematic effects due to the observed instrumental drift may still be present. To account for RV shifts not caused by the stellar reflex motion and the RME itself, we fitted the out-of-transit points of our RV measurement using a quadratic model (see Fig. 3) and subtracted the quadratic term

Table 1. Priors and sampling results.

Prior information		
Quantity[a]	Prior	Source[c]
$\upsilon\sin(I_s)$ [km s^{-1}]	11.46 ± 0.37	B08
λ [°]	7.1 ± 5	B08
K [km s^{-1}]	0.563 ± 0.014	A08
i [°]	87.84 ± 0.1	A08
p	0.1667 ± 0.0053	A08/C09
L_3 [%]	5.6 ± 1	A08
a [R_s]	6.7 ± 0.03	A08
ϵ, T_0, V_0	uniform	
e	0 (fixed)	
Posterior		
Quantity	Value and 95% HPD[b]	
$\upsilon\sin(I_s)$ [km s^{-1}]	11.95 (11.4, 12.53)	
λ [°]	−1 (−7.7, 6)	
K [km s^{-1}]	0.564 (0.541, 0.587)	
i [°]	87.84 (87.67, 88)	
p	0.1639 (0.1621, 0.1656)	
L_3 [%]	5.2 (3.2, 7.1)	
a [R_s]	6.73 (6.69, 6.76)	
ϵ	0.33 (0.28, 0.37)	
T_0 [s]	−76.7 (−88.2, −65.3)	
V_0 [m/s]	63.3 (52.9, 72.6)	

Notes. [a] We use the nomenclature of Ohta et al. (2005); in addition, K is the radial velocity semi-amplitude, V_0 the RV offset, and L_3 the third light contribution. [b] In parentheses, the 95% HPD credibility intervals are given. [c] A08 = Alonso et al. (2008), B08 = Bouchy et al. (2008), C09 = Czesla et al. (2009).

(4.08 km d^{-2}). The resulting RV curve is shown in the top panel of Fig. 4 and was used in the modeling.

The parameters in question had already been measured in previous works. To take the existing information into account in our modeling, we specified Gaussian priors based on previous results for the parameters: $\upsilon\sin(I_s)$, λ, K, V_0, r_p/R_s, L_3, a, and i. For the radius ratio, r_p/R_s, we used the difference between the values derived by Alonso et al. (2008) and Czesla et al. (2009) as the width of the prior. For all other parameters, except for the eccentricity, which was neglected, we used uniform priors covering the full physically reasonable space. The information on parameters and priors is summarized in Table 1.

We proceeded by sampling from the posterior probability distribution using a Markov-chain Monte Carlo (MCMC) approach. In Fig. 4, we show the most likely model given the data and the prior information. The expectation values for the parameters and 95% credibility intervals derived from the posterior are given in Table 1. We note that the prior information has a noticeable influence on the posterior, especially that on the stellar rotation velocity, $\upsilon\sin(I_s)$. If we neglect this prior information by using a broad uniform prior, the posterior yields $\upsilon\sin(I_s)$ = 12.9 (11.9, 13.9) km s^{-1}, increasing the amplitude of the RME model.

Our analysis shows that CoRoT-2A's companion, 2MASS J19270636+0122577, provides 5.2% of the total flux in the PROMPT band, which is comparable to the number of 5.6% derived by Alonso et al. (2008) in the CoRoT band. The observed transit center, T_0, shows a slight displacement of −76.7 s if compared to the ephemerides given by Alonso et al. (2008).

The numbers are, however, compatible considering that the 1 σ uncertainty in the Alonso et al. ephemerides amounts to 95 s at the given epoch, which covers our value. Using the reference point, $T_{0,A}$, given by Alonso et al. and our transit center, T_0, we can slightly improve the estimate of the planet's orbital period using the equation

$$P_o = \frac{(2\,455\,354.796\,312\,\mathrm{d} - 76.7\,\mathrm{s}) - T_{0,A}}{641} = 1.742\,995\,02 \pm 0.000\,001\,\mathrm{d}. \quad (1)$$

We caution that large starspots may affect the transit timing, but as our period estimate lies within the error given by Alonso et al. (2008), their effect is unlikely to be larger than the observed offset of −77 s. Whether the small deviation is due to starspots, cannot be decided on the basis of the data at hand.

In the upper panel of Fig. 4, we show our data points (see also Table A.1), our best-fit RME model, and the model derived by Bouchy et al. (2008) (their "combined MCMC fit" shifted to our RV offset); in Table 1, we list the associated parameter values and the 95% highest probability density (HPD) credibility intervals derived using MCMC sampling.

The RME observed with UVES shows a slightly larger amplitude than reported by Bouchy et al. (2008), which causes the larger $v\sin(I_s)$ value derived from our data. While the derived linear limb-darkening coefficient, ϵ, of 0.3 appears to be low compared to the number of 0.66 reported by Claret (2004) for a star like CoRoT-2A in the r' band, it is in better agreement with the number of 0.41 ± 0.03 given by Alonso et al. (2008), neglecting their small (0.06) quadratic term.

Although the amplitude of the RV shift produced by the orbital motion of the planet, K, cannot be reliably determined given that our data cover only about 10% of the orbital period, we find our number of 564 (541, 587) m s^{-1} to be in good agreement with the value of 563 ± 14 m s^{-1} derived by Alonso et al. (2008) using the full orbit.

CoRoT-2A is an active star, which had a substantial spot coverage during the half-year long CoRoT observation (Alonso et al. 2008; Czesla et al. 2009; Huber et al. 2010). It is likely that spots were also present during the transit under consideration. Parameter uncertainties imposed by stellar activity on the order of a few percent have been found for CoRoT-2A, e.g., by Czesla et al. (2009), and we expect to find a similar effect in our current measurements.

Our photometry suggests that the planet-to-star radius ratio is about 2% smaller than observed by Alonso et al. (2008). Such a decrease may be caused by a corresponding decrease in the total spot coverage of the star, which would make the planet appear smaller. A smaller planet could also account for the larger model value of the stellar rotation velocity, which would then counterbalance the less pronounced RME effect produced by a smaller planet. Alternatively, the spot coverage on the eclipsed section of the star may be larger, thus, making the transit appear less deep (Czesla et al. 2009). We refrain from pointing out individual spot-crossing events in our photometry, because the data do not allow a unique identification.

Strong stellar activity as observed on CoRoT-2A can mask the true values of the physical parameters, leading to differences between individual measurements. To quantify this activity scatter, a larger sample of measurements, allowing a statistical analysis, would be needed.

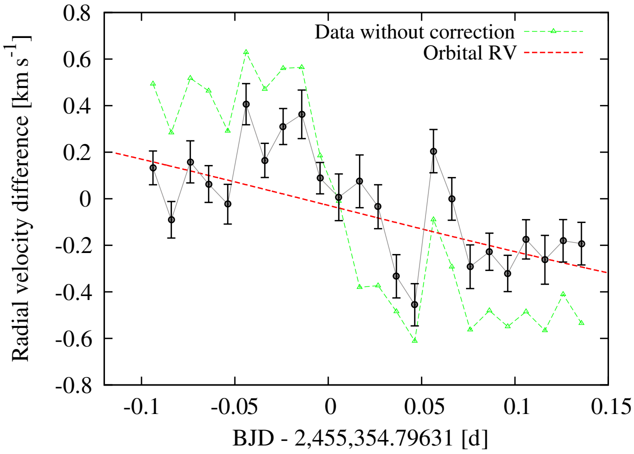

Fig. 5. Chromospheric Rossiter-McLaughlin effect: radial velocity shift of the Ca II H and K lines. Circular data points: RV corrected for telluric drift; triangles: uncorrected RV shift; and dashed line: orbital radial velocity model.

3.3. The chromospheric Rossiter-McLaughlin effect

As the planet eclipses the chromosphere during the transit, the RME should also be observable in chromospheric emission lines. Among the chromospheric features in CoRoT-2A's spectrum, we find that only the cores of the Ca II H and K lines are usable for our analysis. These lines are both strong enough and sufficiently uncontaminated by photospheric emission. A detailed analysis of the chromospheric features in Hα, Hβ, the Na I lines, or the Ca infrared triplet is impeded by a comparably large photospheric background, which is small in the Ca II H and K emission-line cores (see Fig. 7, or Fig. 4 in Schröter et al. 2011).

In the red, we used the telluric lines as standards to improve our wavelength calibration (cf., Sect. 3.1). Because this procedure remains impossible in the blue owing to the lack of appropriate telluric lines, we adopted another approach to obtain a correction for the instrumental drift: We derived the photospheric RME in the blue part of the spectrum using a synthetic spectrum and a line list obtained from VALD (Piskunov et al. 1995) to determine the wavelength of 38 unblended stellar absorption lines between 3800 and 4300 Å. Our previously calculated red RME model was then subtracted and the residual signal was attributed to the drift. While we used the thus derived correction to model the chromospheric RME, we emphasize that the detection of the effect is independent of this correction.

To estimate the apparent RV shift of the Ca II H and K line cores, we determined their barycenters using small 0.5 Å-wide segments centered around the cores' nominal positions (cf., Fig. 7). As both should be similarly affected, we averaged the results yielding a mean RV shift in the Ca II H and K emission line cores.

In an alternative approach, we approximated the Ca II H and K emission-line cores with Gaussians and used MCMC sampling to explore the posterior probability distribution. The measurement errors were assumed to obey a normal distribution and were derived by comparing the observed spectrum to an appropriate synthetic template. Both the barycenter and the Gaussian fit approach yielded comparable results. The resulting RV shifts are listed in Table A.1, and the outcome of the MCMC analysis is shown in Fig. 5, which shows an RV curve with a signature strongly reminiscent of the photospheric RME; the errors correspond to 68% credibility intervals. We found that the center of the Gaussian is not correlated with any other parameter and concluded that the estimate is insensitive to the shape of the emission-line core.

To check the significance of the detection, we tested the null hypothesis that the RV variation in the Ca II H and K cores is described by the orbital motion of the planet alone. Applying χ^2 statistics, the null hypothesis can be rejected with a p-value of 10^{-10}, indicating that our data include an additional contribution to the RV variation, which we attribute to the chromospheric RME.

To exclude the possibility that we merely detected the RME present in the residual photospheric flux underneath the Ca II H and K emission-line cores, we used simulated spectra. First, we obtained a synthetic spectrum of the Ca II H and K line region without emission-line cores, shifted it according to the observed photospheric RME, and applied noise to simulate the observation. We then used the same barycenter method applied to the UVES spectra and found that no RV shift can be detected that can be distinguished from noise. This is a consequence of the broad Ca II H and K line wings. Second, we added the emission-line cores. Our simulations show that both the RV signal resulting from the barycenter method and the Gaussian fit to the cores are dominated by the shift in the cores and virtually unaffected by the underlying photospheric flux. We, therefore, conclude that the observed additional RV shift is not a relic of the photospheric RME, but is, indeed, related to the chromospheric emission.

3.3.1. Interpreting the radial velocity signature

The similarity of the chromospheric RV signature (see Fig. 5) and the photospheric RME suggests that the surface of CoRoT-2A is covered by active regions – at least the fraction eclipsed by the planet. The chromospheric and photospheric RME can, however, be described by the same model with different parameter values accounting for the physical conditions in the chromosphere and the photosphere. In particular, the wavelength-dependent center-to-limb variation and a, potentially, wavelength-dependent radius ratio must be taken into account (Vidal-Madjar et al. 2003; Dreizler et al. 2009).

In a first attempt to model the chromospheric RME, we considered only the RV offset, V_0^c, and the center-to-limb variation, i.e., the limb-darkening coefficient, ϵ, as free parameters. The remaining model parameters remained fixed at the photospheric values given in Table 1. We, again, imposed uniform priors on all parameters and used MCMC sampling to explore the posterior probability distribution. The optimal solution found after 10^6 iterations is shown in Fig. 6. The fit describes the data qualitatively, but, formally, the quality remains poor with a χ^2-value of 76.3 for 22 degrees of freedom.

In a second fitting attempt, we allowed for an extended chromosphere, i.e., a larger radius of the star, by introducing a scaling factor. Using a uniform prior for the scaling, we repeated the MCMC sampling and found that the data are reproduced best if the chromospheric radius is a factor of 1.16 (1.1, 1.23) larger than the photospheric radius, $R_{\rm ph}$. Formally, the fit is improved yielding a χ^2-value of 58.8 with 21 degrees of freedom for the lowest deviance solution.

Clearly, the 95% highest probability density (HPD) interval favors a larger chromospheric radius (see Table 2). To solidify

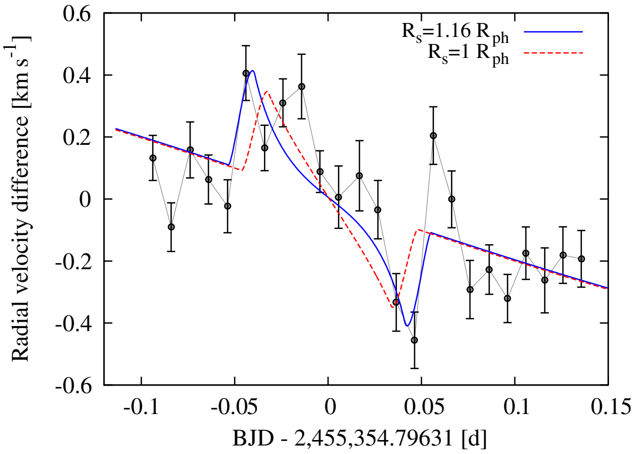

Fig. 6. Chromospheric Rossiter-McLaughlin effect: data points (filled black circles), best-fit model with radii fixed at *photospheric* values (dashed red), and best-fit model with free stellar radius (solid blue).

Table 2. Results of the modeling of the chromospheric Rossiter-McLaughlin effect.

Quantity	Value[a]	95 % HPD
ϵ	−0.4	[−16.5, 1.0[b]]
V_0^c [km s^{-1}]	21.953	[21.918, 21.987]
ϵ	−4.4	[−20.0[b] , −0.6]
V_0^c [km s^{-1}]	21.957	[21.922, 21.992]
R_s [$R_{\rm photo}$]	1.16	[1.10, 1.23]

Notes. [(a)] We report the value pertaining to the lowest deviance solution after 10^6 iterations. [(b)] This limit of the credibility interval is determined by the finite range of our uniform prior.

the significance of the result, we used an F-test to compare the vying models. We calculated the estimator

$$\hat{F} = \frac{(\chi_a^2 - \chi_b^2)/(\nu_a - \nu_b)}{\chi_b^2/\nu_b} \quad (2)$$

and compared its value to an F-distribution with $\nu_a - \nu_b$ and ν_b degrees of freedom (e.g., Rawlings et al. 1998). We found that the improvement is significant at the 98% confidence level.

In an alternative approach, we used the method described by Newton & Raftery (1994, see their Sect. 7, Eq. (13)) to estimate the marginal likelihood using the harmonic mean computed from the posterior sample generated by the Markov chain. Given the marginal likelihoods, we computed the Bayes factor, B, and obtained $\log_{10}(B) = 3.5$. In the scale introduced by Jeffreys (see, e.g., Kass & Raftery 1995, and references), this yields “decisive” evidence in favor of the model that proposes a larger chromospheric radius for CoRoT-2A. We conclude that this model provides a significantly better description of the data.

We note that a model in which the planetary radius is enlarged to account for the prolonged transit is not supported by our data. To explain the longer transit, the planetary radius would have to be larger by about a factor of two, which would drastically increase the amplitude of the RME as a whole and is inconsistent with the data.

Taking the stellar radius into account, the relative enlargement of 16% can be converted into an absolute “chromospheric” scale of 100 000 km. For the Sun, Beck & Rezaei (2011) observed Ca H and K emission up to 5000 km above the solar limb. The largest solar prominences such as the "Grand Daddy Prominence" reach projected heights of 112 000 km as measured in Hα emission (Pettit 1946). Reverting to the solar analog, we speculate that CoRoT-2A is covered with structures reminiscent of the Grand Daddy Prominence in size. Whether these structures are stable cannot be decided on the basis of the data, although, in our measurement, the chromospheric RME appears to be symmetric, which indicates the presence of extended structures on both sides of the star. We interpret this as evidence of a stable configuration or at least a high filling factor of active regions creating large chromospheric structures.

We found that ϵ, which parametrizes the chromospheric center-to-limb variation, appears to be negative. This indicates that the chromosphere is limb-brightened. At some point, the limb-brightened RME model effectively becomes a "ring model", which is relatively indifferent to further changes in ϵ. As our data do not rule out this region, the exact level of chromospheric limb-brightening cannot currently be determined.

As shown in Fig. 6, some data points are incompatible with either RME model. This may be due to the following reasons: statistics and systematics, chromospheric inhomogeneities, and intrinsic variability.

During the transit, the RME curve could be affected by plage-crossing events. We checked that features with RV amplitudes of $\approx$150 m s^{-1} can be reproduced assuming a plage region with a size similar to that of the planetary disk and twice the photospheric brightness (cf., Sect. 3.3.2). Additionally, the chromospheric emission may show intrinsic variability unrelated to the transit. However, we argue that neither intrinsic variability nor systematics due to the wavelength calibration are likely to mimic the prolonged transit signature observed in Ca II H and K. Nevertheless, such an effect cannot ultimately be excluded.

3.3.2. Distribution of chromospheric and photospheric emission

The detection of the RME in the Ca II H and K lines shows that a significant fraction of the chromospheric emission regions must be eclipsed during the entire transit. Any differences in the distribution of chromospheric and photospheric surface brightnesses should be reflected by a variable equivalent width (EW) of the Ca II H and K emission-line cores during the transit, because chromospheric emission would be measured relative to the photospheric continuum. To obtain an estimate of the EW, we summed the signal in 1.4 Å wide bands centered on the Ca II H and K emission-line cores (see Fig. 7) and compared it to the signal obtained in the two photospheric bands in the regions 3981–3996 Å and 3861–3909 Å. The choice of these bands is arbitrary, but we verified that our results depend only weakly on this choice. The resulting ratio, R, is a measure of the quantity

$$R(t) = \frac{\langle b_{\rm vis}(\lambda_{\rm Ca})\rangle(t)}{\langle b_{\rm vis}(\lambda_{\rm Ph})\rangle(t)}, \tag{3}$$

where $\langle b_{\rm vis}(\lambda_{\rm Ca,Ph})\rangle$ is the mean surface brightnesses of the visible fraction of the star in Ca II H and K and the photosphere.

Figure 8 shows the outcome. No variation in the observed EW is detectable within the limits of our uncertainties. The ratio of Ca II H and K signal to the continuum signal in the aforementioned bands amounts to $R = (2.31 \pm 0.028) \times 10^{-2}$. The given error corresponds to the sample standard deviation. It does not differ for in- and out-of-transit points and is attributed to a combination of measurement errors and intrinsic variability.

If the photospheric and chromospheric emission were equally distributed on the visible surface of CoRoT-2A, the EW

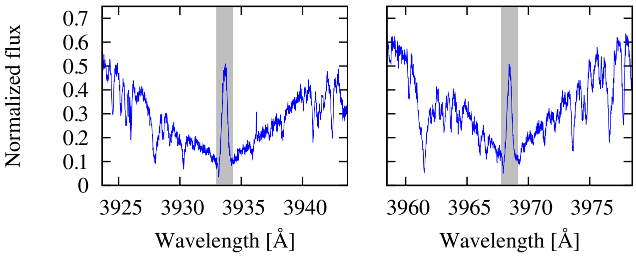

Fig. 7. CoRoT-2A's Ca II H and K lines. Gray intervals indicate the bands used to measure the flux in the emission-line cores (see text for details).

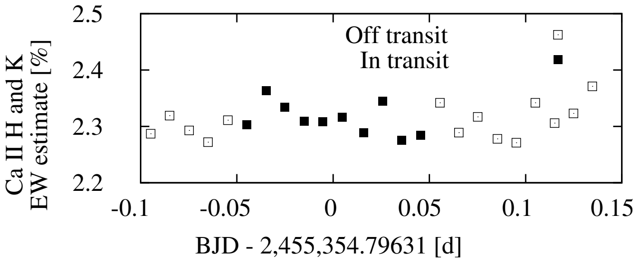

Fig. 8. Ratio of integrated fluxes in both the Ca II H and K emission-line cores (see Fig. 7) to those in the comparison bands (see text).

of the Ca II H and K cores and, therefore, R would remain constant during transit, because the occultation has the same effect on both photospheric and chromospheric emission. A change in R indicates a deviation from the equal distribution on the currently occulted section of the stellar disk. If, for example, an active region is occulted, more chromospheric than photospheric emission should be blocked, leading to a decrease in R.

In the following, we quantify the relation between surface brightness distribution and R. The brightness, $B(\lambda)$, of the entire stellar disk at any wavelength, λ, can be written as

$$B(\lambda) = f\langle b_{\rm occ}(\lambda)\rangle + F\langle b_{\rm vis}(\lambda)\rangle \tag{4}$$

where f is the occulted area of the stellar disk and F the visible area. For the special case of $\langle b_{\rm occ}\rangle = \langle b_{\rm vis}\rangle = b_0$, we obviously obtain $B = (f + F)b_0$. Starting from exactly this situation, we introduce a bright chromospheric plage region with a local surface brightness, $\langle b'_{\rm occ}(\lambda_{\rm Ca})\rangle$, which is a factor of α higher than the mean surface brightness. Hence, we write $\langle b'_{\rm occ}(\lambda_{\rm Ca})\rangle = \alpha b_0(\lambda_{\rm Ca})$.

The conservation of total brightness demands that a local increase in the surface brightness across the eclipsed section of the star must be balanced by an adjustment of the mean brightness of the visible fraction, $\langle b_{\rm vis}(\lambda_{\rm Ca})\rangle$, which we parametrize by β so that $\langle b'_{\rm vis}(\lambda_{\rm Ca})\rangle = \beta b_0$.

Assuming that the photospheric surface brightness remains unaffected, the ratio R is proportional to β (see Eq. (3)). Starting from $B = f\alpha b_0 + F\beta b_0$, we obtain the relation

$$\beta = 1 + \frac{f}{F}(1 - \alpha). \tag{5}$$

In the case of CoRoT-2A, the factor f/F amounts to $\approx$0.03. Thus, if a plage region with a local Ca II H and K surface brightness that is a factor of $\alpha = 15$ higher than the mean brightness were eclipsed, the observed EW would be a factor of 2 lower. The relative stability of R, which varies by only about 3%, suggests that the surface brightness of the Ca II H and K emission does not strongly deviate from that of the photosphere. According to our result, the photospheric and chromospheric surface brightnesses are the same to within a factor of about 2.

An analysis of the chromospheric emission in the Ca II infrared triplet, which is visible as a substantial filling-in of the line cores, yielded compatible but less conclusive results due to the much larger photospheric contribution.

3.4. Searching for planetary Na I absorption

During a primary eclipse, stellar light passes through the planetary atmosphere, potentially giving rise to planetary absorption features. These features have, indeed, been detected in several systems using the Hubble Space Telescope and more recently ground-based data (e.g., Charbonneau et al. 2002; Redfield et al. 2008). According to Seager & Sasselov (2000), the most prominent planetary absorption features in the optical should be caused by neutral sodium.

To search for planetary sodium absorption features in our spectra, we combined them to yield in- and out-of-transit templates with a S/N ratio of 90 and 110 around Na I, respectively. As discussed by Schröter et al. (2011), the sodium doublet is affected by strong blue-shifted interstellar absorption. Additionally, the line core is contaminated by residual sky emission. In the course of our observations, the strength of the sky contribution increased monotonically following the airmass. We found that a correction for the sky emission is problematic, because the sky spectrum shifts in wavelength relative to the stellar spectrum producing spurious absorption in the in-transit template. The quality of our combined template spectra does not allow us to subtract a heuristic model of the sky emission without introducing additional residuals. Therefore, we found it impossible to deduce a reasonable upper limit to the planetary sodium absorption.

4. Discussion and conclusion

We have presented our analysis of 24 high-resolution UVES spectra of CoRoT-2A and simultaneously obtained photometry, observed during a planetary transit. We have reported on the – to the best of our knowledge – first detection of a prolonged RME in the chromospheric Ca II H and K emission-line cores. Furthermore, we have presented a joint analysis of the photospheric RME and the transit photometry.

During our analysis, we found that the wavelength calibration of UVES undergoes a substantial drift, which we corrected using telluric standards. While the modeling of the RME depends on the details of this correction, neither the detection of the photospheric nor the chromospheric RME does.

Our modeling yielded an improved estimate of the orbital period of the planet and shows that our data favor an RME amplitude slightly larger than that reported by Bouchy et al. (2008) using HARPS and SOPHIE data. This results in a larger estimate of the projected rotational velocity, $\upsilon \sin(I_s)$, of the star. This difference potentially reflects a change in the total stellar spot coverage between the observations. As Alonso et al. (2008), we derived a weak limb-darkening relative to the theoretical numbers given by Claret (2004). We speculate that a larger contribution from plage regions and, therefore, the observed activity, may be responsible for this. While the planet clearly passes across the stellar disk, our search for planetary absorption features in sodium remained inconclusive, owing to the lack of signal and contaminating sky emission.

The presence of the chromospheric RME indicated that chromospheric emission was eclipsed during every phase of the visual transit – and beyond. We present evidence that the transit observed in Ca II H and K lasts about 15% longer than its visual counterpart. Our modeling shows that the data are most closely reproduced by increasing the size of the stellar chromosphere. In contrast, boosting the planetary radius by a factor of two, as would be needed to explain the longer transit, is incompatible with the data. The observed chromospheric scale of 100 000 km is compatible with large solar structures such as the "Grand Daddy Prominence". Our observations indicate that such structures could cover a substantial fraction of the surface of CoRoT-2A and other very active stars.

The analysis of the chromospheric RME favors chromospheric limb-brightening. However, in a subsequent analysis of the EW of the Ca II H and K emission-line cores, we found no differences between the surface brightness distributions of chromospheric and photospheric emission to within the uncertainties of our data.

Besides the scale height of the chromosphere, the analysis of the chromospheric RME allows to explore the structure of the stellar chromosphere covered by the planetary disk, i.e., the center-to-limb variation and inhomogeneities due to active regions. Indeed, the asymmetry of the chromospheric RME curve (see Fig. 6; $0 <$ time < 0.05 d) may be a consequence of inhomogeneities in the chromospheric surface-brightness distribution. However, the sparse phase coverage, the uncertainties imposed by the instrumental RV drift, and the likely presence of intrinsic variability do not allow to safely attribute these variations to surface features. Nonetheless, both points could be addressed by dedicated observations with today's instrumentation. In particular, what is needed to verify our results is higher temporal resolution, spectra of equivalent or higher S/N, and improved RV stability – hence, a brighter target.

To increase the amount of chromospheric signal, future observations could include other emission-line cores in the UV region such as the Mg II H and K lines at ≈2800 Å, which are not covered by the present data. As for Ca II H and K, these lines have weak photospheric contributions, but are, unfortunately, impossible to observe from the ground.

As an alternative to the chromospheric RME, the chromospheric center-to-limb variation and inhomogeneities could also be studied using narrow-band transit-photometry centered on chromospheric emission lines (Assef et al. 2009; Schlawin et al. 2010). In contrast to the RME, however, this method relies on a precise photometric calibration (Snellen 2004), which is difficult to achieve especially in ground-based observations.

Our analysis demonstrates the power of the Rossiter-McLaughlin effect for the exploration of the stellar atmosphere and clearly underlines the need for dedicated observations.

Acknowledgements. We thank the anonymous referee for thoughtful comments. This work makes use of observational data obtained with UVES at the ESO Very Large Telescope, Paranal, Chile. S.C., C.v.E., and K.F.H. are supported in the framework of the DFG-funded Research Training Group "Extrasolar Planets and their Host Stars" (DFG 1351/1). and U.W. acknowledge support from the DLR under grant 50OR0105. S.S. acknowledges support from the DLR under grant 50OR0703. PROMPT observations were made possible by the Robert Martin Ayers Science Fund.

Appendix A: Details of observations and data analysis

Table A.1. Details of data and data analysis.

No.	HJD −2 400 000 d	IS[a]	Airmass	Seeing [″]	Pressure [hPa]	Temp. [°C]	T^b	RV [km s^{-1}]	ΔRV Ca II [km s^{-1}]
1	55 354.701526	n	1.377	0.94	744.27	10.62	n	23.424 ± 0.017	0.16 ± 0.07
2	55 354.711337	n	1.319	1.07	744.31	10.59	n	23.412 ± 0.017	−0.06 ± 0.08
3	55 354.721503	n	1.270	0.89	744.32	10.57	n	23.400 ± 0.017	0.19 ± 0.09
4	55 354.731315	n	1.231	1.08	744.32	10.52	n	23.389 ± 0.017	0.09 ± 0.08
5	55 354.741612	n	1.196	0.95	744.29	10.38	n	23.335 ± 0.016	0.01 ± 0.09
6	55 354.751424	n	1.170	1.03	744.25	10.26	y	23.357 ± 0.017	0.44 ± 0.09
7	55 354.761459	n	1.149	1.07	744.19	10.24	y	23.559 ± 0.017	0.20 ± 0.07
8	55 354.771271	n	1.133	1.12	744.16	10.23	y	23.528 ± 0.017	0.34 ± 0.08
9	55 354.781191	n	1.122	1.36	744.08	10.26	y	23.422 ± 0.022	0.41 ± 0.10
10	55 354.791007	n	1.115	1.31	743.96	10.20	y	23.376 ± 0.016	0.12 ± 0.07
11	55 354.801043	n	1.113	1.15	743.89	10.26	y	23.233 ± 0.020	0.03 ± 0.10
12	55 354.812237	y	1.116	1.45	743.80	10.12	y	23.086 ± 0.019	0.08 ± 0.11
13	55 354.822116	y	1.124	1.29	743.78	10.13	y	22.940 ± 0.023	−0.04 ± 0.09
14	55 354.831931	y	1.135	0.98	743.73	9.91	y	22.990 ± 0.019	−0.32 ± 0.09
15	55 354.841743	y	1.152	0.98	743.74	9.91	y	23.100 ± 0.020	−0.44 ± 0.09
16	55 354.851776	y	1.174	0.95	743.70	9.85	n	23.152 ± 0.021	0.23 ± 0.09
17	55 354.861589	y	1.201	0.92	743.78	9.92	n	23.096 ± 0.030	0.03 ± 0.09
18	55 354.871404	y	1.235	0.83	743.80	9.86	n	23.056 ± 0.051	−0.26 ± 0.09
19	55 354.881691	y	1.277	0.85	743.75	9.89	n	23.121 ± 0.033	−0.20 ± 0.08
20	55 354.891506	y	1.326	0.83	743.68	9.77	n	23.048 ± 0.029	−0.29 ± 0.08
21	55 354.901320	y	1.385	0.71	743.68	9.78	n	23.014 ± 0.037	−0.15 ± 0.09
22	55 354.911400	y	1.456	0.73	743.71	9.91	n	22.950 ± 0.044	−0.23 ± 0.11
23	55 354.921213	y	1.539	0.86	743.74	10.15	n	22.984 ± 0.058	−0.15 ± 0.09
24	55 354.931026	y	1.640	1.18	743.79	9.98	n	22.890 ± 0.034	−0.16 ± 0.09

Notes. [(a)] Was the Image Slicer (IS) used? (Yes/No). [(b)] Was the observation obtained during transit? (Yes/No).

References

Albrecht, S., Winn, J. N., Johnson, J. A., et al. 2011, ApJ, 738, 50
Alonso, R., Auvergne, M., Baglin, A., et al. 2008, A&A, 482, L21
Ammler-von Eiff, M., Santos, N. C., Sousa, S. G., et al. 2009, A&A, 507, 523
Assef, R. J., Gaudi, B. S., & Stanek, K. Z. 2009, ApJ, 701, 1616
Beck, C. A. R., & Rezaei, R. 2011, A&A, 531, A173
Bouchy, F., Queloz, D., Deleuil, M., et al. 2008, A&A, 482, L25
Charbonneau, D., Brown, T. M., Noyes, R. W., & Gilliland, R. L. 2002, ApJ, 568, 377
Claret, A. 2004, A&A, 428, 1001
Czesla, S., Huber, K. F., Wolter, U., Schröter, S., & Schmitt, J. H. M. M. 2009, A&A, 505, 1277
Dekker, H., D'Odorico, S., Kaufer, A., Delabre, B., & Kotzlowski, H. 2000, in SPIE Conf. Ser. 4008, ed. M. Iye, & A. F. Moorwood, 534
Dreizler, S., Reiners, A., Homeier, D., & Noll, M. 2009, A&A, 499, 615
ESO Quality Control Group 2005, UVES – general pipeline information, http://www.eso.org/observing/dfo/quality/UVES/pipeline/
Fabrycky, D. C., & Winn, J. N. 2009, ApJ, 696, 1230
Figueira, P., Pepe, F., Lovis, C., & Mayor, M. 2010, A&A, 515, A106
Gillon, M., Lanotte, A. A., Barman, T., et al. 2010, A&A, 511, A3
Giménez, A. 2006, ApJ, 650, 408
Gray, R. O., & Corbally, C. J. 1994, AJ, 107, 742
Hirano, T., Suto, Y., Taruya, A., et al. 2010, ApJ, 709, 458
Huber, K. F., Czesla, S., Wolter, U., & Schmitt, J. H. M. M. 2009, A&A, 508, 901
Huber, K. F., Czesla, S., Wolter, U., & Schmitt, J. H. M. M. 2010, A&A, 514, A39
Jones, E., Oliphant, T., Peterson, P., et al. 2001, SciPy: Open source scientific tools for Python, http://www.scipy.org
Kass, R. E., & Raftery, A. E. 1995, J. Am. Stat. Assoc., 90, 773
Kaufer, A., Dumas, C., & Monaco, L. 2011, UV-Visual Echelle Spectrograph User manual, VLT-MAN-ESO-13200-1825, Issue 88.2
Knutson, H. A., Howard, A. W., & Isaacson, H. 2010, ApJ, 720, 1569
Kurucz, R. L. 1993, SYNTHE spectrum synthesis programs and line data (Cambridge, MA: Smithsonian Astrophysical Observatory)
Lanza, A. F., Pagano, I., Leto, G., et al. 2009, A&A, 493, 193
McLaughlin, D. B. 1924, ApJ, 60, 22
Newton, M. A., & Raftery, A. E. 1994, J. R. Statist. Soc. B, 56, 3
Ohta, Y., Taruya, A., & Suto, Y. 2005, ApJ, 622, 1118
Pál, A. 2008, MNRAS, 390, 281
Patil, A., Huard, D., & Fonnesbeck, C. J. 2010, J. Stat. Soft., 35, 1
Pettit, E. 1946, PASP, 58, 310
Piskunov, N. E., & Valenti, J. A. 2002, A&A, 385, 1095
Piskunov, N. E., Kupka, F., Ryabchikova, T. A., Weiss, W. W., & Jeffery, C. S. 1995, A&AS, 112, 525
Radick, R. R., Lockwood, G. W., Skiff, B. A., & Baliunas, S. L. 1998, ApJS, 118, 239
Rawlings, J. O., Pantula, S. G., & Dickey, D. A. 1998, Applied regression analysis, 2nd edn., Springer texts in statistics (New York, NY: Springer)
Redfield, S., Endl, M., Cochran, W. D., & Koesterke, L. 2008, ApJ, 673, L87
Reichart, D., Nysewander, M., Moran, J., et al. 2005, Nuovo Cimento C Geophysics Space Physics C, 28, 767
Reiners, A. 2009, A&A, 498, 853
Rossiter, R. A. 1924, ApJ, 60, 15
Rothman, L. S., Gordon, I. E., Barbe, A., et al. 2009, J. Quant. Spec. Radiat. Transf., 110, 533
Schlawin, E., Agol, E., Walkowicz, L. M., Covey, K., & Lloyd, J. P. 2010, ApJ, 722, L75
Schlesinger, F. 1910, Publications of the Allegheny Observatory of the University of Pittsburgh, 1, 123
Schröter, S., Czesla, S., Wolter, U., et al. 2011, A&A, 532, A3
Seager, S., & Sasselov, D. D. 2000, ApJ, 537, 916
Snellen, I. A. G. 2004, MNRAS, 353, L1
Snellen, I. A. G., de Mooij, E. J. W., & Burrows, A. 2010, A&A, 513, A76
Triaud, A. H. M. J., Queloz, D., Bouchy, F., et al. 2009, A&A, 506, 377
Vidal-Madjar, A., Lecavelier des Etangs, A., Désert, J., et al. 2003, Nature, 422, 143
Wolter, U., & Schmitt, J. H. M. M. 2005, A&A, 435, L21
Zucker, S. 2003, MNRAS, 342, 1291

Astronomy & Astrophysics manuscript no. corot7˙Xray˙final
March 16, 2012

The high-energy environment in the super-earth system CoRoT-7

K. Poppenhaeger[1], S. Czesla[1], S. Schröter[1], S. Lalitha[1], V. Kashyap[2], and J.H.M.M. Schmitt[1]

[1] Hamburger Sternwarte, Gojenbergsweg 112, 21029 Hamburg, Germany
e-mail: katja.poppenhaeger@hs.uni-hamburg.de
[2] Harvard-Smithsonian Center for Astrophysics, 60 Garden Street, Cambridge, MA 02138, USA

Received 23 November 2011; accepted 28 February 2012

ABSTRACT

High-energy irradiation of exoplanets has been identified to be a key influence on the stability of these planets' atmospheres. So far, irradiation-driven mass-loss has been observed only in two Hot Jupiters, and the observational data remain even more sparse in the super-earth regime. We present an investigation of the high-energy emission in the CoRoT-7 system, which hosts the first known transiting super-earth. To characterize the high-energy XUV radiation field into which the rocky planets CoRoT-7b and CoRoT-7c are immersed, we analyzed a 25 ks XMM-*Newton* observation of the host star. Our analysis yields the first clear (3.5σ) X-ray detection of CoRoT-7. We determine a coronal temperature of ≈ 3 MK and an X-ray luminosity of 3×10^{28} erg s^{-1}. The level of XUV irradiation on CoRoT-7b amounts to $\approx 37\,000$ erg cm^{-2} s^{-1}. Current theories for planetary evaporation can only provide an order-of-magnitude estimate for the planetary mass loss; assuming that CoRoT-7b has formed as a rocky planet, we estimate that CoRoT-7b evaporates at a rate of about 1.3×10^{11} g s^{-1} and has lost $\approx 4 - 10$ earth masses in total.

Key words. Stars: activity – Stars: planetary systems – Planets and satellites: atmospheres – X-rays: stars – X-rays: individuals: CoRoT-7 – Stars: coronae

1. Introduction

After more than a decade of finding Jovian exoplanets, planetary research has entered a new stage heralded by the discovery of low-mass — possibly Earth-like — exoplanets. Léger et al. (2009) reported on the detection of the first known transiting super-earth, CoRoT-7b. In quick succession, intense radial-velocity follow-up revealed a second, CoRoT-7c (Queloz et al. 2009), and potentially a third planet, CoRoT-7d (Hatzes et al. 2010), making CoRoT-7 a compact super-earth system.

CoRoT-7b orbits its host star every 0.85 d, has a mass of $\approx$ 7.4 M$_\oplus$, and a semi-major axis of 0.017 AU (Hatzes et al. 2011). CoRoT-7c orbits at a distance of 0.046 AU, has roughly twice CoRoT-7b's mass, and an orbital period of 3.7 d (Queloz et al. 2009). The spectral properties of the host star, CoRoT-7, have been analyzed before (Léger et al. 2009; Bruntt et al. 2010). CoRoT-7 has an effective temperature of 5250 ± 60 K, a surface gravity of $\log(g) = 4.47 \pm 0.05$, and a metal overabundance of [M/H]= 0.12 ± 0.06 with an abundance pattern consistent with that of the Sun. Bruntt et al. (2010) concluded that CoRoT-7b orbits a main-sequence star of spectral type G8V-K0V.

The two super-earths CoRoT-7b and CoRoT-7c cause RV amplitudes of only $\approx$ 5 m s^{-1}. Accurate RV measurements in the CoRoT-7 system are made difficult because of the host star's activity; indeed, the analysis of Queloz et al. (2009) showed that the dominating RV signal can be attributed to stellar rotation and, thus, activity. Those authors found a mean $\log(R'(HK))$ index of -4.612 and a 2% variation in phase with the 23 d stellar rotation period. This result is in line with the optical variability observed in the CoRoT light-curve (Léger et al. 2009). Pinpointing the exact mass of CoRoT-7b has proven to be difficult because of the fairly high activity of the host star. The mass estimates of various authors differ by several Earth masses, see for example Queloz et al. (2009), Hatzes et al. (2010), and Ferraz-Mello et al. (2011); here we use the mass determination from Hatzes et al. (2011) of $M_p = 7.4$ M$_\oplus$, yielding a mean planetary density of $\rho_p = 10.4$ g cm^{-3}.

Interestingly, the known super-earths differ drastically in their physical properties. For example, the Earth-like density of 7 – 10 g cm^{-3} found for CoRoT-7b (Bruntt et al. 2010; Hatzes et al. 2011) is in sharp contrast to findings for GJ 1214b, which shows a density of only 1.9 ± 0.4 g cm^{-3}, suggesting the existence a gaseous envelope (Rogers & Seager 2010; Nettelmann et al. 2011). One possible source of this differences is the high-energy irradiation from the planets' host stars, which has been identified as the main driver of planetary mass-loss and is therefore an important factor for their evolution (e.g., Sanz-Forcada et al. 2010). Observational evidence for ongoing evaporation has been found for two transiting Hot Jupiters: HD 209458b (Vidal-Madjar et al. 2003) and HD 189733b (Lecavelier Des Etangs et al. 2010). The accumulated effect of stellar high-energy emission could have left fingerprints on today's planetary population (Sanz-Forcada et al. 2010). For CoRoT-7b, Valencia et al. (2010) showed that the accumulated planetary mass-loss may be as high as 100 M$_\oplus$ if the planet initially hosted a massive hydrogen-helium envelope and ca. 3 – 4 M$_\oplus$ if the inital planetary density was similar to today's value.

To shed light on the possible atmospheric evaporation of CoRoT-7b, we present here the first measurement of the high-energy emission of the super-earth host-star CoRoT-7.

2. Data analysis

CoRoT-7 was observed with XMM-*Newton* for approximately 25 ks on September 22, 2010 (ObsID 0652640201, PI V. Kashyap). The observation does not cover any planetary transit. For our analysis of the X-ray data we used SAS version 11.0 and followed standard routines for data reduction. The observation, carried out with the thin filter, is afflicted by strong background

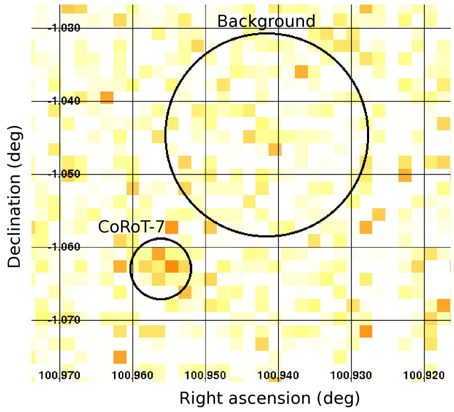

Fig. 1. Soft X-ray image of CoRoT-7, merged data from XMM-*Newton*'s MOS1, MOS2, and PN camera in the 0.2-2 keV energy band.

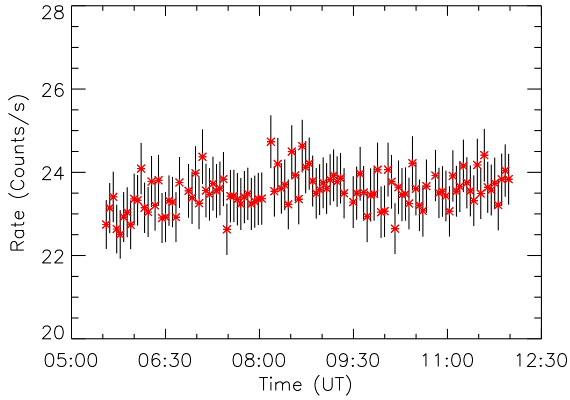

Fig. 2. UV light curve of CoRoT-7 recorded with XMM-*Newton*'s Optical Monitor and rebinned to 200 s time resolution.

after the first 10 ks; the background contribution is particularly strong in the PN detector. In our analysis we did not disregard time intervals of strong background, as this would have meant losing most of the data, too. However, the EPIC background contributes strongest at energies above 2 keV and can therefore be reduced by choosing an approriate low-energy range where moderately active stars have their strongest X-ray emission.

In Fig. 1 we show the soft X-ray image of CoRoT-7. We extracted the source signal from a circular region with 15" radius centered on the nominal, proper-motion corrected position of CoRoT-7 from SIMBAD; the background signal was measured in a source-free region close to CoRoT-7 and subtracted from the signal in the source region.

Our analysis was carried out in the soft energy band from 0.2 – 2 keV, as this is where stellar emission is typically strong for weakly to moderately active stars as CoRoT-7, see for example Telleschi et al. (2005). In this way, the strength of the background in relation to the source signal was reduced.

XMM-*Newton*'s Optical Monitor (OM) was used in the fast mode with the UVW1 filter inserted during the observation. The UVW1 filter covers a wavelength range of ca. 240-360 nm. In Fig. 2, we show the OM light-curve with 200 seconds binning obtained from the raw data.

To obtain a distance estimate from interstellar absorption-features, we analyzed 46 optical VLT-UVES spectra of CoRoT-7 obtained during five nights (Sept. 14 2008, Dec. 28 2009, Jan. 03 2010, Jan. 07 2010, Feb. 07 2010; programs 081.C-0413(C) and 384.C-0820(A)). The data were reduced using the ESO UVES-pipeline in version 4.4.8 (Ballester et al. 2000). These data have been analyzed before to study possible emission and absorption features of the planetary atmosphere, resulting in a nondetection and an upper limit of $2 - 6 \times 10^{-6} L_*$ for planetary emission in the Ca I, Ca II, and NaD lines (Guenther et al. 2011).

3. Results

To determine the X-ray luminosity of CoRoT-7 and the resulting evaporation rates, the distance to the system is crucial. Therefore, we start our discussion by deriving new and complementary distance estimates based on interstellar absorption and the Wilson-Bappu effect.

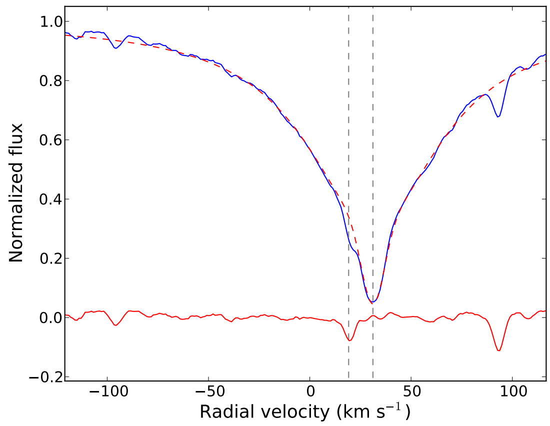

Fig. 3. Combined UVES spectra of CoRoT-7 showing the Na I D_2 line and interstellar absorption. After subtracting a Voigt profile (dashed red) from the data (blue) the blueshifted absorption feature becomes visible in the residuals (solid red); the RV shift of the interstellar feature (+19 km s^{-1}) and the CoRoT-7 system (+31 km s^{-1}) are marked by vertical, dashed lines. The absorption lines in the outer parts of the line wing are due to Fe I.

3.1. The distance to CoRoT-7

In Fig. 3 we show an excerpt of the combined optical UVES spectra of CoRoT-7. In the blue wings of the Na I absorption-line doublet, we detected an additional, narrow absorption feature, which shows a relative displacement of −12 km s^{-1} with respect to CoRoT-7 in radial velocity. This corresponds to a barycentric velocity shift of +19 km s^{-1}. Because the feature is visible in all spectra and shows no intrinsic variability, we attribute it to interstellar Na I absorption.

The equivalent widths (EWs) of the Na D_2 and Na D_1 features are 12.1 ± 1.6 mÅ and 6.8 ± 1.8 mÅ. Using the line-ratio method (Strömgren 1948), we converted this measurement into a column density of 7×10^{10} cm^{-2}. Welsh et al. (2010) compiled a catalog of interstellar Na absorption lines and provide a map of the local interstellar medium, which we used to obtain a

Table 1. X-ray net source counts of CoRoT-7 in the soft energy band (0.2-2 keV). Net counts obtained by subtracting the background signal after scaling it to the same area (factor 0.09).

	MOS 1+2	PN	EPIC merged
Source region	183	567	750
Background	1389	5578	6967
Net counts	58	65	123
Significance	3.4σ	2.1σ	3.5σ

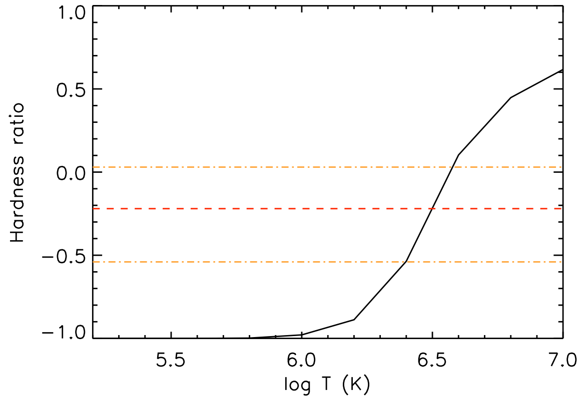

Fig. 4. Expected hardness ratio in XMM-*Newton*'s MOS and PN detectors, depending on the mean coronal temperature (black); measured hardness ratio of CoRoT-7 (red dashed) shown with 68% credibility interval (orange dash-dotted).

distance estimate from the absorption measured along the line-of-sight. Comparing the Na $D_{1,2}$ EWs with the catalog data, we determined distance estimates of 160±80 pc (D_2) and 110±70 pc (D_1) for CoRoT-7; the errors were estimated as the standard deviation of the distances of stars with interstellar Na EWs in a ±5 mÅ band around the measured EWs (cf., Schröter et al. 2011).

Using the Wilson-Bappu effect, Bruntt et al. (2010) obtained an absolute visual magnitude of 5.4 ± 0.6 mag for CoRoT-7. Given the apparent brightness of $V = 11.7$ mag, this translates into a distance of 180 ± 50 pc for CoRoT-7.

Although the results derived from Na D_2 and the photometric parallax favor a value of ≈ 170 pc, all estimates remain consistent with the distance of 150 ± 20 pc given by Léger et al. (2009). Therefore, we assume the same distance of 150 pc in our analysis.

3.2. X-ray and UV properties

We report a clear X-ray detection of CoRoT-7. The merged EPIC image (MOS1, MOS2, and PN) shows an X-ray excess at the nominal position of CoRoT-7 (see Fig. 1). The detailed source and background count numbers are given in Table 1. From the merged data, we derived a detection significance of 3.5σ in the soft energy band (0.2-2 keV).

Owing to the strong background signal a detailed analysis of the source's temporal variability and spectral properties remained impossible. To obtain an estimate of the coronal temperature despite this, we determined a hardness ratio from the collected source counts in the MOS1, MOS2, and PN detector. Using a soft band of 0.2 – 0.7 keV and a hard band of 0.7 – 2.0 keV, we determined a hardness ratio of $HR = -0.22^{+0.25}_{-0.22}$; the given errors denote the equal-tail 68% credibility interval.

We proceeded by calculating theoretical predictions for the hardness ratio assuming different coronal temperatures. The modeling was carried out using Xspec v12.0 and the result is shown in Fig. 4 along with our measurement. From this analysis, we can constrain the coronal temperature of CoRoT-7 to be between 2.5 and 3.7 MK, which is compatible with the coronal temperatures seen in moderately active stars such as the Sun at its maximum activity. Consequently, we assume a coronal temperature of 3 MK to calculate CoRoT-7's X-ray luminosity.

At a stellar distance of 150 pc, interstellar hydrogen might produce noticeable absorption of the X-ray flux. According to Ferlet et al. (1985), the interstellar Na column density is a suitable tracer for hydrogen. Our measurement of the sodium column density $N(\mathrm{Na}) = 7 \times 10^{10}$ cm^{-2} converts to a hydrogen column density of $N(\mathrm{H\,I} + \mathrm{H_2}) = 3 \times 10^{19}$ cm^{-2}. Assuming a distance of 150 pc to CoRoT-7 (see Sect. 3.1), this corresponds to a number density of about 0.1 cm^{-3} compatible with typical densities observed in the Local Cavity (Cox 2005).

Using WebPIMMS, we converted the mean count rate of a single XMM-*Newton* MOS instrument of 1.16×10^{-3} counts s^{-1} into an unabsorbed X-ray flux of 1.0×10^{-14} ergs cm^{-2} s^{-1} in the 0.2–2 keV energy band, taking into account the encircled energy fraction of 68% for our 15" extraction region. Given a distance of 150 pc, this translates into an X-ray luminosity of $3{\times}10^{28}$ erg s^{-1}. This is well in line with previous estimates derived from chromospheric Ca II H and K line emission, which yielded a predicted X-ray luminosity of $\approx 2 \times 10^{28}$ erg s^{-1} (Poppenhaeger & Schmitt 2011). For a star of spectral type late G to early K, CoRoT-7 displays a typical moderate level of coronal activity, which is also observed in stars with solar-like activity cycles (Hempelmann et al. 2006; Favata et al. 2008): with a bolometric correction of −0.437 (Flower 1996), we derived a bolometric luminosity of $\log L_{bol} = 33.3$ and, therefore, an X-ray activity indicator, $\log L_X/L_{bol}$, of −4.8.

The UV light-curve seen with the OM does not show strong flares (see Fig. 2). To determine the level and slope of the light curve, we fitted it with a linear model with free offset and gradient and determined errors using a Markov-Chain Monte-Carlo (MCMC) analysis. The mean count-rate amounts to 23.5(23.4-23.6) counts s^{-1}, where the 95% credibility interval is given in parenthesis. Using the count-to-energy conversion factors for a star of spectral type K0 from the XMM-*Newton* handbook, we calculated a flux of 9×10^{-15} erg cm^{-2} s^{-1} in the covered band of 240-360 nm. Combining this with a distance of 150 pc, we obtain a luminosity of 2.4×10^{28} erg s^{-1} in the same band.

According to our analysis, the slope amounts to $8(1.8 - 14) \times 10^{-2}$ counts h^{-1}, indicating a slight increase in UV luminosity during the observation, which may be due to intrinsic short-term variability induced by active regions or rotational modulation. Although a temporal analysis of the X-ray flux was not possible, the lack of pronounced UV variability indicates that it can be interpreted as quiescent emission.

4. Discussion: Evaporation of CoRoT-7b and CoRoT-7c

Although an X-ray luminosity of $\approx 3{\times}10^{28}$ erg cm^{-2} s^{-1} does not place CoRoT-7 among the very active stars, the extreme proximity of its planets exposes them to high levels of high-energy irradiation.

Given semi-major axes of 0.017 AU and 0.046 AU for CoRoT-7b and CoRoT-7c (Queloz et al. 2009), we calculated X-ray fluxes of $f_{X,b} = 3.7 \times 10^4$ erg cm^{-2} s^{-1} and $f_{X,c} = 5 \times 10^3$ erg cm^{-2} s^{-1} at the orbital distances of the planets. Assuming a solar X-ray luminosity of 10^{27} erg s^{-1}, these fluxes exceed the solar X-ray flux on Earth by factors of 100 000 and 14 000.

We now derive an order-of-magnitude estimate for the amount of mass that has been evaporated from CoRoT-7b due to the stellar high-energy emission. Planetary evaporation is thought to be mainly driven by X-ray and EUV irradiation. The process is hydrodynamical (Tian et al. 2005; Murray-Clay et al. 2009) and is much more efficient than pure Jeans escape. The approach has been refined for expanded absorption radii and mass-loss effects through Roche lobe overflow (Lammer et al. 2003; Erkaev et al. 2007). However, there are still considerable uncertainties about the dynamics of the process. In addition, we assume here that CoRoT-7b has formed as a rocky planet and that the orbital distance is stable; there are other calculations that consider planetary migration as well as CoRoT-7b being the solid core of an evaporated gaseous planet, which consequently derive very different mass loss histories (Jackson et al. 2010). Here, we apply the same formula as used by Sanz-Forcada et al. (2011) and Valencia et al. (2010). The latter authors argue that the mass-loss rates, originally estimated for gaseous planets, can in principle remain true also for rocky planets, because the rate of sublimation in close vicinity to the star should be able to counterbalances the mass-loss:

$$\dot{M} = \frac{3\epsilon F_{XUV}}{4G\rho_p K}, \tag{1}$$

where F_{XUV} is the incident XUV flux at the planetary orbit, G is the gravitational constant, ρ_p the mean planetary density, which we assume to be 10.4 g cm^{-3} according to Hatzes et al. (2011), and ϵ is a factor to account for heating efficiency of the planetary atmosphere, with $\epsilon = 1$ denoting that all incident energy is converted into particle escape. Several authors chose $\epsilon = 0.4$ (Valencia et al. 2010; Jackson et al. 2010), inspired by observations of the evaporating Hot Jupiter HD 209458b, and we follow their approach. However, this can only be a rough estimate of the true heating efficiency, which cannot be stated more precisely without detailed models of the dynamics of the exoplanetary atmosphere. K is a factor for taking into account effects from mass loss through Roche lobe overflow; we neglect these effects by assuming $K = 1$. This is justified because the approximate Roche lobe radius (Eggleton 1983) is about three times today's radius of CoRoT-7b . If the planetary mass had been three times as large initially, the Roche lobe radius would still have exceeded the initial planetary radius, as modeled by Seager et al. (2007) for rocky planets, by a factor of approximately two. Roche-lobe influenced mass loss was therefore likely insignificant for the planetary evolution.

Because we have not measured CoRoT-7's EUV flux, we use a relation between X-ray (0.1 – 2.5 keV) and EUV (100 – 920 Å) flux (Sanz-Forcada et al. 2011):

$$\log L_{EUV} = (4.80 \pm 1.99) + (0.860 \pm 0.073) \log L_X. \tag{2}$$

We measured the X-ray luminosity in the 0.2-2 keV band to be 3×10^{28} erg s^{-1}; we used WebPIMMS to extrapolate this to the required energy band of 0.1 – 2.5 keV, the result being 3.3×10^{28} erg s^{-1}. This leads to an EUV luminosity of $L_{EUV} = 2.1 \times 10^{29}$ erg s^{-1}, and thus a combined XUV (X-ray and EUV) luminosity of $L_{XUV} = 2.4 \times 10^{29}$ erg s^{-1}of CoRoT-7, which is about ten times higher than the X-ray luminosity alone. Substituting this number into Eq. 1 yields an estimate of 1.3×10^{11} g s^{-1} for CoRoT-7b's current mass-loss rate.

This number is higher than the one derived by Valencia et al. (2010), who estimated the XUV flux purely from an age-activity relation for solar-like stars given by Ribas et al. (2005), since no X-ray detection of the star was available. CoRoT-7 has a slightly sub-solar mass, being of spectral type G8-K0; however, for our order-of-magnitude estimate of the mass loss, the difference in activity evolution of G and early K stars is small (Lammer et al. 2009) and can be neglected. Valencia et al. (2010) estimate the XUV luminosity as 5×10^{28} erg s^{-1}. Assuming a lower planetary density than in this work, 4 – 8 g cm^{-3}, they derived a lower mass loss rate of $0.5 - 1 \times 10^{11}$ g s^{-1}.

For CoRoT-7c, we estimate that the mass-loss rate should be about an order of magnitude lower than for CoRoT-7b due to the weaker irradiation. Because this planet does, however, not transit, its radius—and thus density—remains unknown.

Planetary mass-loss rates have been measured for two Hot Jupiters so far by using the transit depth in the hydrogen Ly α line as an indicator for extended and escaping planetary atmospheres. Vidal-Madjar et al. (2003) reported a lower limit for the mass loss rate of HD 209458b of $\sim 10^{10}$ g s^{-1}. Similarly, Lecavelier Des Etangs et al. (2010) derived a mass loss rate between 10^9 and 10^{11} g s^{-1} for HD 189733b. The orders of magnitude are compatible with our calculations, even if these observational results were obtained for gaseous, not rocky planets.

Based on our mass-loss rate determination for CoRoT-7b, we can derive an order-of-magnitude estimate for the total planetary mass-loss over time. The possible stellar age range for CoRoT-7 is given by Léger et al. (2009) as 1.2 – 2.3 Gyr; we adopt here an age of 1.5 Gyr. Along the lines of Valencia et al. (2010) we assume a constant density of CoRoT-7b. Likewise, for the stellar activity evolution, we assume that the combined X-ray and EUV luminosity increases at younger stellar ages τ by a factor of $(\tau/\tau_*)^{-1.23}$ with τ_* being the current stellar age in Gyr (Ribas et al. 2005), and that the activity remains at a constant level for ages younger than 0.1 Gyr. Inserting the time-variable XUV flux into Eq. 1 and integrating over 1.5 Gyr yields a total mass loss of ca. 6 $M_\oplus$. This is higher than the result of Valencia et al. (2010) of 3 – 4 $M_\oplus$, who used a lower stellar XUV flux and lower planetary density. If we consider the uncertainty in the age determination of CoRoT-7, our estimated mass loss range extends to 4 – 10 $M_\oplus$. Given the current uncertainties in the analytical models for planetary evaporation, we consider the possible range for the true mass loss of CoRoT-7b to be even wider.

5. Conclusion

We report the first X-ray detection of CoRoT-7, host star to at least two close-in super-earths. After veryfying the distance estimate of 150 pc of Léger et al. (2009), we converted the X-ray flux of 10^{-14} erg cm^{-2} s^{-1} measured with XMM-*Newton* into a luminosity of 3×10^{28} erg s^{-1}(0.2-2 keV).

An X-ray activity indicator of $\log L_X/L_{bol} = -4.8$, combined with a likely coronal temperature of ≈ 3 MK, characterizes CoRoT-7 as a moderately active star. Employing an analytical model for planetary evaporation — with the caveat that many aspects of this evaporation are not yet understood —, the combined X-ray and EUV irradiation can be converted into an order-of-magnitude estimate of the planetary mass loss. We derive a current mass loss rate of 1.3×10^{11} g s^{-1} for the closest planet, CoRoT-7b. Assuming that the planet was formed as a rock and integrating the likely activity history of the CoRoT-7 system, we estimate that CoRoT-7b has suffered a total mass loss of $\approx 4 - 10$ Earth masses.

Acknowledgements. K.P. and S.L. acknowledge funding from the German Research Foundation (DFG) via Graduiertenkolleg 1351. S.C. and S.S. acknowledge financial support from DLR grant 50OR0703.

References

Ballester, P., Modigliani, A., Boitquin, O., et al. 2000, The Messenger, 101, 31
Bruntt, H., Deleuil, M., Fridlund, M., et al. 2010, A&A, 519, A51
Cox, D. P. 2005, ARA&A, 43, 337
Eggleton, P. P. 1983, ApJ, 268, 368
Erkaev, N. V., Kulikov, Y. N., Lammer, H., et al. 2007, A&A, 472, 329
Favata, F., Micela, G., Orlando, S., et al. 2008, A&A, 490, 1121
Ferlet, R., Vidal-Madjar, A., & Gry, C. 1985, ApJ, 298, 838
Ferraz-Mello, S., Tadeu Dos Santos, M., Beaugé, C., Michtchenko, T. A., & Rodríguez, A. 2011, A&A, 531, A161
Flower, P. J. 1996, ApJ, 469, 355
Guenther, E. W., Cabrera, J., Erikson, A., et al. 2011, A&A, 525, A24
Hatzes, A. P., Dvorak, R., Wuchterl, G., et al. 2010, A&A, 520, A93
Hatzes, A. P., Fridlund, M., Nachmani, G., et al. 2011, ApJ, 743, 75
Hempelmann, A., Robrade, J., Schmitt, J. H. M. M., et al. 2006, A&A, 460, 261
Jackson, B., Miller, N., Barnes, R., et al. 2010, MNRAS, 407, 910
Lammer, H., Odert, P., Leitzinger, M., et al. 2009, A&A, 506, 399
Lammer, H., Selsis, F., Ribas, I., et al. 2003, ApJ, 598, L121
Lecavelier Des Etangs, A., Ehrenreich, D., Vidal-Madjar, A., et al. 2010, A&A, 514, A72
Léger, A., Rouan, D., Schneider, J., et al. 2009, A&A, 506, 287
Murray-Clay, R. A., Chiang, E. I., & Murray, N. 2009, ApJ, 693, 23
Nettelmann, N., Fortney, J. J., Kramm, U., & Redmer, R. 2011, ApJ, 733, 2
Poppenhaeger, K. & Schmitt, J. H. M. M. 2011, Astronomische Nachrichten, 332, 1052
Queloz, D., Bouchy, F., Moutou, C., et al. 2009, A&A, 506, 303
Ribas, I., Guinan, E. F., Güdel, M., & Audard, M. 2005, ApJ, 622, 680
Rogers, L. A. & Seager, S. 2010, ApJ, 716, 1208
Sanz-Forcada, J., Micela, G., Ribas, I., et al. 2011, A&A, 532, A6+
Sanz-Forcada, J., Ribas, I., Micela, G., et al. 2010, A&A, 511, L8
Schröter, S., Czesla, S., Wolter, U., et al. 2011, A&A, 532, A3+
Seager, S., Kuchner, M., Hier-Majumder, C. A., & Militzer, B. 2007, ApJ, 669, 1279
Strömgren, B. 1948, ApJ, 108, 242
Telleschi, A., Güdel, M., Briggs, K., et al. 2005, ApJ, 622, 653
Tian, F., Toon, O. B., Pavlov, A. A., & De Sterck, H. 2005, ApJ, 621, 1049
Valencia, D., Ikoma, M., Guillot, T., & Nettelmann, N. 2010, A&A, 516, A20
Vidal-Madjar, A., Lecavelier des Etangs, A., Désert, J., et al. 2003, Nature, 422, 143
Welsh, B. Y., Lallement, R., Vergely, J., & Raimond, S. 2010, A&A, 510, A54

Part III.

Conclusions

7. Closing thoughts

7.1. Summary and conclusions

In this thesis, orbital dynamics of extrasolar planetary systems and stellar activity in planet-bearing stars were studied in the landmark systems TrES-2, CoRoT-2, and CoRoT-7. Different observational techniques like ground- and space-based photometry, and X-ray and optical spectroscopy were used in concert to study the structure and evolution of these planetary systems and their host stars.

7.1.1. TrES-2

Ground-based photometry was used to search for secular changes of the orbit inclination of the transiting exoplanet TrES-2b. In a first step, my coworkers and I demonstrated that our data comprising several transits indeed confirm the presence of a secular inclination change (Mislis et al., 2010, Sect. 5.2). We tried to carefully rule out errors introduced by the adopted limb-darkening prescription using simultaneous multicolor photometry. Our results indicate that the transit can be modeled consistenly in the four filter bands using theoretically computed limb-darkening coefficients. We showed that the observed change in orbital inclination can be interpreted as regression of the nodes of the planetary orbit. While the observed effect would require an implausibly large oblateness of the host star, it can be readily explained as being caused by an external Jovian-mass perturber. As a perturber should reveal itself through transit-timing variations (TTV), we performed numerical simulations showing that the expected amplitude for TTVs is below our upper limits.

Several studies from other authors tried to corroborate or reject our results, however, the available ground-based data still remained insufficient to decide upon the issue. This changed with the advent of the Kepler space telescope, which included TrES-2 as one of its short-cadence targets from the very beginning of the mission. In a second step, my coworkers and I presented a consistent analysis of the first four quarters of Kepler data of TrES-2 together with all publicly available ground-based data covering a time span of three years since the discovery of the system (Schröter et al., 2012, Sect. 5.3). We further took into account the latest information regarding the presence of a third light and the most recent set of limb-darkening coefficients computed from PHOENIX spectra.

The superior quality of the Kepler data allows to constrain all parameters of the system at once. However, we found that the orbital geometry of the system itself introduces a strong degeneracy between the limb-darkening parameters. We therefore fixed the limb-darkening at their theoretically calculated values using a four-parametric non-linear prescription.

Using the accurately determined orbital parameters of the system, we reanalyzed the ground-based data searching for changes in the orbital inclination and TTVs. Our study shows that ground- and space-based photometry can be analyzed in a common scheme if one carefully accounts for wavelength-dependent limb-darkening and third light contributions. The secular trend in inclination is still visible in our first set of ground-based observations, however, the reduced errors clearly show that these observations do not yield consistent results. Our analysis of the Kepler data rules out the previously claimed change in orbital inclination.

We searched for effects that could cause the observed deviation, but found no simple explanation related to the modeling. However, we cannot exclude subtleties in the data reduction and problems during the observations like time-dependent noise, which would yield underestimated parameter errors.

The Kepler data further reveal indications for a much smaller secular inclination change just below our detection threshold but display no detectable TTV signal. Our study points out the intricacies present in the search for long-term variations in the orbital elements of extrasolar planetary systems. Complications can be introduced during the observation, reduction, and modeling especially of ground-based data. It further demonstrates the potential of space-based photometry as a tool to calibrate ground-based observations by fixing the system parameters.

7.1.2. CoRoT-2

The next study presented a thorough characterization of CoRoT-2, an outstanding system comprising a particularly active star orbited by a close-in Jovian planet. Its host star shows a pronounced, regular pattern of optical variability caused by magnetic activity. My coworkers and I analyzed newly obtained time-resolved VLT/UVES spectroscopy and a 15 ks Chandra snapshot, both obtained during planetary transit.

In the first publication (Schröter et al., 2011, Sect. 6.2), we provided an analysis of the co-added optical spectrum of CoRoT-2A. The optical data was used to derive the fundamental stellar parameters confirming and improving earlier estimates. We analyzed several activity diagnostics, all pointing towards strong chromospheric activity, and investigated indicators such as Li abundance and interstellar absorption to provide constraints on the age and distance of the system. Our results indicate that CoRoT-2 is a young stellar system with an age between 100 and 300 million years located at a distance of about 270 parsec. We further extracted a spectrum of the late-type stellar companion of CoRoT-2A from our observations. Our data provide the first detailed spectroscopic characterization of this object and confirm that it is most likely gravitationally bound.

The Chandra snapshot clearly reveals the presence of coronal X-ray emission originating in hot plasma at temperatures of about 8 million Kelvin. An activity level of $\log L_X/L_{\rm bol} = -4.2$ indicates that CoRoT-2A is an active star, also by X-ray standards. The close-in planet is thus prone to a large amount of high-energy radiation, which is thought to lead to the gradual evaporation of the planetary atmosphere (cf. Fig. 7.1).

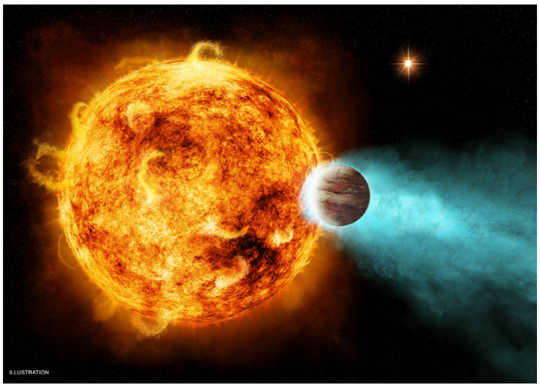

Figure 7.1.: *"CoRoT-2A: Star Blasts Planet With X-rays."* Artist's view of the CoRoT-2 system illustrating a NASA press release based on our results (Credit: NASA/CXC/M. Weiss).

The late-type stellar companion remains undetected in X-rays. Our upper limit on its luminosity of 9×10^{26} erg s^{-1} is two orders of magnitude below the typical values for K-type dwarfs of Pleiades age, but would be compatible with an evolved object on the main-sequence. These findings challenge our understanding of the stellar system, because, apparently, both stellar components may not be in the same evolutionary stage. Either, the late-type companion is old enough to have already become sufficiently inactive, or CoRoT-2A appears to be younger than it actually is.

The Chandra X-ray light curve shows no indications for the occultation of substantial parts of the corona during the planetary transit. Apparently, the planet did not occult a strong concentration of X-ray emitting material. This implies that the coronal emission is either distributed homogeneously or concentrated at higher latitudes not covered by the planetary disk.

The CoRoT-2 system provides ideal conditions to resolve surface features on the active host star using the spatial information provided by planetary transits. In our second study focusing on CoRoT-2, my coauthors and I followed this approach by analyzing the time-dependent spectroscopic and photometric data obtained during the transit (Czesla et al., 2012, Sect. 6.3).

The UVES spectra taken during a single planetary transit provide a time resolution of 800 s. We presented a joint analysis of the Rossiter-McLaughlin effect visible in photospheric absorption lines together with simultaneously obtained PROMPT photometry. Telluric lines were used to correct the wavelength calibration, originally obtained using ThAr spectra, for instrumental and environmental trends. Our results are in line with earlier measurements and show the feasibility of our approach to use telluric lines as wavelength calibration.

Furthermore, we reported on the first detection of the Rossiter-McLaughlin effect in the chromospheric emission cores of the Ca II H and K lines. Our data indicate, that the chromospheric Rossiter-McLaughlin effect sets in before the photospheric transit and lasts longer. We show that such a prolonged effect is compatible with the stellar chromospheric radius being 16 % larger than the photospheric radius of the star. A detailed analysis of the variability of the H and K emission features shows that the distributions of photospheric and chromospheric surface brightnesses are the same to within a factor of about two. Our results suggest that CoRoT-2A is covered (at least beneath the planetary path) with chromospheric plages and off-limb prominences comparable to the largest prominences occasionally visible on the Sun.

Our study demonstrates that the Rossiter-McLaughlin effect can be used as a tool for the exploration of the stellar chromosphere. However, the detected signal is easily obliterated by instrumental effects and intrinsic variability of the star. Our observations therefore underline the need for dedicated observations.

7.1.3. CoRoT-7

My coauthors and I reported the first X-ray detection of the active G8- to K0-type dwarf CoRoT-7A (Poppenhaeger et al., 2012, Sect. 6.4). The CoRoT-7 system comprises two planets in the terrestrial mass regime, one of them transiting, in close orbits around their host star.

Archival UVES spectra were used to derive a distance estimate from interstellar sodium absorption and the previously measured Wilson-Bappu effect. The coronal X-ray flux of CoRoT-7A obtained from an XMM-Newton exposure of the system translates into an X-ray activity level of $\log L_X/L_{\mathrm{bol}} = -4.8$. The extreme proximity of the two super-earth planets exposes them to high levels of high-energy irradiation. Employing a simple model for the decrease of X-ray and EUV radiation with age, we estimate that CoRoT-7b has suffered a total mass loss of about $4-10$ Earth masses since its formation.

7.2. Future work

Long-term space-based photometry obtained by CoRoT and Kepler has ushered in a new era of exoplanet research. Both telescopes provide photometric data of unparalleled quality. Kepler's recent discovery of a stellar system comprising a solar-like star with three Neptunes and two Earth-sized planets (Fressin et al., 2012) shows that astronomers are close to the discovery of a possibly large number of Goldilocks planets, Earth-like worlds in the habitable zone around their host star.

The data gathered by these instruments is also extremely valuable in the study of stellar activity, because both missions study a large number of objects for a long time. While the work at hand concentrated on a small number of landmark targets, future analyses will be able to derive statisticial properties of a large sample of stars.

During the course of this study, a large number of late-type stars were detected showing a distinct kind of photometric variability astoninglishly similar to the light curve of CoRoT-2A, however, without transits. These objects show dominant rotation periods between 1 and 10 days as well as a beating period on the order of weaks. Their variability amplitudes are on the order of a few percent; their photometric similarity suggests that these objects form a distinct class of active stars, possibly corresponding to a special evolutionary state or a common "flip-flop"-like dynamo mechanism. The study of these objects could help to understand the evolutionary stage of the CoRoT-2 system. We succesfully proposed spectroscopic follow-up observations with the TNG/SARG on La Palma to derive the fundamental stellar parameters of a sample of these stars and search for signatures of stellar activity. These observations have been carried out in December 2011 and will be analyzed in the near future.

Despite the superior quality of space-based photometry, our analysis of seven months of short-cadence Kepler data of TrES-2 shows that it is still difficult to unambiguously pinpoint the system parameters without ad hoc assumptions regarding the stellar limb darkening. In fact, the accuracy required to detect *variations* in the orbital parameters requires well-known limb-darkening coefficients. Especially in the case of near-grazing transits, uncertainties in the limb darkening directly translate into the remaining parameters mediated by the strong correlations. On the one hand, limb darkening is often approximated by analytical two-parameter "laws", because these models are advantageous from a model fitting perspective. On the other hand, these models are known to provide a poor description of synthetic model atmospheres, in particular for spherical models. It would therefore be much more consistent to directly incorporate the angle-dependent model atmosphere into the transit model. In comparison with Kepler's high-quality data this approach can even provide an important cross-check for atmosphere models.

Our spectroscopic study of the CoRoT-2 system has left us with a number of puzzling results and unanswered questions, especially regarding the nature of CoRoT-2A's companion:

- The late-type stellar companion seems to be gravitationally bound as indicated by our radial velocity measurements. If true, the companion could have an impact on the evolutionary dynamics of the whole system. In fact, it could account for the slight eccentricity (Gillon et al., 2010) and may even be responsible for the anomalously inflated radius of the planet (Guillot & Havel, 2011).
- CoRoT-2A and its companion should be a coeval pair. However, the companion is X-ray dark compatible with an evolved main-sequence object. This raises the question, whether CoRoT-2A could appear younger than it actually is due to interaction with its close-in planet. Similar discrepancies have been found in other systems and possible explanatory scenarios would be tidal interactions (Brown et al., 2011) or interacting magnetospheres of star and planet (Lanza, 2010; Cohen et al., 2010).
- CoRoT-2A is among the most active planet hosts stars, as evidenced for example by its strong chromospheric Ca II H and K emission. In view of the close-in orbit of its hot Jupiter, this raises the question, whether increased activity is typical for this kind of exoplanetary system. In their sample of exoplanet host stars, Knutson et al. (2010) find indications for a correlation between stellar chromospheric activity and the presence of a temperature inversion in the atmosphere of close-in massive planets. However, so far no significant correlations between chromospheric activity and other planetary parameters have been found (Canto Martins et al., 2011a).

Clearly, dedicated spectroscopic follow-up observations of CoRoT-2A's companion are desirable to reliably estimate the age of the system and confirm or refute the pair as a coeval binary. U. Wolter obtained observations with VLT/UVES under ESO program 088.D-0383, which will be analyzed in the near future.

Our studies demonstrate that the Rossiter-McLaughlin effect in chromospheric emission lines offers a method to resolve the extent of the chromosphere and the presence of plages and prominences on latitudes beneath the planetary path. However, our results are close to the noise limit and require further confirmation. An interesting target would be HD 189733, a much brighter ($V = 7.7$ mag) but similarly active planet host star (Knutson et al., 2010), which shows strong indications for planetary evaporation in the light of Lyα (Lecavelier Des Etangs et al., 2010). In the case of HD 189733, the transiting planet could even be used to simultaneously scan the bloated planetary exosphere and the stellar chromosphere with high resolution. Our group succesfully proposed spectroscopic observations of HD 189733 with VLT/UVES, which will be carried out under ESO program 089.D-0701.

From the instrumental point of view, future observations require a better wavelength stability of the spectrograph and simultaneously obtained calibration spectra. An interesting alternative are observations in the UV region such as an analysis of the Mg II h and k lines. These lines have even weaker photospheric background than the Ca II lines, however, they are only accessible with space-based instrumentation.

Regarding star-planet interactions, there is currently no unambiguous evidence that the mere presence of close-in Jovian planets has a direct influence on the host star. However, our studies of the two systems CoRoT-2 and CoRoT-7 showed that stellar activity should directly affect the planet and its evolution—at least, according to simple order-of-magnitude estimates assuming energy-limited escape. We found that high-energy radiation yields the evaporation of the planetary atmosphere, contributes to planetary mass loss, and, therefore, can play an important role in the evolution and formation of hot Jupiters oder close-in super-earths.

Planetary evaporation has been observed directly, e.g., in the case of HD 209458b (Vidal-Madjar et al., 2003). However, the detailed physical mechanisms leading to the evaporation of the atmosphere are far from understood. The complexity of the extreme environments in these systems currently allows to model only certain aspects of the problem via numerical simulations.

Studies of stellar activity in extrasolar planetary systems, like those presented in this thesis, can contribute to constrain the parameter space of available theoretical models. In the future, similar investigations will help to deepen our understanding of this vibrant field of research.

7.3. Epilogue

This thesis presents merely a glimpse of the strange new worlds populating our Universe. Today, astronomers exploring the diversity of extrasolar planetary systems are well on their way to find an answer to the fundamental question, whether Earth is unique—or one among many habitable worlds like our own. Recent results from a statistical analysis of microlensing observations indicate that on average every star in our galaxy should be orbited by $1.6^{+0.7}_{-0.9}$ planets at orbital distances between 0.5 and 10 AU (Cassan et al., 2012).

However, what kind of existential difference would it make, if we knew that we are not alone? Following the German philosopher Jonas (1996), such knowledge would make no difference at all (besides, of course, satisfying our scientific curiosity): There would certainly be no practical difference, given the immense light travel times involved in interplanetary communication. Further, the bare knowledge about the existence of other extraterrestrial civilizations in our Galaxy could hardly cure Pascal's feeling of loneliness and forlornness in the vastness of space, given that it cannot be cured facing a population of 7 billion human beings on our Earth. Neither would it change our ethical responsibility for our planet and its future. However, according to Jonas (1996) there *is* an important existential lesson to be learned about our role in the Universe:

> "That *our* signal going out somewhere or other in the universe may not be a death notice—with this we have enough at our hands. Let us concern ourselves with our Earth. [...] Let us care about it *as if* we were, in fact, unique in the universe."

Bibliography

Adams, E. R., López-Morales, M., Elliot, J. L., Seager, S., & Osip, D. J. 2010, *ApJ*, 714, 13

Adams, J. C. 1846, *MNRAS*, 7, 149

Agol, E., Steffen, J., Sari, R., & Clarkson, W. 2005, *MNRAS*, 359, 567

Aigrain, S., Pont, F., Fressin, F., et al. 2009, *A&A*, 506, 425

Albrecht, S. 2011, ArXiv e-prints 1109.1750, to be published in the proceedings for IAU Symposium 282, *From Interacting Binaries to Exoplanets: Essential Modeling Tools* by Cambridge University Press

Alonso, R., Auvergne, M., Baglin, A., et al. 2008, *A&A*, 482, L21

Alonso, R., Brown, T. M., Torres, G., et al. 2004, *ApJL*, 613, L153

Alsubai, K. A., Parley, N. R., Bramich, D. M., et al. 2011, *MNRAS*, 417, 709

Anderson, D. R., Hellier, C., Gillon, M., et al. 2010, *ApJ*, 709, 159

Andretta, V., Busà, I., Gomez, M. T., & Terranegra, L. 2005, *A&A*, 430, 669

Auvergne, M., Bodin, P., Boisnard, L., et al. 2009, *A&A*, 506, 411

Ayres, T. R. 2002, *ApJ*, 575, 1104

Ayres, T. R. & Testerman, L. 1981, *ApJ*, 245, 1124

Bakos, G. Á., Lázár, J., Papp, I., Sári, P., & Green, E. M. 2002, *PASP*, 114, 974

Baliunas, S. L., Donahue, R. A., Soon, W., & Henry, G. W. 1998, in Astronomical Society of the Pacific Conference Series, Vol. 154, Cool Stars, Stellar Systems, and the Sun, ed. R. A. Donahue & J. A. Bookbinder, 153

Baliunas, S. L., Donahue, R. A., Soon, W. H., et al. 1995, *ApJ*, 438, 269

Ballard, S., Fabrycky, D., Fressin, F., et al. 2011, *ApJ*, 743, 200

Barklem, P. S. 2008, Physica Scripta Volume T, 133, 014023

Barnes, J. W. & Fortney, J. J. 2003, *ApJ*, 588, 545

Barnes, J. W. & Fortney, J. J. 2004, *ApJ*, 616, 1193

Barnes, S. A. 2003, *ApJ*, 586, 464

Barnes, S. A. 2007, *ApJ*, 669, 1167

Bastian, T. S., Ewell, Jr., M. W., & Zirin, H. 1993, *ApJ*, 415, 364

Baumann, P., Ramírez, I., Meléndez, J., Asplund, M., & Lind, K. 2010, *A&A*, 519, A87

Beck, C. A. R. & Rezaei, R. 2011, *A&A*, 531, A173

Bell, S. J. & Hewish, A. 1967, *Nature*, 213, 1214

Berdyugina, S. V., Pelt, J., & Tuominen, I. 2002, *A&A*, 394, 505

Berdyugina, S. V. & Usoskin, I. G. 2003, *A&A*, 405, 1121

Berger, T. E., Rouppe van der Voort, L., & Löfdahl, M. 2007, *ApJ*, 661, 1272

Bertemes, F., Biehl, P., Nothe, A., & Schröder, O. 2004, Arch. Sachsen Anhalt, 2, 137

Bessel, F. W. 1838, *MNRAS*, 4, 152

Bigg, E. K. 1964, *Nature*, 203, 1008

Bohlin, R. C., Savage, B. D., & Drake, J. F. 1978, *ApJ*, 224, 132

Borucki, W. J., Koch, D., Basri, G., et al. 2010, Science, 327, 977

Borucki, W. J., Koch, D., Jenkins, J., et al. 2009, Science, 325, 709

Boss, A. P. 2001, Working Group on Extrasolar Planets: Position statement on the definition of a planet. `http://www.dtm.ciw.edu/boss/definition.html` (accessed February 21st, 2012)

Bouchy, F., Queloz, D., Deleuil, M., et al. 2008, *A&A*, 482, L25

Brandt, P. N. & Steinegger, M. 1998, *Sol. Phys.*, 177, 287

Briggs, K. R. & Pye, J. P. 2003, *MNRAS*, 345, 714

Brown, D. J. A., Collier Cameron, A., Hall, C., Hebb, L., & Smalley, B. 2011, *MNRAS*, 415, 605

Brown, T. M., Charbonneau, D., Gilliland, R. L., Noyes, R. W., & Burrows, A. 2001, *ApJ*, 552, 699

Bruntt, H., Deleuil, M., Fridlund, M., et al. 2010, *A&A*, 519, A51

Bubar, E. J. & King, J. R. 2010, *AJ*, 140, 293

Burnight, T. R. 1949, Phys. Rev., 76, 165

Busà, I., Aznar Cuadrado, R., Terranegra, L., Andretta, V., & Gomez, M. T. 2007, *A&A*, 466, 1089

Butler, R. P., Marcy, G. W., Williams, E., et al. 1996, *PASP*, 108, 500

Campbell, B., Walker, G. A. H., & Yang, S. 1988, *ApJ*, 331, 902

Canto Martins, B. L., Das Chagas, M. L., Alves, S., et al. 2011a, *A&A*, 530, A73

Canto Martins, B. L., Lèbre, A., Palacios, A., et al. 2011b, *A&A*, 527, A94

Canup, R. M. & Asphaug, E. 2001, *Nature*, 412, 708

Cassan, A., Kubas, D., Beaulieu, J.-P., et al. 2012, *Nature*, 481, 167

Castelli, F. & Kurucz, R. L. 2004, ArXiv Astrophysics e-prints 0405087

Catura, R. C., Acton, L. W., & Johnson, H. M. 1975, *ApJL*, 196, L47

Cecchi-Pestellini, C., Ciaravella, A., & Micela, G. 2006, *A&A*, 458, L13

Cecchi-Pestellini, C., Ciaravella, A., Micela, G., & Penz, T. 2009, *A&A*, 496, 863

Chapman, G. A. & Ziegler, B. 1996, *Sol. Phys.*, 168, 259

Charbonneau, D., Brown, T. M., Latham, D. W., & Mayor, M. 2000, *ApJL*, 529, L45

Christensen-Dalsgaard, J., Gough, D. O., & Thompson, M. J. 1991, *ApJ*, 378, 413

Christiansen, J. L., Ballard, S., Charbonneau, D., et al. 2011, *ApJ*, 726, 94

Claret, A. & Bloemen, S. 2011, *A&A*, 529, A75

Claret, A. & Hauschildt, P. H. 2003, *A&A*, 412, 241

Clarke, J. T., Ajello, J., Ballester, G., et al. 2002, *Nature*, 415, 997

Cohen, O., Drake, J. J., Kashyap, V. L., et al. 2009, *ApJL*, 704, L85

Cohen, O., Drake, J. J., Kashyap, V. L., Sokolov, I. V., & Gombosi, T. I. 2010, *ApJL*, 723, L64

Copernicus, N. 1543, De revolutionibus orbium coelestium (Johannes Petreius, Nuremberg, Holy Roman Empire of the German Nation)

Cowling, T. G. 1933, *MNRAS*, 94, 39

Cox, D. P. & Reynolds, R. J. 1987, *ARA&A*, 25, 303

Cuntz, M., Saar, S. H., & Musielak, Z. E. 2000, *ApJL*, 533, L151

Czesla, S., Huber, K. F., Wolter, U., Schröter, S., & Schmitt, J. H. M. M. 2009, *A&A*, 505, 1277

Czesla, S., Schröter, S., Wolter, U., et al. 2012, *A&A*, 539, A150

Daemgen, S., Hormuth, F., Brandner, W., et al. 2009, *A&A*, 498, 567

Desort, M., Lagrange, A.-M., Galland, F., Udry, S., & Mayor, M. 2007, *A&A*, 473, 983

Díaz, R. F., Rojo, P., Melita, M., et al. 2008, *ApJL*, 682, L49

Donahue, R. A. 1998, in Astronomical Society of the Pacific Conference Series, Vol. 154, Cool Stars, Stellar Systems, and the Sun, ed. R. A. Donahue & J. A. Bookbinder, 1235

Donati, J.-F., Semel, M., Carter, B. D., Rees, D. E., & Collier Cameron, A. 1997, *MNRAS*, 291, 658

Dreizler, S., Reiners, A., Homeier, D., & Noll, M. 2009, *A&A*, 499, 615

Eastman, J., Siverd, R., & Gaudi, B. S. 2010, *PASP*, 122, 935

Eaton, J. A. 1993, *ApJ*, 404, 305

Eddy, J. A. 1976, Science, 192, 1189

Edlén, B. 1942, Z. Astrophys., 22, 30

Einstein, A. 1916, Annalen der Physik, 354, 769

Eker, Z. 1994, *ApJ*, 420, 373

Erdélyi, R. & Ballai, I. 2007, Astronomische Nachrichten, 328, 726

Erkaev, N. V., Kulikov, Y. N., Lammer, H., et al. 2007, *A&A*, 472, 329

Favata, F., Micela, G., Orlando, S., et al. 2008, *A&A*, 490, 1121

Ferlet, R., Vidal-Madjar, A., & Gry, C. 1985, *ApJ*, 298, 838

Figueira, P., Pepe, F., Lovis, C., & Mayor, M. 2010, *A&A*, 515, A106

Fontenla, J. M., Avrett, E., Thuillier, G., & Harder, J. 2006, *ApJ*, 639, 441

Ford, E. B., Rowe, J. F., Fabrycky, D. C., et al. 2011, *ApJS*, 197, 2

Fossati, L., Haswell, C. A., Froning, C. S., et al. 2010, *ApJL*, 714, L222

Fressin, F., Torres, G., Rowe, J. F., et al. 2012, *Nature*, 482, 195

Fuhrmann, K. 1998, *A&A*, 330, 626

Fuhrmann, K. 2004, Astronomische Nachrichten, 325, 3

Fuhrmann, K., Axer, M., & Gehren, T. 1993, *A&A*, 271, 451

Fuhrmann, K., Axer, M., & Gehren, T. 1994, *A&A*, 285, 585

Fuhrmann, K., Pfeiffer, M., Frank, C., Reetz, J., & Gehren, T. 1997, *A&A*, 323, 909

Fukui, A., Narita, N., Tristram, P. J., et al. 2011, *PASJ*, 63, 287

Fulton, B. J., Shporer, A., Winn, J. N., et al. 2011, *AJ*, 142, 84

Galilei, G. 1613, Istoria e dimostrazioni intorno alle macchie solari e loro accidenti. Comprese in tre lettere scritte all'illvstrissimo signor Marco Velseri (G. Mascardi, Roma)

Galle, J. G. 1846, *MNRAS*, 7, 153

Gehren, T. 1981, *A&A*, 100, 97

Gelman, A., Carlin, J. B., Stern, H. S., & Rubin, D. B. 2004, Bayesian Data Analysis, 2nd edn. (Chapman & Hall, CRC Press, Florida)

Getman, K. V., Broos, P. S., Salter, D. M., Garmire, G. P., & Hogerheijde, M. R. 2011, *ApJ*, 730, 6

Ghezzi, L., Cunha, K., Smith, V. V., & de la Reza, R. 2010, *ApJ*, 724, 154

Gilliland, R. L., Chaplin, W. J., Dunham, E. W., et al. 2011, *ApJS*, 197, 6

Gilliland, R. L. & Dupree, A. K. 1996, *ApJL*, 463, L29

Gilliland, R. L., Jenkins, J. M., Borucki, W. J., et al. 2010, *ApJL*, 713, L160

Gillon, M., Lanotte, A. A., Barman, T., et al. 2010, *A&A*, 511, A3

Giménez, A. 2006, *ApJ*, 650, 408

Goldreich, P. & Lynden-Bell, D. 1969, *ApJ*, 156, 59

Gomes, R., Levison, H. F., Tsiganis, K., & Morbidelli, A. 2005, *Nature*, 435, 466

Gounelle, M. & Meibom, A. 2007, *ApJL*, 664, L123

Gray, D. F. 1992, The observation and analysis of stellar photospheres., ed. Gray, D. F. (Camb. Astrophys. Ser., Vol. 20,)

Gray, D. F. 1994, *PASP*, 106, 1248

Gray, D. F. & Johanson, H. L. 1991, *PASP*, 103, 439

Grether, D. & Lineweaver, C. H. 2006, *ApJ*, 640, 1051

Griffin, R. & Griffin, R. 1973, *MNRAS*, 162, 255

Grotrian, W. 1939, Naturw., 27, 214

Güdel, M. 2004, *A&A Rev.*, 12, 71

Güdel, M., Arzner, K., Audard, M., & Mewe, R. 2003, *A&A*, 403, 155

Guedel, M., Guinan, E. F., & Skinner, S. L. 1997, *ApJ*, 483, 947

Guillot, T. & Havel, M. 2011, *A&A*, 527, A20

Hale, G. E. 1908, *ApJ*, 28, 315

Hale, G. E., Ellerman, F., Nicholson, S. B., & Joy, A. H. 1919, *ApJ*, 49, 153

Hall, J. C. 2008, Living Reviews in Solar Physics, 5

Hatzes, A. P. 1995, *ApJ*, 451, 784

Hatzes, A. P. 1999, in Astronomical Society of the Pacific Conference Series, Vol. 185, IAU Colloq. 170: Precise Stellar Radial Velocities, ed. J. B. Hearnshaw & C. D. Scarfe, 259

Hatzes, A. P., Cochran, W. D., Endl, M., et al. 2003, *ApJ*, 599, 1383

Hébrard, G., Bouchy, F., Pont, F., et al. 2008, *A&A*, 488, 763

Hempelmann, A., Robrade, J., Schmitt, J. H. M. M., et al. 2006, *A&A*, 460, 261

Henry, G. W., Marcy, G. W., Butler, R. P., & Vogt, S. S. 2000, *ApJL*, 529, L41

Herschel, M. & Watson, D. 1781, Royal Society of London Philosophical Transactions Series I, 71, 492

Hirano, T., Suto, Y., Taruya, A., et al. 2010, *ApJ*, 709, 458

Holman, M. J., Fabrycky, D. C., Ragozzine, D., et al. 2010, Science, 330, 51

Holman, M. J. & Murray, N. W. 2005, Science, 307, 1288

Holt, J. R. 1893, Astronomy and Astro-Physics, 12, 646

Howarth, I. D. 2011, *MNRAS*, 418, 1165

Hoyer, S., Rojo, P., & Lopez-Morales, M. 2012, ArXiv e-prints 1201.3616

Huber, K. F. 2010, PhD thesis, University of Hamburg

Huber, K. F., Czesla, S., Wolter, U., & Schmitt, J. H. M. M. 2009a, *A&A*, 508, 901

Huber, K. F., Czesla, S., Wolter, U., & Schmitt, J. H. M. M. 2010, *A&A*, 514, A39

Huber, K. F., Wolter, U., Czesla, S., et al. 2009b, *A&A*, 501, 715

Hulse, R. A. & Taylor, J. H. 1975, *ApJL*, 195, L51

Hunger, H. 1992, Astrological reports to Assyrian kings., ed. Hunger, H. (Helsinki University Press)

Ineson, S., Scaife, A. A., Knight, J. R., et al. 2011, Nature Geoscience, 4, 753

Israelian, G., Delgado Mena, E., Santos, N. C., et al. 2009, *Nature*, 462, 189

Janson, M., Carson, J., Lafreniere, D., et al. 2012, ArXiv e-prints 1201.4388

Jaynes, E. T. 2003, Probability Theory: The Logic of Science (ed. G. Larry Bretthorst, Cambridge University Press, New York)

Jonas, H. 1996, Matter, Mind, and Creation: Cosmological Evidence and Cosmogonic Speculation, ed. Vogel, L. (Northwestern University Press), translated by Paul Schuchmann und Lawrence Vogel

Jones, C. A., Thompson, M. J., & Tobias, S. M. 2010, *Space Sci. Rev.*, 152, 591

Jones, E., Oliphant, T., Peterson, P., et al. 2001, SciPy: Open source scientific tools for Python, `http://www.scipy.org`

Jordán, A. & Bakos, G. Á. 2008, *ApJ*, 685, 543

Jordan, S. 2008, Astronomische Nachrichten, 329, 875

Judge, P. G., Solomon, S. C., & Ayres, T. R. 2003, *ApJ*, 593, 534

Jurić, M., Ivezić, Ž., Brooks, A., et al. 2008, *ApJ*, 673, 864

Kalas, P., Graham, J. R., Chiang, E., et al. 2008, Science, 322, 1345

Kashyap, V. L., Drake, J. J., & Saar, S. H. 2008, *ApJ*, 687, 1339

Kepler, J. 1609, Astronomia nova (G. Voegelinus, Heidelberg)

Kepler, J. 1619, Ioannis Keppleri Harmonices mvndi libri v. (Lincii Austriae, sumptibus Godofredi Tampachii excudebat Ioannes Plancvs)

Khodachenko, M. L., Lammer, H., Lichtenegger, H. I. M., et al. 2007, *Planet. Space Sci.*, 55, 631

Kipping, D. & Bakos, G. 2011, *ApJ*, 733, 36

Kipping, D. M. 2008, *MNRAS*, 389, 1383

Kipping, D. M. 2009, *MNRAS*, 392, 181

Kipping, D. M. 2010, *MNRAS*, 407, 301

Kleine, T., Mezger, K., Palme, H., Scherer, E., & Münker, C. 2005, *Geochim. Cosmochim. Acta*, 69, 5805

Knutson, H. A., Howard, A. W., & Isaacson, H. 2010, *ApJ*, 720, 1569

Koch, D. G., Borucki, W. J., Basri, G., et al. 2010, *ApJL*, 713, L79

Korhonen, H., Berdyugina, S. V., & Tuominen, I. 2002, *A&A*, 390, 179

Kron, G. E. 1947, *PASP*, 59, 261

Lagrange, J.-L. 1811, Mécanique Analytique (Courcier, Paris)

Lammer, H., Selsis, F., Ribas, I., et al. 2003, *ApJL*, 598, L121

Lanza, A. F. 2008, *A&A*, 487, 1163

Lanza, A. F. 2009, *A&A*, 505, 339

Lanza, A. F. 2010, *A&A*, 512, A77

Latham, D. W., Stefanik, R. P., Mazeh, T., Mayor, M., & Burki, G. 1989, *Nature*, 339, 38

Le Verrier, U. 1859, Lettre de M. Le Verrier à M. Faye sur la théorie de Mercure et sur le mouvement du périhélie de cette planète. Comptes rendus hebdomadaires des séances de l'Académie des sciences, Paris., 49, 379

Le Verrier, U. J. 1846, Astronomische Nachrichten, 25, 85

Lecavelier Des Etangs, A., Ehrenreich, D., Vidal-Madjar, A., et al. 2010, *A&A*, 514, A72

Lecavelier des Etangs, A., Vidal-Madjar, A., McConnell, J. C., & Hébrard, G. 2004, *A&A*, 418, L1

Leenaarts, J., Carlsson, M., Hansteen, V., & Rutten, R. J. 2007, *A&A*, 473, 625

Leitzinger, M., Odert, P., Kulikov, Y. N., et al. 2011, *Planet. Space Sci.*, 59, 1472

Linsky, J. L., Hunten, D. M., Sowell, R., Glackin, D. L., & Kelch, W. L. 1979, *ApJS*, 41, 481

Lissauer, J. J., Fabrycky, D. C., Ford, E. B., et al. 2011, *Nature*, 470, 53

Lobel, A., Aufdenberg, J., Dupree, A. K., et al. 2004, in IAU Symposium, Vol. 219, Stars as Suns : Activity, Evolution and Planets, ed. A. K. Dupree & A. O. Benz, 641

Lovis, C., Pepe, F., Bouchy, F., et al. 2006, in Society of Photo-Optical Instrumentation Engineers (SPIE) Conference Series, Vol. 6269, Society of Photo-Optical Instrumentation Engineers (SPIE) Conference Series

Maciejewski, G., Dimitrov, D., Neuhäuser, R., et al. 2010, *MNRAS*, 407, 2625

Maciejewski, G., Dimitrov, D., Neuhäuser, R., et al. 2011, *MNRAS*, 411, 1204

Maggio, A., Sciortino, S., Vaiana, G. S., et al. 1987, *ApJ*, 315, 687

Mandel, K. & Agol, E. 2002, *ApJL*, 580, L171

Marcy, G. W. & Butler, R. P. 1992, *PASP*, 104, 270

Marcy, G. W. & Butler, R. P. 2000, *PASP*, 112, 137

Martínez-Sykora, J., Hansteen, V., & Moreno-Insertis, F. 2011, *ApJ*, 736, 9

Mayor, M. & Queloz, D. 1995, *Nature*, 378, 355

McCullough, P. R., Stys, J. E., Valenti, J. A., et al. 2006, *ApJ*, 648, 1228

McLaughlin, D. B. 1924, *ApJ*, 60, 22

Megier, A., Strobel, A., Bondar, A., et al. 2005, *ApJ*, 634, 451

Megier, A., Strobel, A., Galazutdinov, G. A., & Krełowski, J. 2009, *A&A*, 507, 833

Meller, H. 2002, Arch. Sachsen Anhalt, 1, 7

Melo, C., Santos, N. C., Pont, F., et al. 2006, *A&A*, 460, 251

Mewe, R., Heise, J., Gronenschild, E. H. B. M., et al. 1975, *ApJL*, 202, L67

Mihalas, D. 1978, Stellar atmospheres 2nd edition, ed. Hevelius, J. (San Francisco, W. H. Freeman and Co., 1978. 650 p.)

Miralda-Escudé, J. 2002, *ApJ*, 564, 1019

Mislis, D., Heller, R., Schmitt, J. H. M. M., & Hodgkin, S. 2012, *A&A*, 538, A4

Mislis, D. & Schmitt, J. H. M. M. 2009, *A&A*, 500, L45

Mislis, D., Schröter, S., Schmitt, J. H. M. M., Cordes, O., & Reif, K. 2010, *A&A*, 510, A107

Mojzsis, S. J., Arrhenius, G., McKeegan, K. D., et al. 1996, *Nature*, 384, 55

Morbidelli, A., Levison, H. F., Tsiganis, K., & Gomes, R. 2005, *Nature*, 435, 462

Moreton, G. E. 1960, *AJ*, 65, 494

Morrill, J. S. & Korendyke, C. M. 2008, *ApJ*, 687, 646

Morrison, R. & McCammon, D. 1983, *ApJ*, 270, 119

Morton, T. D. & Johnson, J. A. 2011, *ApJ*, 729, 138

Murray-Clay, R. A., Chiang, E. I., & Murray, N. 2009, *ApJ*, 693, 23

Neilson, H. R. & Lester, J. B. 2011, *A&A*, 530, A65

Newton, I. 1687, Philosophiae naturalis principia mathematica (Jussu Societatis Regiaec Typis Joseph Streater, London)

Nordström, B., Mayor, M., Andersen, J., et al. 2004, *A&A*, 418, 989

Noyes, R. W., Weiss, N. O., & Vaughan, A. H. 1984, *ApJ*, 287, 769

O'Brien, D. P., Morbidelli, A., & Levison, H. F. 2006, *Icarus*, 184, 39

O'Donovan, F. T., Charbonneau, D., Mandushev, G., et al. 2006, *ApJL*, 651, L61

Ohta, Y., Taruya, A., & Suto, Y. 2005, *ApJ*, 622, 1118

O'Neal, D., Saar, S., & Neff, J. 1996, Astrophys. J., 463, 766

Orosz, J. A. & Hauschildt, P. H. 2000, *A&A*, 364, 265

Ottmann, R. 1994, *A&A*, 286, L27

Pál, A. 2008, *MNRAS*, 390, 281

Pál, A., Sárneczky, K., Szabó, G. M., et al. 2011, *MNRAS*, 413, L43

Parker, E. N. 1955a, *ApJ*, 122, 293

Parker, E. N. 1955b, *ApJ*, 121, 491

Parker, E. N. 1970, *ApJ*, 162, 665

Parker, E. N. 1993, *ApJ*, 408, 707

Patil, A., Huard, D., & Fonnesbeck, C. J. 2010, Journal of Statistical Software, 35, 1

Perryman, M. A. C., Lindegren, L., Kovalevsky, J., et al. 1997, *A&A*, 323, L49

Pettit, E. 1946, *PASP*, 58, 310

Pinsonneault, M. H. 1994, in Astronomical Society of the Pacific Conference Series, Vol. 64, Cool Stars, Stellar Systems, and the Sun, ed. J.-P. Caillault, 254

Piskunov, N. & Kochukhov, O. 2002, *A&A*, 381, 736

Pollacco, D. L., Skillen, I., Collier Cameron, A., et al. 2006, *PASP*, 118, 1407

Poppenhaeger, K., Czesla, S., Schröter, S., et al. 2012, accepted for publication in *A&A*

Poppenhaeger, K., Lenz, L. F., Reiners, A., Schmitt, J. H. M. M., & Shkolnik, E. 2011, *A&A*, 528, A58

Poppenhaeger, K., Robrade, J., & Schmitt, J. H. M. M. 2010, *A&A*, 515, A98

Poppenhäger, K., Robrade, J., Schmitt, J. H. M. M., & Hall, J. C. 2009, *A&A*, 508, 1417

Queloz, D., Eggenberger, A., Mayor, M., et al. 2000, *A&A*, 359, L13

Quirrenbach, A., Amado, P. J., Mandel, H., et al. 2010, in Society of Photo-Optical Instrumentation Engineers (SPIE) Conference Series, Vol. 7735, Society of Photo-Optical Instrumentation Engineers (SPIE) Conference Series

Rabus, M., Deeg, H. J., Alonso, R., Belmonte, J. A., & Almenara, J. M. 2009, *A&A*, 508, 1011

Radick, R. R., Mihalas, D., Hartmann, L., et al. 1982, *PASP*, 94, 934

Raetz, S., Maciejewski, G., Mugrauer, M., et al. 2011, Detection and Dynamics of Transiting Exoplanets, St. Michel l'Observatoire, France, Edited by F. Bouchy; R. Díaz; C. Moutou; EPJ Web of Conferences, Volume 11, id.05007, 11, 5007

Raetz, S., Mugrauer, M., Schmidt, T. O. B., et al. 2009, Astronomische Nachrichten, 330, 459

Rast, M. P. 2003, *ApJ*, 597, 1200

Reiners, A., Bean, J. L., Huber, K. F., et al. 2010, *ApJ*, 710, 432

Rice, J. B. 2002, Astronomische Nachrichten, 323, 220

Roberts, W. O. 1945, *ApJ*, 101, 136

Robrade, J., Schmitt, J. H. M. M., & Hempelmann, A. 2007, *Mem. Soc. Astron. Italiana*, 78, 311

Rossiter, R. A. 1924, *ApJ*, 60, 15

Russell, C. T. 1999, Australian Journal of Physics, 52, 733

Rutten, R. G. M. 1984, *A&A*, 130, 353

Rutten, R. J. 2007, in Astronomical Society of the Pacific Conference Series, Vol. 368, The Physics of Chromospheric Plasmas, ed. P. Heinzel, I. Dorotovič, & R. J. Rutten, 27

Rutten, R. J. 2010, in Recent Advances in Spectroscopy, ed. R. K. Chaudhuri, M. Mekkaden, A. V. Raveendran, & A. Satya Narayanan, Astrophysics and Space Science Proceedings (Springer Berlin Heidelberg), 163–175

Sanz-Forcada, J., Micela, G., Ribas, I., et al. 2011, *A&A*, 532, A6

Sanz-Forcada, J., Ribas, I., Micela, G., et al. 2010, *A&A*, 511, L8

Scharf, C. A. 2010, *ApJ*, 722, 1547

Schlesinger, F. 1910, Publications of the Allegheny Observatory of the University of Pittsburgh, 1, 123

Schmitt, J. H. M. M. 2009, in American Institute of Physics Conference Series, Vol. 1094, American Institute of Physics Conference Series, ed. E. Stempels, 473–476

Schmitt, J. H. M. M. & Favata, F. 1999, *Nature*, 401, 44

Schmitt, J. H. M. M. & Kürster, M. 1993, Science, 262, 215

Schmitt, J. H. M. M., Ness, J.-U., & Franco, G. 2003, *A&A*, 412, 849

Schneider, J. 2000, in ESO Astrophysics Symposia, Vol. 15, From Extrasolar Planets to Cosmology: The VLT Opening Symposium, ed. J. Bergeron & A. Renzini (Springer Berlin / Heidelberg), 499–504

Schneider, J. 2012, The Extrasolar Planets Encyclopaedia. `http://exoplanet.eu/index.php` (accessed February 21st, 2012)

Schneider, J., Rauer, H., Lasota, J. P., Bonazzola, S., & Chassefiere, E. 1998, in Astronomical Society of the Pacific Conference Series, Vol. 134, Brown Dwarfs and Extrasolar Planets, ed. R. Rebolo, E. L. Martin, & M. R. Zapatero Osorio, 241

Schröter, S., Czesla, S., Wolter, U., et al. 2011, *A&A*, 532, A3

Schröter, S., Schmitt, J. H. M. M., & Müller, H. M. 2012, *A&A*, 539, A97

Scuderi, L. J., Dittmann, J. A., Males, J. R., Green, E. M., & Close, L. M. 2010, *ApJ*, 714, 462

Seager, S. & Mallén-Ornelas, G. 2003, *ApJ*, 585, 1038

Shkolnik, E., Walker, G. A. H., Bohlender, D. A., Gu, P.-G., & Kürster, M. 2005, *ApJ*, 622, 1075

Siarkowski, M., Pres, P., Drake, S. A., White, N. E., & Singh, K. P. 1996, *ApJ*, 473, 470

Skumanich, A. 1972, *ApJ*, 171, 565

Smith, B. A. & Terrile, R. J. 1984, Science, 226, 1421

Smith, G. & Drake, J. J. 1987, *A&A*, 181, 103

Sneden, C. A. 1973, PhD thesis, University of Texas at Austin.

Snellen, I. A. G. 2004, *MNRAS*, 353, L1

Soderblom, D. R. 2010, *ARA&A*, 48, 581

Soderblom, D. R., Duncan, D. K., & Johnson, D. R. H. 1991, *ApJ*, 375, 722

Soderblom, D. R., Jones, B. F., Balachandran, S., et al. 1993, *AJ*, 106, 1059

Sousa, S. G., Alapini, A., Israelian, G., & Santos, N. C. 2010a, *A&A*, 512, A13

Sousa, S. G., Fernandes, J., Israelian, G., & Santos, N. C. 2010b, *A&A*, 512, L5

Sousa, S. G., Santos, N. C., Israelian, G., Mayor, M., & Monteiro, M. J. P. F. G. 2007, *A&A*, 469, 783

Sousa, S. G., Santos, N. C., Mayor, M., et al. 2008, *A&A*, 487, 373

Steenbeck, M. & Krause, F. 1969, Astronomische Nachrichten, 291, 49

Strassmeier, K. G. 2009, *A&A Rev.*, 17, 251

Strömgren, B. 1948, *ApJ*, 108, 242

Struve, O. 1929, *ApJ*, 69, 173

Struve, O. 1952, The Observatory, 72, 199

Tas, G. & Evren, S. 2000, Information Bulletin on Variable Stars, 4992, 1

Tatum, J. B. 2004, Physics - Stellar Atmospheres. `http://orca.phys.uvic.ca/~tatum/stellatm.html` (accessed February 28th, 2012)

Webster's encyclopedic dictionary. 1989, Webster's encyclopedic unabridged dictionary of the English language (Gramercy Books, dilithium Press, Ltd., New Jersey)

Thompson, M. J., Christensen-Dalsgaard, J., Miesch, M. S., & Toomre, J. 2003, *ARA&A*, 41, 599

Tierney, L. 1994, The Annals of Statistics, 22, 1701

Tingley, B. & Sackett, P. D. 2005, *ApJ*, 627, 1011

Toomer, G. J. 1998, Ptolemy's Almagest (Princeton University Press)

Touboul, M., Kleine, T., Bourdon, B., Palme, H., & Wieler, R. 2007, *Nature*, 450, 1206

Triaud, A. H. M. J., Collier Cameron, A., Queloz, D., et al. 2010, *A&A*, 524, A25

Triaud, A. H. M. J., Queloz, D., Bouchy, F., et al. 2009, *A&A*, 506, 377

Tsiganis, K., Gomes, R., Morbidelli, A., & Levison, H. F. 2005, *Nature*, 435, 459

Uchida, Y., Altschuler, M. D., & Newkirk, Jr., G. 1973, *Sol. Phys.*, 28, 495

Unsöld, A., Struve, O., & Elvey, C. T. 1930, *ZAp*, 1, 314

Vainshtein, S. I. & Cattaneo, F. 1992, *ApJ*, 393, 165

Vaughan, A. H., Preston, G. W., & Wilson, O. C. 1978, *PASP*, 90, 267

Vernazza, J. E., Avrett, E. H., & Loeser, R. 1981, *ApJS*, 45, 635

Vidal-Madjar, A., Lecavelier des Etangs, A., Désert, J.-M., et al. 2003, *Nature*, 422, 143

Vogt, S. S., Butler, R. P., Rivera, E. J., et al. 2010, *ApJ*, 723, 954

Vogt, S. S. & Penrod, G. D. 1983, *PASP*, 95, 565

Wang, Y.-M., Sheeley, Jr., N. R., & Nash, A. G. 1991, *ApJ*, 383, 431

Watson, A. J., Donahue, T. M., & Walker, J. C. G. 1981, *Icarus*, 48, 150

Watson, C. A. & Marsh, T. R. 2010, *MNRAS*, 405, 2037

Weisberg, J. M. & Taylor, J. H. 2005, in Astronomical Society of the Pacific Conference Series, Vol. 328, Binary Radio Pulsars, ed. F. A. Rasio & I. H. Stairs, 25

Weiss, N. O. & Thompson, M. J. 2009, *Space Sci. Rev.*, 144, 53

Welsh, B. Y., Lallement, R., Vergely, J.-L., & Raimond, S. 2010, *A&A*, 510, A54

Williams, J. P. 2010, Contemporary Physics, 51, 381

Wilson, O. C. & Bappu, M. K. V. 1957, *ApJ*, 125, 661

Winn, J. N., Fabrycky, D., Albrecht, S., & Johnson, J. A. 2010, *ApJL*, 718, L145

Winn, J. N., Noyes, R. W., Holman, M. J., et al. 2005, *ApJ*, 631, 1215

Wolszczan, A. & Frail, D. A. 1992, *Nature*, 355, 145

Wolter, H. 1952, Annalen der Physik, 445, 94

Wolter, U., Schmitt, J. H. M. M., Huber, K. F., et al. 2009, *A&A*, 504, 561

Zucker, S. 2003, *MNRAS*, 342, 1291

Zucker, S. & Mazeh, T. 2002, *ApJL*, 568, L113

Acknowledgments

I would like to thank *Astronomy & Astrophysics* (copyright owned by ESO) for the kind permission to reproduce the papers Mislis et al. (2010), Schröter et al. (2011), Schröter et al. (2012), Czesla et al. (2012), and Poppenhaeger et al. (2012).

Für die finanzielle Unterstützung während meines Promotionsstudiums bedanke ich mich beim Deutschen Zentrum für Luft- und Raumfahrt unter der Projektnummer 50OR0703 und bei der Deutschen Forschungsgesellschaft für Förderung im Rahmen des Graduiertenkollegs 1351/2 „Extrasolar Planets and their Host Stars“.

Mein aufrichtiger Dank gilt Prof. Jürgen Schmitt für die Gelegenheit, als Teil seiner Arbeitsgruppe an der Hamburger Sternwarte das Universum der (aktiven) Sterne zu erforschen, sowie für stete Aufmunterung, unbedingten Rückhalt und fachlichen Rat. Stefan Czesla danke ich für die wissenschaftliche Wegweisung, Betreuung und Inspiration. Es ist selten, dass sich herausragende fachliche Kompetenz mit menschlicher Wärme und Geduld gegenüber Unerfahrenheit paaren. Seine Bedeutung für das Gelingen dieser Arbeit kann nicht hoch genug veranschlagt werden.

Den Autoren der Publikationen, bei denen ich mitwirken durfte, namentlich Stefan Czesla, Dimitris Mislis und Katja Poppenhäger, danke ich für die Bereitschaft, mich in ihre Arbeit einzubinden. Allen Mitautoren danke ich für die Zusammenarbeit und ihre wertvollen Anregungen und Beiträge. Prof. Ansgar Reiners danke ich für die bereitwillige Begutachtung dieser Arbeit.

Für gemeinsame Gespräche, Anregungungen, Diskussionen, hilfreiche Anmerkungen und alles, was „fröhliche Forschung“ sonst so auszeichnet, danke ich insbesondere Stefan Czesla, Carolina von Essen, Klaus Huber, Holger Müller, Uwe Wolter, meinen Bürogenossen, Jan Robrade und Christian Schneider, sowie der ganzen Arbeitsgruppe.

Uwe Wolter möchte ich dafür danken, mir im Rahmen der Astronomie-Werkstatt ein spannendes und für mich womöglich zukunftsweisendes Betätigungsfeld eröffnet zu haben.

Allen Mitarbeiterinnen und Mitarbeitern der Hamburger Sternwarte sei für ein unvergleichliches Arbeitsklima gedankt.